Analysis and dynamics of multiple-spike waves in neural networks



Joshua Leonard Davis

School of Mathematical Sciences

University of Nottingham

This dissertation is submitted for the degree of

Doctor of Philosophy

Supervisors:
Daniele Avitabile
Mikhail Tretyakov

August 2017

I dedicate this thesis to my mum and dad—the most loving parents anyone can ever hope for.

Declaration

I am aware of and understand the university's policy on plagiarism and I certify that this thesis is my own work, except where indicated by referencing, and the work presented in it has not been submitted in support of another degree or qualification from this or any other university or institute of learning.

Joshua Leonard Davis

August 2017

Acknowledgements

To my supervisor Daniele Avitabile, I offer my sincerest gratitude for your invaluable guidance, genorosity and wisdom—the inspiration and encouragment you have given me, through all the toils and turns, has made this PhD a reality.

I would also like to thank Kyle Wedgwood for the sound advice and useful insights you have given me throughout these years. I have enjoyed our many discussions, these I find always contextualise and enrich my knowledge of the matter at hand.

Huge thanks also go out to the other academics I have made a connection with, including: Michael Tretyakov for keeping a watchful eye on my progress and the experienced words on uncertainty quantification, Steve Coombes for the engaging seminars and useful pointers on wave stability, Rudiger Thul for our very first conversation which helped solidfy my motivation to study at the department and all the great teachings in mathematical biology that followed, Mathieu Desroches for introducing me to the intricacies of fast-slow analysis and superb wit, and then finally to Reuben O'Dea and Keith Hopcraft for their many thought-provoking questions and enthusiasm regarding my research.

Many thanks too for the fantastic university support staff: Sarah Burton, Helen Cunliffe, Hilary Lonsdale, Krys Glowczewska, Andrea Blackbourn and Daisy Carter for their prompt and much needed help in administrative matters.

I will always remember with fondness the countless breaks from PhD work I have had with Mayte Quintana Bonilla and our progressive critique of university infrastructure. In addition, I thank Wilhelm Braun, Aytul Goçke, Agne Tilunaite, Áine Byrne for various interesting discussions and their contributions to journal club.

Great thanks to my friends and housemates who have always supplied copious amounts of much needed distractions and fun. Then also my sisters for helping me through the toughest moments and their patience. Finally, I thank my remarkable parents, who have unconditionally given me their neverending love and support throughout my life. One day I hope to find a way of thanking you enough.

This PhD has been funded by Nottingham University.

Abstract

Spatially structured bursts of propagating neural activity revealed in cortical slice experiments and *in vivo* tantalise many scientists on their possible functional mechanisms. Theoretical studies suggest waves with complex firing patterns afford a great capacity for the transmission of information across the brain. This thesis develops a framework for analysing the dynamics of such waves within spiking neuronal networks. We seek to investigate important questions concerning how the wave's spatiotemporal voltage properties, propagation speed and spike time interval distributions depend on the underlying network structure and the intrinsic features of the neurons that make up the network. These are often difficult to extract with biophysically detailed network models. We therefore analyse simplified spiking networks of synaptically connected neurons, capable of supporting a rich repertoire of propagating activity, yet, amenable to mathematical analysis. Useful information is then obtained on the dynamics of waves found in this network in relation to the model's parameters. These results can be compared to the findings obtained from more detailed computational studies and experimental observations.

Numerical simulations in discrete networks of integrate-and-fire neurons reveal localised bumps that can wander diffusively across the network. These wandering bumps are seen to evolve into persistent synchronous coherent propagating structures, where neurons fire multiple times as the wave envelope passes over. We call these structures multiple-spike waves. An intrinsic feature of the neuron, describing how quickly neurons process synaptic current, is shown to be an important determinant in the emergent network activity.

Waves with different number of spiking events co-exist across most parameter regimes, and with lateral-inhibition synaptic connectivity structure, can

exhibit large variability in wave speed that has not been reported in studies of networks with purely excitatory connectivity. As a result, we investigate the interaction dynamics of multiple-spike waves on a large spatial domain. Here we find that multiple-spikes waves can merge to form a composite system, with greater complexity in the firing patterns, increasing the wave's information content.

Mathematical progress is made by studying a partial integro-differential equation that is equivalent to the discrete network as the number of neurons tends to infinity. We develop a method of solving the wave speed of the multiple spike waves and its set of spike-times, which then allows us to construct the network's exact voltage and synaptic profiles and formulate a non-local eigenvalue problem to compute asymptotic stability. This is achieved by considering general perturbations around the wave's firing times.

An in-depth numerical study on the multiple-spike wave's bifurcation structure is performed, uncovering various mechanisms behind propagation failure and how the wave's dynamics depend on the network's system parameters. The analysis of waves with a large number of spikes poses interesting questions regarding the existence of stationary bump solutions in the continuum limit.

Uncertainty quantification is performed on waves, revealing how different types of uncertainty in system parameters influence the wave solutions statistical properties. This allows for predictions of the spatial regions of the waves profile most vulnerable to destabilisation.

We finally analyse synaptically generated waves in a similar spiking network of Morris-Lecar neurons, where we find interesting transitions from single to double spike waves. Also, similar to what was seen in the integrate-and-fire network, the wave's dynamics at the network level is strongly influenced by the neuron's intrinsic features.

Contents

Nomenclature **xi**

1 Introduction and Background **1**

1.1 Motivation 1

1.2 Neurons: biological features and models 5

1.2.1 Action potential 6

1.2.2 Synaptic processing 8

1.2.3 Single neuron models 11

1.3 Network topology 14

1.3.1 Lateral-inhibition 15

1.4 Coherent structures in the brain 17

1.4.1 Localised bumps 18

1.4.2 Propagating activity 20

1.5 Propagation mechanisms in neural networks 24

1.6 Neural network models 26

1.6.1 Weakly coupled networks 28

1.6.2 Rate-based models 30

1.6.3 Simplified spiking network models 34

1.7 Overview of the thesis 39

2 Discrete integrate-and-fire network **43**

2.1 Introduction 43

2.2 Model description 44

2.3 Description of the event-driven model 45

2.4 Spatially localised bumps 48

2.4.1 Dependence on initial stimulus 50

2.4.2 Multiple bumps on larger domains 51
2.5 Stationary bumps firing rate and existence condition 52
2.6 Wandering bumps 55
2.7 Drifting bumps 61
2.8 Propagating multiple-spike coherent structures 63
2.8.1 Waves in purely excitatory network 67
2.9 Wave interaction dynamics 70
2.10 Summary 75

3 Continuum limit multiple-spike waves 77
3.1 Introduction 77
3.2 Discrete network to the continuum limit 79
3.3 Continuum spiking network 81
3.3.1 Single-spike waves in continuum spiking network 82
3.4 Characterisation of travelling waves in terms of firing functions . . 84
3.5 Travelling wave construction 89
3.6 Wave Stability 91
3.6.1 Computation of eigenvalues for multiple-spike waves and translation eigenmode 101
3.6.2 Single-spike case 102
3.7 Summary 102

4 Bifurcation analysis of multiple spike waves 104
4.1 Introduction 104
4.2 Bifurcations 106
4.2.1 Grazing points 107
4.2.2 Hopf bifurcations 109
4.2.3 Testing validity of Hopf instabilities in discrete networks . 111
4.2.4 Analysing the firing-time history of a slowly destabilising wave 112
4.3 Contrasting bifurcation structures of TW_2 and TW_3 114
4.4 Composite states 118
4.5 Balance of excitation and inhibition 121

4.6 Effect of finite rise time in $\alpha(t)$ . . . 123
4.7 Increasing the number of threshold crossings . . . 126
4.8 Comparison with purely excitatory network . . . 130
4.9 Summary . . . 134

5 Uncertainty quantification of multiple-spike waves 136
5.1 Introduction . . . 136
5.2 Uncertainty quantification of homogeneous network . . . 138
5.2.1 Monte Carlo approach . . . 139
5.2.2 Law of the unconscious statistician . . . 139
5.2.3 Uncertainty in β and b_1 . . . 144
5.2.4 Uncertainty quantification of TW_3 spatial profiles . . . 145
5.3 Heterogeneity in synaptic processing rate . . . 149
5.3.1 Heterogeneous network evolution equation . . . 149
5.3.2 Monte Carlo simulations . . . 150
5.4 Summary . . . 154

6 Morris-Lecar spiking network 156
6.1 Introduction . . . 156
6.2 Synaptically connected network of conductance-based neurons . . . 157
6.3 Single neuron Morris-Lecar . . . 160
6.3.1 Excitability . . . 164
6.3.2 Bistability and transition to oscillatory state . . . 166
6.4 Waves in Morris-Lecar network . . . 168
6.5 Deriving a first-order system . . . 174
6.6 Necessary condition for homoclinic connections . . . 175
6.7 Travelling wave solutions bifurcation structure . . . 179
6.7.1 Wave speed dependence on I_{app} . . . 179
6.7.2 Snaking connections to double pulse . . . 182
6.8 Multi-point boundary value problem . . . 184
6.8.1 Construction of pulse in Heaviside limit . . . 185
6.9 Enhanced Morris-Lecar Network . . . 189
6.10 Summary . . . 196

7 Conclusions and Future Directions **198**

7.1 Conclusions 198

7.2 Future directions 200

Bibliography **204**

Chapter 1

Introduction and Background

1.1 Motivation

The basic components of our physical reality—light, sound, smell, taste and touch—are constantly being transformed into electrical signals and transported around a gargantuan network of around 10^{10} tree-like cells, which form approximately 10^{15} connections with each other. The human brain is, as one could imagine, an incredibly complex system, processing all the electrical signals received from the virtue of living, at staggering frequencies, across multiple spatiotemporal scales (see fig. 1.1). The net result is manifested in our actions—the way we interact with the external world, as it interacts with us. Understanding how the brain achieves this is at the heart of neuroscience research.

Neuroscience has come a long way in the last few centuries, leading to many more questions than started with. A common question posed in neuroscience is how do microscopic and macroscopic processes relate? In mathematical neuroscience, one would usually view ion channel dynamics, dendritic tree structure and the single neuron voltage dynamics itself as the microscopic realm. Conversely, blood flow and metabolic processes measured using PET or fMRI scanners, or scalp EEG recordings measuring the large scale regional electrical activity of the whole brain are widely regarded as macroscopic [65].

Mesoscopic brain dynamics usually refers to the neural activity or dynamics at intermediate spatial scales of a few millimeters to centimeters, and temporally ranging from milliseconds to seconds. Neuronal activity at the mesoscopic scale is characterised by noisy and seemingly chaotic dynamics of great complexity,

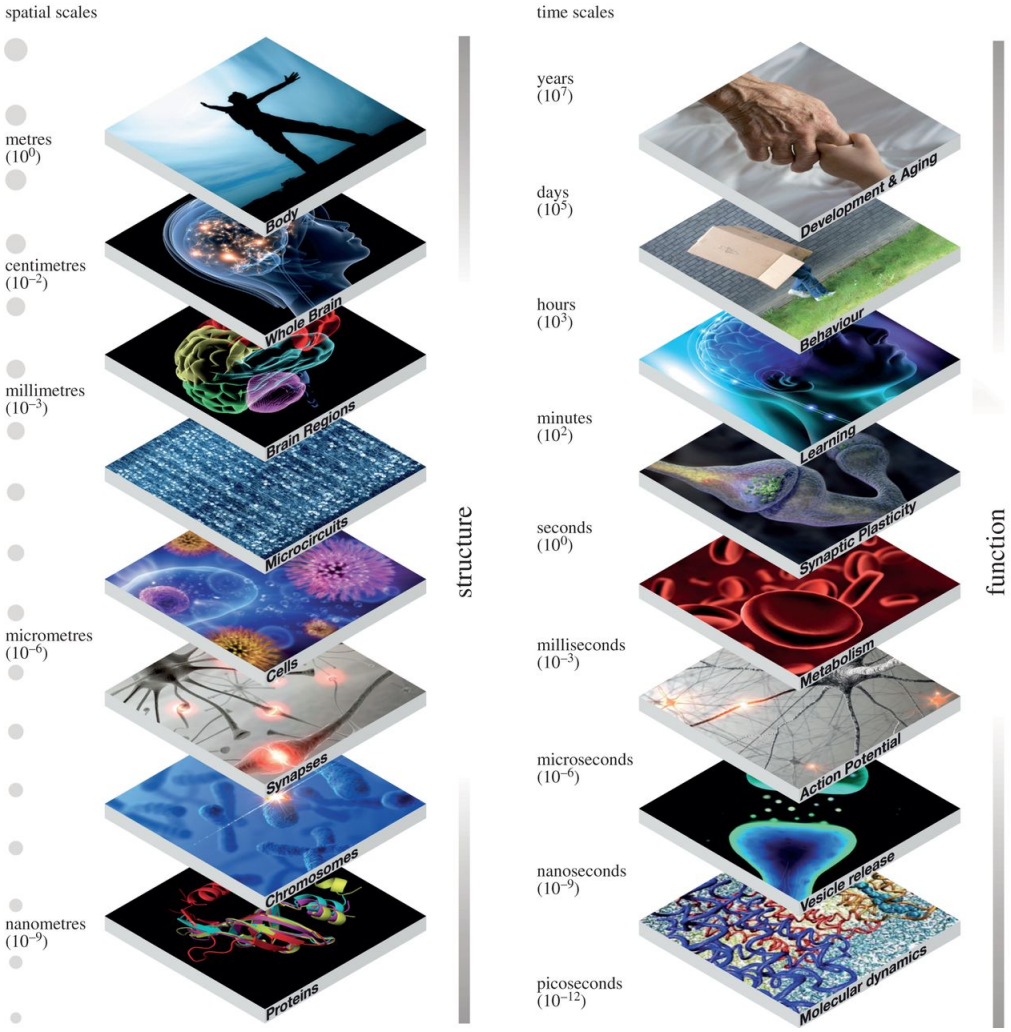


Figure 1.1 The human brain is an intrinsically multi-scale, multi-level organ operating across spatial scales ranging from nanometres (proteins) to centimetres (the human body) and temporal scales from picoseconds (atomic interactions) to years (the lifespan of a human being). The illustration here of the spatial and temporal hierarchy of structures and functional properties that make up neuroscience today is courtesy of Richard Frackowiak and Henry Markram [65].

but within this, emergent coherent structures of spatiotemporal activity exist. Spatially localised bumps and propagating waves of neuronal activity are two key examples of coherent structure observed in experiment and have been associated with a large variety of mental processes. The analysis and dynamics of these coherent structures is the main focus of this study.

There are numerous approaches to modelling neural networks; deciding upon an appropriate modelling strategy is made a lot easier if one has a specific question one wishes to answer. If, on the other hand, you were to wake up in the morning and

arbitrarily decide to model a neural network, this fateful decision will inevitably initiate a colossal cascade of further decisions.

A major decision involves deciding the level of biophysical detail at which you wish to model the neurons that compose your network. Mathematical descriptions describing the wide variety of nonlinear dynamics neurons exhibit is an abundant resource. Hodgkin-Huxley's Nobel prize winning contribution in the 1950*s* provides a good place to start for biophysical realism [99], but there have been numerous refinements and abstractions of their model since.

Additionally, what cell type and morphology should be used? Also, how many cell types and morphologies should be modelled? The same applies for the number of ion channels and synaptic terminals, if you would also like to model the short-term neurotransmitter dynamics. Stochastic dynamics may also spring to mind, which would then involve deciding upon what random process to use and how to place that within the neuron and perhaps the wider context of the network.

Once you have settled on an appropriate (set of) neuron model(s), the next step is to decide how the neurons communicate with each other. It is fair to say that with approximately 10^{15} neuronal connections in the human brain, the number of topologies to choose from may be fairly large. Perhaps isolating a specific region of the brain's anatomy with a known connectivity structure would work best, or would you prefer to model the macroscopic-scale network dynamics between a few of these regions? In both cases, the number of excitatory and inhibitory connections, along with the relative strengths of these connections would also have to be taken in to account. Should you then be so bold as to include the long-term dynamics of the connection strengths? There is a lot of research out there on plasticity after all.

At this point, you may ask yourself why you want(ed) to model a neural network in the first place. Traub et al. propose an answer, and built a large-scale model of a single-column thalamocortical network with 3560 multicompartmental neurons [182]. Their reason was to increase the understanding of the neural network mechanisms underpinning simple phenomena, such as pharmacologically induced network oscillations. In the introduction of their paper they commented

on the problems they had to overcome in the development of such a vastly complex network:

"Any model, even a small bit of cortex, is subject to difficulties and hazards: limited data, large numbers of parameters, criticisms that models with complexity comparable to the modelled system cannot be scientifically useful, the expense and slowness of the necessary computations, and serious uncertainties as to how a complex model can be compared with experiment and shown to be predictive."

A possible research project for a psychologist could perhaps be how neuroscientists generally address these issues. Some possible cases to consider: Traub et al. said that the adoption of a 'state of denial' is needed in order to persevere; Henry Markram, once the executive leader of the Human Brain Project (HBP), a plan to construct a model of an entire brain from first principles and simulate it, states "[I want] to be able to step inside a simulation of my son's brain and see the world as he sees it"; Peter Dayan implies that limiting uncertainties in network models is best, claiming Markram's attempts to be "radically premature"; members of the HBP respond by saying that they share the uncertainty surrounding large-scale simulation, but "reconstructing and simulating the human brain is a vision, a target; the benefits will come from the technology needed to get there. That technology, developed by the HBP, will benefit all of neuroscience as well as related fields".

We acknowledge the many possible benefits of advancing neuroscience in any direction and the ever present potential for novel unexpected discoveries. In this study, we have decided to analyse a simplified network of neurons, limiting biological complexity wherever possible. This offers opportunities through mathematical analysis and efficient numerical simulation to reveal general principles embodying the dynamics of various types of coherent structures in neural activity, with the hope that these finding are also relevant to more biophysically realistic network models.

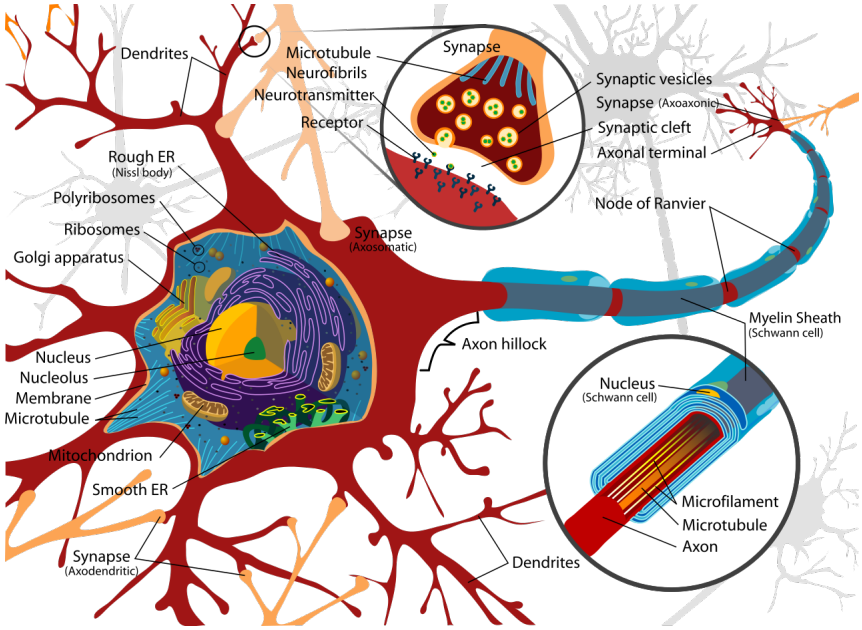


Figure 1.2 Schematic illustration of a typical neuron cell. Produced and released voluntarily into public domain under Wikipedia commons by Mariana Ruiz Villarreal.

1.2 Neurons: biological features and models

The human brain consists of around 100 billion electrically excitable cells called *neurons*. Neurons exist in numerous different shapes and sizes and are typically classified by their morphology and function. Most neurons possess three main anatomical constituents: the soma, dendrites, and axon.

The soma is the cell's body, containing the nucleus where most protein synthesis occurs. Dendrites are a collection of branches that extend outwards from the soma, forming a tree-like structure known as the dendritic tree. The axon is a cable-like projection from the soma, capable of connecting to the dendritic branches of other neurons vast distances away relative to the size of the soma. In fig. 1.2 an annotated schematic of a neuron is given.

The neuron is a complicated nonlinear system. Many of the brain's functions are determined by the neuron's highly specialised ability to transmit and process electrical signals known as *action potentials* (AP) [26].

1.2.1 Action potential

Hodgkin and Huxley provided the first complete quantitative description of the action potential—balancing experimentation and theory with remarkable elegance [94, 99]. Their Nobel prize winning work arose from the experimental study of a squid axon, where they made the first intracellular recording of an action potential (see fig. 1.3(a)), along with quantitative measurements of its ionic currents. In doing so, they found two distinct current components: a rapid inward current carried by sodium (Na^+) ions, and a more slowly activating outward current carried by potassium (K^+) ions. They concluded that the two ionic currents arise from independent permeability mechanisms with time dependent conductances and membrane potential. It was then possible to describe the action potential in terms of the neuron's ion channel dynamics.

The first phase of the action potential is characterised by the opening of channels, allowing Na^+ ions to flow inwards. This causes a displacement of the membrane's resting potential, which facilitates more and more channels to open. The process continues rapidly until all channels are open, this results in a sharp upwards movement in the membrane's potential—a *depolarisation phase*.

The rapid depolarisation of the membrane leads to a fast reversal in the polarity of the plasma membrane, quickly inactivating the Na^+ channels. Now Na^+ ions cannot enter the neuron through its membrane and they are also actively transported out of the neuron itself, thus lowering the membrane's permeability to Na^+ relative to K^+, driving the membrane voltage back towards the resting potential. Meanwhile, the heightened voltage levels have opened voltage-sensitive K^+ channels, generating an outward current, which also acts to drive the membrane voltage back to rest. The net result is a comparably sharp downwards movement in the membrane potential—a *repolarisation phase*.

The final phase is marked by an undershoot (or hyperpolarisation) past the neuron's resting potential, this is because there are many more open K^+ channels than usual, and these take a relatively long time to close. Once the membrane's K^+ permeability returns to normal values, the neuron is at its resting potential and this *afterhyperpolarization* phase comes to an end.

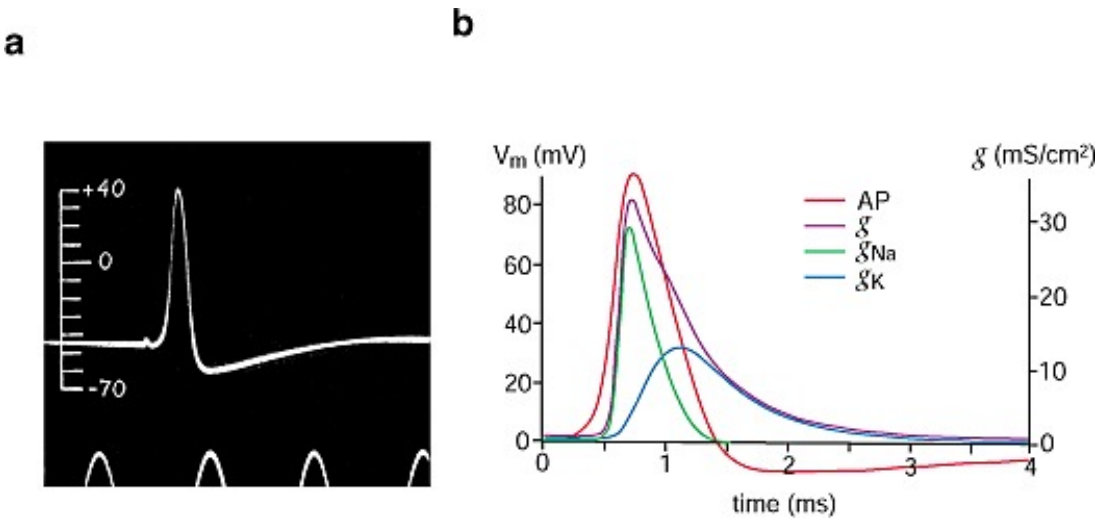


Figure 1.3 (a) First ever experimental recording of an action potential, found in a squid axon, taken from [98]. The intracellular voltage signal was recorded for 2ms. (b) Hodgkin-Huxley model showing time signature of a neuron's voltage and ionic conductances underlying the action potential, taken from the quantitative model proposed in Nobel prize winning paper [99] given by eq. (1.1). courtesy of [94].

Hodgkin and Huxley developed a statistical model of ionic channel conductances, whereby individual channel gates open or close independently of one another (but as a function of membrane voltage) in a probabilistic fashion. They then were able to represent the membrane voltage dynamics in terms of the sum of the separate Na^+, K^+ and leak currents. This seminal model consists of four coupled non-linear ordinary differential equations:

$$C\frac{\mathrm{d}v}{\mathrm{d}t} = -g_{\mathrm{Na}}m^3h(V-E_{\mathrm{Na}}) - g_{\mathrm{K}}n^4(V-E_{\mathrm{K}}) - g_{\mathrm{leak}}(V-E_{\mathrm{leak}}) + I_{\mathrm{ext}} \qquad (1.1)$$
$$\frac{\mathrm{d}z}{\mathrm{d}t} = \alpha_z(v)(1-x) - \beta_z(v)z \qquad \text{for} \quad z = n, m, h$$

where the gating variables m and h (for activation and inactivation of g_{Na}) and n (for activation of g_{K}) have separate voltage-dependent equations. The resting potentials are given as $E_{\mathrm{K}}, E_{\mathrm{Na}}, E_{\mathrm{leak}}$ and I_{ext} represents all other currents external to the membrane.

These seminal equations established a firm link between the microscopic realm of ion channels, to the (relatively) macroscopic level of currents and action potentials. In fig. 1.3(b) the voltage and conductance time signatures of an action potential modelled using the Hodgkin-Huxley equations is given [99].

The Hodgkin–Huxley model is considered to be a biophysically realistic model, capable of reproducing and explaining a remarkable range of experimental data. Most biophysical spiking neuron models are in fact based on these equations.

So far, we have summarised the key ionic mechanisms responsible for the action potential, under the assumption the neuron has received a sufficiently large depolarising current to initiate the action potential response. This summary has been based on [107, 115]. Experimentally this can be achieved by directly injecting a stimulus current to the neuron. But, in reality, action potentials are initiated by the integration of synaptic potentials generated across thousands of *synaptic* connections linking the neuron to thousands of other neurons in a network [178].

Thus, to understand the complicated signalling in the brain, it is important to not simply study neurons in isolation, but within context of neurons continually exchanging action potentials in neural networks.

1.2.2 Synaptic processing

With this in mind we now describe the electrical response induced across the synaptic terminals of a postsynaptic neuron, due to the arrival of an action potential from a presynaptic neuron. This response is commonly referred to as a postsynaptic potential (PSP) [168]

There are two main types of synaptic terminals: the chemical and electric synapse. The chemical synapse is the most common type of synapse in the brain with a typical neuron giving rise to several thousand synaptic terminals, mostly connecting axons to dendrites, but other types of connections including axon-to-axon, axon-to-soma and dendrite-to-dendrite are known to exist. The electrical synapse is a completely different type of transmission mechanism involving the passive and bi-directional ionic current flow from one neuron to another through gap junction pores. These electrical synapses transfer current considerably faster than the chemical synapses, but are in distinctly smaller numbers and play more of a synchronising role between coupled neurons. For the purposes of this study, we focus on the PSPs formed at chemical synapses.

The production of a PSP begins with the arrival of a wave of electrochemical excitation (action potential) at the presynaptic terminal of a chemical synapse.

A complex chain of bio-chemical processing interactions lead to the release of neurotransmitters from synaptic vesicles within the presynaptic terminal, which then diffuse across the synaptic cleft. Ligand-gated ion channels (LGICs) then bind with the neurotransmitters and result in the opening or closing of specific ion channels. The regulating ligands lead to the selective uptake of specific ions such as K^+, Na^+, Ca^{2+} and Cl^- across the postsynaptic cell membrane, the re-configuring ion channels represent a changing synaptic conductance over time and results in a net ionic current passing into the postsynaptic cell.

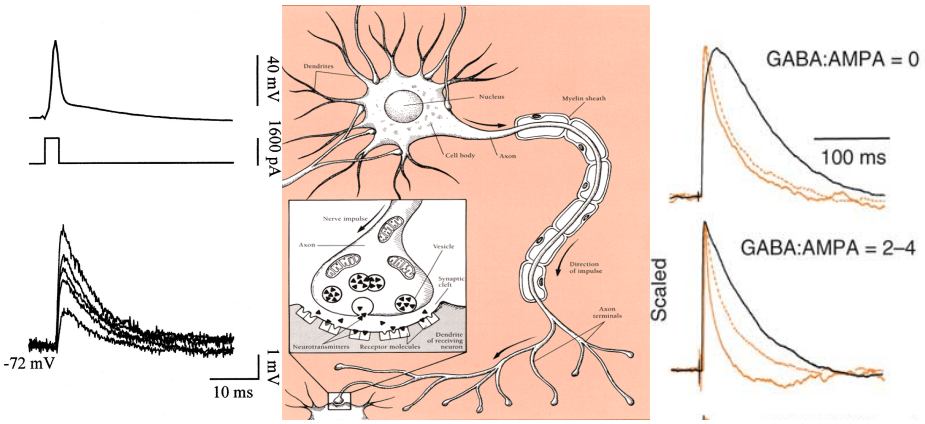


Figure 1.4 Illustrations adapted from [104, 133]. Left column: five superimposed EPSPs elicited in an interneuron in response to action potentials triggered by brief depolarizing current pulses in the pre-synaptic pyramidal cell. There is a large variation in amplitude of each PSP. Central panel: annotated pre-synaptic neuron and synapse diagram. Right Column: thalamocortical PSPs in stellate cells with different neurotransmitter $GABA : AMPA$ ratios pharmologically manipulated. Note the change in timescale of decay from the control in black [104].

PSPs come in two main forms: excitatory and inhibitory. If the net effect of the opening of ion channels is an increase in positively charged ions across the postsynaptic cell membrane, then the synapse is excitatory (EPSP), because the membrane has been depolarised bringing the neuron closer to triggering an action potential. This will occur when the LGICs are permeable to both K^+ and Na^+. In contrast, an inhibitory postsynaptic potential (IPSP) arises when the net effect in ion channel configurations lead to a negative charge across the postsynaptic cell membrane, known as hyperpolarisation, this leads to a change of potential across the membrane that moves the neuron's voltage away from firing an action potential.

Modelling the entire process leading to a PSP is extremely challenging; however, simple phenomenological models of synapses can represent the time-course of the postsynaptic current reasonably well. Most ion channels display a linear current-voltage relationship which means a time dependent ohmic conductance $g_{\text{syn}}(t)$ multiplied by the difference in voltage $\Delta V(t)$ across the membrane from its resting state represents the postsynaptic current

$$\alpha(t) = g_{syn}(t)\Delta V(t). \tag{1.2}$$

Now by taking an often valid assumption of no voltage time dependence, i.e., $\Delta V(t) = \Delta V$, the synapses can be considered sources of current rather than changes in conductance or voltage. A good model for the synaptic current time-course is a difference of exponentially decaying functions, such that

$$\alpha(t - t_0) = I_{\text{syn}}\big[\exp(-(t - t_0)/\tau_{\text{D}}) - \exp(-(t - t_0)/\tau_{\text{R}})\big], \qquad t > t_0 \tag{1.3}$$

with τ_{D} and τ_{R} representing the respective decay and rise time constants, t_0 the spike arrival time and I_{syn} a normalisation factor.

The dynamics of the PSP current is strongly influenced by the types of receptor the synapses have, which in turn dictates the relative concentrations of neurotransmitters. The AMPA receptor is one of the most commonly found across the brain and is characterised by very fast PSP responses, where $\tau_{\text{R}} \to 0$. This allows one to reduce eq. (1.3) to a simpler single decaying exponential model for the PSP current time-course, hence

$$\alpha(t - t_0) = \frac{1}{\tau_{\text{D}}} \exp(-(t - t_0)/\tau_{\text{D}}), \qquad t > t_0 \tag{1.4}$$

where τ_{D} is the synaptic decay time and the pre-factor ensures all pulses are normalised such that

$$\int_{t_0}^{\infty} \alpha(s - t_0)\, \mathrm{d}s = 1. \tag{1.5}$$

In a network, the neuron receives numerous PSP currents, which are processed in the neuron's cell body, or soma. The spatial and temporal integration of all these synaptic inputs constitutes a neural computation, with the single output

being the triggering of an action potential or not. The complexity of such a computation is dependent on the type of neuron and the presynaptic neurons collective activity, which has inevitably led to many different models for synaptic integration. Some generic models are summarised in [71].

1.2.3 Single neuron models

Neuronal dynamics is governed by highly nonlinear dynamical processes, spanning multiple spatio-temporal scales. As previously discussed, the Hodgkin-Huxley model is able to encapsulate a remarkable range of observed neuronal activity. However, unsurprisingly, the four coupled nonlinear differential equations is considered a hard problem to analyse, making it difficult to gain an intuitive understanding of the dynamics [73]. Added to that, conductance based models like the Hodgkin-Huxley model have further increased in complexity, as more advanced experimental methods have shown that many neurons possess a larger number of voltage-dependent conductances [71, 109].

As a result, we must turn to more mathematically and conceptually simple models such as those used by Lapique [24], FitzHugh [64], McCulloch and Pitts [136], Abbott and Kepler [1], Hopfield [100] and Morris and Lecar [139]—to name a few. Many of these neuronal caricatures are reductions of the complex conductance-based model, preserving direct relations between parameters measured experimentally and the abstract models parameters [100, 109]. All can be expressed under the following generic functional form describing a conductance-based neuron consisting of l ion channel currents, hence,

$$\begin{aligned} \frac{\mathrm{d}v}{\mathrm{d}t} &= f(v, z) \\ \frac{\mathrm{d}z}{\mathrm{d}t} &= g(v, z), \end{aligned} \tag{1.6}$$

with voltage $v \in \mathbb{R}$ and the ionic gating variables $z \in \mathbb{R}^l$ dynamics governed by the functions f and g respectively.

Of particular interest, Gertner et al have shown that the Hodgkin-Huxley equations can be reduced to a simplified model with a single scalar variable ($l = 0$), using a spike response method [73]. This provided a generalised and realistic

foundation for an integrate-and-fire neuron—an example of one of the simplest models of neuronal spike dynamics, dating back to Lapicque in 1907 [24]. It has become especially popular in neural networks modelling, due to its computational efficiency. Also, as we will show later, the ability to construct mathematical expressions for coherent structure found at the network level.

The leaky integrate-and-fire model (LIF) is categorised as a spiking neuron model. It bypasses the intrinsic complexity that arise in conductance based models such as the Hodgkin-Huxley model [99] and allows for a simple phenomenological model that tracks only the time of firing of an action potential. In doing so it has proven highly popular in studies of neural coding and network dynamics.

A basic circuit describing the LIF model consists of a resistor and a capacitor connected in parallel with a drive current $I(t)$. Since, the circuit is in parallel, the drive current can be split into two separate components, $I(t) = I_{\mathrm{R}} + I_{\mathrm{C}}$. By Ohms law the resistive current I_{R} will pass through a resistor R and thus can be expressed as $I_{\mathrm{R}} = v/R$, where v is the voltage across the resistor. The current applied to the capacitor can be transformed by using the definition for capacitance $C = q/v$ and charge $q = It$. Substituting the charge definition into the capacitance and differentiating with respect to time gives an expression for I_{C} in terms of the capacitance and rate of change of voltage, such that $I_{\mathrm{C}} = C\frac{\mathrm{d}v}{\mathrm{d}t}$. Now we can write a formal description of the drive current $I(t)$

$$I(t) = \frac{v(t)}{R} + C\frac{\mathrm{d}v}{\mathrm{d}t}, \tag{1.7}$$

and by introducing the membrane time constant $\tau = RC$ and multiplying both sides of eq. (1.7) by R, an evolution equation describing the leaky integrate-and-fire neuron is found

$$\tau\frac{\mathrm{d}v}{\mathrm{d}t} = -v(t) + RI(t). \tag{1.8}$$

We note that the LIF model neglects the form of the action potential, instead it classifies a spike event as the time when the membrane potential v reaches a threshold potential ϑ_{th} from below. The jth firing time τ^j is defined by the

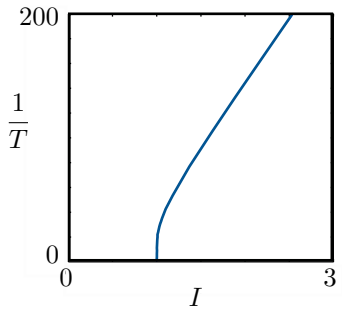


Figure 1.5 Mean firing frequency or gain function for a leaky integrate-and-fire neuron, plotted as a function of constant stimulus current I using the reciprocal of eq. (1.13). Parameter values are: $R = 1$, $\vartheta_{\mathrm{r}} = 0$, $\tau = 0.01$ and $\vartheta_{\mathrm{th}} = 1$.

following threshold criterion

$$\tau^j = \inf(t : v(t) = \vartheta_{\mathrm{th}}, t > \tau^{j-1}), \tag{1.9}$$

when this condition is met, the neuron's voltage is instantaneously reset to a voltage ϑ_{r}, such that

$$\lim_{t \to \tau^j_+} v(\tau^j) = \vartheta_{\mathrm{r}}, \tag{1.10}$$

the system will then take the same dynamics given by equation eq. (1.8) once the reset action has taken place. In the case when the drive current $I(t)$ is a constant value I and $\vartheta_{\mathrm{r}} = 0$, the governing equation eq. (1.8) can be integrated between times τ^j and t using integrating factors, hence

$$\left[v(t)e^{t/\tau}\right]_{\tau^j}^{t} = \frac{RI}{\tau}\int_{\tau^j}^{t} e^{s/\tau} ds, \tag{1.11}$$

leading to an expression for the voltage

$$v(t) = RI\left[1 - e^{-(t-\tau^j)/\tau}\right], \tag{1.12}$$

now substituting $t = \tau^{j+1}$ we arrive at an expression for the common time period T between spikes by noting that $v(\tau^j) = v(\tau^{j+1}) = \vartheta_{\mathrm{th}}$

$$T = \tau \ln \frac{RI}{RI - \vartheta_{\mathrm{th}}}. \tag{1.13}$$

The mean firing rate for the neuron is taken to be $1/T$, assuming the stimulus remains constant. In fig. 1.5 a plot of the firing frequency as a function of stimulus current level I is given, with a firing threshold $\vartheta_{\text{th}} = 1$. The neuron will not fire for $I < 1$, however at $I = 1$ the voltage tends towards the threshold infinitely slowly and as a result has an infinitesimally small firing frequency. This is the characteristic feature of a type I neuron, with which LIF neurons are associated.

1.3 Network topology

The topological organization of networks is important for their overall function, performance and behaviour [172]. Since the late nineteenth century it has been recognized that many features of the brain's topological organisation can be attributed to a parsimonious principle aimed at minimising the wiring costs involved in anatomically connecting neurons to form networks. This fundamental insight was first articulated by Ramón y Cajal in 1899 based on his microscopic studies of Golgi-stained neurons [70, 197]. He is quoted as saying:

"All of the various conformations of the neuron and its various components are simply morphological adaptations governed by laws of conservation for time, space and material"

In essence, brain networks that are wired to minimise cost must have a regular lattice-like topology. In general, the cost of forming and maintaining synaptic connections, as well as maximising the speed of signal transmission, is assumed to increase with wiring volume, which itself is proportional to the length or spatial separation of inter-neuronal connections [31].

However, this structured topology does not favour global integration of information processing, because there is not a sufficient level of topologically direct long range connections between the regions of the brain. A random network topology would maximise the efficiency of integrative processing of the brain at a global level [25].

These basic considerations support the hypothesis that brain networks negotiate an economical trade-off between maximising the brain's integrative processing capacity and minimising the costs of forming connections and directly transferring

information. The brain's topology represents a compromise between these two competing demands [25].

However, specific modules of the brain form lattice-like, short range connections, often aggregated topologically [25]. One example is the mammalian neocortex, where connection probabilities among cortical neurons generally exhibit distance dependence, with stronger levels of synaptic connectivity between cells that are spatially close to each other [96, 173]. This is supported by functional magnetic resonance imaging (fMRI) studies that have observed that strengths of functional connectivity between brain regions decays as an inverse square of physical distance [165].

In the construction of mathematical models for network connectivity, this distance dependence is commonly applied, such that the strengths of connection depend only on the distance between two nodes, meaning the network structure is considered spatially translation invariant. This approach has provided a useful insight into the dynamical states of activity in neural networks [88].

It should be noted that intracellular recordings from multiple neurons have shown that different types of neurons have different connection probabilities and different numbers and distributions of synapses [179, 180]. In addition, connection probabilities between cortical neurons are known to vary according to the layer of the cortex in which they reside [150, 198]. However, for the purposes of this study, we consider networks of homogeneous neurons aggregated onto a single layer.

1.3.1 Lateral-inhibition

A commonly used network architecture in modelling neuronal connectivity in the cortex is Lateral-inhibition (LI). This spatial connectivity structure first gained broad acceptance as a mechanism for neuronal processing in response to a series of experiments on the retina of the horseshoe crab Limulus polyphemus [93, 152]. The Limulus retina is composed of a lattice of light-sensitive cells, each having a direct inhibitory effect on its neighbours; the effect is relatively weak for nearest neighbours, but stronger for cells separated by some distance, and negligible for pairs at greater distances apart.

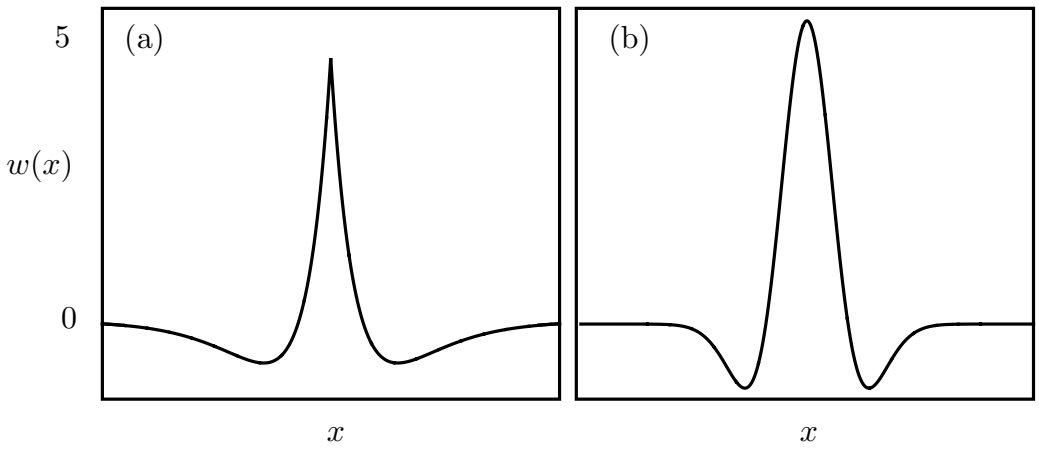


Figure 1.6 Two functions eliciting Lateral-Inhibition connectivity structure. (a) Wizard hat function is less biologically realistic due to the non-smooth cusp, but leads to simpler analytically solvable solutions. (b) Mexican Hat is composed of the superposition of oppositely signed Gaussian curves, a more statistically feasible distribution. Both cases lead to qualitatively similar dynamics as shown later.

In 1977 Amari presented a seminal contribution to pattern formation in neuronal networks [7], whereby he used a functional form for lateral-inhibition to illustrate five key types of neuronal activity. A flurry of activity in the theoretical analysis of spatiotemporal activity in neural systems followed Amari's work [17, 40, 120, 152]. The notion of lateral-inhibition has been used widely across various fields within neuroscience to model cortical networks [131]. A difference of two exponential or Gaussian functions is typically used to mathematically model these features (see fig. 1.6).

However, interpretation at face value of the so-called Wizard or Mexican hat functions in fig. 1.6 require a certain degree of justification [113]. Firstly, using such a function implies a single homogeneous population of neurons exchanging both excitatory and inhibitory feedback. This contradicts Dale's law, which states that neurons cannot ever exhibit both qualities [188]. Secondly, experimentation has shown that inhibitory interneurons in the cortex predominantly project short-range connections, while excitatory neurons (pyramidal cells) typically project over a much larger domain [71, 73].

The first issue is solved by viewing the network as an aggregate of a set of excitatory and inhibitory neurons. Moreover, the second problem is remedied when the pool of excitatory neurons project long range input to inhibitory neurons and excite themselves locally upon stimulation. Inhibitory neurons in receiving

the input from distant excitatory cells will in turn inhibit their local excitatory cells, leading to a form of indirect inhibition, which then justifies the rationale behind the lateral-inhibition form (locally excitatory but distally inhibitory). This type of connectivity structure can be shown to arise from a multilayer network with both inhibitory and excitatory populations if the inhibition is fast, as shown by Ermentrout [55].

Additional layers of complexity can be added to the lateral-inhibition weight kernels seen in fig. 1.6) by, for example: adding oscillatory distal tails [123, 157]; introducing various forms of stochastic uncertainty into neuronal connections; modelling patchy lateral connections that combine translational invariance with the biophysically based assumptions of heterogeneity in connection strengths that is present between certain groups of neurons in a network [88]; or including synaptic plasticity into the neuron's connections, which will then take the weight function to be time dependent [34, 73]. Our network study will not adopt any of these extensions. We will predominantly use a lateral-inhibition architecture characterised by the wizard hat function. This is due to the wizard hats relative simplicity in forming compact mathematical expressions, which will allow us to study how changing levels of inhibition influence the dynamics of the coherent structure we observe in the network.

1.4 Coherent structures in the brain

Improvements in the accuracy of recording neural activity have facilitated the observation of more detailed spatiotemporal activity in the brain. Voltage-sensitive dye imaging was pioneered over forty years ago, but recent advances have led to highly temporally sensitive observations of coarse-grained voltage activity in large networks of neurons [36, 195]. Furthermore, improvements in multielectrode array technology allow for an increasingly large number of neuron's voltage potential signals to be simultaneously resolved [87, 153]. We now summarise some key findings that have harnessed these improvements in experimental techniques and can relate some important neural computational mechanisms to two fundamental types of coherent structure found in neuronal networks—bumps and waves.

1.4.1 Localised bumps

Persistent, localised spatial regions of neural activity (or 'bumps') have been closely linked to the mechanisms behind a variety of cognitive functions such as visuospatial working memory and feature selectivity [27, 191]. A key question is how the coherent behaviour across a neural network emerges from the activity of individual cells.

Experiments performed on primates, monitoring prefrontal cortex activity, show that sensory cues can initiate the persistent firing of spatially localised groups of neurons during the delay period of an oculomotor–delayed response task [67, 68, 137]. The experiment requires monkeys to fix their gaze on a central target on a screen, while a cue is introduced peripherally to another area of the screen. Upon removal of this stimulus, the monkey is trained to wait for a specified period of time, and then confirm that it has recalled the position of the peripheral cue by making a saccadic eye movement to the area on the screen where it was presented. The results from these experiments have spurred much interest from experimentalists and theoreticians alike [27, 149, 191]. In fig. 1.7 we provide results obtained from a modern experimental study of this phenomena, showing two trials of the delayed response task in monkeys.

Here, the experimental observations have led to an intriguing result from a modelling perspective: the recorded neuronal activity from the pre-frontal cortex showed spatially localised bumps of activity from specific groups of neurons firing throughout the delay time where the monkey must remember the location of the cue, but stopped once the task had been completed. This has been put forward as a mechanism for working memory, which involves the holding and processing of information on the time scale of seconds, not driven by external sensory stimulus.

It has been suggested that predominant excitation with lateral inhibition connectivity facilitates the persistent firing of localised groups of neurons [77]. A supplementary claim is that slow recurrent excitation due to the increased presence of NMDA receptors is the underlying synaptic mechanism for the persistence of localized activity [186]. However, there are still many questions concerning the precise mechanism underlying working memory bumps.

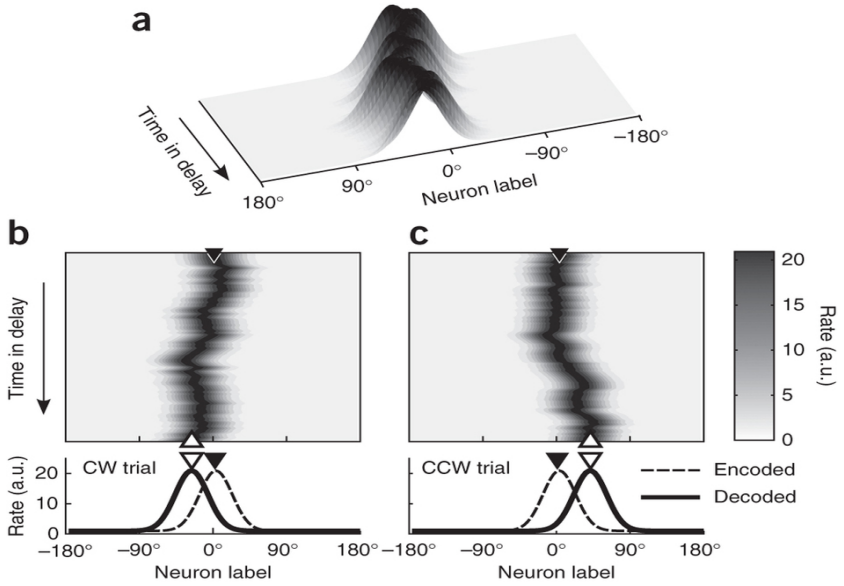


Figure 1.7 (a) Spatio-temporal depiction of network activity during the delay period of one trial of an oculomotor–delayed response task. Grey levels and z axis elevations schematize the neuronal firing rates. (b) The same trial is presented as in (a), but now presented on the space-time plane. The gray scale represents firing rate elevations. The black triangle denotes the location of the initial cue, right before the beginning of the delay (encoded population activity, bottom). The white triangle indicates the behavioral response decoded from network activity at the end of the delay (decoded population activity, bottom). (c) Data is presented as in (b) but for a another trial. These results have been adapted from the experiment performed by Wu et al. [191]

.

Experimental studies have reported bumps of localised activity (associated with memory) are not completely stationary, but instead drift left and right in a random fashion [37], as illustrated in fig. 1.7. The variance in the bump's position was shown to increase linearly from zero with time for a given network size [37, 191]. Such dynamics have been associated to a memory destabilisation and a resultant recall inaccuracy. Robust memory storage against random drift of bump state was conjectured to be enhanced by neuromodulation of recurrent synaptic activity [186]. More recent work by [138] using spiking network models have shown that the stability of a memory state is greatly enhanced by stochastic synaptic facilitation and reduced by synaptic depression.

Other biological mechanisms associated with localised bumps of neuronal activity include the rat head direction system [52, 170] where distributed cells fire preferentially at specific head orientations, as well as feature selectivity in models of the visual system [92, 97].

1.4.2 Propagating activity

Recent research has suggested the importance of propagating neural activity in the cortex. It is a common paradigm in electroencephalogram (EEG), magnetoencephalography (MEG) and electrocorticography (ECoG) imaging to analyse cortical activity using trial-averaging and difference imaging, which considers the brain as a set of static activity sources. Recent studies have reported that this can be misleading, and that a large proportion of variance in the EEG, MEG and ECoG signals is attributed to not accounting for the inseparable spatio-temporal structure of cortical activity [5]. Travelling waves have been measured across a wide range of spatial scales in the cortex, including: individual cortical columns [126, 141], isolated regions of the cerebral cortex known as Brodmann areas, which are defined by their cytoarchitecture [11, 66, 69, 164], and also across spatial scales spanning the entire cortex [4, 105, 134, 142, 158].

Cortical waves observed on large spatial scales have been found at a variety of frequencies [105, 134, 158, 167], these wave structures are seen to dominate the cortical phase dynamics, such that they account for more than 50 percent of variance in phase [5]. Many forms of propagating coherent neural activity have

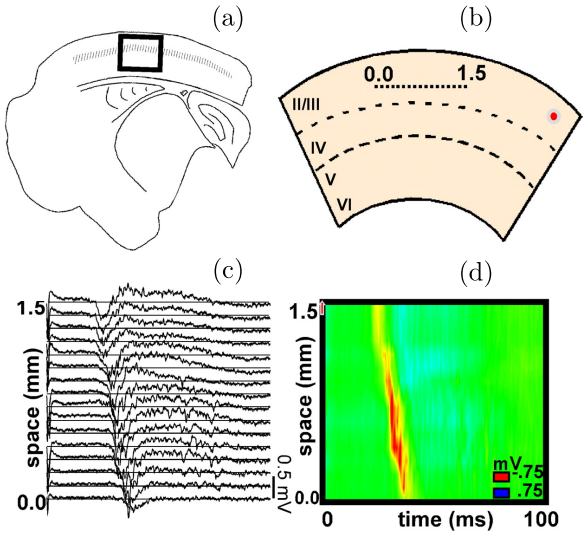


Figure 1.8 Wave of propagating activity in a cortical slice experiment, in this case inhibition has been pharmacologically blocked. (a-b) Schematics of the slice that was removed from the somatosensory cortex of the rats. (c) A multielectrode array recording of the extracellular activity during an evoked wave. (d) Color-plot of propagating wave. These results have been adapted from [153].

been observed, including: pulses, target waves, fronts, and spirals, seen to arise during almost every type of cortical processing [195].

A common experimental paradigm is to record electrical activity in vitro using pharamcologically prepared slices of cortical tissue, where inhibition has been suppressed by blocking GABA receptors with an antagonist such as bicuculline [30, 80, 153, 159]. Weak electrical stimulus will then give rise to synchronized discharge patterns. Following rapid vertical propagation, each discharge propagates away from the stimulus in both horizontal directions at a mean velocity of about $6 - 9$ cm/s, see fig. 1.8. The underlying mechanism behind the propagation of these waves is thought to be synaptic in origin rather than diffusive, which draws a stark contrast with the much faster propagation of action potentials along the axonal cables of individual neurons [19]. In some cases, locally applied stimuli of disinhibited slice preparations has been shown to induce spatially localised oscillations in the population activity at frequencies of $1 - 10$ Hz, whereby each oscillation cycle leads to the population emitting elevated activity that propagates as a localised pulse [3]. On the other hand, if the cortical slice is instead bathed in cerebral fluid, so that there is no artificially induced inhibition, the speed of the propagating activity is significantly slower and the propagating activity has a

much more complicated oscillatory profile, where the neurons fire multiple action potentials within a single wave envelope [12, 38, 193].

Voltage-sensitive dye imaging has revealed that the oscillations in the local field potential recordings were actually caused by a propagating population activation oscillating between $7 - 10$ Hz, as the wave envelope passes over a neuron an epoch of spiking takes place, characterised by a synchronized spike and then $3 - 200$ cycles of oscillation afterward [194].

A number of studies of vertebrate and invertebrate olfactory bulbs have shown odour stimuli can produce propagating waves and population oscillations [45, 124]. Similarly, low frequency propagating oscillations are observed in both ongoing neural activity and activity induced by visual stimuli [155]. Higher frequency oscillations were observed only in response to the stimuli and the propagation of spiral and more complex wave forms was also reported in some cases [11, 90, 155]. Additionally, stimulating a single whisker triggers similar wave responses in a rats barrel cortex [151].

Propagating activity has not not only been associated with sensory stimuli, but has also shown to precede motor commands. For example, evoked waves observed in monkey motor cortex during movement preparation and execution [164].

Travelling waves are also a characteristic feature of certain neurological disorders such as epilepsy [135]. Investigating the underlying mechanisms of wave propagation in neural tissue is important for understanding what factors differentiate normal and pathological brain states.

Pioneering work by [111] identified perplexing EEG signals during slow-wave sleep or drowsiness that are characterised by synchronized slow oscillations of neural activity propagating across the cortex. These waves can be initiated experimentally with a transient local excitatory electrical stimulation, see fig. 1.9.

Sweeping waves thought to represent dominant visual perception can be monitored by subjecting two eyes to distinctly different stimuli [189]. The resultant fluctuating perceptual dominance arising from these sweeping waves is coined binocular rivalry. It is thought to be a clue to the neural dynamics determining our conscious visual awareness [48, 177]. Kleinfeld *et al* studied waves of electrical

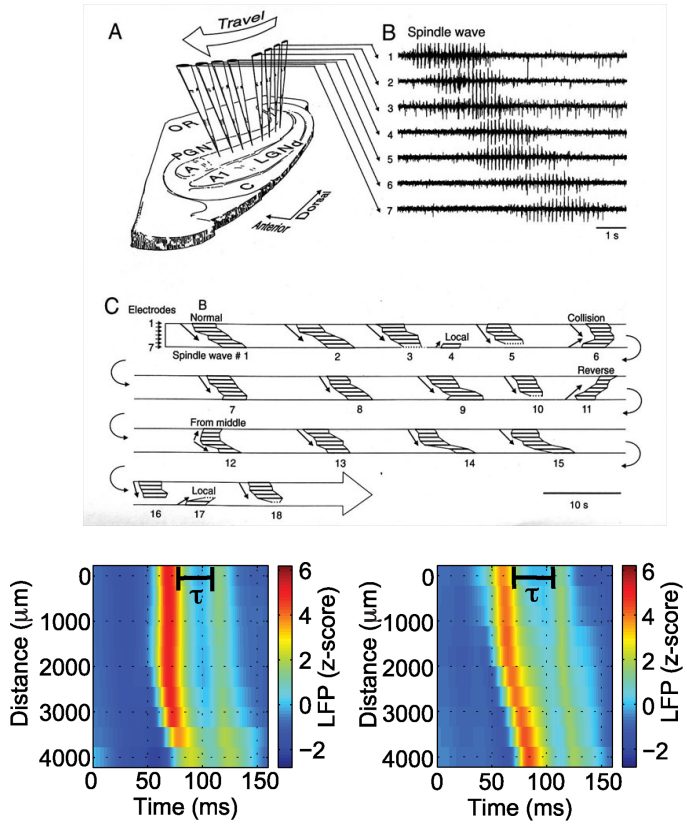


Figure 1.9 Top: Illustration of EEG signals showing the propagation of slowly oscillating neural activity across the cortex [111]. Bottom: Two large amplitude waves observed prior to the cessation of an epileptic seizure using a dense electrode array [85].

activity in a brain area largely responsible for olfaction in a mollusk's procerebral lobe [114]. Groups of neurons were seen to oscillate with the same frequency and a phase shift propagated across the network as a wave. Interestingly, under the application of an odour stimulus, a quick transition from travelling waves to synchronous activity was observed. As a result, Ermentrout and Kleinfeld hypothesised that travelling waves could act as a "searchlight" for novel sensory stimuli [60]. When an input arrives, the time and location of the stimulus is marked by a unique phase in the continuum of phase–shifts of the wave. It is therefore thought that localised travelling waves could cause sensory areas to act as a "bar-code scanner", providing an energy efficient mechanism for scanning the entire sensory field [60].

To summarise, the propagation of neural activity is thought to be a key computational mechanism, which underpins many sensory and cognitive functions of cortical tissue [84, 95]. At present the intrinsic mechanisms of these wave-like activity patterns remain inconclusive [195]. Spatiotemporal waves of electrical activity are now known to be a ubiquitous phenomenon in the cortex, although the intrinsic functional relevance of these activity patterns remain unknown [195]. Based on the prevalence of experimental evidence, many researchers claim that waves serve as a fundamental neural computational mechanism [42, 84, 95]. However, some believe cortical waves could be just an epiphenomenon. Some of these arguments are reviewed in [60].

1.5 Propagation mechanisms in neural networks

The analysis of propagating activity is a central component of this thesis, it is therefore important to highlight the general mechanisms thought to be behind the formation of propagating waves in neural networks. Ermentrout and Kleinfield [60] have proposed three fundamental mechanisms associated to the generation of propagating activity in cortical neural circuits and networks (see fig. 1.10).

The first mechanism arises from a single oscillator exciting other neighbouring oscillators with increasing time delays, depicted in fig. 1.10(a). The net result is the production of a fictive propagating wave in a network of oscillators. It

is regarded as fictive because the wave is not due to the interaction between the network of oscillators themselves, but instead, apparent only because of the different projections made by a single oscillator to the network. This type of wave has been proposed as the underlying mechanism for travelling waves in anesthetized visual cortex, attributing the spread of activity to axonal time delays in the long-range horizontal connections between neurons on the cortex [11, 86].

The second mechanism involves a single oscillator, or localised group of oscillators, supplying an excitatory driving effect on a chain of oscillators, as shown in fig. 1.10(b). The number of driving oscillators and their frequency determines the number of propagating pulses and its spatial structure. If the driving oscillator(s) is (are) only active for a finite time, the net result is the production of a localised travelling wave structure. This mechanism has been associated to solitary waves observed in cortical slice experiments, offering a framework for understanding slow-wave sleep waves and pathological epileptic seizure states, characterised by the focal-spread of activity (see fig. 1.9). At this point we note that the waves observed in the network models studied in this thesis will correspond to this particular wave production mechanism.

The third mechanism proposed in [60] assumes the entire network is in oscillatory state. Propagating activity in this case is defined in terms of a spatial gradient in the phase of the oscillators, these are often referred to as *phase waves*. These types of waves have been observed in sensory cortical areas, and also used to describe central pattern generators in locomotion.

Another mechanism was suggested by Wu *et al* [195], whereby the generation of a new wave structure arises from the interaction between independently formed coherent network structures. This mechanism differs from the mechanisms described in [60] because it considers the wave generation to be a top-down, or an emergent effect. In fig. 1.10(d) two network pulses on a two-dimensional domain interact to form spiral waves, where the system is driven by the rhythmic activation cycles of the rotating waves.

An important question concerns what the fundamental unit of oscillation is in these propagation mechanisms—it could be a single neuron, or a population

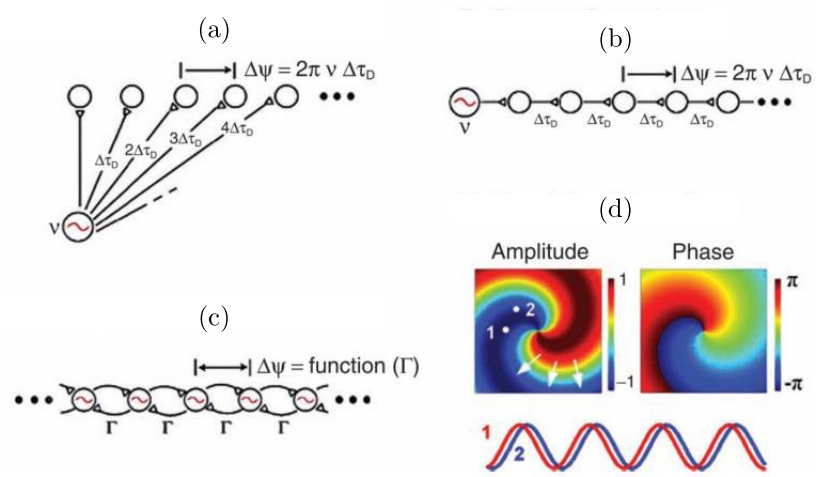


Figure 1.10 Four mechanisms behind the generation of propagating waves. (a) Fictive waves arising from a local oscillator stimulating regions with increasing time delays τ_D. (b) A local oscillator initiates a chain of oscillators, leading to the transmission of an excitatory pulse along it. (c) Propagation described in terms of a phase lag between neighboring oscillators. The function Γ determines the frequency and spatial phase shift. (d) Example of population level interactions between two pulses leading to the formation of a spiral wave. Different positions on the wave have phase lags arising from the rotation of the wave. Network level interactions can often be the main driver determining the spatial phase distribution, as opposed to the individual oscillators in the other examples. Illustrations adapted from [60] and [195].

of neurons [19]. In the next section, we review the work done so far in network models that are founded on these two key assumptions.

1.6 Neural network models

Here we provide a review of some of the main classes of network that have been studied to date. We start by introducing a general form of neural network that forms the basis behind many of the network models seen in literature today. This generic network model tracks the collective voltage dynamics of a set of synaptically connected single neurons. Here the output spike train of any given neuron acts as an input to a subset of neurons in the network. In turn, their output responses are innervated back to this particular neuron.

Consider a network of n synaptically coupled neurons indexed using the set $\mathbb{N}_n = \{1, 2, \ldots, n\}$. Taking $v_i(t)$ to denote the ith neuron's somatic voltage time dynamics, which evolves according to a (in this case generic) conductance-based

neuron model, consisting of l ion channel currents, such that

$$\begin{aligned} \frac{\mathrm{d}v_i}{\mathrm{d}t} &= f(v_i, z_i) + s_i(t) \\ \frac{\mathrm{d}z_i}{\mathrm{d}t} &= g(v_i, z_i), \end{aligned} \tag{1.14}$$

where voltage $v_i \in \mathbb{R}$ and the ionic gating variables $z_i \in \mathbb{R}^l$ are governed by the functions f and g respectively. If the network has all-to-all connectivity, the synaptic current of the ith neuron is dependent on the spike trains it receives from all neurons in the set $\mathbb{N}_n$. For $j \in \mathbb{N}_n$, the sequence of firing times of the jth neuron can be given by $\{\tau_j^m, m \in \mathbb{Z}\}$, with

$$\tau_j^m = \inf\{t, t > \tau_j^{m-1} | v_j(t) = \vartheta_{\text{th}}, \dot{v}_j(t) > 0\}, \tag{1.15}$$

where ϑ_{th} defines a voltage threshold. The synaptic current contribution into the postsynaptic neuron i as a result of receiving the spike train $\{\tau_j^m, m \in \mathbb{Z}\}$, from the presynaptic neuron j, can be expressed in general form by $\sum_m \Phi_{ij}(t - \tau_j^m)$. Here the function $\Phi_{ij}(t - \tau_j^m)$ can represent the temporal filtering effects due to synaptic and dendritic processing (see section 1.2.2), but can also include the strengths of connections between neuron i and j. If all synaptic inputs are assumed to sum linearly, the total synaptic input $s_i(t)$ of the ith neuron is expressed as

$$s_i(t) = \sum_{j=1}^{n} \sum_m \Phi_{ij}(t - \tau_j^m) = \sum_{j=1}^{n} \int_{-\infty}^{t} \Phi_{ij}(t - \tau)\eta_j(\tau)\,\mathrm{d}\tau, \tag{1.16}$$

where

$$\eta_j(t) = \sum_{m \in \mathbb{Z}} \delta(t - \tau_j^m). \tag{1.17}$$

Here the output spike train of the jth neuron is composed within a sum of Dirac delta functions.

In general, the analysis of eqs. (1.14) to (1.16) is particularly difficult when n is large, and made more difficult if the functions f and g are non-linear, with multiple gating variable dependencies [19]. Moreover, defining the precise firing-time sequences of the neurons composed within these networks is non-trivial, and requires one to make various approximations to proceed further in any meaningful

mathematical analysis. We now discuss some of the simplifications to eq. (1.14) that have provided valuable insights into the mechanisms and properties of a broad range of coherent structure observed in neural activity.

1.6.1 Weakly coupled networks

Various reductions can be made to eqs. (1.14) to (1.16) if one assumes the neurons interact weakly with each other. Hoppensteadt and Izhikevich [101] have put forward a general theory of weakly coupled neural network models. Here it is supposed that, for each neuron, the dynamics is close to a bifurcation and the neurons have only weak interactions with other similar neurons. The net result is that high-dimensional neuron models can be reduced to a much lower-dimensional system, taken to be the normal form at the presumed bifurcation. For instance, each neuron near a Hopf bifurcation can be represented by a complex scalar z_i, with the evolution equation

$$\frac{\mathrm{d}z_i}{\mathrm{d}t} = z_i(a_i - b_i z_i \bar{z}_i) + \sum_j w_{ij} z_j, \tag{1.18}$$

where all the parameters are complex numbers. The complete analysis of models of this form is, however, still considered an open question [55]. It has been shown that even in the case where there is just two interacting neurons, the dynamics is extremely complex [8].

Another approach is to consider the network of conductance-based neurons in an oscillatory dynamical regime, such that all neurons will act as limit cycle oscillators even in the absence of synaptic interactions, such that

$$\frac{\mathrm{d}\theta_i}{\mathrm{d}t} = \omega_0, \tag{1.19}$$

where ω_0 is the natural frequency of each oscillating neuron and θ_i is the phase variable.

Provided (again) that the synaptic interactions are sufficiently weak, such that they can be treated as a weak time dependent perturbations to the voltage

dynamics of eq. (1.14), giving

$$\frac{\mathrm{d}v_i}{\mathrm{d}t} = f(v_i, z_i) + \epsilon \sum_{j=1}^{n} \sum_{m} \Phi_{ij}(t - \tau_j^m), \tag{1.20}$$

where $\epsilon \ll 1$. The method of isochrones [76, 192] can be used to obtain a system of coupled equations describing the phase of the oscillating neurons

$$\frac{\mathrm{d}\theta_i}{\mathrm{d}t} = \omega_0 + \epsilon \sum_{j=1}^{n} \sum_{m} Z(\theta_i(t))\Phi_{ij}(t - \tau_j^m), \tag{1.21}$$

where $Z(\theta_i)$ is the phase-resetting curve (PRC), which describes the transient change in the cycle period of the ith oscillator induced by the synaptic perturbation as a function of the phase at which it is received. The PRC is a useful quantity to obtain because it can be related directly to experimental measurements of the change in inter-spike intervals exhibited by actual neurons, in response to small applied perturbations in current [192].

Analysis of weakly coupled oscillating systems like that seen in eq. (1.21) have mainly been made through the application of various phase reduction methods to reduce the network dynamics to a system in which a function describing the relative phase between oscillators, known as a phase interaction function, can be obtained directly or approximated [23, 116]. This has been utilised for a number of models including the Hodgkin-Huxley model and other more general descriptions of neural oscillators to find and analyse the dynamics of phase-locked solutions [54, 57, 58, 61, 91, 101]. Phase-locking has also been found in weakly heterogeneous networks [32]. In the special case of leaky-integrate-and-fire neurons, phase-locking equations can be derived without the need of weak coupling assumptions [74, 145] and their stability can be analysed directly in terms of firing times [21, 185].

Furthermore, if oscillators are arranged in a one-dimensional spatial lattice structure it is possible for the network to support phase-locked states, in which a near constant phase gradient can be shown to exist, corresponding to phase waves. Considerable insights into the various conditions required for phase gradients to occur have been elucidated in studies of central patten generators for swimming

locomotion in primitive vertebrates such as lampreys and invertebrates such as leeches [35, 132].

Recently the study of the collective dynamics of neural oscillators has experienced a major breakthrough due to the results of Ott and Antonsen [146, 147]. Very recently, the Ott-Antonsen ansatz has been applied to networks of quadratic integrate-and-fire neurons, or theta neurons, in the limit of an infinite number of neurons [118, 119, 129].

1.6.2 Rate-based models

The conductance-based spiking network eqs. (1.14) to (1.16) can be reinterpreted drastically if the total synaptic current $s_i(t)$ is considered slow when compared to the voltage dynamics given in eq. (1.14). This is justified when the spiking network is partitioned into multiple homogeneous subnetworks consisting of a population of identical neurons that fire action potentials asynchronously [72], assuming that there are no correlations in the spike trains of neurons within the same homogeneous population. The activity variables $\eta_i(t)$ and $s_i(t)$ should then be reinterpreted as mean fields (averages) of the local populations. Alternatively, a slowly varying synaptic current would occur if the synaptic processing speeds of the neurons are adequately slow [21, 53]. By adopting these simplifying assumptions and taking the short-term temporal average of eq. (1.16), where we assume the output spike train $\eta_j(t)$ is approximated by the instantaneous firing rate function F_j, such that $\eta_j(t) = F_j(s_j(t))$, eq. (1.16) now takes the form of the following closed system of integral equations

$$s_i(t) = \int_{-\infty}^{t} \sum_{j=1}^{n} \Phi_{ij}(t-\tau) F_j(s_j(\tau)) d\tau, \tag{1.22}$$

where within this mean-field framework F_i represents the population-averaged rate function of a local homogeneous population of neurons, as opposed to a single neuron's input response function. Typically, in rate models, F_i is approximated by a sigmoid or Heaviside function.

It has been noted in [55, 63], that with some small restrictions on the time dependence of $\Phi_{ij}(t)$ we can reduce eq. (1.22) to a system of ODEs. Suppose that

$\Phi_{ij}(t) = w_{ij}\Phi_i(t)$, where w_{ij} is the synaptic connectivity strength linking the jth to the ith neuron and $\Phi_i(t)$ denotes the time course of the input, which depends only on the ith postsynaptic neuron. Now if we also suppose that there exists some differential operator $\mathcal{L}_i$ such that

$$\mathcal{L}_i\Phi_i(t) = \delta(t). \tag{1.23}$$

Applying $\mathcal{L}_i$ to both sides of eq. (1.22) yields the following system of differential equations

$$\mathcal{L}_i s_i(t) = \sum_{j=1}^{n} w_{ij}F(s_j(t)). \tag{1.24}$$

The total synaptic current $s_i(t)$ can easily be converted into an input voltage by considering the input conductance σ of the neurons, such that $v_i(t) = s_i(t)/\sigma$, hence, eq. (1.24) is usually regarded as a voltage equation. It is important to note that eq. (1.24) forms the foundation of most classical neural networks, such as the Hopfield network model [100].

If, on the other hand, the time course of inputs depends primarily on the presynaptic features, such that $\Phi_{ij}(t) = w_{ij}\Phi_j(t)$, we now have an inverse differential operator $\mathcal{L}_j$ for Φ_j, giving a different system of differential equations for what is usually referred to as synaptic drives

$$v_i(t) = \int_{-\infty}^{t} \Phi_i(t-\tau)F_i(s_i(\tau))d\tau. \tag{1.25}$$

If we now state that $s_i(t) = \sum_{j=1}^{n} w_{ij}v_j(t)$ and apply $\mathcal{L}_i$ to both sides of eq. (1.26) then we arrive at the activity-based model

$$\mathcal{L}_i v_i(t) = F_i\Big(\sum_{j=1}^{n} w_{ij}v_j(t)\Big), \tag{1.26}$$

where normally the differential operator $\mathcal{L}$ is taken to be first order in time with the form

$$\mathcal{L} = \frac{\partial}{\partial t} + \beta, \tag{1.27}$$

with an inverse kernel $\Phi_k(t) = \exp(-\beta_k t)H(t)$.

So far there has been no specific assumptions made on the neural network's topology. Spatially structured rate models are often referred to as neural field models. A heuristic argument for incorporating spatial-structure into the rate-based models was put forward by Gerstner and Kistler [72]. It starts by partitioning space into intervals of length δ with $N = \rho\delta$ neurons within each interval $[n\delta, (n+1)\delta]$, where ρ is the neuron density. All neurons within any given interval are taken to be a homogeneous population denoted by the integer n, and synaptic interactions between the mth and nth population is assumed to depend only on the discrete locations of the populations on the line. Now writing $\Phi_{nm}(t) = \rho\delta\Phi(n\delta, m\delta, t)$ and $s_n(t) = s(n\delta, t)$, the population rate eq. (1.22) becomes

$$s(n\delta, t) = \rho\delta \sum_m \int_{-\infty}^{t} \Phi(n\delta, m\delta, t-\tau) F(s(m\delta, \tau)) d\tau, \tag{1.28}$$

which when $\delta \to 0$ and $n\delta \to x$ along with $m\delta \to y$ we arrive at

$$s(x, t) = \int_{-\infty}^{\infty} \int_{-\infty}^{t} \Phi(x, y, t-\tau) F(s(m\delta, \tau)) d\tau dy. \tag{1.29}$$

By introducing a new spatial connectivity function $w(x, y)$, we decompose $\Phi(x, y, t)$ as follows

$$\Phi(x, y, t) = w(x, y)\Phi(t), \qquad \Phi(t) = \exp(-\beta t)H(t), \tag{1.30}$$

where the kernel $\Phi(t)$ is now only temporally dependent. We note that a homogeneous network of neurons is assumed in this case. Now, in a similar manner to the derivation of the voltage-based model given in eq. (1.24), we apply the commonly used first order in time differential operator $\mathcal{L}_t = \partial_t + \beta$ to both sides of eq. (1.29), and arrive at the scalar neural field equation

$$\frac{\partial s(x, t)}{\partial t} = -\beta s(x, t) + \int_{-\infty}^{\infty} w(x, y) F(s(y, t)) dy. \tag{1.31}$$

Additionally, the activity-based neural field model with synaptic drive $v(x,t) = \int_{-\infty}^{t} \Phi(t-\tau)F(s(x,\tau))d\tau$ is given by

$$\frac{\partial v(x,t)}{\partial t} = -\beta v(x,t) + F\Big(\int_{-\infty}^{\infty} w(x,y)v(y,t)dy\Big). \tag{1.32}$$

Both the activity-based eq. (1.32) and voltage-based eq. (1.31) neural field models introduced have been arrived at by a sequence of approximations and assumptions from the full conductance-based network model. By tracking the mean activity, neural field models typically neglect the correlations between spike timings of action potentials that are intrinsic to biophysically realistic neural networks. In addition, the models are limited to modelling slow synaptic interactions. The modelling assumption is therefore top-down macroscopic in its nature, with no rigorous link to microscopic dynamics [44]. Recently, Byrne and Coombes [41] have tackled this problem by developing a so-called *next generation neural mass model*, which, in certain circumstances, provides an exact macroscopic description of underlying microscopic spiking neurodynamics.

Much more work has been focussed on incorporating a variety of additional physiological features into these rate-based models, such as: synaptic depression, axonal propagation delays, adaptive threshold dynamics and short-term plasticity. Such models have built upon the original work of Wilson, Cowan and Amari [7, 190]. The relative simplicity of these models of spatially-extended excitable systems often allow for explicit construction of solutions and facilitates the employment of analytical techniques including regular and singular perturbation methods, weakly nonlinear analysis, Turing instability analysis, symmetric bifurcation theory, Evans functions, homogenization theory and stochastic processes [18, 40].

Additionally, neural fields support a rich repertoire of spatiotemporal dynamics including: localised patches [9, 122, 157], travelling bumps and fronts [20, 62], as well as more exotic structures such as spiral waves [117], lurching waves [81, 144, 187] and Turing-like patterns [40, 55].

When the model is extended to two dimensions, stripes and chequerboard patterns are facilitated under this construction. These types of dynamics have been associated to drug induced visual hallucinations [17, 18, 55]. Multi-bump

solutions have also been shown to exist in an Amari type neural field formulation when the connectivity function has a decaying oscillatory tail [123].

Moreover, stochastic neural fields have been analysed in a variety of ways, with numerous possibilities in the application of noise to the models. Kilpatrick and Ermentrout [110] introduced multiplicative and additive stochastic noise term in the mean activity variable. This facilitated bump wandering in what would have previously been a stationary bump solution, an important feature observed in experiment (fig. 1.7) [37]. Regarding waves, methods have been developed to compute stochastic travelling waves in equivalent neural field models, focussing on the effect noise played on the wave speed[128]. It should be noted that applying stochastic noise to neural field equations is not necessarily addressing the underlying mechanism for bump destabilisation and wave propagation variants. Instead, it poses further questions regarding the origin of noise in the first place and highlights the abstract assumptions taken in the construction of the model.

In recent years, neural fields have been used to model a wide range of neurobiological phenomena, including wave propagation in cortical slices [152, 159] and in vivo [102], short term working memory [27, 123], motion perception [75], EEG rhythms [125], geometric visual hallucinations [22, 59], orientation tuning in primary visual cortex (V1) [171] and control of head direction [199].

1.6.3 Simplified spiking network models

Neural field equations describe the spatiotemporal evolution of coarse grained variables such as the synaptic or firing rate activity in homogeneous populations of neurons, these are often referred to as tissue level models. Indeed, there has been a vast quantity of invaluable progress made analysing the spatiotemporal dynamics of coherent structure observed at this particular spatiotemporal scale. However, many important phenomena of the brain involve dynamics that occur on a finer scale, where the activity of the individual neurons must be taken into account, so there is no loss of detailed spike timing information that occurs through spatial averaging.

In section 1.6.1 we have mentioned that analytical progress can be made in weakly connected networks of generic conductance-based neurons if the neurons

are assumed to be in an oscillating regime or near a bifurcation. But, for networks of excitable conductance-based neurons with strong coupling this analysis does not apply.

Computational studies of such spiking network models with multi-compartmental conductance-based neurons have found an abundant range of coherent structure, for instance, localised waves with multiple spiking events [47, 79, 80, 183], which we are interested in analysing throughout this thesis. In these studies the membrane properties exhibited by individual neurons have been explicitly modelled; but, due to the computational model's complexity, the networks are often deemed mathematically intractable. Thus, determining which aspects of the biophysical model determine the coherent structure's macroscopic features, such as the speed of the waves, is extremely hard to extract [145].

However, the mathematical treatment of networks of simplified spiking neurons has been shown to lead to important general principles that can also be applied to the more biophysically realistic network models. Studies have shown that for networks of excitable leaky integrate-and-fire neurons, where the function f describing the neurons voltage dynamics is simply $f(v_i) = -v_i$ (with no gating variable dependencies in eq. (1.14)), significant mathematical analysis can be made in terms of the network's firing times [13, 16, 56]. In particular, this mathematical framework has been shown to provide an exhaustive analysis of the speed and stability for single-spike travelling waves in such a network. This thesis will provide an extension to this framework that also allows for the complete analysis of multiple-spike waves in a similar network construction. We therefore summarise here the work done in analysing the single-spike waves.

First, consider a network of LIF neurons distributed along a one-dimensional lattice, giving the first-order voltage equation for the ith neuron as

$$C\frac{\mathrm{d}v_i}{\mathrm{d}t} = -\frac{v_i}{R} + I_{\mathrm{ext}}(t) + s_i(t), \tag{1.33}$$

with threshold conditions defined by eq. (1.15) upon which the voltage is instantaneously reset to ϑ_{R} such that

$$\lim_{t\to[\tau]^+} v_i(t) = \vartheta_{\mathrm{R}}. \tag{1.34}$$

A single-spike wave solution is defined as one upon which there is a constant time lag between adjacent neurons on the lattice, such that $\tau_i = m\Delta$. Now by setting $C = R = 1$, $\vartheta_{\mathrm{R}} = 0$, $\vartheta_{\mathrm{th}} = 1$, $I_{\mathrm{ext}}(t) = I$ and combining eqs. (1.15), (1.16) and (1.35), with a synaptic response function $\Phi_{ij}(t) = W(i-j)\Phi(t)$, we arrive at an evolution equation for a synaptically connected LIF network modelling a single-spike wave

$$\frac{\mathrm{d}v_i}{\mathrm{d}t} = -v_i + I + g\sum_{j=1}^{n} W(i-j)\Phi(t - m\Delta), \tag{1.35}$$

where g is a synaptic coupling constant and I is a constant background current. We note that the LIF network can be split into two operating regimes: excitatory and oscillatory. We focus on the case where the background current input I is less than than the voltage threshold ϑ_{th}, i.e. $I < \vartheta_{\mathrm{th}}$. Under these conditions the network is said to be in an excitatory regime, because extra synaptic input is required to make the neurons fire.

From an analytical point of view, it is convenient to consider eq. (1.35) on the continuum. This is achieved by introducing a lattice spacing δ and then setting $v(x,t) = v_{x/\delta}(t)$, $w(x-y) = W([(x-y)/\delta])$ and $\tau(y) = \tau_{y/\delta} = m\Delta$. By taking the continuum limit for the lattice spacing δ and lag time Δ, it is assumed that $\delta \to 0$ and $\Delta \to 0$, the wave speed $c = \delta/\Delta$ is then a fixed constant, and also $\tau(y) = y/c$. Now we obtain the continuum equivalent of eq. (1.35)

$$\frac{\partial v(x,t)}{\partial t} = I - v(x,t) + g\int_{-\infty}^{\infty} w(x-y)\Phi(t - y/c)dy. \tag{1.36}$$

From here, Ermentrout and Bressloff [13, 16, 56] assumed that $I = 0$ and the weight function $w(x)$ was a positive, symmetric and monotonically decreasing function taking the following exponential form

$$w(x) = \frac{1}{2\sigma}e^{-|x|/\sigma}. \tag{1.37}$$

Note that this models a network of neurons exchanging only positive feedback (excitatory), in contrast to the lateral-inhibition model described in section 1.3

where there is also negative feedback (inhibition). Later in this thesis we will analyse how these different connectivity regimes affect the wave dynamics.

A self-consistency condition for the wave speed c was shown by Ermentrout [56] to be obtainable by multiplying both sides of eq. (1.36) by e^t and doing a time-integral over the interval $-\infty < t \leq \tau(x) = x/c$ and then applying the threshold condition $v(x, \tau(x)) = 1$, hence,

$$\begin{aligned} 1 &= g \int_{-\infty}^{x/c} e^t \Big[\int_{-\infty}^{\infty} w(x-y)\Phi(t-y/c)dy \Big] dt \\ &= g \int_0^{\infty} w(x) e^{-x/c} \int_0^{x/c} e^t \Phi(t) dt\, dx. \end{aligned} \tag{1.38}$$

The integral condition can be evaluated explicitly by performing a Fourier expansion on $\Phi(t)$. By applying the property of $\tilde{\Phi}(k) = \int_{\infty}^{\infty} e^{-ikt}\Phi(t)dt$, where, $\tilde{\Phi}(k)$ is analytic in the lower-half complex k-plane if one notes that $\Phi(t) = 0$ for $t \leq 0$. Hence, the contour integral with $w(x)$ defined in eq. (1.37) gives the following result for eq. (1.38)

$$1 = \frac{gc}{2(\sigma + c)} \tilde{\Phi}(-ic/\sigma). \tag{1.39}$$

Bressloff used an alpha-function to describe the functional form of $\Phi(t)$, which is written as

$$\Phi(t) = \alpha^2 (t - \tau_d) e^{-\alpha(t-\tau_d)} H(t - \tau_d), \tag{1.40}$$

where H is the Heaviside step function and τ_{d} is a constant axonal time delay. An implicit equation for the wave speed of the single-spike pulse can now be obtained explicitly

$$1 = \frac{\alpha^2 g c e^{-c\tau_d/\sigma}}{2(\sigma + c)(\alpha + c/\sigma)^2}. \tag{1.41}$$

In the case where the axonal delays are neglected ($\tau_d = 0$), the wave speed has the power-law scaling $c \sim \alpha\sigma\sqrt{g/2}$, which has been shown to be consistent with similar waves found in networks composed of more biophysically realistic neurons [56, 80].

Plotting c as a function of g yields one stable fast branch and one unstable slow branch of solutions that meet at a critical g^*, such that for $g < g^*$ no travelling wave solutions exist. Bressloff [13] showed that the asymptotic stability of the single-spike can be determined by considering perturbations of the firing times.

Here he supposed that $\tilde{\tau}(x) = x/c + \varphi(x)$ with $\varphi(x) = \mathcal{O}(\varepsilon)$ and $\varphi(x) = \varphi_0(x)$ for $x \leq 0$, taking $\varphi_0(x)$ to be a bounded function on $(-\infty, 0]$. Asymptotic stability is then related to the condition that $\varphi(x) \to 0$ as $x \to \infty$ for an arbitrary initial state $\varphi_0(x)$. Substituting the perturbed expression for the firing times $\tilde{\tau}(x)$ into eq. (1.36) and then integrating over the interval $(-\infty, \tilde{\tau}(x)]$ gives

$$e^{x/c+\varphi(x)} = g \int_{-\infty}^{x/c+\varphi(x)} e^t \int_{-\infty}^{\infty} w(x-y)\Phi(t-y/c-\varphi(y))dy\,dt, \tag{1.42}$$

which if one expands to the first-order in $\varphi(x)$ and ensures the self-consistency condition in eq. (1.38) is satisfied, the following linear integral equation is obtained

$$\int_{-\infty}^{0} e^t \Big[\int_{-\infty}^{\infty} w(x-y)\Phi'(t+(x-y)/c)[\varphi(x)-\varphi(y)]dy \Big] dt = 0. \tag{1.43}$$

If one considers perturbations of the form $\varphi(x) = e^{\lambda x}$ and substitutes into eq. (1.43), it can be shown by changing variables and switching the order of integration to yield a characteristic equation in terms of λ, hence

$$E(\lambda) = \int_0^{\infty} \big[e^{-\lambda x} - 1\big] w(x)\Psi(x/c)dx = 0, \tag{1.44}$$

where

$$\Psi(\tau) = \int_0^{\tau} e^{-(\tau-t)}\Phi'(t)dt. \tag{1.45}$$

The single-spike wave's asymptotic stability is confirmed if all non-zero solutions λ have negative real part. A theorem for the stability of the fast and slow branches is given in precise detail in [13]. Here it was shown that for sufficiently large axonal delays τ_d solutions on the fast branch can become unstable via a Hopf instability. Golomb and Ermentrout have made the fascinating observation that these discrete delays arising in synaptic interactions can lead to the formation of non-smooth lurching waves that propagate with discontinuous, periodic spatiotemporal dynamics [81].

Further extensions to the integrate-and-fire network can be made by incorporating into the one-dimensional network both excitatory and inhibitory neurons [83]. By proceeding on similar lines to the analysis of the solely excitatory case described above [13], the existence and stability of single-spike travelling pulses

can be found. Simulation results confirm that there are in fact two types of stable waves solutions: a fast pulse, that is broadly similar to the waves seen in the excitatory network, and a slow pulse characterised by the inhibitory cells firing before their excitatory partners [83]. It has been shown in detailed conductance-based models that spiking-networks can support two propagating speeds [39]. In fact, in later chapters we will show that when multiple-spike waves are considered, the integrate-and-fire network can support a large variety of speeds, which can lead to interesting interaction dynamics between co-existent multiple-spike waves.

1.7 Overview of the thesis

In **Chapter** 2 we start by introducing a fully deterministic, non-smooth dynamical system in the form of a spatially structured spiking network model composed of leaky integrate-and-fire (LIF) neurons [120].

We rewrite the model as a system of 2n piecewise-linear ordinary differential equations (ODE), appropriately defining time intervals defined by the neuron's firing times. We then use a 4th-order time stepper with an event detection methodology which is capable of accurately computing the complete firing time history of the network.

Applying a brief, spatially localised, excitatory stimulus to the discrete network is shown via numerical simulation to give rise to a variety of coherent structure, for instance: stationary asynchronous bumps, wandering bumps, single-spike waves, multiple-spike waves and composite multiple-spike waves. The network is bistable, with both the coherent structures and the quiescent state stable.

It is known that the timescale upon which postsynaptic neurons process the synaptic input that is received due to presynaptic neurons firing, is important in determining the type of emergent coherent state the network supports [56, 80, 120]. We show that stationary bump solutions like those found in [120] only exist at slow synaptic timescales. Increasing the timescale parameter causes the bump state to wander diffusively across the network. We verify this is in fact a random diffusion process and show that the diffusion coefficient scales exponentially with the neuron's timescale.

We then show that there is a large family of coexistent multiple-spike waves, propagating at a well defined constant speed c, with neurons spiking m times as the wave envelope passes over it. We refer to these waves as TW_m. These states emerge post-stimulus at faster synaptic timescales. Interestingly, the wave states can also co-exist with some bump states in some intermediate parameter regimes. Comparisons are made between waves in the network with lateral-inhibition synaptic connectivity and a simpler case where all neurons exchange only excitatory synaptic input. We finally show how composite multiple-spike wave systems can form on a larger spatial domain. In doing so, we also summarise the multitude of ways waves and bumps interact.

In **Chapter** 3, we mathematically analyse the multiple-spike waves found in the discrete network simulations. We first show that the spatially discrete n dimensional ODE system can be justifiably transformed into a partial integro-differential equation similar to that seen in [13, 56, 143], adopting the thermodynamic limit, in which the number of neurons in the network tend to infinity.

To facilitate the construction of multiple-spike waves, steady state voltage and synaptic spatial profiles must be found. We define functions that quantify the times of firing across the domain and construct operators which map these functions to solutions of the integro-differential equation. For a wave with an arbitrary number of spikes, m, a concrete method of obtaining travelling wave solutions is achieved by solving a set of m equations for the wave's speed and spike-time interval distribution. These are the variables which make up the firing-time functions, and thus fully define the multiple-spike wave.

The characterisation of the wave solutions in terms of firing-time functions is achieved from the explicit computation of the wave speed and spike-times. This method is then shown to facilitate a study of the stability of multi-spike waves, which is addressed by perturbing around the wave firing time functions (similar to [181]) and using our operators. We then examine the linear stability of the multiple-spike waves by deriving a non-local eigenvalue problem. We find at the core of our linear stability analysis is an analytic function whose zeros are eigenvalues of the linearised system. To our knowledge, the stability analysis of multiple-spike waves in spiking networks has not been achieved to date. The

analysis has been kept deliberately generic by maintaining the weight function $w(x)$ and postsynaptic potential form $\alpha(t)$ in general form.

Chapter 4 is a numerical study on the multiple-spike wave analysis developed in the previous chapter. In doing so, we explore the bifurcation structure of the multiple-spike wave's macroscopic variables as a function of the network's system parameters. In addition, we numerically compute the wave's stability properties, which has not been achieved to date.

We present results that suggest the waves propagating in a network with lateral-inhibition connectivity architecture have fundamental differences in bifurcation structure compared to the waves found in the various computational and theoretical studies, where a purely excitatory architecture was taken [13, 16, 21, 56, 80, 143, 145]. As a result, we focus mainly on the waves in the lateral-inhibition network. We classify the important bifurcations multiple-spike waves can undergo and perform a number of validations on the stability analysis developed. This is followed by bifurcation diagrams contrasting the different instability mechanisms for a TW_2 and TW_3. Then composite wave solutions corresponding to those found in discrete network simulations on a large spatial domain are obtained and their dynamics analysed. We also analyse the TW_3 in detail, producing two-parameter diagrams uncovering the importance of the balance between excitatory and inhibitory synaptic connections, and investigate the effect of finite rise times in the neuron's postsynaptic response function $\alpha(t)$. Moving past the TW_3, we reveal how the number of spikes m plays an important role in determining the wave speed and stability regions of a TW_m (with lateral-inhibition). In the case where m is large, an interesting link to the dynamics of the stationary bump state found in [120] is highlighted, which provokes thoughts on the true meaning of stationary bumps in the continuum network. Finally, multiple-spike waves in the purely excitatory network are analysed and compared to the lateral-inhibition case studied here.

In **Chapter** 5 we undertake an *Uncertainty Quantification* analysis of multiple-spike waves. Our work so far has produced a known functional relationship between the multiple-spike wave's output variables and the network's system parameters. As a result, we are able to easily assess how the statistical properties of the wave

speed and spike-times are affected by uncertainty in system parameters (or inputs). These results have been verified via Monte-Carlo simulations. The knowledge of the wave's bifurcation points has allowed for the complete evaluation of the TW_m state's expectation and standard deviation across its entire region of stability. We find that with sufficiently large levels of parameter variability, the bifurcation points have a significant impact on the expectation values when compared to the bifurcation diagrams obtained in chapter 4, where there is no uncertainty.

In **Chapter** 6 we construct a synaptically connected neural network composed of more biophysically realistic Morris-Lecar neurons in a fast spiking parameter regime. The formulation of this network has similar structural properties to the leaky integrate-and-fire network, and as a result, is on a comparable spatio-temporal scale. A necessary condition for the existence of the various homoclinic connections observed in travelling wave solutions is derived, where the characteristic polynomial for the Morris-Lecar single neuron scaled by the wave speed c is found to be a factor. Travelling wave solutions are then solved numerically and continued in parameter space to explore how the intrinsic neuron dynamics effects the bifurcation structure of the travelling waves.

Chapter 7 draws conclusions and outlines some particular areas of interest for potential future studies.

Chapter 2

Discrete integrate-and-fire network

2.1 Introduction

In this chapter we introduce a spatially structured spiking network model composed of leaky integrate-and-fire (LIF) neurons. The LIF neuron chosen is a highly simplified abstraction of a real neuron, however, the collective dynamics at a network level offer an abundant variety of complex network activity. The core aim of this chapter is to explore the dynamics of some of the emergent coherent structure found from numerical simulations of the network.

We are motivated by the work done by Laing and Chow [120], where in simulations of a discrete spatially-structured network model, similar to that used in this chapter, they found that a brief localised excitatory stimulus produced persistent localised bumps of asynchronous neuronal activity. It is thought that these coherent structures are associated to the mechanisms behind working memory and visual orientation tuning. Furthermore, it was observed that the neuron's microscopic synaptic time-scale was shown to be important in determining the stability of the macroscopic network bump state. It was shown that slow synapses correspond to stationary bump states, whose mean population firing rate is well approximated by a population rate model, provided the neuron's firing patterns is sufficiently asynchronous. However, for faster synapses the bump was found to wander and eventually destabilise into a coherent pulsating wave state, composed of multiple, synchronously firing neurons in a localised region of the spatial domain. The biophysical phenomena related to all of these activity structures have been discussed in the previous chapter.

We are interested in studying this particular network because it displays many of the qualitative features observed from experimental findings and, most importantly, it is sufficiently simple to allow for a fair amount of mathematical analysis, which we carry out in chapter 3.

This chapter begins by putting forward a description of the network as a non-smooth dynamical system. We then describe an event detection methodology to time-step the model, allowing for accurate computation of the network's firing time history up to 4th-order. We present simulations summarising work done so far in analysing some of the wide variety of coherent structures found in the network, including: stationary asynchronous bumps, wandering bumps, single-spike waves, multiple-spike waves and composite multiple-spike waves. The main focus of this study is the analysis of the large family of localised wave states with complex firing patterns. This chapter describes how all these states can be formed, along with their dynamics and how they destabilise under certain conditions. The chapter also discusses the discrete nature of the waves and lays out a path for their mathematical analysis in the following chapters.

2.2 Model description

The model under consideration is a nonlocal spatially-extended system of $n+1$ LIF neurons, posed on a ring of width $2L$, $\mathbb{S} = \mathbb{R}/2L\mathbb{Z}$. Neurons are indexed using the set $\mathbb{N}_n = \{0, \ldots, n\}$ and occupy the discrete positions $x_i = -L + 2iL/n$, for $i \in \mathbb{N}_n$. A continuous, bounded, even and exponentially decaying function w models the synaptic connections between neurons. The strength of the connections from the jth to the ith neuron depend solely on their mutual distance, hence it is given by $w(x_i - x_j)$, for $i, j \in \mathbb{N}_n$. The synaptic kernel is therefore homogeneous and the model invariant to spatial translations by a multiple of the inter-neural distance $2L/n$.

To each neuron is associated a time-dependent voltage function $v_i(t)$, which is assumed to be left-continuous at countably many distinct points in $\mathbb{R}_+$. As we shall see, discontinuities are due to the incorporation of voltage threshold conditions into the evolution equations. The evolution of the model is formally

prescribed by the following set of evolution equations

$$\dot{v}_i(t) = I_i(t) - v_i(t) + \frac{2L}{n} \sum_{k\in\mathbb{N}_n} \sum_{j\in\mathbb{Z}_+} W_{ik}\alpha(t-\tau_k^j) - \sum_{j\in\mathbb{Z}_+} \delta(t-\tau_i^j), \quad i \in \mathbb{N}_n, \tag{2.1}$$

$$v_i(0) = v_{0i}, \qquad i \in \mathbb{N}_n, \tag{2.2}$$

where the synaptic connectivity matrix is $W_{ij} = w(x_i - x_j)$, an external input to the ith neuron is denoted by $I_i(t)$, and the post-synaptic potential input form is written as $\alpha(t) = p(t)H(t)$, such that it is expressed as the product of a continuous bounded function p and the Heaviside function H to enforce causality. Throughout this chapter p is taken to be a simple decaying exponential, although, other more biophysically realistic post-synaptic functions are also applicable to this analysis.

At the time τ_i^j, when the voltage v_i attains the value 1 from below for the jth time, a firing event occurs. Hence, we set for all $i \in \mathbb{N}_n$ and $j \in \mathbb{Z}_+$ [13]

$$\tau_i^0 = 0, \quad \tau_i^j = \inf\left\{t \in \mathbb{R} \colon t > \tau_i^{j-1},\ \lim_{\mu\to 0^+} v(t-\mu) = 1,\ \lim_{\mu\to 0^+} \dot{v}(t-\mu) > 0\right\}. \tag{2.3}$$

The Dirac delta function in evolution equation eq. (2.1) is responsible for resetting the ith neuron's voltage back to 0 when it reaches voltage threshold at the firing time $t = \tau_i^j$. In this case, at the firing time, a post-synaptic current is sent to all other neurons in the network instantaneously, with intensity proportional to the strength of the synaptic connections.

2.3 Description of the event-driven model

Even though most of the analysis presented below is applicable to generic post-synaptic and synaptic kernel functions, we will present concrete calculations for

$$\alpha(t) = \beta \exp(-\beta t)H(t), \qquad w(x) = a_1 \exp(-b_1|x|) - a_2 \exp(-b_2|x|). \tag{2.4}$$

and with a possibly time-dependent stimulus of the type

$$I_i(t) = I + d_1 H(\tau_{\text{ext}} - t)/\cosh(d_2 x_i), \quad i \in \mathbb{N}_n. \tag{2.5}$$

Table 2.1 Parameter description

Parameter	Symbol	Value(s)
Number of neurons	n	80
Domain half-width	L	1.0
Synaptic efficacy and time scale	β	[0.0,25.0]
Synaptic excitation coefficient	a_1	[10.0, 12.0]
Synaptic inhibition coefficient	b_2	7.0
Synaptic excitation spatial scale	b_1	[4.7, 6.5]
Synaptic inhibition spatial scale	b_2	3.5
Constant external input	I	0.90
Time-dependent external input duration	τ_{ext}	2.0
Time-dependent external input strength	d_1	[0.0,2.0]
Time-dependent external input spatial scale	d_2	[10.0,12.0]

Laing and Chow [120] time-step model eqs. (2.1) and (2.2) using a Euler scheme and a first-order interpolation technique to obtain the firing times. We use a different approach by rewriting the model as a system of $2n$ piecewise-linear ODEs and then using a 4th-order time stepper and a standard event detection technique to determine the firing times. Throughout this study we use Matlab's ODE45 timestepper and event detection algorithm. Our event driven approach allows us to compute firing times more accurately than a first-order Euler scheme, and to evolve the system without storing in memory the sums in eq. (2.1).

We now introduce the synaptic current variable $s_i(t)$. We do this because it is useful to distinguish between two types of discontinuous responses as the ith neuron reaches threshold: the voltage reset applied to the ith neuron and then the resultant synaptic current contribution supplied to the entire network. The synaptic current variable is also a useful quantity to compute directly because the synaptic input profile of the network is an important component in driving the coherent structure's dynamics. We write the synaptic input variable as

$$s_i(t) = \frac{2L}{n} \sum_{k \in \mathbb{N}_n} \sum_{j \in \mathbb{Z}_+} W_{ik} \alpha(t - \tau_k^j), \qquad i \in \mathbb{N}_n, \tag{2.6}$$

where by combining eq. (2.4) and eq. (2.1) we obtain formally

$$\dot{v}_i(t) = I_i(t) - v_i(t) + s_i(t) - \sum_{j\in\mathbb{Z}_+} \delta(t - \tau_i^j),$$
$$\dot{s}_i(t) = -\beta s_i(t) + \frac{2L\beta}{n} \sum_{k\in\mathbb{N}_n} \sum_{j\in\mathbb{Z}_+} W_{ik}\delta(t - \tau_k^j).$$

To define more precisely the firing times and the evolution of the system, we introduce the notation

$$f([t]_-) = \lim_{\mu\to 0^+} f(t-\mu), \qquad g([t]_+) = \lim_{\mu\to 0^+} g(t+\mu)$$

for a right-continuous function f and a left-continuous function g, respectively. Following section 2.2, we set for all $i \in \mathbb{N}_n$ and $j \in \mathbb{Z}_+$ [13]

$$\tau_i^0 = 0, \quad \tau_i^j = \inf\left\{t \in \mathbb{R} \colon t > \tau_i^{j-1},\ v([t]_-) = 1,\ \dot{v}([t]_-) > 0\right\}, \tag{2.7}$$

and arrange the firing times in a monotonically non-decreasing sequence

$$0 = \tau_{i_0}^{j_0} \le \tau_{i_1}^{j_1} \le \ldots \le \tau_{i_k}^{j_k} \le \ldots \tag{2.8}$$

so that time can be partitioned as follows:

$$t \in \mathbb{R}_+ = \bigcup_{k=0}^{\infty} \left[\tau_{i_k}^{j_k}, \tau_{i_{k+1}}^{j_{k+1}}\right). \tag{2.9}$$

We then arrive at the desired set of $2n$ piecewise-linear evolution equations, defined on each interval $\left[\tau_{i_k}^{j_k}, \tau_{i_{k+1}}^{j_{k+1}}\right)$ as follows:

$$\dot{v}_i(t) = I_i(t) - v_i(t) + s_i(t), \qquad t \in \left(\tau_{i_k}^{j_k}, \tau_{i_{k+1}}^{j_{k+1}}\right), \quad i \in \mathbb{N}_n, \tag{2.10}$$
$$\dot{s}_i(t) = -\beta s_i(t) \qquad t \in \left(\tau_{i_k}^{j_k}, \tau_{i_{k+1}}^{j_{k+1}}\right), \quad i \in \mathbb{N}_n, \tag{2.11}$$

with reset conditions

$$v_{i_k}([\tau_{i_k}^{j_k}]_+) = 0, \tag{2.12}$$

$$s_l([\tau_{i_k}^{j_k}]_+) = s_l([\tau_{i_k}^{j_k}]_-) + \frac{2L\beta}{n} W_{li_k}, \qquad l \in \mathbb{N}_n. \tag{2.13}$$

In the case where we see m simultaneous threshold crossings, such that

$$\tau_{i_k}^{j_k} = \tau_{i_{k+1}}^{j_{k+1}} = \cdots = \tau_{i_{k+m}}^{j_{k+m}}, \qquad m \in \mathbb{Z}_+,$$

the resets are applied on all firing times within the simulation framework. The dynamical system above implies immediately that $v_i(t)$ and $s_i(t)$ are continuous in $[\tau_{i_k}^{j_k}, \tau_{i_{k+1}}^{j_{k+1}})$.

We note that the dynamical system is still perfectly valid for simultaneous threshold crossings, in fact as $n \to \infty$ it is shown later that such events are entirely possible. Practically, the event detection code could, in principle, be subject to numerical difficulties as both $n \to \infty$ and $m \to \infty$, leading to possible errors in capturing all simultaneous spike-times and recording neurons evolving with voltages above threshold. However, we note that for the size of networks and waves simulated throughout this study, no such errors have been reported.

Henceforth, we will present simulations and analysis for the system eqs. (2.10) to (2.13) with time partitions defined by eqs. (2.7) to (2.9) and synaptic functions given by eq. (2.4). A list of control parameters has been included in table 2.1. We remark that the dynamical system presented above is fully *deterministic*.

2.4 Spatially localised bumps

It was first reported in [121] that LIF network models are capable of supporting bumps of localised activity, and in fig. 2.1 we present numerical simulations showing this particular coherent structure. We prescribe a random initial condition

$$v_i(0) \overset{\text{i.i.d.}}{\sim} \mathcal{U}([0,1]), \quad s_i(0) = 0, \quad i \in \mathbb{N}_n, \tag{2.14}$$

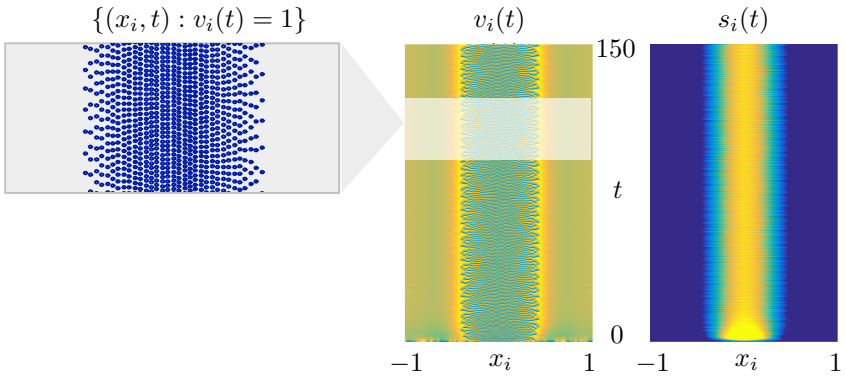


Figure 2.1 Bumps obtained via direct numerical simulation of system eqs. (2.10) to (2.13) with time partitions eqs. (2.7) to (2.9), synaptic functions eq. (2.4), external input eq. (2.5) and initial condition eq. (2.14). We visualise a raster plot of the firing events for a selected portion of the pattern (left) and contour plots of the voltage variables $\{v_i(t)\}_i$ (centre) and of the corresponding synaptic currents $\{s_i(t)\}_i$ (right). Parameters as in table 2.1 with $d_1 = 2$ $d_2 = 10$, $\beta = 1$, $L = 1$ and $n = 500$. Stationary bumps are supported for sufficiently low values of β.

and a short transient external stimulus with functional form given by eq. (2.5). For sufficiently low values of the control parameter β, a bump forms and co-localises with the stimulus (centred around $x = 0$ in this experiment).

The bump is characterised by a localised region of active neurons that receive a sufficient level of synaptic input to fire. Neurons at the edge of the bump and outside are said to be in a homogeneous 'quiescent' or 'all-off' state, here the neuron's voltage never reaches the voltage threshold to facilitate firing.

A bump solution has been shown to exist in this spiking network under the conditions that neurons fire asynchronously within the bump envelope [121]. This means that the firing times of each neuron are uncorrelated, so there is no time dependency in the synaptic input profile. We anticipate that our numerical simulations and future numerical bifurcation analysis will verify that this asynchronicity condition is never truly met for discrete networks. Understanding how a bump is generated as $n \to \infty$ will be one of the main themes in the following chapters.

In fig. 2.1 we present simulation results of the discrete network model with slow synaptic processing ($\beta = 1$), an essential condition for the stationary bump state. The voltage and synaptic histories of a stationary asynchronous bump state depict persistent activity emerging after the transient excitatory stimulus $I_i(t)$ in eq. (2.5). Additionally, a proportion of the simulation is presented as a raster plot marking the space-time position of firing events composing the set

$S = \{(x_i, t) : v_i(t) = 1\}$, which are computed via a Runge-Kutta event-driven method as described in section 2.3. As expected, qualitatively, the results match up to Laing and Chow's findings under an Euler scheme.

Upon closer inspection of the synaptic history plot in fig. 2.1 fluctuations in the synaptic current can be seen for the firing neurons in the bump. The fluctuations are particularly prominent at the edge of the bump. It should be noted that finite-systems do not have a spatially fixed firing rate, and finite fluctuations seem to act as a noise term, which shifts the spatial position of the bumps.

2.4.1 Dependence on initial stimulus

The external stimulus is an important feature of network simulations. In [120] it was shown that the bump state can be switched on and off by an excitatory stimulus. This was interpreted physiologically as an external region of the brain, that projects onto the cortex, being able to turn memories on and off. If all neurons at $t = 0$ are in the all-off state, such that

$$v_i(0) = I \quad s_i(0) = 0, \quad i \in \mathbb{N}_n,$$

the network is in a steady-state of eq. (2.1), remembering that I is subthreshold as defined in table 2.1, such that the network is in its excitable regime. The application of a short transient excitatory stimulus $I(t; d_1, d_2)$, with a functional form given by eq. (2.5), results in a variety of network states emerging, which depend on the parameters governing the stimulus' amplitude d_1 and spatial scale d_2. In each experiment, all other system parameters remain fixed.

The outcomes of numerical simulations based on the initial stimuli are documented in fig. 2.2. In the case $\beta = 0.5$, the synaptic timescale is slow and the network exhibits either the all-off state (blue) or the stationary bump state (green). We find that there is a region of parameter space representing stimuli with low amplitude and large spatial-widths that will always decay back to the all-off state. However, most of parameter space is dominated by the stationary bump state. Interestingly, at the faster synaptic timescale $\beta = 2.5$ the size of the basin of attraction for the stationary bump state diminishes. Synaptic inputs exchanged

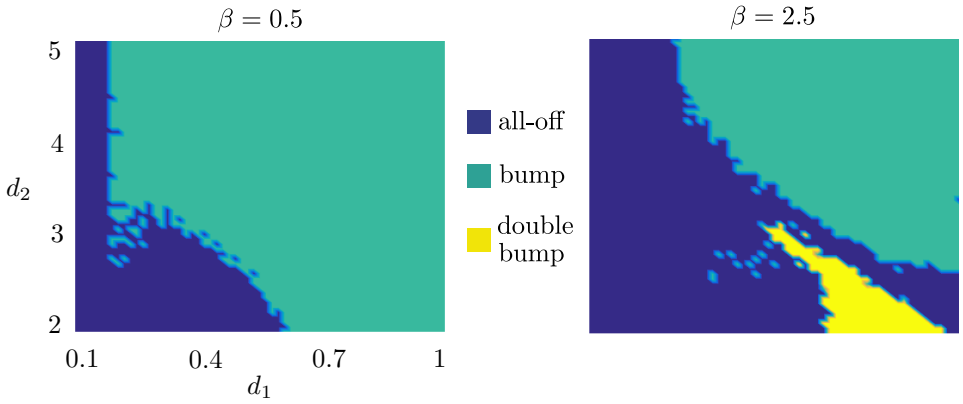


Figure 2.2 Dependence on the initial external given by stimulus eq. (2.5) on outcome of numerical simulations. Each stimuli lasts for $\tau_{\text{ext}} = 1$ and for the symmetric initial conditions $(v_i(0), s_i(0)) = (I, 0)$ for all $i \in \mathbb{N}_n$. The stimulus amplitude and spatial scale are determined by d_1 and d_2 respectively. Note that smaller d_2 equates to larger spatial-width of stimulus. Dark blue corresponds to the all-off state, green a single persistent stationary bump and yellow a double bump. Here $\beta = 0.5$ and $\beta = 2.5$, representing slow and intermediate synaptic processing speeds. Network size $n = 200$ and domain half-width $L = 2$.

amongst neurons decay exponentially with time for only a linear increase in amplitude. As a result, the network requires stronger and more localised stimuli to generate a bump.

We also find a basin of attraction for a persistent double bump state when the strength of the stimulus is strong combined with relatively large spatial-width. The connectivity structure determines the spatial width of the bump state, inhibiting firing neurons at the peripheries of an active localised region and maintaining a sufficient excitatory feedback to neurons firing in its excitatory envelope. If the active localised region is large enough and suitably strong it can branch into two localised bump states connected by a region of inhibition.

2.4.2 Multiple bumps on larger domains

We observed that the number of bumps a network can support is dependent on the spatial scale of the connectivity function and the network domain size. As the domain size is increased, the network can support a greater number of bump states for fixed connectivity parameters. In fig. 2.3 a multiple bump state is initiated with the symmetric initial stimulus:

$$I_{\text{ext}}(x, t) = \sin^2(0.9x)H(\tau_{\text{ext}} - t). \tag{2.15}$$

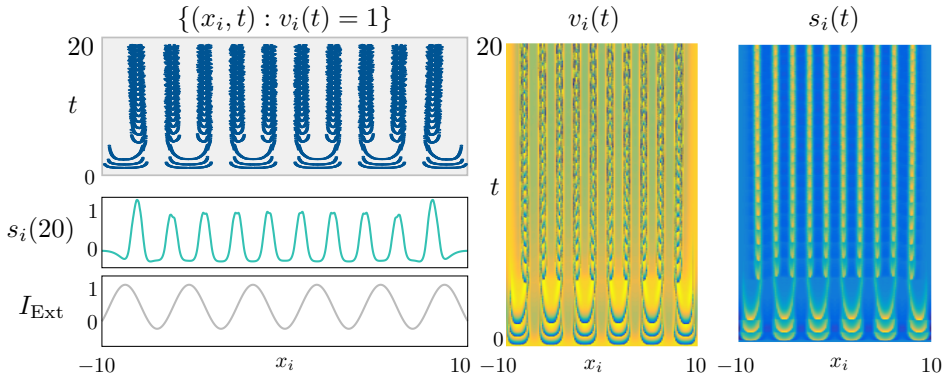


Figure 2.3 Emergence of a multiple bump state on large spatial domain $L = 10$. A brief excitatory stimulus given by eq. (2.15) is applied to a network, with $n = 2000$, for $\tau_{\text{ext}} = 1$. The initial conditions are taken as $(v_i(0), s_i(0)) = (I, 0)$, for all $i \in \mathbb{N}_n$, with synaptic processing rate $\beta = 1.5$ and simulated as before. We depict the resultant raster plot, voltage and synaptic histories and a snap-shot of the synaptic profile at $t = 20$ and the initial stimulus $I_{\text{ext}}(x, t)$.

The wavelength of the initial stimulus is large relative to the spatial-width of the connectivity function. Hence, the central four peaks in $I_{\text{ext}}(x, t)$ each result in a double bump forming with an inhibitory synaptic connection centred over the peaks.

The peaks in $I_{\text{ext}}(x, t)$ closest to $x_i = \pm 10$ only lead to the formation of a single bump, because the remaining network domain is too small for two bumps to form. All bumps with a neighbour on both sides have settled at positions equidistant to one another, connected via a region of negative synaptic current. The outer bumps have only one inhibitory connection and this provides a possible explanation why the amplitude of the outer bumps synaptic current input are greater than the inner bumps. We regard this as a boundary effect.

2.5 Stationary bumps firing rate and existence condition

Laing and Chow have shown that the stationary bump state in this spiking network model can be related to various rate models, including one of the earliest formulations of a bump state in a neural field model introduced by Amari [7]. This is on the condition that the synaptic timescale is slow and the firing neurons making up the bump have uncorrelated firing-times. A snap-shot of a bump's

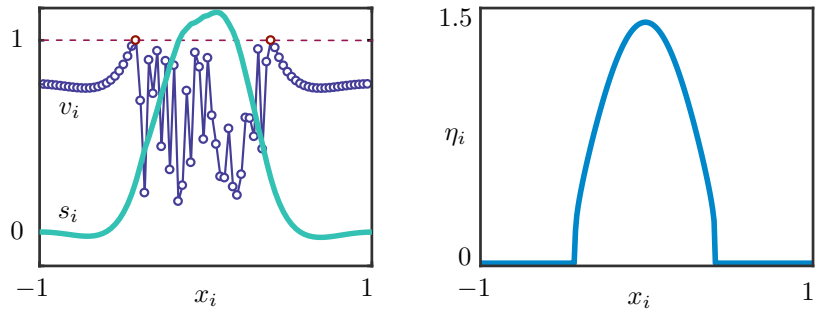


Figure 2.4 (a) A timesnap at $t = t^*$ illustrating the voltage and synaptic spatial profiles $(v_i(t^*), s_i(t^*))$ taken from a simulation of system eqs. (2.10) to (2.13) with $n = 200$ and $\beta = 1.0$. Here it can be seen that the voltages of neurons within the bump envelope have no correlation in firing times and asynchronicity is safely assumed in this discrete network case. (b) The firing rate η_i^* is found by solving eq. (2.23), the central neuron has maximal firing rate, falling to zero at the bump edge.

voltage profile taken from a discrete network simulation is given in fig. 2.4(a) illustrating bump asynchronicity.

We will now discuss the characterisation of the bump states proposed in [121]. We follow their derivation, which we will later compare to and contrast with our bump definition obtained through entirely different means in chapter 4. We start by noting that the LIF neuron is a special case of the Spike Response Model [71], which can be manipulated by formally integrating the differential formulation in eq. (2.1) to arrive at an equivalent formulation for the voltage dynamics in terms of filters. Hence, for $t > \tau_i^j$ and past firing times at τ_i^j, where $j = -1, -2, \ldots, -\infty$, the spike response model takes the following form [121]

$$v_i(t, t') = I - [I + s_i(t')] \exp(t' - t) + s_i(t), \quad t > t', \quad v_i(t', t') = 0, \tag{2.16}$$

where

$$s_i(t) = \frac{2L}{n} \sum_{k \in \mathbb{N}_n} \sum_{j \in \mathbb{Z}_+} W_{ik} \int_{\tau_k^j}^{t} \exp(t' - t) \alpha(t' - t) dt', \qquad i, k \in \mathbb{N}_n. \tag{2.17}$$

A useful definition of the activity history of the ith neuron is $\eta_i(t) = \sum_{j \in \mathbb{Z}_+} \delta(t - \tau_i^j)$, which allows one to rewrite the synaptic input in the following form

$$s_i(t) = \int_0^{\infty} s_i(t') \eta_k(t - t') dt'. \tag{2.18}$$

A commonly used approach is to split the activity into time independent and dependent terms, such that $\eta_i(t) = \eta_i^* + \Delta\eta_i(t)$, where the time-independent activity is simply the mean firing rate [71, 121], thus

$$\eta_i^* = \lim_{T\to\infty} \frac{1}{T} \int_0^T \eta_i(t')dt', \tag{2.19}$$

this is equivalent to counting the total number of firing events m_i in the time window $t \in [\tau_i^0, \tau_i^0 + T]$, such that

$$\eta_i^* = \lim_{T\to\infty} \frac{m_i}{T}. \tag{2.20}$$

Under these considerations the synaptic input can now be expressed as $s_i(t) = s_i^* + \Delta s_i(t)$. However, the asynchronous state in the limit $n \to \infty$ has no time dependent synaptic input, so that $\Delta s_i(t) = 0$ and the synaptic input is taken to be a constant

$$s_i^* = \frac{2L}{n} \sum_{k\in\mathbb{N}_n} W_{ik}\eta_k^*. \tag{2.21}$$

Finally, by noting that the local firing period at the ith neuron is $1/\eta_i^*$, Laing and Chow showed that a set of self-consistent equations can be found for the asynchronous bump state, by substituting s_i^* and η_i^* into the spike response form eq. (2.16) as follows:

$$v_i(1/\eta_i^* + t', t') = 1 = I - [I + s_i^*]\exp(-1/\eta_i^*) + s_i^*. \tag{2.22}$$

The solution to eq. (2.22) is expressed in terms of a gain function such that the bump's firing rate is given by

$$\eta_i^* = F(s_i^*), \tag{2.23}$$

where

$$F(s^*) = \begin{cases} -1/\ln(\frac{I+s^*-1}{I+s^*}) & \text{if} \quad s^* + I > 1 \\ 0 & \text{if} \quad s^* + I \leq 1. \end{cases}$$

In fig. 2.4(b) the firing rate of a bump solution is shown. The existence condition for the stationary bump state is:

$$s_i^* = \frac{2L}{n} \sum_{k \in \mathbb{N}_n} W_{ik} F(s_k^*), \tag{2.24}$$

which is expressed in terms of the intrinsic neuronal dynamics of eq. (2.1) [121]. The all-off state exists for any level of $\frac{2L}{n} \sum_{k \in \mathbb{N}_n} W_{ik}$, but a bump exists only if there is a spatially-localised group of neurons with a non-zero solution s_i^* to eq. (2.24) with $s_i^* + I > 1$.

In summary, the spiking network model can be connected to a rate model in the continuum limit and for slow synapses that facilitate low levels of synchrony. Laing and Chow also generalise this approach to more generic rate models. It is not uncommon to connect spiking network models to rate models in this manner, because this strategy provides useful conditions for the existence of bumps in the network, which are closely related to that seen from discrete simulations.

One of the main contributions of the present study is to show that an alternative mechanism for the formation of stationary bumps is possible, as a well-defined limit of slow travelling waves with a localised profile. This mechanism could also explain wandering bumps, without making any hypothesis on the firing rate function (or on its characteristic time scales). In the following chapters, the firing rate of a bump will be an emergent feature of slowly moving coherent structures, derived in a continuum limit model.

In the next section, we show how networks composed of neurons with faster synapses will result in the connection between this spiking network and rate models breaking down.

2.6 Wandering bumps

Laing and Chow observed that by increasing the synaptic timescale parameter β the stationary bump can destabilise into a wandering bump state. In this section, we reproduce these wandering bump states and then build on this observation by characterising the dynamics of the bump's position in terms of a random diffusion process.

The physiological relevance of this phenomena has been associated to memory destabilisation; experiments from monkey spatial working memory tasks have shown that recall error increases for longer delay times [67, 154, 191]. Furthermore, an oculomotor task performed on human subjects provided the first direct evidence of a temporal limitation of around 20 seconds for spatial working memory [154], citing the "labile" and "transient" nature of working memory representations. In all cases this is indicative of the bump diffusing across the network.

External noise applied to spatially extended neural field models have been shown to induce similar diffusivity in stationary bump solutions. Additive noise can be applied using a spatially extended Langevin system, allowing for an approximation of the bump's diffusion coefficient using a small-noise expansion. In [110], an increase in noise amplitude corresponds to a linear increase in the bump's diffusion coefficient. Although, the distance from a saddle-node bifurcation proved to be more important in determining the stability of the wandering bump state.

We stress that the numerical simulation of a wandering bump in fig. 2.5 is not produced via stochastic effects applied to the network, as studied in [110], but it emerges from the deterministic dynamical evolution eqs. (2.10) to (2.13). Spiking network models like the one considered here are able to capture microscopic timescale dynamics with highly complex or chaotic dynamics, that can be perceived as random without needing to impose an artificial noise term to the system. For this reason, spiking networks have been used effectively to model wandering localised activity states, concluding that the variance of a bump's position scales linearly with time in a purely diffusive manner [27, 33, 37].

The network is translationally symmetric, meaning there is invariance under spatial translations and the bump is marginally stable with respect to any spatial translation. To reiterate, the symmetry allows the bump to be centred initially at any position on the network, but the marginal stability means that this position is fragile and not guaranteed over time [110, 120].

Instead of a finite set of isolated attractors, the networks possesses a continuum of attractors parameterized by their spatial location. Factors that disturb the bump such as: noise, finite fluctuations and what we will refer to as "synchronising effects" all contribute to shift the bump's spatial position.

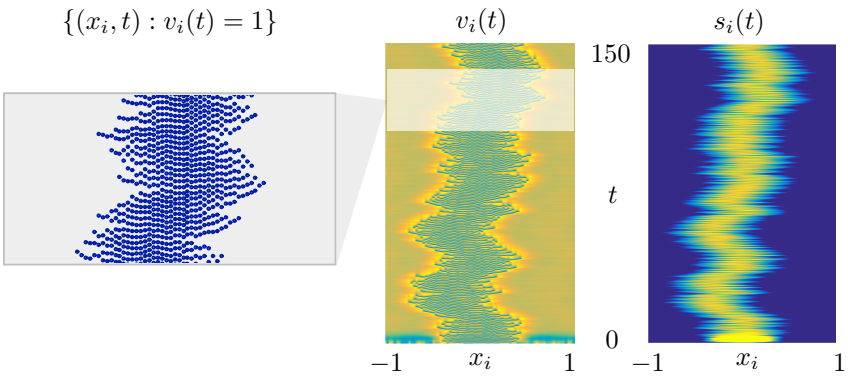


Figure 2.5 Wandering bump obtained via direct numerical simulation of system in the same way as seen in fig. 2.1, but for a faster synaptic timescale of $\beta = 3.5$. Here we visualise a raster plot of the firing events for a selected portion of the pattern (left) and contour plots of the voltage variables $\{v_i(t)\}_i$ (centre) and of the corresponding synaptic currents $\{s_i(t)\}_i$ (right). Parameters as in table 2.1 with $d_1 = 2$ and $d_2 = 10$. It is seen that the increased level of β results in the bump meandering across the network.

Laing and Chow demonstrated that external noise can be used to pin the stationary bump in position and partially prevent the bump wandering, in contrast to that seen in [110]. Although, the increase in β will inevitably dominate the dynamics and lead to bump wandering and further instabilities. To understand this, one must acknowledge that an increase in β corresponds to neurons integrating faster and stronger excitatory synaptic inputs from neighbouring active neurons, which increases the neurons tendency to synchronise. This is a known feature of class 1 integrate-and-fire neurons in response to fast excitation [54, 92].

As previously discussed, the stationary bump must have slow synaptic processing, matching up to desynchronised voltage activity in the bump envelope, whereby, the synaptic input of the ith neuron is a time independent constant s_i^* given by eq. (2.21). In discrete simulations of a stationary bump state, finite sized fluctuations will be present and there will always be a latent level of deviation around the synaptic input mean for each neuron. This would not be expected to change in response to increases β. It is instead the intrinsic synchronising dynamics of the class 1 integrate-and-fire neurons that lead to increasing levels of volatility around a neuron's mean synaptic input as the speed of synaptic processing increases.

To emphasise this point we show in fig. 2.6(a) the average standard deviation σ_i for the ith neuron's synaptic current history $s_i(t)$, over multiple long-time simulations for a bump state with different values of β, plotted as a function of x_i.

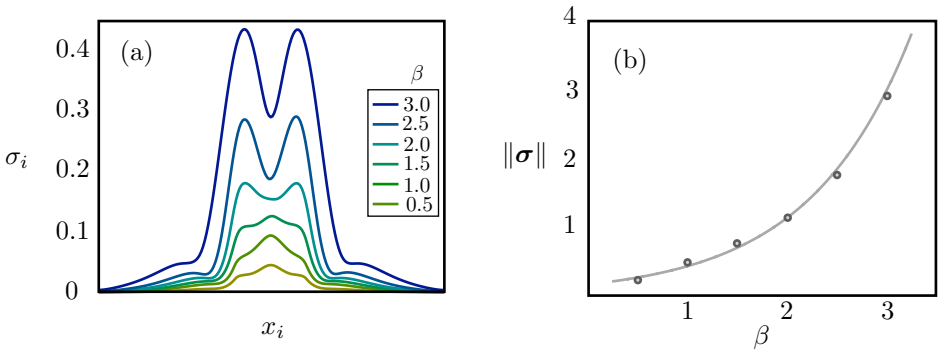


Figure 2.6 We perform $M = 20$ independent time-simulations of network system eq. (2.10)–eq. (2.13) with $n = 200$ neurons for $T = 500$ time units. The synaptic current history of kth run at ith neuron is taken to be $s_i^k(t)$. The history of the kth run is sampled at $\Delta t = 0.1$ time intervals and has standard deviation σ_i^k, which is centred at $x_i = 0$, in (a) the sample mean σ_i over M runs is plotted as a function of x_i for $\beta \in [0.5, 3]$. (b) The L_2-norm $\|\sigma\|$ is plotted as a function of β which is fitted with the exponential $\|\sigma\| = k_1 \exp(k_2 \beta)$, where $k_1 = 0.163, k_2 = 0.968$ and $R^2 = 0.989$.

Low levels of β have low-amplitude standard deviation spatial distributions, with a maximum centred over the synaptic input's maximum; also, the spatial width is more or less unchanged relative to the stationary bump's width. However, for $\beta \geq 2$ the width increases, along with the amplitude. Also, the spatial σ-profile, which had a single peak, now displays two peaks.

The L_2-norm of the standard deviation spatial profile $\|\sigma\|$ is a measure for the network's overall level of fluctuation around the synaptic mean. In fig. 2.6(b) it is found that $\|\sigma\|$ scales exponentially with β.

It is hypothesised that for intermediate levels of β the bump's position follows a random walk on a lattice. The noisy synaptic input fluctuations suggest the bump edge is equally likely to shift left or right. Additionally, the measure of a network's fluctuations around the synaptic mean $\|\sigma\|$ is likely to scale in a similar fashion to the mobility of the bump edges across the network as a function of β. This is because the amplitude of fluctuations in the synaptic input determines the flux of neurons passing through the synaptic input threshold $s_{\min}$.

In order to test this we must track the bump position accurately in time. We define the space-time trajectory of the left edge of a single wandering bump on the discrete lattice $x_i = -2L + 2iL/n$ with $i \in \mathbb{N}_n$ for $t \in \mathbb{R}_+$ as follows

$$x_{\mathrm{L}}(t) = \big\{(x_i, t) : s_{i-1} < s_{\min}, s_i > s_{\min}\big\}, \tag{2.25}$$

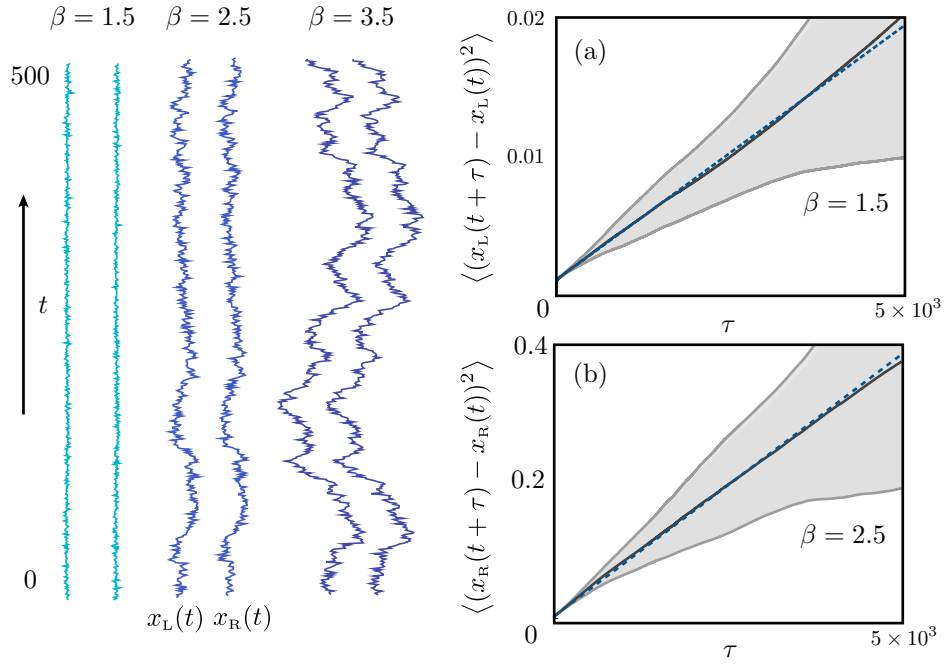


Figure 2.7 On the left are space-time trajectories of three wandering bump edges $x_{\mathrm{L}}(t)$ and $x_{\mathrm{R}}(t)$ for $\beta = 1.5, 2.5, 3.5$, sampled at time intervals of $\Delta t = 0.1$. The results show the bumps domain of wandering increases as β is increased. (a) and (b) are results from $M = 20$ long time simulations lasting $T = 20000$ tracking the left and right bump edge $x_{\mathrm{L,R}}(t)$ for $\beta = 1.5$ and $\beta = 2.5$ respectively. The black line is the ensemble mean arising from M mean-square displacement curves with time delays $\tau \in [0, T/4]$ and the dashed line is its linear fit. The shaded area depicts the weighted standard deviation.

where $s_{\min} = 1 - I$. Similarily, the right edge is defined as

$$x_{\mathrm{R}}(t) = \big\{(x_i, t) : s_i > s_{\min}, s_{i+1} < s_{\min}\big\}. \tag{2.26}$$

In fig. 2.7 the edge trajectories $x_{\mathrm{L,R}}(t)$ are illustrated for three synaptic processing rates. In a random diffusive process the mean square displacement of the edge trajectories scale linearly with time [51], such that $x_{\mathrm{L,R}}(t)$ satisfy

$$\Big\langle \big(x_{\mathrm{L,R}}(t+\tau) - x_{\mathrm{L,R}}(t)\big)^2 \Big\rangle = D\tau, \tag{2.27}$$

where τ is a lag time and D is the bump's diffusion coefficient. We can see from fig. 2.7, obtained from multiple long time simulations of the LIF network model, that the bump is indeed wandering across the network diffusively as expected.

Moreover, the straight line plot in fig. 2.8 clearly shows that, like $\|\sigma\|$, the diffusivity D also increases exponentially with the synaptic processing speed β,

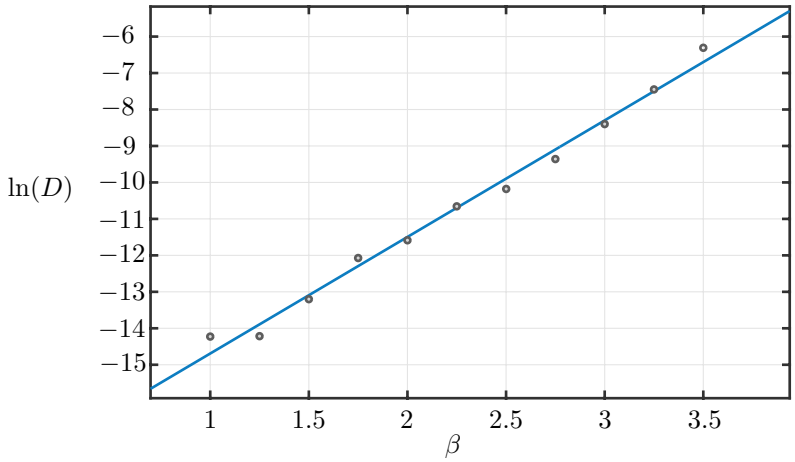


Figure 2.8 The natural log of the diffusion coefficient D plotted as a function the synaptic processing parameter for $\beta \in [1, 3.5]$. The diffusion coefficient is obtained from the slope of the fitted mean square displacement curves using the same method illustrated in fig. 2.7. Therefore, there is an exponential relationship between the diffusion coefficient D and β with formula: $D = k_1 \exp k_2 \beta$, where $k_1 = 1.7 \times 10^{-8}$, $k_2 = 3.20$ and $R^2 = 0.99$.

confirming the hypothesis that the increasingly large fluctuations in synaptic inputs due to faster synapses is a key mechanism behind bump wandering.

The diffusion analysis of wandering bumps is performed for $\beta \in [0.75, 3.5]$, with a network size of $n = 200$, corresponding to a lattice spacing of $\Delta x = 0.02$. We note that if β is too low, the mean-square displacement is too small to provide an accurate slope measurement with the grid-size. On the other hand, the upper bound is selected because for $\beta \geq 3.5$ and a given set of random initial conditions, the maximum bump displacement is likely to exceed the spatial half-width L of the network within the total simulation time. This leads to difficulties in tracking the bump edges. The easiest resolution would be to increase the spatial domain. This would require an increased number of neurons to maintain a constant lattice spacing. However, since the diffusivity scales exponentially with β, there are naturally going to be limitations with this approach.

In conclusion, we have found that bumps in the discrete LIF network wander in a purely diffusive manner. The tracking of the space-time trajectories of the wandering bump's edge over multiple realisations has allowed for the numerical estimation of the bump's diffusion coefficient. As a result, it has been confirmed that the diffusion coefficient scales exponentially with the synaptic processing rate β.

Similar analysis was carried out on another type of spiking neuronal network populated with pulse-coupled neurons, known as the lighthouse model [33]. It is a hybrid network model, with neuron dynamics somewhere between a spiking neuron and firing rate description. This network was also found to support wandering bump dynamics [89]. Unlike the bumps in the LIF network, the neurons that make up the bump in the lighthouse model all fire at a constant firing rate. However, by tracking the neurons that are promoted to the bump's firing rate over time, it was also shown that the edge neurons of the bump display many of the same features as the wandering bump dynamics in the LIF network studied here. In particular, faster synaptic interactions led to wandering and the diffusion coefficient of the bump's position scales exponentially with their measure of synaptic processing speed. It was also shown that lattice spacing scales linearly with the synaptic processing speed.

A key difference between the wandering bumps in the lighthouse model and the LIF network is the dynamical response to excessively high synaptic processing speeds. The wandering bumps in the lighthouse model cannot support such high levels of diffusivity and destabilises into the all-off network state. In contrast, as will be shown in the next section, the wandering bumps in the LIF network will begin to drift.

2.7 Drifting bumps

As β is increased in the LIF network, the bump's edge-trajectories develop noisy oscillations with increasingly large spatio-temporal scales. This can be seen by comparing the bump edge trajectories for $\beta = 2.5$ and $\beta = 3.5$ in fig. 2.7. For $\beta = 3.5$ two timescales have clearly formed, on a microscopic spatio-temporal scale the bump's edge shifts left and right randomly, whereas on a macroscopic scale, clear long term oscillations are present. The origin of these oscillations is due to the class 1 neuron's tendency to synchronise in response to fast excitatory inputs [92]. In fig. 2.9(a) the synaptic input time signals of two neurons in a wandering bump clearly show correlated long term oscillations and uncorrelated smaller-scale random fluctuations as well. The dynamics of wandering bumps is governed by

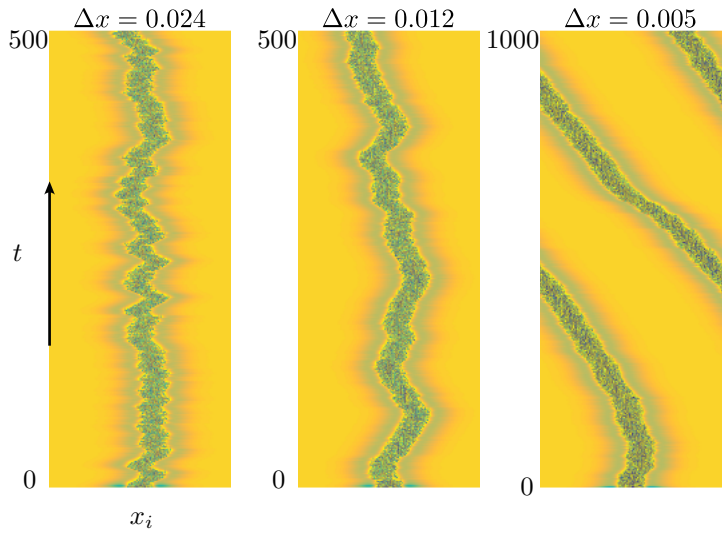


Figure 2.9 Wandering bumps obtained via direct numerical simulation of system eqs. (2.10) to (2.13), synaptic functions eq. (2.4), external input eq. (2.5) and initial condition eq. (2.14). We visualise the voltage histories $v(x,t)$ obtained from simulations of a network with spatial separations $\Delta x = 0.024, 0.012, 0.005$ with $L = 2$. Parameters as in table 2.1 with $d_1 = 2$ $d_2 = 10$ and $\beta = 3.5$.

the relative balance between finite-size fluctuations and the synchronising effects intrinsic to the collective behaviour of neurons. The random fluctuation is the product of the finite-sized network with amplitude scaling as $\mathcal{O}(1/n)$ and can occasionally disrupt synchronisation and cause a shift in the bump's direction.

Long time simulations of the voltage activity history in fig. 2.9 show that the increase in network size and the resultant decrease in size of the noisy fluctuations decrease the number of reversals in direction the bump takes. The network simulation in fig. 2.9(c) illustrates a case where the network size is large enough to prevent any reversals at all, meaning the bump can be seen to drift across the network. The random fluctuations have not diminished entirely; the speed of the drifting varies slightly with transient changes in the bump's voltage activity.

This result is interesting because it clearly highlights the role of the synchronising effect in producing propagating activity in one particular direction. Thus, implying that in the limit $n \to \infty$, the synchronising effect is dominant. We note that the previously discussed lighthouse model differs from this LIF network in two important ways. Firstly, it does not facilitate bump drift, because, it switches directly to the all-off state if the synaptic timescale is too fast. Secondly, the large n limit of lighthouse model on a lattice tends to a stationary bump similar in form to that studied by Amari [7], whereas the continuum limit of the LIF

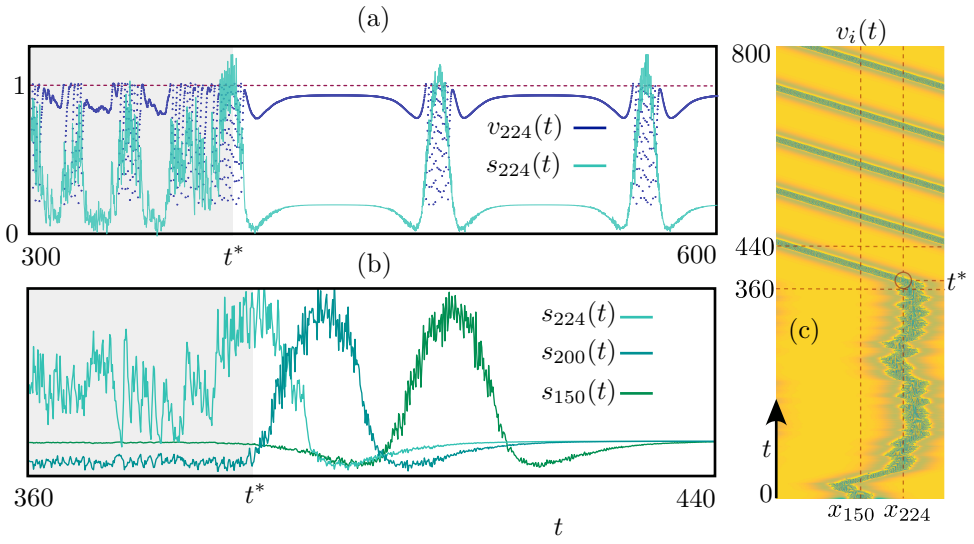


Figure 2.10 Illustrations of transition from wandering bump to travelling wave obtained via direct numerical simulation of system eqs. (2.10) to (2.13), network size $n = 300$, domain half-width $L = 2$ and $\beta = 3.5$. The is network initially in the all-off state where $v_i(0) = I \quad s_i(0) = 0$ for $i \in \mathbb{N}_n$, and stimulated for $t \in [0, 1]$ with eq. (2.5). (a) Synaptic and voltage time evolutions for $t \in [300, 600]$ at spatial position x_{224}, zooming in on transition point at $t^* \approx 385$, (b) shows the synaptic time signals at spatial positions $x_i = x_{224}, x_{200}, x_{150}$ for $t \in [360, 440]$. In both (a) and (b) the wandering bump region is shaded. (c) Network voltage history $v(x, t)$ with circled region highlighting the approximate space-time point where there is the bump to wave transition at t^* and x_{224}.

network is propagating activity. In the following chapters we use semi-analytical techniques to study the continuum limit of the LIF network within the sole context of propagating activity.

2.8 Propagating multiple-spike coherent structures

In discrete networks the random diffusion of a bump's position is governed by the disruptive finite-sized fluctuations and the latent tendency for the bump to propagate via neuronal synchronisation. At intermediate synaptic processing speeds, providing the network size is sufficiently large, it can be seen that propagating activity is the underlying process. However, even for small networks there is a critical synaptic processing speed, whereby the wandering bump in a discrete network makes a spontaneous transition to stable propagating activity. We stress that the criticality of β is not well-defined because it will vary with the network size n, the initial conditions and the spatio-temporal form of the initial stimulus. In fig. 2.10 a network's wandering bump is close to this pseudo-critical β, because

it persists for a relatively long time before making a spontaneous transition to a stable propagating coherent structure at t^*. The synaptic and voltage history of a neuron positioned at the spatial point of transition from wandering bump to wave is shown in fig. 2.10(a). The shaded region depicts the volatile synaptic activity displayed by neurons in a wandering bump state, the neuron's voltage activity regularly make fast transitions from quiescent to firing in direct correspondence to the surges and crashes of the synaptic activity. The transition point is marked by the volatile synaptic time signal being attracted close enough to the coherent localised structure observed in the propagating state. In fig. 2.10(b), the partial synaptic signal emerges from an edge neuron of the wandering bump at t^* and is seen to be effectively transmitted to its neighbouring neurons on the left. The amplitude of finite-sized fluctuations is reduced for neurons further away. There is still an unavoidable background level which is most prominent around the synaptic signal's peak. However, it is clear from fig. 2.10(c) that the propagating state is robust to such levels of noise.

We find that in this network a wave can still emerge from a symmetric set of initial conditions. Post stimulation, the network's symmetry breaks and the asymmetric travelling wave forms and propagates in the positive or negative direction. This was not reported in [120], probably because the network parameters and Mexican hat connectivity function used made it very unlikely for symmetry breaking to occur and the stimulated region instead quickly decays to the all-off state.

As β is increased past the network's pseudo-critical β, we see that the network state is more strongly attracted to the propagating state. The model displays an abundance of coexistent coherent structures travelling with positive or negative speed [120], and variable spatial profiles (see fig. 2.11).

In fig. 2.11 there are two simulations of the discrete network with $n = 80$, taken with a different set of initial conditions, but the same synaptic processing speed $\beta = 4.5$. A close inspection of the firing patterns of the emergent waves post-stimulation reveals two different wave states. In fig. 2.11(a) it appears as if two neurons reach threshold and fire as the synaptic input profile passes over it, and in fig. 2.11(b) a slightly wider synaptic profile results in four neurons firing.

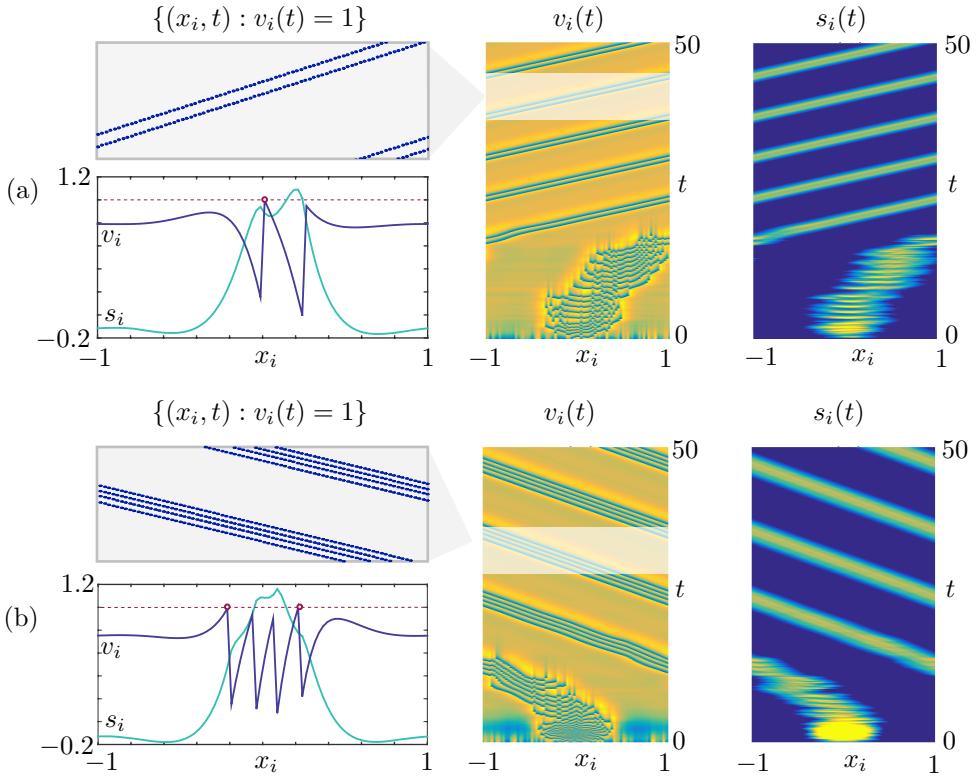


Figure 2.11 Stable coexisting waves obtained via direct numerical simulation of system eq. (2.10)–eq. (2.13) with time partitions eq. (2.7)–eq. (2.9), synaptic functions eq. (2.4), external input eq. (2.5) and initial condition eq. (2.14). Parameters as in table 2.1 with $\beta = 4.5$ and (a) $d_1 = 0.4$, $d_2 = 12$, (b) $d_1 = 2$, $d_2 = 10$. Depending on the initial condition and transient stimulus the model displays: (a) a structure propagating with positive speed, formed by pairs of neurons firing asynchronously, but at short time differences from each other; (b) a similar structure involving a quartet of neurons. Coexisting structures with variable number of firing neurons have also been found (not shown). The spatial profiles indicate that neurons reach threshold (dashed red line) one at a time within a pair in (a) and two at a time within a quartet in (b).

It is observed that the form of the synaptic input pulse is important in dictating how many firing events take place. Another qualitative observation is that the propagation speed is higher for waves with fewer voltage threshold crossings within them.

From the raster plots it would seem that neurons fire simultaneously in pairs (fig. 2.11(a)) or quartets (fig. 2.11(b)) as the structure travels across the network. A closer inspection of the instantaneous profiles $v_i(t)$ reveals that this is not the case, as the threshold (red dashed line) is attained by one neuron at a time (within a pair) and by two neurons at a time (within a quartet). Neurons in a raster pair simply fire alternatively at short time differences from each other, whereas a quartet has a more complex firing patterns.

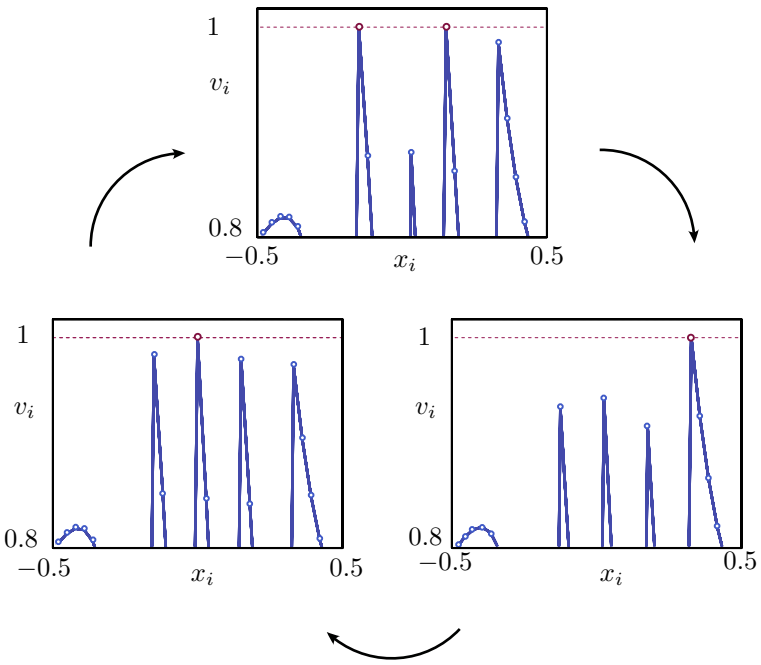


Figure 2.12 Voltage profiles illustrating one example of a repeated firing pattern found from the numerical simulation of a TW_4 wave state, $n = 200$. Red circles mark the neurons that have reached the voltage threshold, corresponding to a firing event.

A wave's firing pattern, or sequence of firing, will often take a certain time to stabilise, one example of a stable firing pattern for a wave with four spikes is illustrated in fig. 2.12. In a network with no extrinsic noise applied, or other forms of heterogeneities, the wave firing sequence will remain locked and results in periodic temporal oscillations in the synaptic input profiles. The question of whether there are specific unstable or stable sequences of firing was not investigated in this study. Neither is the effect of different sequences on macroscopic network dynamics.

At this point it is important to note that, owing to the temporal oscillations in the synaptic profiles, the coherent structure in fig. 2.11 is not a true travelling wave, in the sense that they do not satisfy a travelling wave ansatz. Instead, they are better referred to as saltatory waves. Formally defined travelling waves, obeying a travelling wave ansatz will be investigated in later chapters. With this in mind, henceforth, we will cautiously refer to a propagating state with m voltage threshold crossing and a well defined constant wave speed c by a TW_m, dismissing spike sequences for the sake of later comparison with states found in the continuum limit analysis, where there are expected to be no temporal oscillations.

2.8.1 Waves in purely excitatory network

So far, the connectivity structure of the network has been of a lateral-inhibition form, whereby inhibitory connections have a larger spread than the strong and local excitatory connections. This ensures that the bumps and waves remain localised, facilitating strong self-excitation, keeping the centre excited, while lateral-inhibition prevents the spread of excitatory activity [55].

Numerical simulations of the network with a purely excitatory connectivity structure ($a_2 = 0$) indicate that the network will also support a large family of localised traveling wave solutions in which each cell fires multiple spikes. This was said to be the case in [143], but no simulations results were explicitly shown. In fig. 2.13 we present three example numerical simulations, each with a different initial stimulus and synaptic processing speed. Our observations suggest a complex relationship between these network parameters, with the network activity very sensitive to small parameter changes.

It was shown previously in the lateral-inhibition case that increasing synaptic processing rates can result in post-stimulus activity producing a large variety of travelling wave activity, which tends to propagate in one direction only. This is also the case for the waves found in this purely excitatory network, with the crucial exception that now a pair of localised multiple-spike waves emerge from the stimulated region of the network and propagate in both positive and negative directions. These states are attractive for symmetric and asymmetric initial conditions. In fig. 2.13(a–b) the stimulated central region emits two single-spike waves in both directions successively, before decaying to the all-off state. The emitted wave has a greater synaptic-input amplitude than the second. In fig. 2.13(c–d) a slower synaptic processing speed and wider stimulus spatial width results in the centrally stimulated neurons firing four times before cessation. Interestingly, all the spikes quickly reach a collective constant speed and travel as a co-moving four-spike state, in contrast to the two single-spike waves where the spikes are well-separated and travel at different speeds. It can be seen that all voltage and synaptic activity is contained within a localised structure with a fixed spatial-width.

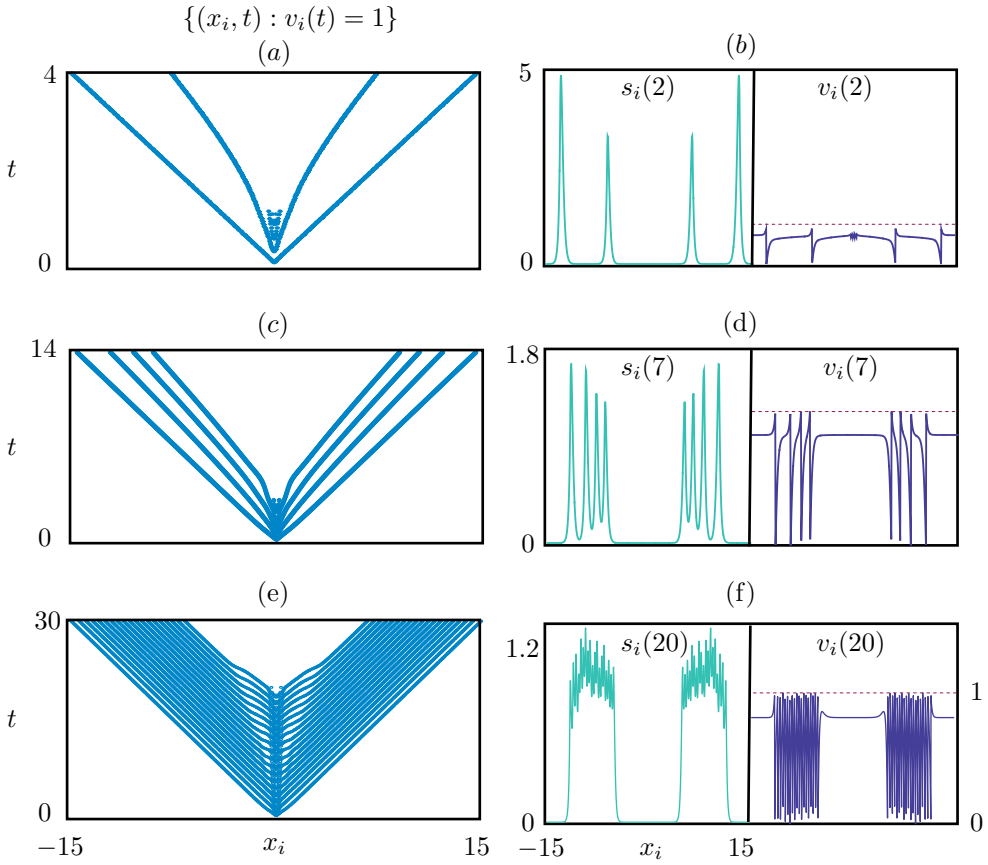


Figure 2.13 Raster plots of firing times for three multiple spike waves found to emerge in direct numerical simulations of the network with pure excitation (no inhibitory connections), in each case snapshots of the voltage and synaptic profiles are given.(a–b): $d_1 = 0.8$, $d_2 = 12$, $\beta = 20$. (c–d): $d_1 = 1$, $d_2 = 10$, $\beta = 7$ (e–f): $d_1 = 2.5$, $d_2 = 4$, $\beta = 4$. Network parameters: $I = 0.81$, $n = 1000$, $L = 15$, $a_1 = 2$ and $b_1 = 5$.

The final simulation in fig. 2.13(e–f) show that the central neurons can continue to oscillate numerous times, producing slow propagating activity with a large number of spikes. In this case, a total of 19 times. Here the modulations in the synaptic profile are smaller in amplitude, but with greater frequency. It was found that slow synaptic processing rates increase the likelihood of a multiple-spike wave emerging post-stimulus.

In fact, at even slower synaptic processing rates, simulations have shown that the central set of neurons appears to fire indefinitely, producing what appears to be periodic wave structures. It is not possible from simulation alone to ascertain whether the central neurons do actually fire indefinitely, or simply an arbitrarily large number of times (too long to be picked up within practical simulation times).

Periodic waves have been studied in this excitatory network by Bressloff [16]; a special case of periodic wave, with the firing time history assumed to be characterised as:

$$\tau_n(x) = (kx + n)T, \tag{2.28}$$

where n is an integer and c is taken to be $1/kT$. Under this ansatz, Bressloff derives a dispersion relation between wave speed c and the wave number k. He then studies the relationship between these wave features and the rise-time of synaptic coupling, synaptic delays, and dendritic cable properties [15, 143].

In this study, we aim to achieve a similar set of results, but under a more generic firing time history function, allowing for the characterisation of waves with a finite number of spikes and different spike-time intervals.

We note that the multiple-spike waves found in simulations here have a large diversity in wave speed. Ermentrout has previously noted that "multiple spikes do not have that much of an impact on the velocity of the initial spike". While the first spike emerging from the stimulated region does indeed set the upper bound for the wave speed, this is not the only defining feature of the wave. We will show in chapter 4 that the knowledge of the neuron's spike-time intervals, as the wave passes over it, is also necessary to fully analyse the multiple-spike waves bifurcation structure and stability properties. It is then possible to understand how the multiple-spike wave speed, spike-time interval distributions and corresponding voltage and synaptic profiles vary with the network's system parameters. Parallels

can then be made with a computational and experimental study investigating propagating neuronal discharges in disinhibited neocortical slices [80]. We find similar dynamics between this relatively simple network model and the complex multi-variate biophysical network used to model the neocortical slices.

2.9 Wave interaction dynamics

In this section we summarise how the localised wave and bump states interact in a larger network. We focus primarily on the interaction between the coherent structure found in the network with lateral-inhibition. There are three main reasons for this:

1. The lateral-inhibition network supports a greater variety of co-existent TW_m states at slow synaptic processing rates, where stationary and wandering bumps can also be found. As a result, we are able to investigate how the multiple-spike waves influence the dynamics of bumps. This is not the case in the purely excitatory network, because at slow synaptic processing rates only waves with a large number of threshold crossings emerge from numerical simulation.

2. Co-existent TW_m states in the lateral-inhibition network have a greater diversity in wave speed for any particular synaptic processing rate. Wave speed diversity is present in the excitatory network, but not to the same extent. The analysis of the wave states in chapter 4 will present numerical continuations of the wave speeds for different m, as a function of system parameters to justify why this is the case. But for the sake of this investigation, diverse wave speeds lead to more interesting dynamics.

3. The TW_m emerging post-stimulation in the lateral-inhibition network are solitary, propagating in the positive or negative direction. Whereas, in the excitatory network the waves emerge as pairs—travelling in both directions. In this set of experiments, waves are isolated in a separate simulation and their final voltage and synaptic profiles are used as initial conditions in later simulations on a larger spatial domain. Therefore, it is more convenient to

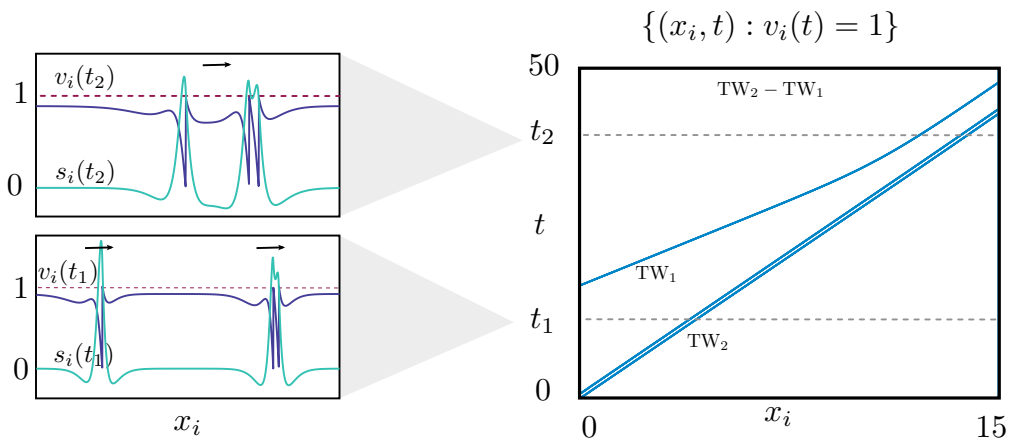


Figure 2.14 Formation of a composite TW_2–TW_1 system. Synaptic and voltage profiles are given at times $t_1 = 15$ and $t_2 = 40$ showing the unconnected TW_2 and TW_1 and the stable TW_2-TW_1. The synaptic processing speed is fixed at $\beta = 6$, and the network parameters are: $n = 3000$, $L = 15$, $\Delta x = 0.01$, $I = 0.9$, $a_1 = 11$, $a_2 = 7$, $b_1 = 5$, $b_2 = 3.5$.

use the lateral-inhibition network because less simulation time is needed to isolate the wave states. In comparison to the excitatory network, where one must wait for the pairs to move far enough away from each other to isolate.

We now present the results of numerical simulations on a large domain. Prior simulations have collated synaptic and voltage profiles corresponding to a variety of bump and TW_m states found in the lateral-inhibition network. Simulations are initialised with a selection of these states glued together on a larger network domain, ensuring the spatial profiles are far enough apart to guarantee no initial interaction between the wave states. We also ensure the lattice spacing Δx is the same as the simulations used to obtain the initial TW_m states.

In fig. 2.14 we show the results of an experiment performed by obtaining the voltage and synaptic profiles of stable TW_1 and TW_2 at $\beta = 5$, both propagating in the positive direction. The TW_2 is positioned in front of the TW_1. A qualitative observation from numerical simulations of the lateral-inhibition network is that for any TW_m found at a fixed β, the wave with fewer threshold crossings m is always the fastest. As a result, it is not a surprise to see in fig. 2.14 the TW_1 eventually catching up with the slower TW_2. The TW_1 is then seen to decelerate as it approaches the TW_2, eventually settling at a constant collective speed, positioned at a fixed distance from the preceding TW_2. Similar to the multiple bumps seen in fig. 2.3, the co-moving system is connected via a region of negative synaptic current. We find that the influence of having such a connection has

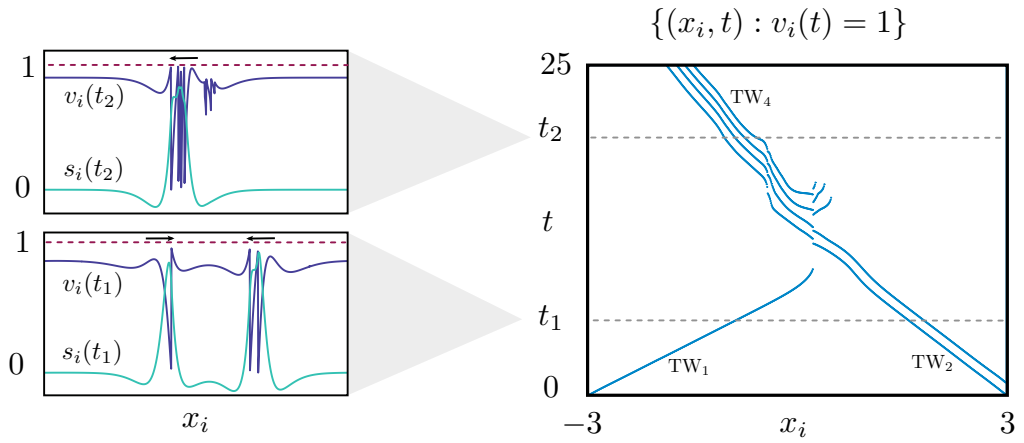


Figure 2.15 Collision between TW_1 and TW_2 pulses leading to the formation of a TW_4. Synaptic and voltage profiles are given at times $t_1 = 7$ and $t_2 = 20$ showing the unconnected TW_2 and TW_1 and the stabilising stable TW_4. The synaptic processing speed $\beta = 3.2$ and the network parameters: $n = 800$, $L = 4$, $\Delta x = 0.01$, $I = 0.9$,$a_1 = 11$,$a_2 = 7$,$b_1 = 5$,$b_2 = 3.5$

resulted in the TW_2 decelerating too. Direct measurements have shown that the co-moving system's collective speed is slightly slower than the speed of the TW_2 when travelling in isolation.

Henceforth, we will call this co-moving system a *composite* wave, and in this particular case refer to it as a TW_2–TW_1, noting that the TW_2 is first because it leads the propagation. It is easily inferred from this experiment that a TW_1–TW_2 state cannot exist, because the TW_2 is always slower than the TW_1 (for fixed β) and can never catch up to form a co-moving state with a single collective speed.

The next experiment, seen in fig. 2.15, investigates what happens when the TW_2 and TW_1 propagate with speeds of opposite signs, and eventually collide. Interestingly, the outcome of the resulting collision leads to the TW_2 being promoted to a TW_4, and the suppression of the TW_1 state. The TW_1 colliding with the TW_2 induces a rapid increase in the synaptic current of neurons at the site of collision, providing enough localised excitatory current to transform the TW_2 into a TW_4. We find this result significant because it offers a dynamic mechanism for increasing the number of threshold crossings of a multiple-spike wave.

We note that this result is just one example of a variety of possibilities. We have found that the results of this experiment are highly variable and sensitive to

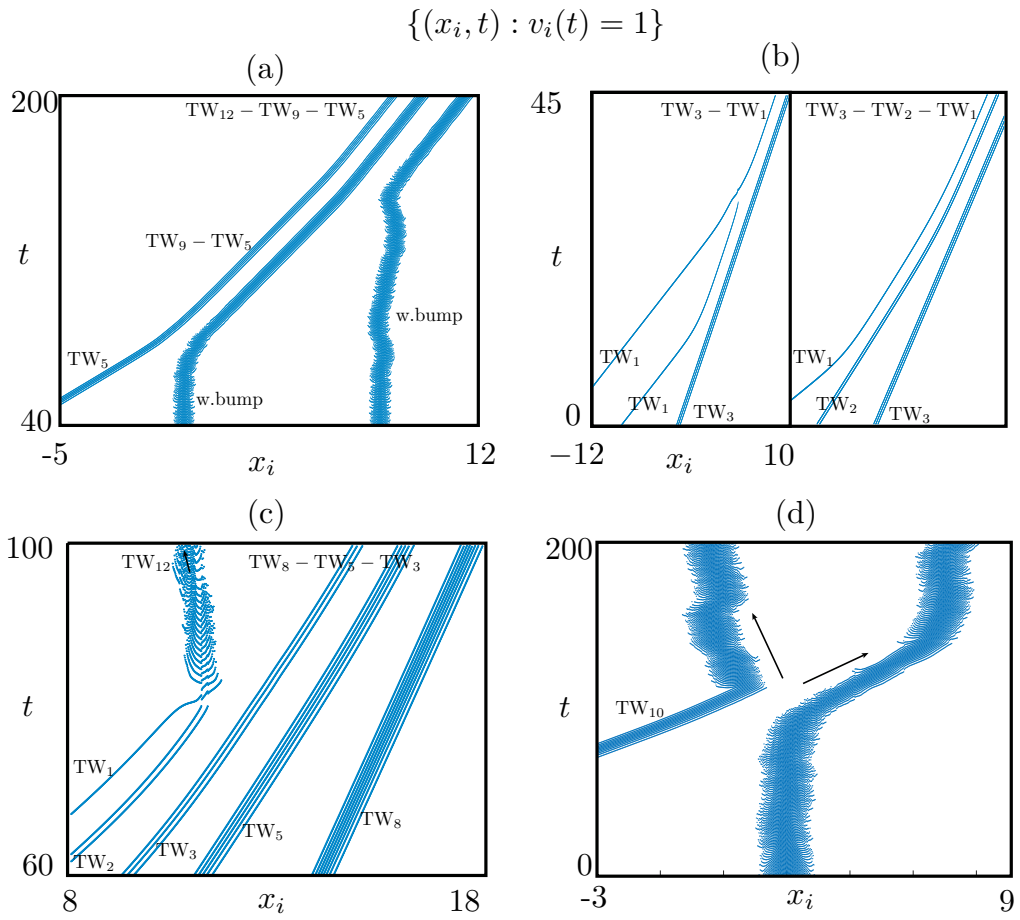


Figure 2.16 Raster plots of the following scenarios (a) two wandering bumps influenced by a TW_5 to eventually form a TW_{12}–TW_9–TW_5, $\beta = 3.6$, (b) Formation of TW_3–TW_1 and TW_3–TW_2–TW_1 with $\beta = 12$ and $\beta = 6$ respectively, (c) formation of TW_8–TW_5–TW_3 and a stabilising TW_{12} propagating in opposite direction, $\beta = 4$ (d) a TW_{10} colliding with stationary bump results in mutual repulsion, $\beta = 3$. All networks have constant lattice spacing $h_x = 0.01$, but variable domain half-width L to capture dynamics, other network parameters: $I = 0.9$, $a_1 = 11$, $a_2 = 7$, $b_1 = 5$, $b_2 = 3.5$.

slight changes in Δx, β and the separation distance of the initial TW_1 and TW_2 states. Some other outcomes generated by the collision of TW_1 and TW_2 include:

- A termination of TW_1 and the emergence of TW_3 with negative speed
- A termination of TW_1, and the persistence of TW_2 with negative speed
- A termination of TW_1 and TW_2, and the emergence of TW_1 with negative speed

It is also thought that the vertical fluctuations of the wave's spatial profiles, due to finite-sized effects, could also effect the outcome of this experiment. We now illustrate the effect multiple-spike waves have on wandering bumps. In fig. 2.16(a)

two wandering bumps and a TW_5 states are initialised. Here we see the TW_5 interacting with the wandering bump and causing it to synchronise into a TW_9, leading to the formation of a TW_9–TW_5 composite wave. This continues to propagate at a constant collective speed until it interacts with the next wandering bump. A similar phenomenon occurs, this time the wandering bump transforms into a TW_{12} state, which results in a stable TW_{12}–TW_9–TW_5 as the final outcome of this experiment.

In fig. 2.16(b) the formation of a TW_3–TW_2–TW_1 and a TW_3–TW_1 is depicted. The simulation on the left panel suggests that the formation of a TW_3–TW_1–TW_1 is not possible, because the TW_1 approaching the TW_3–TW_1 inhibits the TW_1 in the TW_3–TW_1 and takes its place. In chapter 4 we show that the TW_3–TW_1–TW_1 state does not exist in the continuum limit of this network. In contrast, it will be shown that the TW_3–TW_2–TW_1 composite wave does exist and its stability can be analysed, whereby we are able to show that the dynamics closely corresponds to a TW_3 state.

We next devise an experiment to determine if it is possible to keep attaching TW_m states together and form a stable composite wave. The simulation result obtained in fig. 2.16(c) appears to suggest that there are limitations in the range of attached TW_m allowable in a composite wave. We see that the TW_1 at the back of a large slowly moving composite wave will not sustain such a slow speed. Instead it collides with the TW_2 in front of it, causing a bump to be repelled in the opposite direction. Extended simulations have shown that the repelled bump eventually fully synchronises to form a TW_{12} propagating in the opposite direction to the remainder of the composite wave, which continues to propagate unaffected by the drama behind. Cortical waves observed using voltage sensitive dye recording have been shown to exhibit similar exotic dynamics, in particular, waves in the primary and secondary visual cortex can compress and reflect as an evoked wave in the primary cortex enters the secondary cortex [196].

The set-up of the final example in fig. 2.16(d) is similar to fig. 2.16(a), in the sense that it investigates the interaction between a wave and a bump. However, in this case the synaptic processing rate is slightly slower at $\beta = 3$ and a TW_{10} collides with a bump, instead of a TW_5. In this case we observe a mutual repulsion

between the TW_{10} and the bump. Unlike fig. 2.16(a), the TW_{10} propagation is halted, and we observe two bumps propagating in opposite directions.

This section has provided only a flavour of all the possible interactions coherent structures can exhibit. It is outside the scope of this project to exhaustively characterise all of the possible states that can emerge from such simulations, even more so, predict the outcome based upon an initial state. However, as has been alluded to previously, the following chapters will analyse the continuum limit of this network, where we find travelling wave solutions to a variety of composite wave states found from these types of simulation. We also develop a method to compute their stability. Through doing this, we show that there are some simple rules which govern the existence of composite wave solutions.

2.10 Summary

In this chapter we have introduced a spatially distributed network of leaky integrate-and-fire neurons and expressed it as a system of $2n$ piecewise-linear ODEs. A 4th-order time stepper accompanied with a standard event detection technique is used to accurately compute the firing time history of the network. Results from direct numerical simulation have shown that the network supports a rich repertoire of localised coherent structure, including: stationary bumps, wandering bumps, drifting bumps, multiple bumps, a family of coexistent multiple-spike waves and composite wave states.

Our main finding has been the family of coexistent multiple-spike waves, propagating at a well defined constant speed c, with neurons spiking m times as the wave envelope passes over it. We refer to these waves as TW_m. The analysis of multiple-spike waves in the continuum limit will form the next part of this thesis.

At this point we acknowledge the many additional features that could be appended to this LIF network model, for instance: spike frequency adaption, heterogeneity in system parameters, stochastic noise, axonal delays, adding another population of neurons, using different functional forms for connectivity structure and postsynaptic potential functions or taking a more biologically realistic spiking

neuron models with more complex dynamics [106]. However, layering on additional complexities at this point is considered superfluous in light of our central aim—to analyse multiple-spike waves and explore their dynamics.

Chapter 3

Continuum limit multiple-spike waves

3.1 Introduction

In the previous chapter we have investigated via direct numerical simulation the wide variety of coherent structures supported by the discrete integrate-and-fire network. The spatially discrete model consisting of finitely many bistable leaky integrate-and-fire (LIF) neurons, has been shown to support the existence of localised activity patterns (bumps)[120]. We have shown that bump solutions are stable for sufficiently slow synapses, in which the neural field description is a good approximation to the network dynamics, but begin to diffusively 'wander' as the speed of the synapses is increased. For faster synapses, the bumps destabilise into travelling profiles comprising of multiple, synchronously firing neurons in a localised region of the domain. The multiple-spike travelling waves coexist and are stable in a wide range of parameter space.

Computational studies in biophysically realistic network models have long claimed that waves with multiple spiking events exist [47, 79, 80, 183]. In these studies the membrane properties exhibited by individual neurons have been explicitly modelled; however, due to the computational models' complexity, the networks are mathematically intractable. In particular, ascertaining which features of the biophysical model determine the speed of the waves is notably hard [145]. However, the mathematical analysis of networks consisting of simplified spiking neurons has been shown to lead to important general principles that also apply to the more biophysically realistic network models.

In this section we will show that the discrete LIF network studied in chapter 2 can be analysed if considered a spatially continuous network. Continuum spiking networks of LIF neurons with excitatory synapses have been analysed in recent years to investigate single-spike pulses; that is, travelling waves in which each neuron fires once as the wave passes over. For this situation, Ermentrout derived a self-consistency condition, allowing one to obtain expressions for the wave speed in terms of system parameters [56], and Bressloff later analysed the stability of these waves [13, 16].

However, in spite of the model's relative simplicity, similar results for multiple-spike waves have been a lot less prevalent. The reason for this is primarily due to the relative simplicity in analysing the network under a single-spike assumption, where neurons fire only once as the wave passes over it. This avoids the necessity of including multiple resetting conditions in the model, which (as was said in [145]) would require one to obtain solutions for a possibly infinite family of firing times.

That said, an initial framework to study multiple-spike waves was put forward in [143], where it was shown that the network can support a two-spike travelling wave. However, it remained open to determine where such solutions actually exist in parameter space. No details of the waves bifurcation structure or any framework of studying stability was given either.

In this chapter, our main focus is the open problem of multiple-spike waves for the LIF model in chapter 2. To address this problem we first show that the spatially discrete n dimensional ODE system can be justifiably transformed into a partial integro-differential equation similar to that seen in [13, 56, 143], adopting the thermodynamic limit, in which the number of neurons in the network tends to infinity.

To facilitate the analytical construction of multiple-spike wave's steady state voltage and synaptic spatial profiles, we define functions that quantify the times of firing across the domain. Thus, the firing time functions indicate when a neuron at a specific location reaches threshold. We then construct operators which map these functions to solutions of the integro-differential equation. For a wave with an arbitrary number of spike m, a concrete method of obtaining travelling

wave solutions is achieved by solving a set of m equations for the wave's speed and spike-time interval distribution, these are the variables which make up the firing-time functions, and thus fully define the multiple-spike wave.

The characterisation of the wave solutions in terms of firing-time functions—achieved from the explicit computation of the wave's speed and spike-times—facilitates a way to study the stability of multiple-spike waves. This is achieved by perturbing around the firing time functions (similar to [181]) and using our operator, from which we examine the linear stability of the multiple-spike waves through the construction of a non-local eigenvalue problem. At the core of our linear stability analysis is an analytic function whose zeros are eigenvalues of the linearised system. The latter parts of this chapter take the reader through the development of the stability analysis. To our knowledge, the asymptotic stability analysis of multiple-spike waves has not been achieved to date. The analysis has been kept deliberately generic by maintaining the weight function $w(x)$ and postsynaptic potential $\alpha(t)$ in general form. Concrete calculations will be presented in chapter 4 for specific choices of these functions.

3.2 Discrete network to the continuum limit

For a finite number of neurons n, the propagating coherent structures found in chapter 2 are not strictly travelling waves, but are better described as saltatory waves, due to the observed temporal oscillations in the synaptic and voltage profiles as they propagate across the network. As a result, they do not satisfy a travelling wave ansatz.

In section 2.8 it was shown that, after transients, the saltatory waves with $m > 1$ lock into a specific sequence of firing, resulting in periodic temporal oscillations in the networks synaptic input profile $s_i(t)$ (see figs. 2.11 and 2.12). As m increases, the sequence of firing rapidly become more complex in conjunction with the temporal oscillations in the synaptic activity. These patterns of oscillations are primarily due to the discrete numbers of neurons in the network.

In this study, we wish to map the saltatory waves in the discrete network to a travelling wave solution of a partial integro-differential equation, obtained from

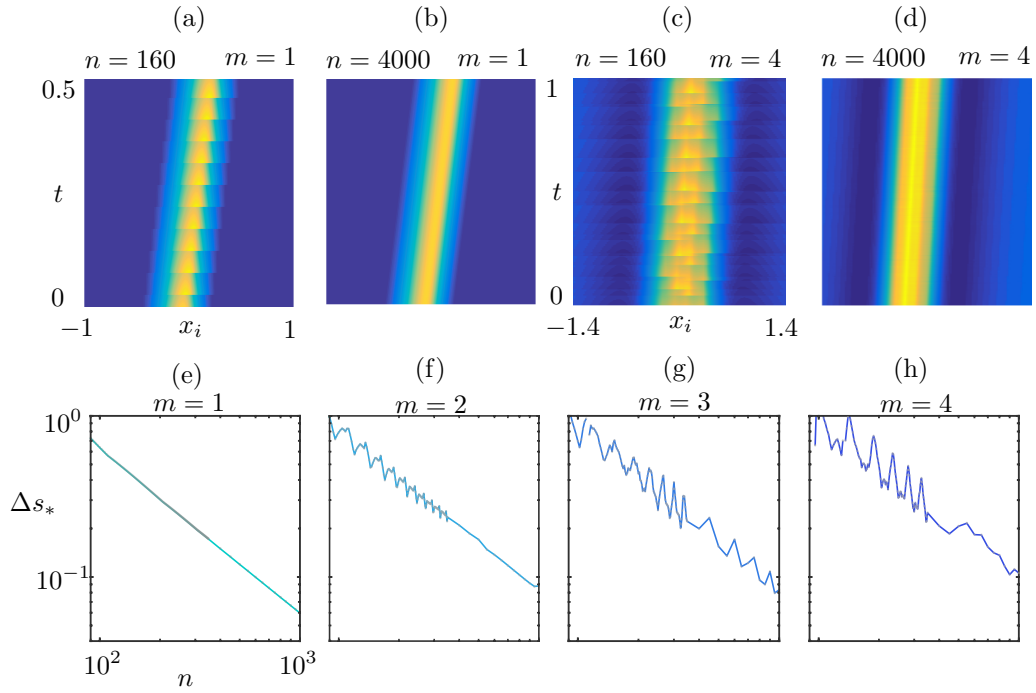


Figure 3.1 The travelling coherent structures found in the discrete model are saltatory waves when n is finite (a)(c) A short time simulation for $n = 160$ highlights oscillations occurring in the patterns, due to the reset conditions eq. (2.13); the oscillations decrease when $n = 4000$ seen in (b)(c). The lower panels monitor oscillations using the quantity Δs_* defined in eq. (3.1), which is plotted against n. The global maximum Δs_* is measured after the network has evolved for 20 time units, allowing plenty of time for transients to dissipate. We find $\Delta s_* = \mathcal{O}(1/n)$, as expected. Spatial half-width $L = 2$ and synaptic processing speed $\beta = 4$. In some cases at small n a wave could not persist.

taking the spatial continuum limit of the discrete network. Here the travelling wave solutions are not expected to have any time-dependent fluctuating component.

A validation of this criteria is found in fig. 3.1, where we show the history plots of the synaptic input $s_i(t)$ of a TW_1 and TW_4 obtained from the network simulation of eq. (2.1) with $n = 160$ and $n = 4000$. In fig. 3.1(a)(c), where $n = 160$, the pulsating fluctuations are clearly visible. A closer inspection shows a simple single mode of oscillation for the TW_1 and a set of complex multi-modal oscillations exhibited by the TW_4. The network simulations in fig. 3.1(b)(d) confirm that the temporal oscillations are diminished for the larger network size.

To further substantiate the claim that temporal oscillations diminish as the network size increases, and also to highlight the possible significance in discrete network dynamics, we estimate variations in the global maximum of $\{s_i(t)\}_i$ using the quantity

$$\Delta s_* = \max_{k,l} |s_*(t_k) - s_*(t_l)|, \qquad \text{where } s_*(t) = \max_{i=1}^{n} s_i(t) \tag{3.1}$$

and plot Δs_* as a function of n for four TW_m states (see the lower panels of fig. 3.1). We find that Δs_* decreases as the network size increases. Interestingly, the curves are not monotonic for $m = 2, 3, 4$, implying that the temporal oscillations of the patterns are not uniformly damped as $n \to \infty$. In the TW_1 case, where there is only one threshold crossing, the curve is monotonic.

Importantly we find from fitting the data that all the trend lines obtained match up to $\Delta s_* = \mathcal{O}(1/n)$, as the resetting conditions eq. (2.13) also suggest.

3.3 Continuum spiking network

The results from the previous section clearly indicate that in the limit $n \to \infty$ the profiles $\{v_i(t)\}_i$ and $\{s_i(t)\}_i$ behave like travelling wave solutions to a continuum spatially extended model. Motivated by this observation we study travelling waves in a continuum, translation-invariant version of the model. In [143] a similar continuum model was introduced where multiple spike states were constructed in terms of past and future currents. A double-spike pulse was analysed, but only for a specific choice of excitatory connectivity kernel. In addition, no

concrete bifurcation curves or stability results were obtained. Here we provide a more compact formulation of multiple spike wave solutions in terms of general connectivity and postsynaptic functions. This formulation will then allow us to derive a nonlocal eigenvalue problem to compute stability of the waves, which has not been reported to date.

We set $d_1 = 0$ in the stimulus eq. (2.5), consider the limit $n \to \infty$ of the discrete model, and pose the model on the real line as opposed to $\mathbb{S}$, obtaining the formal evolution equation

$$\begin{aligned} \partial_t v(x,t) = -v(x,t) + I + \sum_{j\in\mathbb{Z}} \int_{-\infty}^{\infty} w(x-y)\alpha\big(t-\tau_j(y)\big)\,dy \\ - \sum_{j\in\mathbb{Z}} \delta\big(t-\tau_j(x)\big), \qquad (x,t)\in\mathbb{R}\times\mathbb{R}. \end{aligned} \tag{3.2}$$

In the continuum model eq. (3.2) the firing-time functions $\tau_j(x)$ replace the discrete model's firing times τ_k^j. [1]

3.3.1 Single-spike waves in continuum spiking network

The continuum spiking network in eq. (3.2) has been analysed in recent years to investigate the dynamics of single-spike waves [13, 15, 56, 143, 152]. When the network is bistable the existence of traveling waves can be reduced to solving a non-autonomous boundary value problem [56]. The simplicity of the linear integrate-and-fire neuron means the calculation can be done explicitly. Methods have been developed for studying the existence of single-spike travelling waves of activity in continuum integrate-and-fire networks, incorporating a variety of additional features such as axonal or synaptic delays, where, in some parameter regimes, lurching was observed, characteristic of the type of activity found in thalamic tissue [13, 56, 82].

Bressloff and Ermentrout have shown that in the case of a purely excitatory network, a self-consistency condition is easily found, allowing one to obtain expressions for the wave velocity in terms of system parameters [13, 145]. This allowed for the derivation of a series of scaling laws for the wave speed of a

[1] The index j is used as a superscript in the firing times, but for notational convenience we use it as a subscript in the firing functions, so that $\tau_j(x_k) \approx \tau_k^j$.

single-spike pulse as a function of various network parameters. It was found that the velocity of a wave with strong synaptic coupling is essentially independent of the intrinsic ionic details of the neurons, instead the integration rise time from the resting potential to threshold is the critical factor [56]. These results are summarised in chapter 1, as well as the stability of single-spike pulses, also analysed by Bressloff [13], in a network of purely excitable neurons. It was shown that for small axonal delays there is a branch of stable fast waves, transitioning at a saddle-node bifurcation to a branch of unstable slow waves. Interestingly, in the case of long axonal delays and fast synapses, a fast wave will destabilise via a Hopf bifurcation in the firing times.

Our approach is different to existing literature, because it leads to a concrete method of constructing TW_m with arbitrarily large m, as well as computing travelling wave stability. The main idea is to replace the formal evolution eq. (3.2) with a solution operator which maps the firing functions $\{\tau_j\}$ to a spatio-temporal function $v(x,t)$, which satisfies the formal evolution eq. (3.2). By replacing eq. (3.2) with the action of such operator on $\{\tau_j\}$ we manage to compute TW_m and their stability.

We now begin our characterisation of $v(x,t)$ in terms of $\{\tau_j\}$. We stress that this treatment is in the spirit of the interfacial dynamics, proposed by Coombes et al. [43], albeit here we develop it for networks of spiking neurons. Our approach, we claim, is also different from Bressloff and Coombes [14], who constructed non-localised wave trains using a return map on threshold crossings. We instead define an operator that maps firing functions to a spatio-temporal profile. Our approach seems more naturally connected to standard PDE stability analysis, and has the advantage of suggesting immediately a computational procedure to construct travelling waves by solving a low-dimensional problem associated to the travelling wave, as opposed to a boundary value problem for the travelling wave speed and profile. In the latter, space is discretised [50], whereas in our case we solve a coarse exact problem associated with the travelling wave. The coarse problem also suggests a corresponding coarse stability problem, which provides a useful dimension reduction when compared to standard schemes for PDE stability.

3.4 Characterisation of travelling waves in terms of firing functions

The firing times of a wave are a crucial detail in analysing the dynamics of multiple-spikes waves. The full set of firing times can be ascertained from the raster plots in the discrete model, so that a travelling wave corresponding to the $n \to \infty$ limit of the structure in fig. 2.11(a), for instance, will be represented by linear firing functions $\tau_1(x)$ and $\tau_2(x)$. A set of m firing functions can easily be inferred from simulations of the discrete network. In the LIF network studied here, the knowledge of the wave's speed and spike time intervals is all that is required to build up a firing time function, which we show to be invaluable in constructing wave solutions. Specifically, the firing time functions are defined as

$$\tau_j \colon x \mapsto \inf\big\{t \in \mathbb{R} \colon t > \tau_{j-1}(x), \quad v\big(x, [\tau_j(x)]_-\big) = 1, \quad \partial_t v\big(x, [\tau_j(x)]_-\big) > 0\big\}. \tag{3.3}$$

The firing-time functions capture the full firing-time history of the network and can be viewed as level set curves.

As we shall see below, the existence and stability of travelling waves can be studied entirely via the firing time functions $\{\tau_j\}$. In this section, we establish a link between solutions to the continuum model and firing time functions. In addition, we attribute a precise meaning to the formal evolution eq. (3.2). In the discrete case, we turned the discrete formal evolution eqs. (2.1) and (2.2) into a set of piecewise-linear ODEs, defined between consecutive firing times. Here we aim to proceed in a similar fashion, defining a spatiotemporal profile $v(x,t)$ in terms of the firing time functions $\{\tau_j(x)\}$. The $v(x,t)$ defined in this way satisfies the evolution eq. (3.2). We now begin by stating the assumptions that are made upon the synaptic functions: α and w, and the firing-time functions $\{\tau_j\}$. The choice of synaptic and firing-time functions must ensure the following assumptions hold, in order for the upcoming analysis to hold. We assume the following hypotheses:

Hypothesis 3.4.1 (Synaptic functions) *The synaptic kernel $w \colon \mathbb{R} \to \mathbb{R}$ is even, bounded, continuous and such that $\int_{-\infty}^{\infty} |w(x-y)|dy$ is bounded. The post-synaptic function $\alpha \colon \mathbb{R} \to \mathbb{R}_{>0}$ is bounded and can be written as $\alpha(t) = p(t)H(t)$,*

where p is continuous and H is the Heaviside function to ensure causality is preserved.

These properties on the synaptic functions are of course satisfied when w is a Wizard hat function defined by a difference of decaying exponentials, and α is an exponentially decaying function, which have been used in the numerical simulations in chapter 2. However, we note that there are many other variants on these synaptic functions that can be used that have these properties as well.

Hypothesis 3.4.2 (Firing-time functions) *The firing-time functions $\{\tau_j\}$ are continuous, invertible, and satisfy $\tau_j(x) < \tau_{j+1}(x)$ for all $j \in \mathbb{Z}$ and for all $x \in \mathbb{R}$.*

These conditions on the firing-time functions are later shown to be important in defining the domains of integrations, which will facilitate a concise way of addressing the wave stability analysis.

We now aim to characterise a solution of the continuum model eq. (3.2) in terms of its firing-time functions. In order to do this, we define two mappings which are instrumental for this characterisation. The mapping φ is associated to the resetting mechanism built into eq. (3.2) via the Dirac delta functions, whereas, ψ represents the synaptic current input component. We define φ and ψ as follows:

Definition 3.4.3 (Mappings $\boldsymbol{\varphi}$, $\boldsymbol{\psi}$) Let Hypothesis 3.4.1 hold, and let $B(\Omega)$ (respectively $C(\Omega)$) denote the set of bounded (respectively continuous) real-valued functions defined on Ω. We define the mappings $\varphi, \psi \colon C(\mathbb{R}) \to B(\mathbb{R}^2)$ by

$$(\varphi u)(x,t) = \exp(u(x) - t)H(t - u(x)), \tag{3.4}$$

$$(\psi u)(x,t) = \int_{-\infty}^{t} \int_{-\infty}^{\infty} \exp(s-t)w(x-y)\alpha(s-u(y))\,dy\,ds. \tag{3.5}$$

Since $\exp(-x)H(x)$ is bounded, $\varphi u \in B(\mathbb{R}^2)$ for any $u \in C(\mathbb{R})$. We note that φu is discontinuous because of the Heaviside function in eq. (3.4). In addition, by

Hypothesis 3.4.1 there exists $K_\alpha, K_w \in \mathbb{R}_{\geq 0}$ such that

$$\begin{aligned}|(\psi u)(x,t)| &= \left| \int_{-\infty}^{\infty} \int_0^{\infty} \exp(-s) w(x-y) \alpha(t-s-u(y))\, ds\, dy \right| \\ &\leq \int_{-\infty}^{\infty} |w(x-y)| \int_0^{\infty} \exp(-s) \big|\alpha(t-s-u(y))\big|\, ds\, dy \\ &\leq K_\alpha \int_{-\infty}^{\infty} |w(x-y)|\, dy \int_0^{\infty} \exp(-s)\, ds = K_\alpha \int_{-\infty}^{\infty} |w(x-y)|\, dy \leq K_\alpha K_w,\end{aligned}$$

hence $\psi u \in B(\mathbb{R}^2)$ for any $u \in C(\mathbb{R})$. The following properties of the mappings φ, ψ are useful for the upcoming calculations.

Proposition 3.4.4 (Properties of $\boldsymbol{\varphi}$, $\boldsymbol{\psi}$) *Let Hypothesis 3.4.1 hold and let $\{\tau_j\}$ be a set of functions satisfying Hypothesis 3.4.2. Then for all $i, j \in \mathbb{N}_m$ and for all $x \in \mathbb{R}$*

$$(\varphi\tau_j)(x, [\tau_i(x)]_-) = \begin{cases} \exp\big[\tau_j(x) - \tau_i(x)\big] & \text{if } i > j \\ 0 & \text{otherwise,} \end{cases} \tag{3.6}$$

$$(\psi\tau_j)(x, [\tau_i(x)]_-) = (\psi\tau_j)(x, \tau_i(x)). \tag{3.7}$$

In addition, if τ_j is strictly monotonic increasing then $\psi\tau_j$ is given by

$$(\psi\tau_j)(x,t) = \int_{-\infty}^{\tau_j^{-1}(t)} \int_{\tau_j(y)}^{t} \exp(s-t) w(x-y) p\big(t - \tau_j(y)\big)\, ds\, dy. \tag{3.8}$$

Proof The identity eq. (3.6) can be verified directly using Definition 3.4.3, while eq. (3.7) is a consequence of the continuity of $(\psi u)(x,t)$ in the variable t for all $u \in C(\mathbb{R})$. The identity eq. (3.8) is obtained as follows:

$$\begin{aligned}(\psi\tau_j)(x,t) &= \int_{-\infty}^{t} \int_{-\infty}^{\infty} \exp(s-t) w(x-y) \alpha(s - \tau_j(y))\, dy\, ds \\ &= \int_{-\infty}^{\infty} \int_0^{\infty} \exp(-s) w(x-y) \alpha(t - \tau_j(y) - s)\, ds\, dy \\ &= \int_{-\infty}^{\tau_j^{-1}(t)} \int_0^{t-\tau_j(y)} \exp(-s) w(x-y) p(t - \tau_j(y) - s)\, ds\, dy \\ &= \int_{-\infty}^{\tau_j^{-1}(t)} \int_{\tau_j(y)}^{t} \exp(s-t) w(x-y) p(s - \tau_j(y))\, ds\, dy,\end{aligned} \tag{3.9}$$

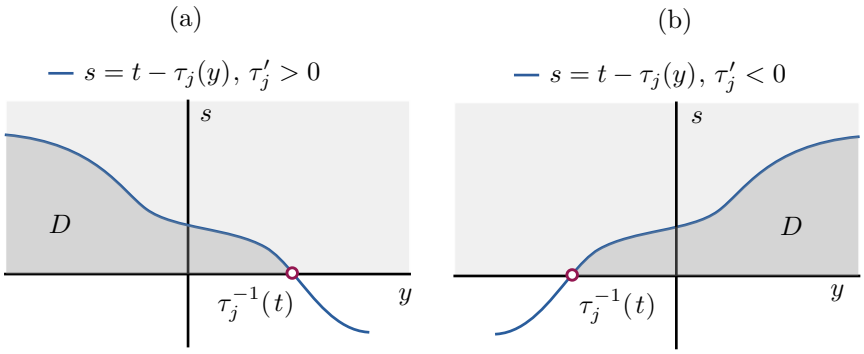


Figure 3.2 Domain of integration for the integral eq. (3.9) when τ_j is (a) monotone increasing and (b) monotone decreasing. The integral is on the domain $(-\infty, \infty) \times [0, \infty)$ (light grey). The integrand has support D, that is, where the function $\alpha(t - \tau_j(y) - s)$ is nonzero.

where we have used a change of variables and the fact that, owing to Hypothesis 3.4.1, $\alpha(t) = p(t)H(t)$ (see also fig. 3.2(a)).

Remark 3.4.5 (Monotonicity of $\{\tau_j\}$) The identity eq. (3.8) is valid if τ_j is a monotone increasing function. The case of a monotone decreasing τ_j can be treated with an identical methodology (see fig. 3.2(b)) and leads to a slightly different expression for eq. (3.8), which we omit for brevity.

We can now characterise special solutions to the continuum model eq. (3.2) in terms of the firing time functions $\{\tau_j\}$, via the mappings φ and ψ.

Proposition 3.4.6 (Solution with m firing functions) *Let Hypothesis 3.4.1 hold and let $\tau = \{\tau_j\}_{j=1}^m$ be a set of monotone increasing functions satisfying Hypothesis 3.4.2. Further, let $V\colon C(\mathbb{R})^m \to B(\mathbb{R}^2)$ be the mapping*

$$V\tau = I + \sum_{j=1}^{m} (\psi\tau_j - \varphi\tau_j), \tag{3.10}$$

where φ and ψ are given by eqs. (3.4) and (3.8), respectively. The function $v(x,t) = (V\tau)(x,t)$ satisfies the formal evolution equation eq. (3.2) with finite m.

Proof When m is finite, the formal evolution equation eq. (3.2) is a rewriting of

$$\begin{aligned} v(x,t) = I &- \sum_{j=1}^{m} \int_{-\infty}^{t} \exp(s-t)\delta(s - \tau_j(x))\, ds \\ &+ \sum_{j=1}^{m} \int_{-\infty}^{t} \int_{-\infty}^{\infty} \exp(s-t) w(x-y)\alpha(s - \tau_j(y))\, dy\, ds. \end{aligned}$$

Using Proposition 3.4.4 and the definition of Dirac distribution we obtain

$$v(x,t) = I - \sum_{j=1}^{m} \exp(\tau(x) - t) H(t(x) - \tau) \\ + \sum_{j=1}^{m} \int_{-\infty}^{\tau^{-1}(t)} \int_{\tau_j(y)}^{t} \exp(s-t) w(x-y) p\big(t - \tau_j(y)\big)\, ds\, dy = (V\tau)(x,t).$$

Proposition 3.4.6's main implication is that a solution to the continuum model with m firing functions is determined once the set $\{\tau_j\}$ is specified. More precisely, the formal equation eq. (3.2) is to be interpreted as a rewriting of eq. (3.10), whenever the functions $\{\tau_j\}$ are monotonic and satisfy Hypothesis 3.4.2. This characterisation is a key part of what follows, and we will state that $v(x,t)$ is a *solution to eq.* (3.2) to indicate that v is the image of a set of suitable functions $\{\tau_j\}$ under V.

We note that Proposition 3.4.6 does not require that $\{\tau_j\}$ satisfy the crossing conditions defined in eq. (3.3), but only Hypothesis 3.4.2. Imposing crossing conditions will allow us to construct travelling waves and study their stability, similarly to what is done for neural fields using interfacial dynamics [43]. A first step in this direction is the definition of the travelling wave using the mapping V.

Definition 3.4.7 (Travelling wave with m firing functions) Let $m \in \mathbb{R}$, $c \in \mathbb{R}_{\neq 0}$ and let $T_1 < \cdots < T_m \in \mathbb{R}$. A travelling wave with m firing time functions and wave speed c (denoted by TW_m), is the image of $\{x/c + T_j\}_{j=1}^m$ under V.

We now show how upon applying the mapping V to the set of firing time functions $\{x/c+T_j\}_{j=1}^m$, an expression for the travelling wave's steady-state voltage profile is obtainable in terms of the travelling wave co-ordinate ξ, thus eliminating the dependence on x and t.

Proposition 3.4.8 (TW_m profile) *A TW_m with positive speed satisfies $(V\tau)(x,t) = \nu(ct - x)$, where $\xi = ct - x$, and the travelling wave profile ν depends on c, $T_1, \ldots, T_m$, given by*

$$\nu(\xi; c, T) = I - \sum_{j=1}^{m} \exp\left(\frac{cT_j - \xi}{c}\right) H\left(\frac{\xi - cT_j}{c}\right) \\ + \frac{1}{c} \sum_{j=1}^{m} \int_{-\infty}^{\xi} \exp\left(\frac{s-\xi}{c}\right) \int_{0}^{\infty} w(y - s + cT_j) p(y/c)\, dy\, ds, \tag{3.11}$$

where $T \in \mathbb{R}^m$ is shorthand for the set of m spike-times $\{T_j\}_{j=1}^m$.

Proof Since c is positive, $x/c+T_j$ are monotone increasing, we can therefore apply Proposition 3.4.6 with $\tau_j = x/c + T_j$. The first sum in eq. (3.11) is immediate, as

$$\begin{aligned}(\varphi\tau_j)(x,t) &= \exp\left(\frac{cT_j - ct + x}{c}\right) H\left(\frac{ct - x - cT_j}{c}\right) \\ &= \exp\left(\frac{cT_j - \xi}{c}\right) H\left(\frac{\xi - cT_j}{c}\right)\end{aligned}$$

The second sum is obtained using directly the definition (3.5) of ψ

$$\begin{aligned}(\psi\tau_j)(x,t) &= \int_{-\infty}^{t}\int_{-\infty}^{\infty} \exp(s-t)w(x-y)p(s-\tau_j(y))\,dy\,ds \\ &= \int_{-\infty}^{t}\int_{0}^{\infty} \exp(s-t)w(x+y-cs+cT_j)\alpha(y/c)\,dy\,ds \\ &= \frac{1}{c}\int_{-\infty}^{ct-x}\int_{0}^{\infty} \exp\left(\frac{s+x-ct}{c}\right)w(y-s+cT_j)\alpha(y/c)\,dy\,ds \\ &= \frac{1}{c}\int_{-\infty}^{\xi}\int_{0}^{\infty} \exp\left(\frac{s-\xi}{c}\right)w(y-s+cT_j)\alpha(y/c)\,dy\,ds.\end{aligned}$$

Proposition 3.4.8 shows that the travelling wave profile ν is completely determined by knowledge of the vector $(c, T_1, \ldots, T_m) \in \mathbb{R}_{>0} \times \mathbb{R}^m$. Associated to each TW_m is the synaptic input profile of the wave which provides a continuum equivalent of the discrete variable $\{s_i(t)\}_i$ of eq. (2.11), via the transformation $s(x,t) = \sigma(ct - x)$, with

$$\sigma(\xi; c, T) = \frac{1}{c}\sum_{j=1}^{m}\int_0^\infty w(y - \xi + cT_j)p(y/c)\,dy. \tag{3.12}$$

In passing, we note that σ occurs as an integrand of eq. (3.11).

3.5 Travelling wave construction

The results of section 3.4 establish a link between solutions of the continuum model and firing time functions $\{\tau_j\}$, and between travelling wave profiles and threshold crossings $\{cT_j\}$. However, they do not provide a concrete way to construct travelling waves. We construct travelling waves as solutions to the following problem:

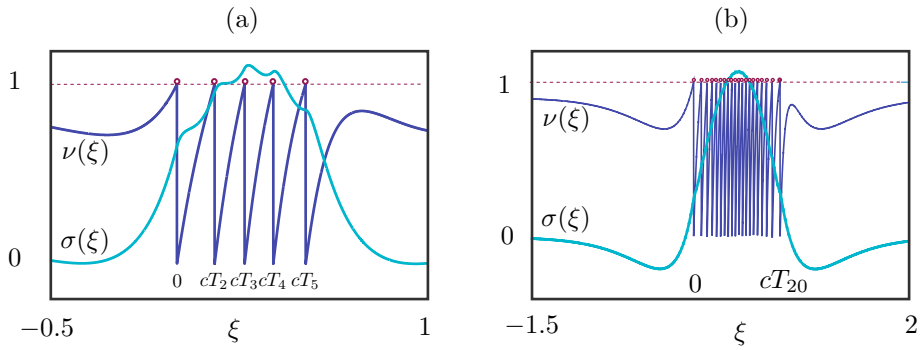


Figure 3.3 Wave profiles for (a) TW_5 and (b) TW_{20} obtained by solving Problem 3.5.1 for $m = 5$ and $m = 20$ and subsitituting the solutions $(c, T_2, \dots, T_m)$ into the expression for voltage profile eq. (3.11) and synaptic profile eq. (3.12). The profile ν is computable at any $\xi \in \mathbb{R}$, but we plot it using an arbitrary grid in the intervals (a) $[-0.5, 1]$ and (b) $[-1.5, 2]$. Parameters as in table 2.1 with (a) $\beta = 4.51$ and (b) $\beta = 7.67$. It is shown that the spatial positions of threshold crossing events are cT_j with $j = 1, 2, \dots, m$.

Problem 3.5.1 (Computation of TW_m) *Find* $(c, T) \in \mathbb{R}_{>0} \times \mathbb{R}^m$ *such that* $T_1 < \cdots < T_m$ *and*

$$T_1 = 0, \tag{3.13}$$

$$\nu([cT_i]_-; c, T) = 1, \quad i \in \mathbb{N}_m. \tag{3.14}$$

Owing to Proposition 3.4.8, the set of $m + 1$ equations above can be evaluated using the mappings ψ, φ. Once (c, T) is computed, the wave profile and synaptic input are obtained from eq. (3.11) and eq. (3.12), respectively. In other words, (c, T) is a vector of *coarse variables* for TW_m, and Problem 3.5.1 is the associated *coarse problem.*

The coarse problem imposes that the travelling wave profile crosses thresholds when $\xi \to cT_j^-$, that is, it requires that $\{\tau_j\}$ do not merely satisfy Hypothesis 3.4.2, but also the firing threshold condition eq. (3.3). As is customary, if ν is a travelling wave profile, then so is $\nu(\xi + \xi_0)$ for any $\xi_0 \in \mathbb{R}$. The first equation of Problem 3.5.1 fixes the phase of the travelling wave, by imposing that the profile crosses threshold as $\xi \to 0^-$.

In the simple case $m = 1$, the coarse problem reduces to a standard compatibility condition for the speed c,

$$c \int_{-\infty}^{0} \int_{0}^{\infty} \exp(s) w\big(c(y - s)\big) p(y)\, dy\, ds = I - 1,$$

which implicitly defines an existence curve for TW_1 in the (c,I)-plane. This result is in agreement with what was found in [13, 56, 143]. Existence curves in other parameters are also possible, and are at the core of the numerical bifurcation analysis presented in section 4.2.

For $m > 1$, the problem must be solved numerically using Newton's method, with initial guesses estimated from direct simulation of the discrete model with large n. A concrete calculation is presented in fig. 3.3, where we show travelling wave profiles and speeds of a TW_5 and a TW_{20}. Depending on the particular choice of α and w, Problem 3.5.1 is either written in closed form, as is the case for the choices eq. (2.4), or approximated using standard quadrature rules. In passing, we note that the synaptic profile of a TW_m is similar to a bump, but displays modulations at the core (visible in fig. 3.3), as predicted by the Heaviside switches in eq. (3.12).

Remark 3.5.2 fig. 3.3 shows that profiles with $\nu([cT_j]_-) = 1$ propagate with *positive* speed, but this does not contradict the numerical simulations in fig. 2.11, where solutions profiles with $v(x, [x/c + T_j]_-) = 1$ propagate with *negative* speed. This is a consequence of choosing $\xi = ct - x$ (as in [143]), hence initial conditions for the time simulations are obtained by reflecting ν about the y axis, since $v(x, 0) = \nu(-x)$.

3.6 Wave Stability

The time simulations in section 2.4 demonstrate that, for sufficiently large values of β, a transient stimulus to the neuronal network elicits travelling waves with a variable number of threshold crossings and, in the previous section, we have seen how to construct these structures semi-analytically. We now present a similar framework to study travelling wave stability. An example of a prototypical wave instability is presented in fig. 3.4 for TW_3, where a travelling wave solution is numerically simulated, and we highlight the corresponding discretised firing time functions (raster plots), observing that they pass from their original form, $\tau_j(x) = x/c + T_j$, to what we regard as a perturbed one, which we refer to as $\tilde{\tau}_j(x) = \tau_j(x) + \varepsilon g_j(x) + O(\varepsilon^2)$. The additional $\mathcal{O}(\varepsilon)$ term captures the growing

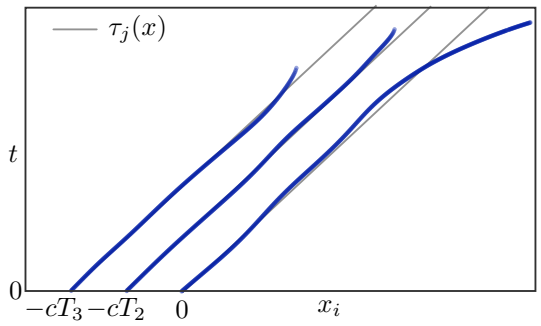


Figure 3.4 Raster plot of a direct simulation with $n = 2000$ showing an unstable TW_3 developing oscillatory perturbations around $\{\tau_j\}$. The firing functions $\{\tau_j\}$ are plotted for reference. The perturbations grow as time increases, and eventually lead to the destruction of the three-spike firing pattern and, hence, of the TW_3 state. In this case, the TW_3 state is in an unstable parameter regime.

oscillatory contribution around τ_j. We will later define g_j more concisely, but for now we state that the wave instabilities are characterised by at least one growing g_j, leading to a wave with a different number of threshold crossings, or to an all-off state (as in fig. 3.4). Similar techniques have been adopted to study stability of travelling wave solutions in networks of excitable systems in [13, 14, 16, 181].

We have constructed travelling waves by specifying the corresponding level-set curves (firing-time functions), as defined in eq. (3.3). Therefore, we now aim to treat stability in a similar fashion, by establishing a relationship between perturbations to a travelling wave solution, and perturbations to the corresponding level set curves. It is instructive to seek this relationship for a generic continuous travelling wave, before moving to the case of discontinuous waves, which is more relevant for the LIF network. We anticipate that the result presented below does not directly apply to our model, as the proposition below assumes the travelling wave profile (and its perturbations) to be smooth. We have decided to include it here as it shows how perturbations on a spatio-temporal travelling wave solution translate to perturbations to level-set curves. This approach will then be adapted to the case under consideration, that is, to the discontinuous spatio-temporal travelling wave solutions of our integrate-and-fire model.

Proposition 3.6.1 (Level curve perturbation) *Let $v, \tilde{v}, z \in C^\infty(\mathbb{R}^2)$ be such that*

$$\tilde{v} = v + \varepsilon z + O(\varepsilon^2), \qquad 0 < \varepsilon \ll 1, \qquad z = O(1), \tag{3.15}$$

and let $\tau, \tilde{\tau}, g \in C^\infty(\mathbb{R})$ *satisfy*

$$\tilde{v}(x, \tilde{\tau}(x)) = v(x, \tau(x)) = \kappa, \qquad \tilde{\tau} = \tau + \varepsilon g + O(\varepsilon^2), \qquad g = O(1) \tag{3.16}$$

for all $x \in \mathbb{R}$ *and for some* $\kappa \in \mathbb{R}$*. Then* g *satisfies*

$$0 = \mathcal{L}(x, \tau) g(x) + O(\varepsilon) \quad x \in \mathbb{R}, \tag{3.17}$$

where $\mathcal{L}(x, \tau)$ *is the linear operator defined by*

$$\mathcal{L}(x, \tau) \colon g \mapsto \partial_t v(x, \tau) g + z(x, \tau). \tag{3.18}$$

Furthermore, if there exist $c \in \mathbb{R}_{\neq 0}$*,* $\lambda \in \mathbb{R}$*,* $\nu, \zeta \in C^\infty(\mathbb{R})$ *such that*

$$v(x, t) = \nu(ct - x), \qquad z(x, t) = \exp(\lambda t)\zeta(ct - x), \tag{3.19}$$

and the set $\mathbb{X} = \{\xi \in \mathbb{R} | \nu(\xi) = \kappa\}$ *has an empty interior, then*

$$\tau(x) = x/c + T, \quad g(x) = -\frac{\zeta(cT)\exp(\lambda T)}{c\nu'(cT)} \exp(\lambda x/c) + O(\varepsilon), \quad x \in \mathbb{R}, \quad cT \in \mathbb{X}. \tag{3.20}$$

Proof From eq. (3.15) and the definition of $\tilde{\tau}$ in eq. (3.16) we obtain

$$\begin{aligned} \tilde{v}(x, \tilde{\tau}(x)) &= v(x, \tilde{\tau}(x)) + \varepsilon z(x, \tilde{\tau}(x)) + O(\varepsilon^2) \\ &= v(x, \tau(x)) + \varepsilon \big[\partial_t v(x, \tau(x)) g(x) + z(x, \tau(x))\big] + O(\varepsilon^2) \end{aligned}$$

and, using the definition of level curves in eq. (3.16),

$$0 = \partial_t v(x, \tau(x)) g(x) + z(x, \tau(x)) + O(\varepsilon), \tag{3.21}$$

where we see that eq. (3.17) holds true when $\mathcal{L}$ is specified by eq. (3.18).

We then proceed to prove the second part of the statement. Without loss of generality, we assume $c > 0$ and set $\mathbb{X} = \{cT_j\}_j$, where $j \in \mathbb{N}$ or $j \in \mathbb{N}_m$ for some integer m. By main hypothesis we have $v(x, \tau(x)) = \nu(c\tau(x) - x) = \kappa$ and, since $\mathbb{X}$ has an empty interior, $c\tau(x) - x = cT$ for all $x \in \mathbb{R}$ and $T \in \{T_j\}_j$ or,

equivalently

$$\tau(x) = x/c + T, \qquad x \in \mathbb{R}, \qquad cT \in \mathbb{X}.$$

Combining the equation above with eq. (3.21) and with the main hypothesis on z we obtain eq. (3.20).

Proposition 3.6.1 shows how perturbations $z(x,t)$ in the frame of reference of a travelling wave solution $v(x,t) = \nu(ct - x)$ translate into perturbations $(x, g(x))$ to a κ level-set curve $(x, \tau(x))$ of the spatio-temporal profile $v(x,t)$. To further explain this concept, we make an analogy with partial differential equations (PDEs): to study the stability of a travelling wave solution $(\nu(\xi), c)$ of a PDE in the state variable $v(x,t)$, one sets $\tilde{v}(x,t) = \nu(ct - x) + \varepsilon z(ct - x, t) + O(\varepsilon^2)$ and linearises the evolution equation for v around ν. This leads to a linear separable evolution equation for the perturbation $z(\xi,t)$ [166], and hence to the decomposition $z(\xi,t) = e^{\lambda t}\zeta(\xi)$ where λ and ζ are solutions to a local eigenvalue problem; in addition, translation invariance implies that for $\lambda = 0$ we have $\zeta(\xi) \propto \nu'(\xi)$.

In PDEs, one is generally not interested in perturbations to the level-set curves of v, as the problem is fully specified in terms of perturbations to the solution profiles. Proposition 3.6.1, however, shows how to choose level-set perturbations g so as to respect the decomposition $\tilde{v}(x,t) = \nu(ct - x) + \varepsilon e^{\lambda t}\zeta(ct - x) + O(\varepsilon^2)$: these perturbations solve (to leading order) the linear problem eq. (3.17) and they are (to leading order) exponentials in the variable x. Furthermore, translation invariance is reflected by the fact that T is arbitrary and that $\lambda = 0$ implies $\zeta(cT) \propto \nu'(cT)$.

It is important to point out that Proposition 3.6.1 does entail a linearisation of an evolution equation for v. In this respect, it should be noted that Proposition 3.6.1 provides a *kinematic argument* to link exponentially growing/decaying perturbations z of v to perturbations g of τ, which relies only on first-order expansion of the full spatio-temporal profile $v(x,t)$. This feature is particularly relevant to our case, because we can only rely on a well-defined solution profile $v(x,t)$, via the mapping V, while the evolution equation for v is only formally expressed.

We now proceed with a similar argument, which will be adapted to solutions $V\tau$ of the continuous model. Since $(V\tau)(x,t)$ is discontinuous along each of the 1 level-set curves $(x,\tau_j(x))$, Proposition 3.6.1 can not be applied.

Lemma 3.6.2 (Linearisation around firing functions) *Let Hypothesis 3.4.1 hold, and let $\{\tau_j\}$, $\{\tilde{\tau}_j\}$ be two sets of firing functions satisfying Hypothesis 3.4.2 such that*

$$\tilde{\tau}_i(x) = \tau_i(x) + \varepsilon g_i(x) + O(\varepsilon^2), \quad 0 < \varepsilon \ll 1, \quad g_i = O(1), \qquad i \in \mathbb{N}_m, \qquad x \in \mathbb{R},$$

that is, $\{\tilde{\tau}_j\}$ are perturbations of the firing functions $\{\tau_j\}$. The corresponding unperturbed and perturbed solutions to eq. (3.2), $V\tau$ and $V\tilde{\tau}$, respectively, satisfy

$$(V\tilde{\tau})(x,[\tilde{\tau}_i(x)]_-) - (V\tau)(x,[\tau_i(x)]_-) = \varepsilon \mathcal{L}_i(x,\tau)g + O(\varepsilon^2), \qquad x \in \mathbb{R}, \quad i \in \mathbb{N}_m, \tag{3.22}$$

where the linear operators $\mathcal{L}_i$ are defined as

$$\begin{aligned}
\mathcal{L}_i(x,\tau)\colon g \mapsto & \sum_{j=1}^{i-1} \exp(\tau_j(x) - \tau_i(x))\big[g_i(x) - g_j(x)\big] \\
& + \sum_{j=1}^{m} \int_{-\infty}^{\tau_j^{-1}(\tau_i(x))} \exp(\tau_j(y) - \tau_i(x)) w(x-y)\big[g_i(x) - g_j(y)\big] p(0)\, dy \\
& + \sum_{j=1}^{m} \int_{-\infty}^{\tau_j^{-1}(\tau_i(x))} \int_0^{\tau_i(x)-\tau_j(y)} \exp(-s) w(x-y)\big[g_i(x) - g_j(y)\big] p'\big(-s + \tau_i(x) - \tau_j(y)\big)\, ds\, dy.
\end{aligned}$$

Proof The statement is obtained by employing Proposition 3.4.6 for τ and $\tilde{\tau}$ separately, and it exploits the properties of φ and ψ found in Proposition 3.4.4. The proof contains a lengthy but conceptually simple calculation, involving Taylor expansions and changes of variables in the integrals. The stability condition proposed in lemma 3.6.2 relating perturbed and unperturbed solutions with firing functions $\{\tau_j\}$ and $\{\tilde{\tau}_j\}$ can be expressed in terms of the mappings φ and ψ set

out in Definition 3.4.3, such that

$$\begin{aligned} 0 = v(x,[\tilde{\tau}_i(x)]_-;\{\tilde{\tau}_j\}) - v(x,[\tau_i(x)]_-;\{\tau_j\}) \\ &= (V\tilde{\tau}_j)\,(x,[\tilde{\tau}_i(x)]_-) - (V\tau_j)\,(x,[\tau_i(x)]_-) \\ &= -\sum_{j=1}^{m}\Big[(\varphi\tilde{\tau}_j)(x,[\tilde{\tau}_i(x)]_-) - (\varphi\tau_j)(x,[\tau_i(x)]_-)\Big] \\ &\quad + \sum_{j=1}^{m}\Big[(\psi\tilde{\tau}_j)(x,[\tilde{\tau}_i(x)]_-) - (\psi\tau_j)(x,[\tau_i(x)]_-)\Big] \end{aligned} \tag{3.23}$$

We use the properties of φ stated in Proposition 3.4.4 to expand the first sum on the right-hand side of eq. (3.23) in powers of ε, as follows

$$\begin{aligned} &\sum_{j=1}^{m}(\varphi\tilde{\tau}_j)(x,[\tilde{\tau}_i(x)]_-) - (\varphi\tau_j)(x,[\tau_i(x)]_-) \\ &\qquad = \sum_{j=1}^{i-1}\exp(\tau_j(x)+\varepsilon g_j(x)-\tau_i(x)-\varepsilon g_i(x)) - \exp(\tau_j(x)-\tau_i(x)) \\ &\qquad = \varepsilon\sum_{j=1}^{i-1}\exp(\tau_j(x)-\tau_i(x))\big[g_j(x)-g_i(x)\big] + O(\varepsilon^2), \end{aligned} \tag{3.24}$$

where we note that the sum on the right-hand side runs only up to $j = i-1$; in this case, we have used the fact that $\{\tilde{\tau}_j\}$ satisfy Hypothesis 3.4.2.

The expansion of the second sum in the right-hand side of eq. (3.23) is more involved. The continuity of ψ defined in Proposition 3.4.4 enables one to write in future

$$\sum_{j=1}^{m}(\psi\tilde{\tau}_j)(x,[\tilde{\tau}_i(x)]_-) - (\psi\tau_j)(x,[\tau_i(x)]_-) = \sum_{j=1}^{m}(\psi\tilde{\tau}_j)(x,\tilde{\tau}_i(x)) - (\psi\tau_j)(x,\tau_i(x)). \tag{3.25}$$

By Definition 3.4.3 we can write the unperturbed ψ component as follows

$$(\psi\tau_j)(x,\tau_i(x)) = \int_{-\infty}^{\tau_j^{-1}(\tau_i(x))}\int_{0}^{\tau_i(x)-\tau_j(y)}\exp(-s)w(x-y)p(-s+\tau_i(x)-\tau_j(y))ds\,dy, \tag{3.26}$$

and similarly for perturbed ψ by

$$(\psi\tilde{\tau}_j)(x,\tilde{\tau}_i(x)) = \int_{-\infty}^{\tilde{\tau}_j^{-1}(\tilde{\tau}_i(x))} \int_0^{\tilde{\tau}_i(x)-\tilde{\tau}_j(y)} \exp(-s)w(x-y)\alpha(-s+\tilde{\tau}_i(x)-\tilde{\tau}_j(y))\,ds\,dy. \tag{3.27}$$

The expression for $\psi(x,\tilde{\tau}_i(x);\{\tilde{\tau}_j\})$ can be expanded in powers of ε, but first we must derive the identity for $\tilde{\tau}_j^{-1}(\tilde{\tau}_i(x))$. To do this, we begin by writing $\tilde{\tau}_j^{-1}(t)$ as an asymptotic expansion in orders of ε

$$\tilde{\tau}_j^{-1}(t) = f_0(t) + \varepsilon f_1(t) + O(\varepsilon^2). \tag{3.28}$$

Then by noting that $\tilde{\tau}_j(x) = \tau_j(x) + \varepsilon g_j(x) + O(\varepsilon^2)$ and $t = \tilde{\tau}_j(\tilde{\tau}_j{}^{-1}(t))$, we can substitute the asymptotic expression for $\tilde{\tau}_j^{-1}(t)$ given by eq. (3.28) into $\tilde{\tau}_j(x)$ and Taylor expand as follows:

$$\begin{aligned} t &= \tau_j(f_0(t) + \varepsilon f_1(t)) + \varepsilon g_j(f_0(t) + \varepsilon f_1(t)) \\ &= \tau_j(f_0(t)) + \varepsilon\tau_j'(f_0(t))f_1(t) + \varepsilon g_j(f_0(t)) + O(\varepsilon^2). \end{aligned}$$

Finally, solving the resulting $O(1)$ and $O(\varepsilon)$ components on both sides gives

$$\tilde{\tau}_j^{-1}(t) = \tau_j^{-1}(t) - \varepsilon h_j(t) + O(\varepsilon^2), \tag{3.29}$$

where

$$h_j(t) = \frac{g_j(\tau_j^{-1}(t))}{\tau_j'(\tau_j^{-1}(t))}.$$

Now we substitute the identity eq. (3.29) into eq. (3.27) and Taylor expand the postsynaptic potential function $p(t)$ to obtain

$$
\begin{aligned}
&(\psi\tilde{\tau}_j)(x,\tilde{\tau}_i(x)) \\
&= \int_{-\infty}^{\tau_j^{-1}(\tau_i(x))} \int_0^{\tau_i(x)-\tau_j(y)} \exp(-s) w(x-y) p(-s+\tau_i(x)-\tau_j(y)) ds\, dy \\
&+ \int_{\tau_j^{-1}(\tau_i(x))}^{\tau_j^{-1}(\tau_i(x))-\varepsilon h_j(\tau_i)} \int_0^{\tau_i(x)-\tau_j(y)} \exp(-s) w(x-y) p(-s+\tau_i(x)-\tau_j(y)) ds\, dy \\
&+ \varepsilon \int_{-\infty}^{\tau_j^{-1}(\tau_i(x))} \int_0^{\tau_i(x)-\tau_j(y)} \exp(-s) w(x-y) \big[g_i(x)-g_j(y)\big] p'(-s+\tau_i(x)-\tau_j(y)) ds\, dy \\
&+ \int_{-\infty}^{\tau_j^{-1}(\tau_i(x))} \int_{\tau_i(x)-\tau_j(y)}^{\tilde{\tau}_i(x)-\tilde{\tau}_j(y)} \exp(-s) w(x-y) \big[g_i(x)-g_j(y)\big] p(-s+\tau_i(x)-\tau_j(y)) ds\, dy \\
&+ O(\varepsilon^2),
\end{aligned}
$$

and by the fundamental theorem of calculus we obtain

$$
\begin{aligned}
&(\psi\tilde{\tau}_j)(x,\tilde{\tau}_i(x)) \\
&= \int_{-\infty}^{\tau_j^{-1}(\tau_i(x))} \int_0^{\tau_i(x)-\tau_j(y)} \exp(-s) w(x-y) p(-s+\tau_i(x)-\tau_j(y)) ds\, dy \\
&+ \varepsilon \int_{-\infty}^{\tau_j^{-1}(\tau_i(x))} \int_0^{\tau_i(x)-\tau_j(y)} \exp(-s) w(x-y) \big[g_i(x)-g_j(y)\big] p'(-s+\tau_i(x)-\tau_j(y)) ds\, dy \\
&+ \varepsilon \int_{-\infty}^{\tau_j^{-1}(\tau_i(x))} \exp(\tau_j(y)-\tau_i(x)) w(x-y) \big[g_i(x)-g_j(y)\big] p(0)\, dy \\
&+ O(\varepsilon^2).
\end{aligned}
$$

Substituting all derived terms into eq. (3.23), the $O(1)$ terms cancel, with the remaining $\mathcal{O}(\varepsilon)$ terms making up the linear operator $\mathcal{L}(x,\{\tau_j\})$, thus

$$
(V\tilde{\tau})\,(x,[\tilde{\tau}_i(x)]_-) - (V\tau)\,(x,[\tau_i(x)]_-) = \varepsilon \mathcal{L}_i(x,\tau)(g_1,\ldots,g_m) + O(\varepsilon^2)
$$

where

$$\begin{aligned}\mathcal{L}_i(x,\tau)\colon g \mapsto &\sum_{j=1}^{i-1} \exp(\tau_j(x)-\tau_i(x))\big[g_i(x)-g_j(x)\big]\\ &+\sum_{j=1}^{m}\int_{-\infty}^{\tau_j^{-1}(\tau_i(x))} \exp(\tau_j(y)-\tau_i(x))w(x-y)\big[g_i(x)-g_j(y)\big]p(0)\,dy\\ &+\sum_{j=1}^{m}\int_{-\infty}^{\tau_j^{-1}(\tau_i(x))}\int_0^{\tau_i(x)-\tau_j(y)} \exp(-s)w(x-y)\big[g_i(x)-g_j(y)\big]p'\big(-s+\tau_i(x)-\tau_j(y)\big)ds\,dy.\end{aligned}$$

which proves the assertion in lemma 3.6.2.

Lemma 3.6.2 shows that small perturbations g to τ induce small perturbations on the left limits

$$(V\tau)(x,[\tau_i(x)]_-)$$

and that, to leading order, g satisfy a linear equation[2].

We note that the solution profile is not (yet) required to satisfies the threshold conditions at τ and $\tilde{\tau}$. In the next corollary, we will make this assumption, and require τ to be firing functions of a TW_m. In doing so, we derive a linear problem useful for the stability analysis of TW_m.

Corollary 3.6.3 (to lemma 3.6.2) *Let the hypotheses of lemma 3.6.2 hold, and let $\tau_i(x) = x/c+T_i$, for $i \in \mathbb{N}_m$, where $(c, T_1, \ldots, T_m)$ is a solution to Problem 3.5.1. Furthermore, assume that $(V\tilde{\tau})(x,[\tilde{\tau}_i(x)]_-) = 1$ for all $i \in \mathbb{N}_m$, $x \in \mathbb{R}$, and that there exist $\lambda \in \mathbb{C}$, $u \in \mathbb{C}^m$ such that $g(x) = u\exp(\lambda x)$ for all $x \in \mathbb{R}$, then*

$$0 = \big[M(\lambda)+A\big]u + O(\varepsilon), \tag{3.30}$$

where $M \in \mathbb{C}^{m\times m}$, $A \in \mathbb{R}^{m\times m}$ have elements

$$\begin{aligned}M_{ij}(\lambda) = c&\int_{-\infty}^{T_{ij}} w(cy)\exp(\lambda cy + y - T_{ij})p(0)\,dy\\ &+ c\int_{-\infty}^{T_{ij}} w(cy)\exp(\lambda cy)\int_0^{T_{ij}-y}\exp(-s)p'(-s+T_{ij}-y)\,ds\,dy,\end{aligned} \tag{3.31}$$

[2] In principle, one could define the additional mapping $\tau \mapsto \big\{(V\tau)(x,[\tau_i(x)]_-)\big\}_i$ and state lemma 3.6.2 in terms of the Fréchet derivative of this operator. We preferred to expose the notation for $(V\tau)(x,[\tau_i(x)]_-)$, which highlights that the limit of the spatio-temporal profile $v(x,t)$ is taken for $t \to \tau_i(x)$ from the left.

and

$$A_{ii} = -\sum_{k=1}^{m} M_{ik}(0) \; - \sum_{k=1}^{i-1} \exp(-T_{ik}), \qquad A_{ij} = \begin{cases} \exp(-T_{ij}) & \text{if } i > j, \\ 0 & \text{if } i < j, \end{cases}$$

respectively, and where we posed $T_{ij} = T_i - T_j$ *for all* $i, j \in \mathbb{N}_m$.

Proof Since $\tau_i(x) = x/c + T_i$ and $(c, T_1, \ldots, T_m)$ is a solution to Problem 3.5.1, we have $(V\tau)(x, [\tau_i(x)]_-) = 1$ for all $x \in \mathbb{R}$ and for all $i \in \mathbb{N}_m$. By the main hypothesis we therefore obtain $0 = (V\tilde{\tau})(x, [\tilde{\tau}_i(x)]_-) - (V\tau)(x, [\tau_i(x)]_-)$. We now specialise the right-hand side of eq. (3.22) using the main assumptions on g, obtaining

$$0 = \big[\mathcal{M}(\lambda, x) + \mathcal{A}(x)\big] u + O(\varepsilon), \tag{3.32}$$

where $u \in \mathbb{C}^m$ is the vector with components u_i, $\mathcal{M} \colon \mathbb{C} \times \mathbb{R} \to \mathbb{C}^{m \times m}$ has elements

$$\begin{aligned} \mathcal{M}_{ij}(\lambda, x) = &\int_{-\infty}^{\tau_j^{-1}(\tau_i(x)) - x} w(y) \exp(\lambda y) \exp(\tau_j(x + y) - \tau_i(x)) p(0) \, dy \\ &+ \int_{-\infty}^{\tau_j^{-1}(\tau_i(x)) - x} w(y) \exp(\lambda y) \int_0^{\tau_i(x) - \tau_j(x+y)} \exp(-s) p'(-s + \tau_i(x) - \tau_j(x + y)) \, ds \, dy, \end{aligned}$$

and where $\mathcal{A} \colon \mathbb{R} \to \mathbb{R}^{m \times m}$ has elements

$$\mathcal{A}_{ii}(x) = -\sum_{k=1}^{m} \mathcal{M}_{ik}(0, x) \; - \sum_{k=1}^{i-1} \exp(\tau_k(x) - \tau_i(x)),$$

$$\mathcal{A}_{ij}(x) = \begin{cases} \exp(\tau_j(x) - \tau_i(x)) & \text{if } i > j \\ 0 & \text{if } i \leq j. \end{cases}$$

We now insert $\tau_i(x) = x/c + T_i$ into eq. (3.32) and take the limit as $x \to cT_i$ from the left (the spatial location of the threshold crossings) to give

$$\begin{aligned} \mathcal{M}_{ij}(\lambda, [cT_i]_-) = &\int_{-\infty}^{cT_{ij}} w(y) \exp(\lambda y) \exp(y/c - T_{ij}) p(0) \, dy \\ &+ \int_{-\infty}^{cT_{ij}} w(y) \exp(\lambda y) \int_0^{-y/c + T_{ij}} \exp(-s) p'(-s + T_{ij} - y/c) \, ds \, dy, \end{aligned} \tag{3.33}$$

and

$$A_{ii} = -\sum_{k=1}^{m} M_{ik}(0) \; -\sum_{k=1}^{i-1} \exp(-T_{ik}), \qquad A_{ij} = \begin{cases} \exp(-T_{ij}) & \text{if } i > j, \\ 0 & \text{if } i < j, \end{cases}$$

finally, rescaling the variable y by c in eq. (3.33) we arrive at eq. (3.31)

$$\begin{aligned} M_{ij}(\lambda) = c \int_{-\infty}^{T_{ij}} w(cy) \exp(\lambda cy + y - T_{ij}) p(0)\, dy \\ + c \int_{-\infty}^{T_{ij}} w(cy) \exp(\lambda cy) \int_{0}^{T_{ij}-y} \exp(-s) p'(-s + T_{ij} - y)\, ds\, dy, \end{aligned}$$

thus, proving the assert in Corollary 3.6.3.

3.6.1 Computation of eigenvalues for multiple-spike waves and translation eigenmode

Corollary 3.6.3 allows us to study linear stability of a TW_m when the structure is subject to small exponential perturbations of the firing functions, such as the ones observed in fig. 3.4. The growth or decay of such perturbations is determined by the real part of λ, which can be computed numerically as the solution of the following nonlinear eigenvalue problem.

Problem 3.6.4 (Eigenvalue computations) *Let $(c, T) \in \mathbb{R}_{\neq 0} \times \mathbb{R}^m$ be a solution to Problem 3.5.1, and let M, A be the (c, T)-dependent matrices defined in Corollary 3.6.3. Find $\lambda \in \mathbb{C}$ such that*

$$E(\lambda) = \det\big[M(\lambda) + A\big] = 0. \tag{3.34}$$

Remark 3.6.5 (Neutral translation mode) We observe that, to leading order, eq. (3.30) holds true for $\lambda = 0$, $u = (1, \ldots, 1)$. Indeed, from the definition of

A we have for all $i \in \mathbb{N}_m$

$$\begin{aligned}\sum_{j=1}^{m} A_{ij} + M_{ij}(0) &= A_{ii} + \sum_{j=1}^{i-1} A_{ij} + \sum_{j=1}^{m} M_{ij}(0) \\ &= -\sum_{k=1}^{m} M_{ik}(0) - \sum_{k=1}^{i-1} \exp(-T_{ik}) + \sum_{j=1}^{i-1} \exp(-T_{ij}) + \sum_{j=1}^{m} M_{ij}(0) \\ &= 0.\end{aligned}$$

Therefore to each TW_m is associated a 0 eigenvalue, corresponding to a translational mode, as expected.

The intersection between contour lines representing the real and imaginary components of eq. (3.34) corresponds to eigenvalue solutions. If all the eigenvalue solutions occupy the left-half plane then the wave is stable. A numerical study of the stability of TW_m states is given in the next chapter.

3.6.2 Single-spike case

In the single spike case, with $m = 1$, the firing function is just $\tau(x) = x/c$ and the eigenvalue problem reduces to the simple characteristic equation derived by Bressloff [13], except for one extra term which allows for instantaneous postsynaptic response, so that $p(0) \geq 0$. Hence, we arrive at

$$c \int_0^\infty w(cy)\big(1 - \exp(-\lambda cy)\big)\Big[\exp(-y)p(0) + \int_0^y \exp(-s)p'(y-s)ds\Big]dy = 0. \tag{3.35}$$

It is now clear that $\lambda = 0$ is always a solution to eq. (3.35), this is expected because of the networks translational invariance.

3.7 Summary

The global maximum of the synaptic activity oscillations scales as $\mathcal{O}(1/n)$ as expected from the reset condition. A mathematical framework has been developed that enables a concise and concrete method of constructing a travelling wave with a finite number of spikes m. A set of firing functions is linked to the wave solutions in the continuum model. It has been shown that the existence and stability

can be framed in terms of these firing-time functions. Multiple-spike waves are easily solved numerically by directly measuring the wave speed and spike-time intervals from simulation and then using as an initial guess to the travelling wave problem. The exact voltage and spatial profiles can then be constructed from these numerically solved macroscopic variables.

The benefits of numerically solving for the firing-functions and framing the continuum equations in terms of the firing functions has allowed for the development of a non-local eigenvalue problem that can be solved numerically via Newton methods (see next chapter). The eigenvalue problem has a generic weight function and postsynaptic potential function, so various comparisons in bifurcation structure can be made. This will be done in the following chapter.

Chapter 4

Bifurcation analysis of multiple spike waves

4.1 Introduction

This chapter presents the results of a numerical study of the multiple-spike wave analysis developed in the previous chapter. A particular focus is given to investigating the bifurcation structure of the multiple-spike wave's macroscopic variables (speed and spike-times) as a function of the network's system parameters. Moreover, we are able to numerically compute the wave's stability properties, which has not been achieved to date.

It is known that the wave speed incorporates many features of the underlying circuitry and provides a useful probe into the mechanisms of wave propagation. We are particularly interested in investigating the relationship wave speed has with the synaptic processing rate β, due to its importance in determining the dynamics of the network. Golomb et al. [80] found a variety of multiple spike discharge patterns in simulations of a network of single-compartment Hodgkin-Huxley type cells with exponentially decaying synaptic connectivity and also concluded that the wave's speed is determined mainly by the integration time of the neuron's postsynaptic potentials.

It was also shown in [80] that, for a small region of parameter space, the waves that possess a larger number of spikes have a greater speed. This was attributed to the neurons at the front of propagation being affected by a larger synaptic field when there are more spikes. However, for most parameter values it was found that the distance between spikes was too large relative to the synaptic footprint shape, such that having more spikes resulted in negligible changes to the

synaptic field of neurons at the front of the wave. As a result, it was concluded that the number of spikes of the wave, in most cases, has no effect on the wave speed. This observation has been used in several studies of the integrate-and-fire network to implicitly justify why it is sufficient to only study the dynamics of a single-spike wave, which, as it happens is far simpler to analyse mathematically. [13, 16, 56, 145]. However, we note that in many cases the single-spike assumption is entirely valid, and has led to important general principles concerning a wave's dynamics in synaptically-coupled networks. These can also be seen to apply to multiple-spike waves in this particular network, as well as various intractable biophysically realistic network models exhibiting multiple-spike waves.

Interestingly, we find that waves propagating in a network with lateral-inhibition connectivity architecture have fundamental differences in bifurcation structure compared to the waves found in the various computational and theoretical studies where a purely excitatory architecture was taken [13, 16, 21, 56, 80, 143, 145]. In this chapter, comparisons are made between multiple-spike waves, with, and without lateral-inhibition. However, due to the abundance of unexplored dynamics exhibited, the majority of analysis is focussed on the lateral-inhibition network.

We arrange the chapter in the following order: First, we classify the important bifurcations multiple-spike waves can undergo. Next, various validations of the stability analysis are performed, followed by bifurcation diagrams contrasting the difference in dynamics between a TW_2 and TW_3. The composite wave states seen to occur in the discrete network on a larger spatial domain are found and their dynamics analysed. We then analyse the TW_3 in detail, producing two-parameter diagrams uncovering the importance of the balance between excitatory and inhibitory synaptic connections, and also investigate the effect of finite rise times in the neuron's postsynaptic response function $\alpha(t)$. Moving past the TW_3, we reveal how the number of spikes m plays an important role in determining the wave speed and stability regions of a TW_m (with lateral-inhibition). In the case where m is large an interesting link to the dynamics of the stationary bump state found in [120] is highlighted, which provokes thoughts on the true meaning of stationary bumps in the continuum network. Finally, multiple-spike waves in

the purely excitatory network are found and analysed, where we highlight some of the differences in dynamics with the waves in the lateral-inhibition case.

4.2 Bifurcations

In the previous chapter we have shown that a TW_m state is fully classified by solving the travelling wave Problem 3.5.1 to obtain a set of m macroscopic variables $(c, T_1, T_2, \ldots, T_m)$ representing the wave speed and spike times. These macroscopic variables are all that is needed to construct the set of m firing functions $\{\tau_j\}$, which is sufficient to construct the voltage and synaptic profiles of the wave. In addition, the asymptotic stability of the wave is determined by solving Problem 3.6.4, which requires *a priori* Problem 3.5.1 to be solved numerically. Here, we implement this routine in Matlab.

We use Newton's method to converge upon solutions to Problem 3.5.1 and a pseudo-arclength continuation package to continue along the solution branch [157]. This continuation method, devised by Keller [108], originates from the observation that the ideal parameterisation of a curve is arclength. The pseudo-arclength is an approximation of the arclength in the tangent space of system's solution curve. Hence, geometrically, it is the most natural continuation method. The resulting modified natural continuation method makes a step in pseudo-arclength as opposed to simply the parameter p. If, there exists a solution (u_0, p_0) to $f(u, p)$, and a normalised direction vector $(\dot{u}_0, \dot{p}_0)$ of the solution branch at (u_0, p_0), then Keller's method consists of solving the following set of equations for u_1 and p_1:

$$f(u_1, p_1) = 0, \qquad (u_1 - u_0)^* \dot{u}_0 + (p_1 - p_0)\dot{p}_0 - \Delta s = 0, \tag{4.1}$$

which is typically solved with Newton's method.

The bifurcation diagram in fig. 4.1(a) shows a continuation of the wave speed as function of the synaptic efficacy parameter β. The branch is found to be stable in the region delineated by two important types of bifurcation. A branch of solutions originates from a grazing point and it is initially stable, before destabilising at a sequence of Hopf bifurcations, as seen in fig. 4.1(a), which uses β as bifurcation parameter and c as solution measure. We note that each TW_m state also has

an unstable slow solution branch, which is expected from [13], however, for the purposes of clarity in depicting the bifurcation types, we only illustrate the stable solution branch in fig. 4.1(a). The next sections describe the bifurcations found and how they are computed.

4.2.1 Grazing points

In a wide region of parameter space, branches of TW_m solutions originate at a grazing point $\beta = \beta_\mathrm{G}$, as seen in fig. 4.1(a)–(b). At a grazing point the TW_m profile crosses thresholds m times, and it attains the threshold tangentially at a further spatial location, cT_G, as shown in fig. 4.1(b). This tangency exists only for $\beta = \beta_\mathrm{G}$, signalling a non-smooth transition and a branch termination. Therefore, the graze point marks an existence condition for the wave state. We note from linear stability analysis that the graze state shown in fig. 4.1(b) is linearly stable. This is unsurprising because the stability analysis works by perturbing around the spike times. The method cannot account for the smooth voltage profile as a whole encroaching on threshold.

For $\beta > \beta_\mathrm{G}$ we observe profiles with exactly m threshold crossings (a branch of TW_m solutions); these profiles exhibit a local maximum, strictly less than 1, at a point $\xi_\mathrm{max} > cT_m$. As $\beta \to \beta_\mathrm{G}^+$ we observe $\xi_\mathrm{max} \to cT_\mathrm{G}^+$ and $\nu(\xi_\mathrm{max}) \to 1^-$, until the threshold is reached at $\beta = \beta_\mathrm{G}$, where the profile has m threshold crossing and the additional tangential crossing at cT_G; for $\beta < \beta_\mathrm{G}$ the solution TW_m is not defined, but the tangential crossing becomes an actual threshold crossing: we can find a branch of TW_{m+1} solutions nearby (as we will show later). We found grazing points for every TW_m with $m \geq 2$ for the parameters in table 2.1. There is in fact another graze point on an unstable lower branch of solutions, but for clarity we do not show this in fig. 4.1(a).

Grazing points are found generically as a secondary control parameter, say γ_G, is varied. It is possible to perform a 2-parameter continuation of the grazing point in the $(\beta, \gamma_\mathrm{G})$-plane by continuing in γ_G solutions the following problem:

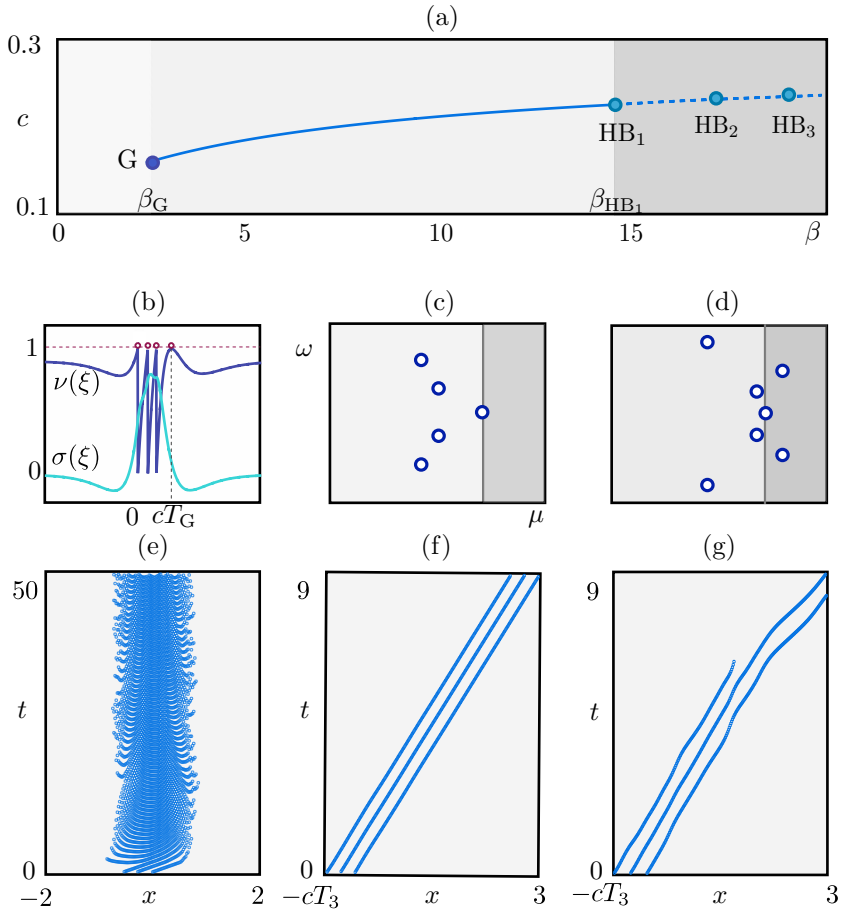


Figure 4.1 Numerical continuation showing how wave speed c of a TW_3 changes with the synaptic efficacy parameter β. The graze point G is illustrated by (b) and defined in Problem 4.2.1. As β increases, three eigenvalue pairs attain positive real parts and are marked as Hopf bifurcation points HB_1, HB_2, HB_3. Panels (c) and (d) show the eigenvalue spectrum at $\beta = 10$ and 16 respectively, where an eigenvalue solution to eq. (3.34) is denoted as $\lambda = \mu + i\omega$. All stable waves eigenvalues have negative real parts such that $\mu < 0$, while unstable waves possess at least one pair with $\mu > 0$.Raster plots (e–g) depict time simulations of the discrete network with $n = 500$, initialised from constructed solutions to the wave problem Problem 3.5.1 at $\beta = 2.17, 10, 16$ respectively illustrate the transition to a stationary bump at G, a persistent stable TW_3 and the destabilisation of an unstable TW_3 to an all-off state, respectively.

Problem 4.2.1 (Graze point computation)

Find $(c, T_1, \ldots, T_m, T_G, \gamma_G) \in \mathbb{R}^{m+2}$ *such that* $T_1 < \cdots < T_m < T_G$ *and*

$$T_1 = 0 \tag{4.2}$$

$$\nu([cT_i]_-; c, T_1, \ldots, T_m) = 1, \quad i \in \mathbb{N}_m \tag{4.3}$$

$$\nu(cT_G; c, T_1, \ldots, T_m) = 1, \tag{4.4}$$

$$\frac{d\nu}{d\xi}(cT_G; c, T_1, \ldots, T_m) = 0, \tag{4.5}$$

where T_G is the time a neuron that fired its first spike at $t = 0$ reaches threshold at the smooth maximum in the voltage profile as the wave envelope passes over it. Note that the last two conditions ensure that there is a tangency at the voltage threshold.

When $\gamma_G = \beta_G$, it is important to note that for $\beta < \beta_G$ the specific TW_m state does not exist. This is explicitly shown from the numerical simulation in fig. 4.1(e) taking initial conditions satisfying the graze Problem 4.2.1 for a TW_3. Here it is seen that the initial profile immediately evolves into a type of synchronised bump solution with a set of neurons firing in near synchrony. In this particular simulation the network size is $n = 500$, therefore relatively large finite size fluctuations in the synaptic input induce a kick to firing activity around the graze event which stalls the wave propagation. As a result, the finite system size effectively delays the onset of stable waves, however as $n \to \infty$ such a delay tends to zero.

4.2.2 Hopf bifurcations

Along the branch, we compute and monitor selected eigenvalues found as solutions to Problem 3.6.4, which we shall write in the form $\lambda = \mu + i\omega$. The eigenvalues are therefore the intersection points of the zero contour-lines for the real and imaginary parts of eq. (3.34) evaluated at a TW_m solution $(c, T_1, T_2, \ldots, T_m)$.

The spectra in fig. 4.1(c) and (d) show the set of eigenvalues closest to the imaginary axis for a TW_3 solution, at $\beta = 10$ and $\beta = 16$ respectively. Simulations of the network in fig. 4.1(f) show that a TW_3 with $\beta = 10$ persists, and it is also robust to various types heterogeneities and uncertainties in system parameters (seen in next chapter). Aside from the expected zero eigenvalue solution, which

denotes the system's translational invariance, all its non-zero eigenvalues have negative real parts ($\mu < 0$). The wave is therefore asymptotically stable and persists indefinitely.

In contrast, the set of eigenvalues for the solution at $\beta = 16$, in fig. 4.1(d) contains a single pair of eigenvalues with positive real part. In this case the simulation in fig. 4.1(g) shows the wave developing growing oscillatory perturbations in its firing times, leading eventually to the TW_3 destabilising into a stable TW_2. It should be noted that the wave can also destabilise into the all-off state, or a variety of stable wave states. Importantly, the emergent wave $\mathrm{TW}_{m'}$ states always have fewer threshold crossings, such that $m' < m$. This is reminiscent of the second law of thermodynamics—a solitary TW_m will never destabilise into a more synchronised state.

We have now shown via direct simulation and the evaluation of the spectrum of the waves that all the hallmarks of a Hopf bifurcation clearly exist. Indeed it is implied that there is an eigenvalue pair crossing of the imaginary axis somewhere in the range $10 < \beta < 16$, marking the end of the stable regime. In addition, we have also found that at larger values of β there can be multiple eigenvalue pairs with positive real components, meaning that the wave destabilises via a sequence of Hopf bifurcations. We order these bifurcation according to the corresponding β value, and denote them via $\{\mathrm{HB}_k\}_k$.

We now present the following numerical problem to solve for the kth Hopf bifurcation of a TW_m state:

Problem 4.2.2 (Computation of HB_k)

Find the solution $(c, T_1, \ldots, T_m, \gamma_{HB_k}, \omega_k) \in \mathbb{R}^{m+2}$ *such that* $T_1 < \cdots < T_m$, *satisfies*

$$T_1 = 0 \tag{4.6}$$

$$\nu([cT_i]_-; c, T_1, \ldots, T_m) = 1, \quad i \in \mathbb{N}_m \tag{4.7}$$

$$E(\lambda) = \det[M(i\omega_k) + A] = 0. \tag{4.8}$$

The continuation plot in fig. 4.1(a) depicts the first three HB_k solutions to Problem 4.2.2 for a TW_3 state when β is a free parameter. The most important

is clearly HB_1 because it marks the transition from the stable to unstable wave at $\beta_{\mathrm{HB}_1} = 14.65$.

4.2.3 Testing validity of Hopf instabilities in discrete networks

We now present an experiment devised to test how closely the Hopf points in the continuum network correspond to the observed critical parameters where destabilisations are seen to occur in the discrete network. We have already seen growing oscillations developing in the firing times in simulations of waves in the neighbourhood of HB_1. Observations have shown that the simulated TW_3 state will always destabilise into the all-off state, a TW_2 or a TW_1 if $\beta > \beta_{\mathrm{HB}_1}$. However, depending on the network size n, the wave can also be seen to destabilise prior to β_{HB_1}. In the case where $n = 250$, destabilisations have been observed at $\beta = 12.2$. It is therefore clear that finite-sized effects play a role in causing the wave to destabilise before the continuum model's prediction.

In fig. 4.2 we quantify this phenomenon by measuring the time taken for a TW_3 to destabilise, τ_d, as a function of β, for $n = 250, 500, 1000$. Each measurement is taken from a numerical simulation initialised with a voltage and synaptic spatial profile produced by solving Problem 3.5.1 with a given β and then constructing the corresponding spatial profiles $(v_i(0), s_i(0))$ for $i \in \mathbb{N}_n$. In doing so, we confirm that as $n \to \infty$ the discrete network's critical parameter tends towards the HB_1 solution's prediction.

The results presented in fig. 4.2 show that the discrete network's true bifurcation point in β is less than β_{HB_1}. For $n = 250$ the wave first destabilises at $\beta = 12.2$ after $\tau_d = 4.8$, but, interestingly for $\beta \in [12.4, 12.8]$ the wave fails to propagate at all—destabilising instantly. Yet for $\beta \in [13.1, 14.3]$, the wave persists with high amplitude oscillations in firing times for a close to constant time $\tau_d \approx 6.7$, then breaks down. It is thought that this variation is a result of the different modes of temporal oscillations the saltatory wave can exhibit in the discrete network. some modes therefore result in faster destabilisations than others (see section 2.8). However, the large variation is also likely to be due, in part, to some inevitable inaccuracies of the measurement of the destabilisation time, since this quantity

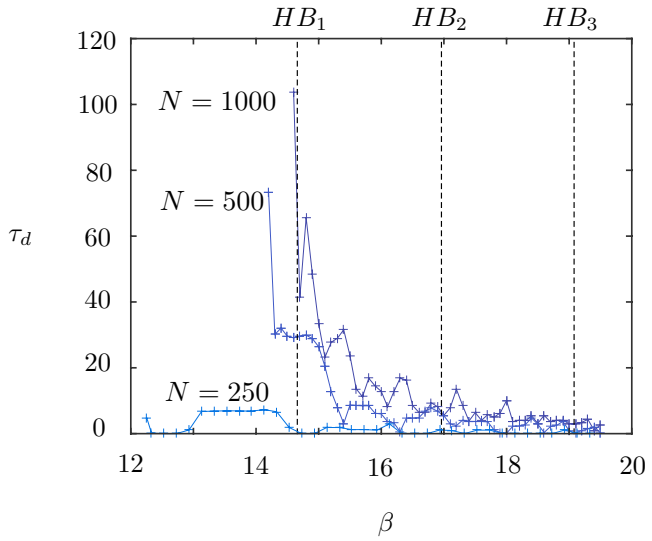


Figure 4.2 Experiment depicting how the network size n determines the time taken for a wave close to the Hopf bifurcation points to destabilise for $n = 250, 500, 1000$. The destabilisation time τ_d is defined as the time taken for the TW_3 to destabilise either via a propagating $\mathrm{TW}_{m'}$ with $m' < 3$, or the all-off state. In this network the spatial half-width is $L = 2$. All initial conditions correspond to solutions found from the numerical continuation in β, shown in fig. 4.1(a)

is hard to precisely define in the context of a variety of different types of wave destabilisations.

In the case where $n = 500$ and $n = 1000$, the first destabilisation events take a long time to observe and take place at progressively closer values to β_{HB_1} ($\beta \approx 14.2$ and $\beta \approx 14.6$ respectively). This confirms the validity of our analysis and shows that the numerically solved Hopf is a good approximation to the true destabilisation points for waves in the discrete network.

We note that even for β significantly beyond β_{HB_1} the wave persists for a reasonably significant amount of time before it fully destabilises. It is seen in fig. 4.2 that the destabilisation times τ_d rapidly decreases as β increases beyond β_{HB_1}. The rate of decay in destabilisation times with β is larger for smaller n, implying that in the limit $n \to \infty$, the destabilisation time is instantaneous at β_{HB_1}.

4.2.4 Analysing the firing-time history of a slowly destabilising wave

The long destabilisation time seen in discrete network waves is due to the unstable eigenvalue pair(s) having real parts close to zero ($\mu \approx 0$), which means that the

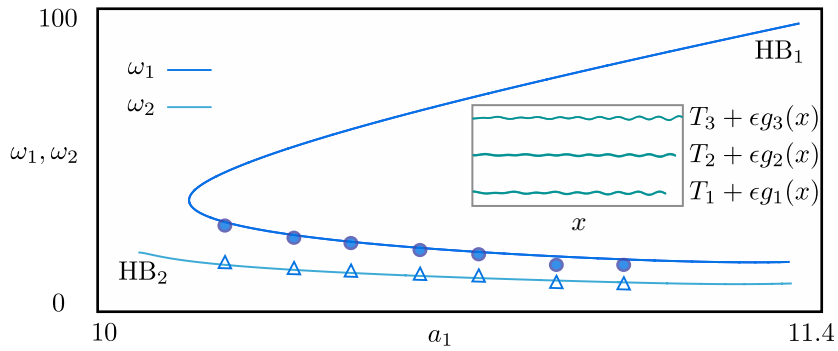


Figure 4.3 Solid lines are results of solving Problem 4.2.2 and using a arc-length continuation to depict the branch of HB_1 and HB_2 as the network parameter a_1 varies. Testing the validity of our stability analysis we find a solution at $\beta = \beta_{\mathrm{HB}_1} + 0.1$ at 7 values of $a_1 \in [10.2, 11]$ and construct initial conditions for time-stepping using eq. (3.11)–eq. (3.12). Simulation time was $T = 25$ and network size $n = 1000$. The firing times were stored and the two dominant modes were extracted and plotted as circles and triangles.

growth of the oscillations in the wave's firing time history is slow. This means we are able to measure directly the modes within the firing time history with sufficient accuracy to predict the eigenvalues, and thus, to test our numerical continuations and stability analysis against results obtained directly from numerical simulation. We compute the TW_3 solution corresponding to $\beta = \beta_{\mathrm{HB}_1} + 0.1$ for seven different values of a_1 (the parameter increasing the balance of excitation relative to inhibition) and then construct initial spatial-profiles for time-simulation of the discrete network. In all cases the firing time history display two clear modes of oscillation—one mode slowly decays, and the other grows. Measuring the average time periods Δ_1 and Δ_2 of these oscillations, we find

$$\omega_1 \approx \frac{2\pi}{\Delta_1} \qquad \omega_2 \approx \frac{2\pi}{\Delta_2},$$

hence, it is clear that the dynamics of the firing times hold the necessary information to accurately predict the first two eigenvalue solutions closest to the imaginary axis ω_1 and ω_2. In fig. 4.3 we present the results of this test and compare them to a two-parameter continuation of numerically solved HB_1 and HB_2 points to Problem 4.2.2. The fit is very good for all values of a_1 for the first and second eigenvalue, and directly validates our stability analysis. These observations suggest that the knowledge of the spectra of a TW_m is all that is needed to characterise the dynamics of a destabilising wave. Future studies could

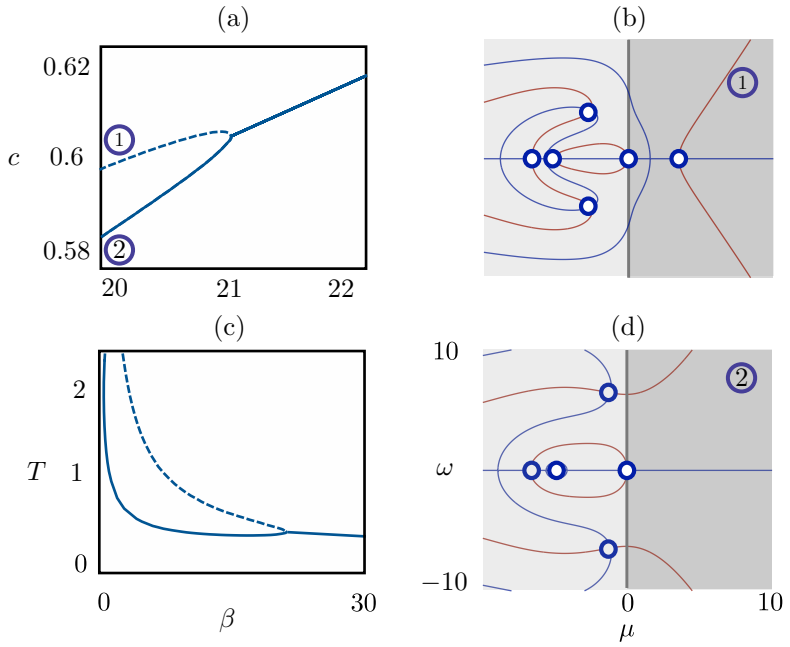


Figure 4.4 (a) Numerical continuation of the wave speed c for $\beta \in [20, 22]$. (c) Continuation of the spike-time interval $T = T_2 - T_1$ for $\beta \in [0, 30]$, T in this case is the only other macroscopic variable needed to fully define the TW_2 state because T_1 is set to zero. Solid lines illustrate stable TW_2 states and dashed depict unstable. (b) and (d) are spectra for an unstable and stable TW_2 solution respectively, $\beta = 20$ as annotated in (a). Here we show the zero-contour lines of the real (red) and imaginary (blue) parts of the wave stability Problem 3.6.4, the point of intersection corresponding to eigenvalue solutions.

therefore attempt to predict what network state the wave will destabilise into—at present there is no way of doing this.

4.3 Contrasting bifurcation structures of TW_2 and TW_3

So far, we have shown that the propagation of a TW_3 fails due to growing oscillations in the firing times, induced via a sequence of Hopf bifurcations. This is later shown to be true for all $m \geq 3$. However, we find that the TW_2 can destabilise via a completely different mechanism. The continuation diagrams in fig. 4.4(a) and (c) show how the wave speed c and spike-time interval T change as a function of β for a TW_2 state. Prior to a bifurcation point at $\beta \approx 21$ we find two branches: a stable branch with increasing speeds and decreasing spike-time intervals as β increases, and an unstable branch with the same qualitative features,

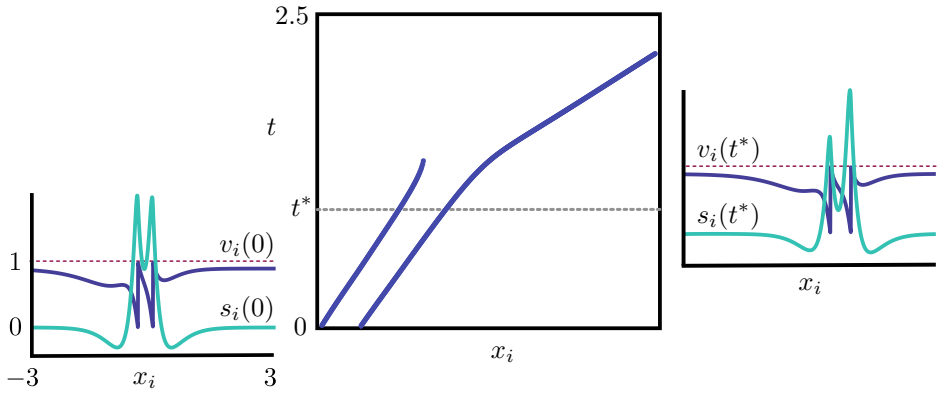


Figure 4.5 Right: numerical simulation of unstable double-spike state at $\beta = 20$, $n = 1000$, all other parameters given in table 2.1. Left: computed synaptic and voltage spatial profiles of the unstable state taken as the initial network state and above is the snapshot of the state destabilising at $t^* = 1$.

but with faster wave speeds and larger spike-time intervals at any given β. Beyond the bifurcation point there is only one stable branch. The spectrum in fig. 4.4(b) clearly shows that the solution annotated on the unstable branch of fig. 4.4(a) has a single eigenvalue with positive real part, confirming it to be unstable. But, the bifurcation point at $\beta \approx 21$ has a different type of instability to the Hopf bifurcations seen previously, because its transition is marked by only a single eigenvalue crossing the imaginary axis, as opposed to an eigenvalue pair.

To investigate how the unstable TW_2 destabilises, we use the voltage and synaptic profiles corresponding to the solution annotated on the unstable branch in fig. 4.4(a) at $\beta = 20$ as initial conditions in a simulation of the network. We see that the synaptic profiles at $t = 0$ and $t = t^*$ have two distinct peaks with a central minimum. The unstable wave state's synaptic input at the central minimum is not sufficient to prevent the wave splitting apart. The propagation of a TW_2 fails due to the synaptic peak corresponding to the front spike growing and the peak at the back decaying. The resultant effect is illustrated in the raster diagram in fig. 4.5, where we see the unstable TW_2 splitting apart. Here the lead spike train accelerates away from the tail spike train, which in turn decelerates to a critically slow speed and results in the spike train terminating. Eventually the now solitary lead spike train reaches a constant speed c corresponding to a stable TW_1 state. It is important to note that the firing time history contains no oscillations, a fact further verified in the spectrum of the unstable state in fig. 4.4(b), where we

see a single unstable eigenvalue with $\omega = 0$. We deduce that the interaction of two-spikes cannot support oscillations in the firing time's history.

From fig. 4.4(a) and (c) there appears to be a branch point at $\beta \approx 21$, where the unstable branch appears from the stable solution branch. However, we have found in numerical continuations of waves with $m \geq 3$ that the TW_m consistently bifurcate with saddle nodes (SN). An example of this is given in fig. 4.6, which clearly show SN bifurcations in the speed solution branches in the case where a wave has $m = 3$ threshold crossings. This result suggests that the apparent branching point seen in fig. 4.4(a) and (c) for the TW_2 state is more likely to actually be two separate branches, with one set of solutions undergoing a SN bifurcation, and another branch of solutions continuing on past the SN (see inset in fig. 4.6), but, prior to the SN, the solutions closely overlap. Unfortunately, due to numerical stiffness, we could not converge onto another branch of solutions in this parameter region to confirm this claim.

As mentioned earlier, numerical continuations of wave solutions with $m = 3$ threshold crossings have shown that a range of SN bifurcations exist. By continuing in β past the first Hopf bifurcation point, we found a succession of unstable branches being formed at SN points. These branches have different spike-time distributions to the stable TW_3 state. When one considers the generality of the firing function $\tau_j(x) = x/c + T_j$, it is clear that we should expect a variety of other types of solutions to Problem 3.5.1, with different forms of spike-time distributions.

In fig. 4.1 the one parameter continuation in β for the wave speed neglected to depict these unstable branches, primarily for clarity. We present in fig. 4.6 the complete set of solution branches that exist for a wave with $m = 3$ spikes. We see that just past HB_3, the unstable TW_3 branch undergoes a SN bifurcation similar to that seen for the TW_2 in fig. 4.4(a). In this case all the branches are unstable.

At $\beta = 12$ the unstable branch bifurcates again in a similar fashion. Tests have shown that all solutions that are connected to the stable TW_3 branch in this parameter regime are unstable. Each branch corresponds to a different way of distributing three spikes, for example the profile labelled TW_{1-1-1} in fig. 4.6 corresponds to a solution where spike time intervals are more or less equally spaced,

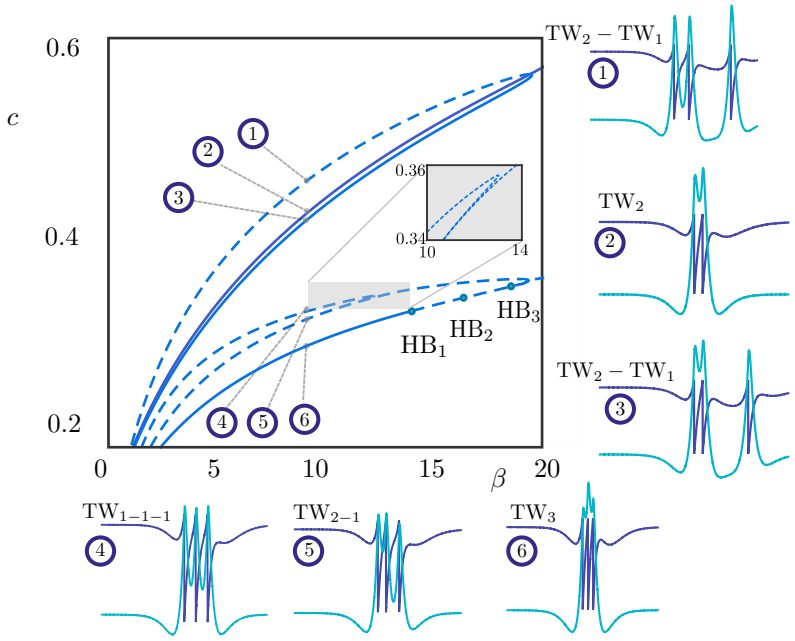


Figure 4.6 A full numerical continuation in β solving Problem 3.5.1 and showing the speed branches of all states that have $m = 3$ threshold crossing events and the TW_2 superimposed. Solutions were probed for stability by computing the spectrum and checking for positive real part eigenvalues. Dashed lines represent unstable solutions and solid lines are stable. Also shown is the stable TW_2 branch. The voltage and synaptic profiles are shown for all the wave solutions at $\beta = 10$, reflecting the variety of spike time distributions.

whereas TW_{2-1} represents a case where there are two spikes in close succession and then a relatively large time interval before the final spike. The TW_{1-2} state is the mirror image of the TW_{2-1} state and its speed branch overlaps the TW_{2-1}. Tests have shown that for $m > 3$ the number of solution branches bifurcating off the main TW_m branch increases. We conjecture that the number of branches will correspond to the number of ways of arranging a set of integers $\{k_i\} \in \mathbb{N}_m$ where $k_i < m$ and $m = \sum_{i=1}^{\max m} k_i$.

It is important to note that the notation TW_{1-1-1},TW_{2-1} and TW_{1-2} is only used to give some distinction between the unstable branches and what spike time distributions they correspond to. Often the distinction is unclear, especially around the SN transitions. Although, one difference is that the synaptic profiles are characterised by a wholly excitatory region of synaptic activity bordered on both sides by a region of inhibition.

The solution profiles in fig. 4.6 corresponding to TW_2–TW_1 and TW_1–TW_2 are from a different family of solutions entirely. Here we have found the stable

'composite solution' TW_2–TW_1, as seen from the numerical simulations in section 2.9, where a TW_1 merged with a TW_2 from behind. As hypothesised, the TW_1–TW_2 is unstable because its collective speed is greater than the TW_2's. We also see in the full TW_3 continuation plot in fig. 4.6 the proximity between the wave speed branches of a TW_2 and TW_2–TW_1. For slow synapses the speed is essentially identical, but for faster synapses the difference in wave speed increases. Importantly, the wave speed of the TW_2–TW_1 is always slightly slower than the TW_2. Hence, the inhibitory connection between attached wave states results in a net-loss of speed.

4.4 Composite states

Complex temporal sequences or repetitions of spike activity have been observed in numerous brain areas [140], which can be related to the composite wave solutions found in this study. The temporal sequence of spikes provides a large capacity for transmitting information [130]. Theoretical studies have highlighted how sequences of spike firing can be used to encode information [2, 49, 156, 175].

This section shows that it is possible to construct stable solutions of complex composites of TW_m states, thus illustrating that waves in the integrate-and-fire network are able to convey persistent signals with high information content. It is not known whether in reality brain activity transmits information across the cortex in this way, we are only stating that this mechanism exists for this network model.

We regard a composite wave as a sequence of k connected TW_{m_i} states $i \in \mathbb{N}_k$ with the state sequence vector $\mathbf{m} \in \mathbb{N}^{k\times 1}$. The composite wave system exists if the set of firing time functions $\{\tau_j\}$ satisfies the travelling wave Problem 3.5.1, for $j \in \mathbb{N}^M$ with $M = \sum_{i=1}^{k} m_i$. A stable composite state will have a single collective wave speed c, with the condition that the voltage profile $\nu(\xi) < 1$ for all $\xi \in \mathbb{R}$. Such a composite wave is referred to by:

$$\mathrm{TW}_{m_1} - \mathrm{TW}_{m_2} - \mathrm{TW}_{m_3} - \cdots - \mathrm{TW}_{m_k}. \tag{4.9}$$

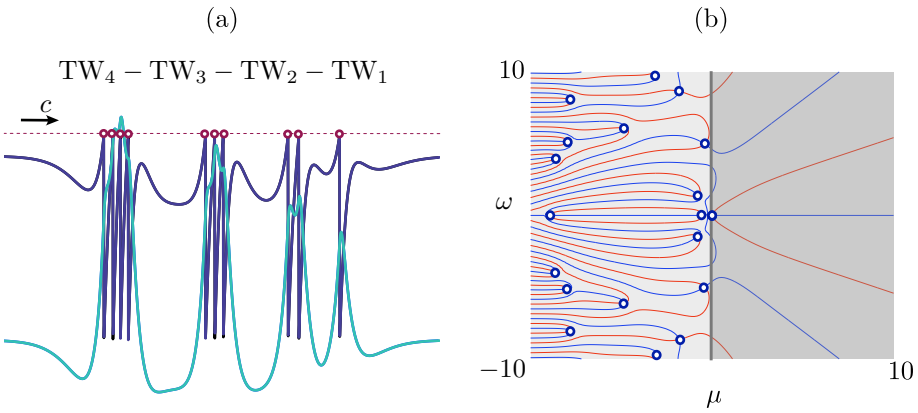


Figure 4.7 Plot on left is the synaptic and voltage profiles $\sigma(\xi)$ and $\nu(\xi)$ of a composite TW_4–TW_3–TW_2–TW_1. Circles mark the positions of the spatial points where the voltage threshold condition is met. The wave speed and spike-time intervals are numerical solutions to the wave Problem 3.5.1 for $\beta = 4.8$ and the speed $c = 0.184$. On the right is the corresponding eigenvalue spectrum, showing all real parts $\mu < 0$, hence the wave is stable.

We note that a rigorous definition must account for the fact that a composite wave with $M = \sum_{i=1}^{k} m_i$ cannot be formally distinguished from the firing times of a single TW_M state, without consideration of the functional forms of the wave's voltage and spatial profiles. However, we found that composite waves' spatial profiles display a sufficient separation between each subgroup so that it is usually possible to characterise a composite wave as the concatenation of smaller TW_m states.

The stability of composite wave solutions have been investigated via a combination of direct simulation of the network and numerically solving Problem 3.5.1 and Problem 3.6.4. From which we give the following remark.

Remark 4.4.1 In this framework the stability of the composite states can be analysed in the same way as the standard TW_m by solving Problem 3.6.4. The leading pulse of the composite wave system consists of m_1 spikes within its local excitatory synaptic envelope. A condition on the composite waves stability is that the composite system must have $m_1 \geq m_i$ for $i \in \mathbb{N}_k$.

With appropriately chosen initial guesses for the wave speed and spike-times, Problem 3.5.1 can be solved to find arbitrarily complex composite spike patterns such as the TW_4–TW_3–TW_2–TW_1 state seen in fig. 4.7. Here the synaptic input profile could be interpreted as something close to a decaying oscillatory signal as the wave propagates over the network. In this case the wave speed is just

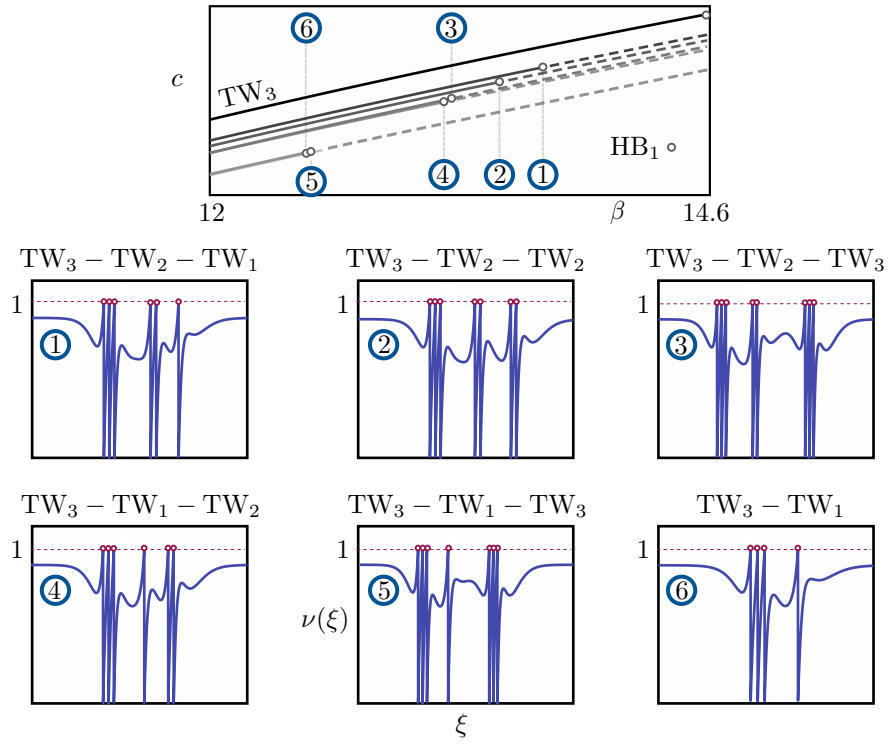


Figure 4.8 (a) Continuation of Problem 3.5.1 in β showing the wave speed and position of the HB_1 for six possible composite states numbered (1)-(6). All states have the condition that a TW_3 is at the front relative to its propagation direction.

below the stable TW_4 speed and will undergo a Hopf bifurcation at slightly slower synaptic processing rates β than the β_{HB_1} of the TW_4.

Moreover, in fig. 4.8 we show the voltage spatial profiles for six possible combinations of arranging the TW_m states with $m \leq 3$. The speed branches are all unique, suggesting the speed is determined by the number and particular arrangement of firing times. It is also found that the HB_1 corresponding to each composite state variation is unique and all occur before the HB_1 of a standard TW_3.

Performing this exercise, we were unable to converge onto a TW_3–TW_1–TW_1 state. Direct numerical simulations also confirm that this particular composite state cannot persist. This also includes other similar composite systems with $k > 3$. However, further investigations are needed to fully confirm this.

A final comment comes from considering the eigenvalue spectrum of the TW_4–TW_3–TW_2–TW_1 state in fig. 4.7. Here we see an eigenvalue on the real line very close to the zero-eigenvalue, suggesting that a SN is nearby in parameter space. This opens up the question: do all waves with $m > 2$ destabilise via a sequence

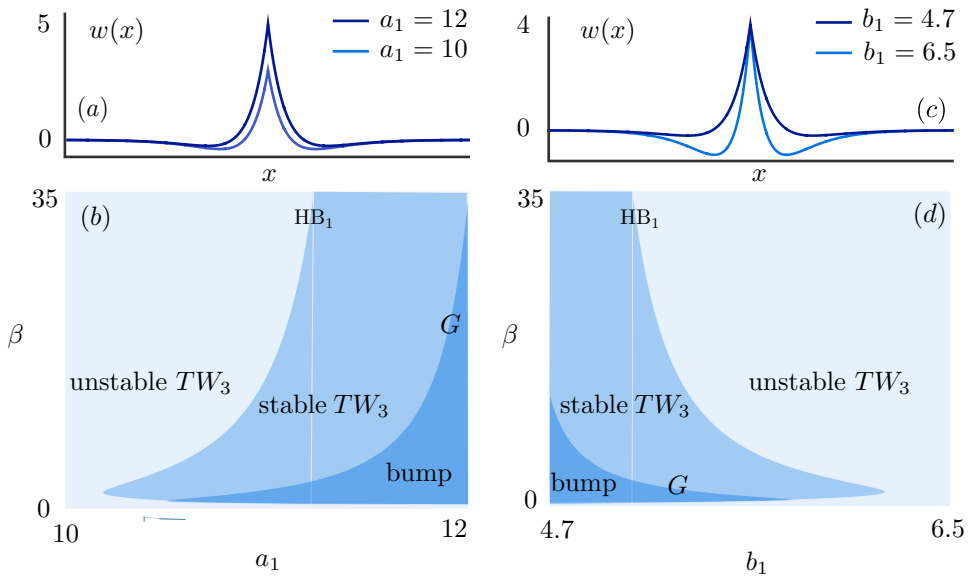


Figure 4.9 (a–b): wizard hat weight function $w(x)$ defined in eq. (2.4) at $a_1 = [10, 12]$ and $b_1 = [4.7, 6.5]$. (c–d): two-parameter continuations showing the stability regions of a TW_3 specified by the boundaries of the branch of Hopf bifurcation points HB_1 and the non-smooth graze of the voltage threshold G. System parameters are fixed according to table 2.1.

of Hopf bifurcations? It is possible in some parameter regimes that the wave loses stability at a saddle node point, like that shown in fig. 4.6, rather than the Hopf bifurcation seen here. Finding these parameter regimes is left as a possible direction for future work.

4.5 Balance of excitation and inhibition

We now investigate how the connectivity structure of the network effects dynamics of a TW_3. We focus on two parameters that govern the form of the connectivity function $w(x)$. The first is the synaptic excitation coefficient a_1 and the second is the synaptic excitation spatial scale b_1. The wizard hat weight kernel is illustrated in fig. 4.9(a)(c) showing how an increase in a_1 increases the strength of excitatory connections and its spatial scale and decreases the relative strength of distal inhibitory connections. In contrast, an increase in b_1 diminishes the spatial scale of excitatory connections and increases the strength of the distal inhibitory connections. In summary, a_1 and b_1 influence the balance of excitation and inhibition in the network. The two-parameter continuations shown in fig. 4.9 depict the branch of graze and HB_1 points computed by solving Problem 4.2.1

and Problem 4.2.2, respectively. An arc-length continuation package was used to numerically continue these solutions in a_1 and b_1. The bifurcation diagrams mark the parameter regions of a stationary bump, the stable TW_3 and unstable TW_3 states. We summarise the qualitative findings below:

1. There is a large unstable TW_3 region for low overall levels of excitation relative to inhibition.

2. For $a_1 < 10.2$ and $b_1 = 5$ we see from fig. 4.9(b) that neither a bump nor a stable TW_3 solution exists for any β. Tests have in fact shown that only a single spike wave is stable in this parameter regime. The strength of excitatory connections is not sufficient to generate large enough synaptic currents across a sufficient spatial scale to drive persistent localised states with multiple threshold crossings.

3. Similarly, fig. 4.9(d) shows that the narrowing in the spatial envelope of excitation marked by an increase in b_1 eventually lead to a critical dominance in inhibition at $b_1 > 6.2$ at $a_1 = 11$. In this case, no stable wave or bump states have been found, because the level of inhibition is too strong and region of excitation too weak.

4. Conversely, as the excitation amplitude parameter a_1 increases the bump states region of stability increases for faster synapses. We see that at $a_1 = 12$ and $b_1 = 5$ there is a graze point at $\beta = 30$, implying that for all reasonable synaptic timescales a bump state exists and there will be no TW_3. A similar story happens when b_1 decreases, effectively expanding the spatial extent of excitation relative to inhibition. At $a_1 = 11$ and $b_1 = 4.7$ we can see from fig. 4.9(d) that no stable TW_3 can exist prior to $\beta = 12.5$.

5. One important consideration taken from fig. 4.9(b)(d) is the relatively small parameter window whereby the TW_3 is stable. We see from both continuations that there must be a balance between levels of excitation and inhibition in the network for stable TW_3 to form.

4.6 Effect of finite rise time in $\alpha(t)$

Performing analysis in terms of generic kernels allows us to append additional complexities to the model. So far, our tests and bifurcation analysis have used a simple decaying exponential function to describe the postsynaptic potential (PSP) time signal $\alpha(t)$ invoked within neurons in response to another neuron firing an action potential. The assumption of an instantaneous response is a valid approximation for AMPA receptors (see section 1.2.2), which are typically very fast. However, slower synaptic responses are often found in other receptors such as the NMDA receptors in cortical pyramidal neurons. Therefore, to obtain a better fit for a wider variety of synaptic receptors it is best to use a difference of exponentials, which includes a finite rise time, and takes the following form:

$$\alpha(t) = \big[\beta_1 \exp(-\beta_1 t) - \gamma\beta_2 \exp(-\beta_2 t)\big] H(t). \tag{4.10}$$

When $\beta_1 \geq \gamma\beta_2$ the PSP $\alpha(t)$ has a rising phase with a rate of increase parametrised by β_2 up until a maxima at time

$$t_{\alpha^*} = \frac{1}{\beta_2 - \beta_1} \ln\Big(\frac{\beta_1^2}{\gamma\beta_2^2}\Big), \tag{4.11}$$

then for $t > t_{\alpha^*}$ $\alpha(t)$ will decay at the rate set by β_1. At $\gamma = 0$ the PSP is equivalent to the decaying exponential form analysed earlier. In fig. 4.10(a) we show results of four numerical continuations of the Hopf (HB_1) and graze points (G) for the TW_3 state in γ. At $\gamma = 0$ there is no rising phase in $\alpha(t)$ and as expected the position of the first Hopf point and the graze point are equivalent to that found in the exponentially decaying case, occurring at $\beta_{\mathrm{HB}_1} = 14.65$ and $\beta_G = 2.17$ respectively.

Continuation in fig. 4.10(a) are performed at four different rising rates β_2. It is found that as γ increases, the Hopf destabilisation point occurs at slower and less volatile synaptic timescales, reducing the region of stability for the TW_3 state. If the rising rate is fast, the rate of decrease in the Hopf point is slower. Relative to the Hopf points, the change in position of the graze points is small. In fig. 4.10(a)

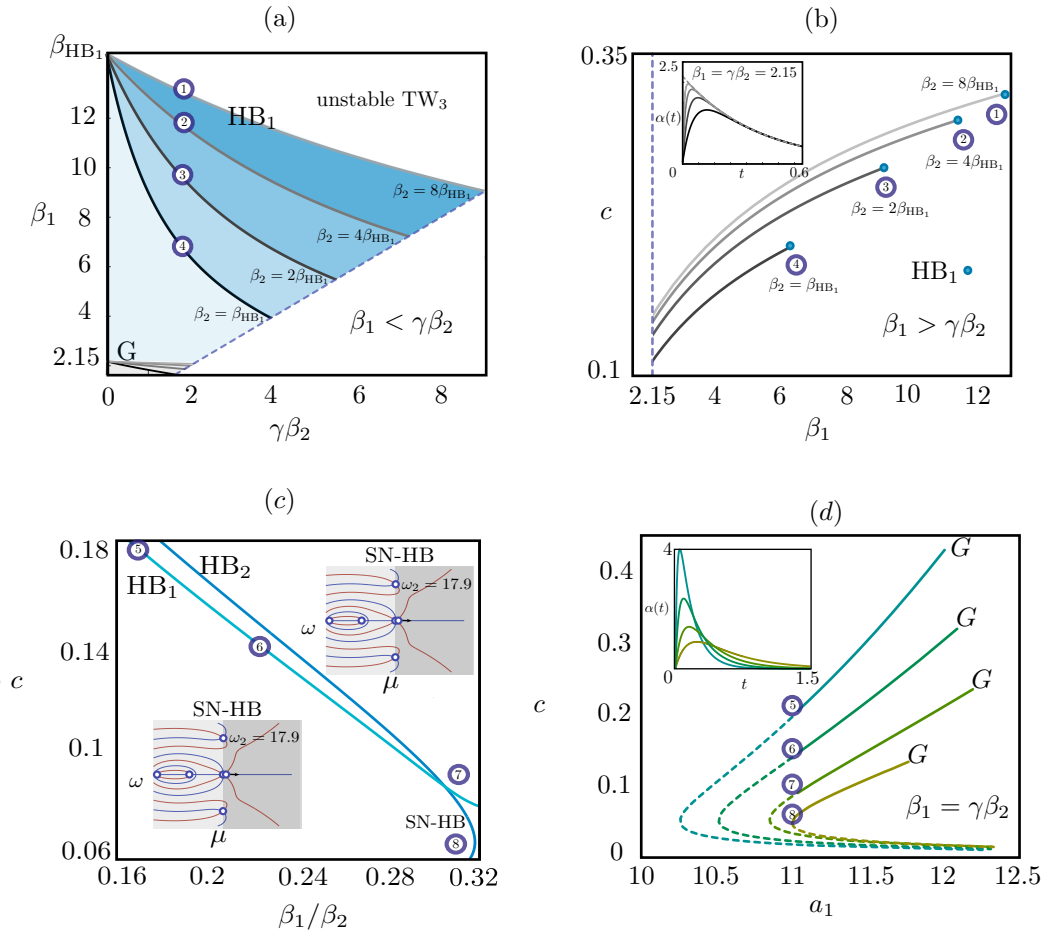


Figure 4.10 (a) two-parameter continuations of first hopf HB$_1$ and graze point G in β_1 and γ for a TW$_3$ at the fixed β_2 annotated, where $\beta_{\text{HB}_1} = 14.65$, the dashed line represents all solutions with $\beta_1 = \gamma\beta_2$. (b) Continuation of wave speed as function of β_1 with the initial time profiles of four $\alpha(t)$ with the difference of exponential form given in eq. (4.10), as β_1 increases, $\alpha(t)$ tends towards a simple exponentially decaying function. (c) Two-parameter continuation of HB$_1$ and HB$_2$ lines as a function of the ratio between decay and rise rates β_1/β_2 with the spectra corresponding to the Hopf-Hopf and fold-Hopf bifurcation points. (d) One-parameter continuation of wave speed as a function of a_1 starting from solutions annotated in (c), and the corresponding $\alpha(t)$ time profiles.

the Hopf and Graze lines intersect with the blue dashed line representing the special case whereby $\beta_1 = \gamma\beta_2$ and therefore $\alpha(0) = 0$.

In this study, we only consider excitatory PSP forms such that $\alpha(t) \geq 0$ for $t \geq 0$, meaning that solutions found for $\beta_1 < \gamma\beta_2$ are not relevant. The bifurcation diagram in fig. 4.10(b) plots the wave speed c as a function of β_1 at four different β_2, starting at $\beta_1 = 2.15$. Slower rising rates correspond to slower wave speeds at any given β_1 and smaller regions of stability. It is clear that for very fast rising rates β_2 tends towards the same dynamics found with exponentially decaying PSPs.

In fig. 4.10(c) and (d) only solutions satisfying the condition $\alpha(0) = 0$ are considered by appending the condition $\beta_1 = \gamma\beta_2$ to the Hopf Problem 4.2.2. Results obtained by the numerical continuation of the TW_3 solutions first two Hopf points HB_1 and HB_2 reveal that when the ratio between the rise and decay rates $\beta_1/\beta_2 = 0.305$ there is a co-dimension two Hopf-Hopf bifucation, characterised by the intersection of the HB_1 and HB_2 lines. The spectrum in fig. 4.10(c) demonstrates the expected double eigenvalue pair crossing at $\mu = 0$. In addition, at $\beta_1/\beta_2 = 0.315$ there is another co-dimension two bifurcation, this time it is a fold-Hopf transition, marked by a simultaneously occurring Hopf and saddle-node bifurcation as seen in fig. 4.10(c). We see in fig. 4.10(d) the solution at the fold-Hopf point corresponds to the saddle-node in the continuation of c as a function of the strength of excitatory connection parameter a_1. Therefore, too much excitation leads to a graze point branch termination.

No Hopf solutions can be found for $\beta_1/\beta_2 > 0.32$, implying a critical ratio between the decay and rising rate where this form of instability mechanism is observed. Another commonly used PSP form known as the Alpha function can be used to test this. The Alpha function models a special case when the rise and decay rates are close, such that $\beta_1/\beta_2 \approx 1$. Preliminary results appear to confirm that no Hopf instabilities exist when this form of PSP is used. Instead, branching bifurcations typically terminate the stable branch.

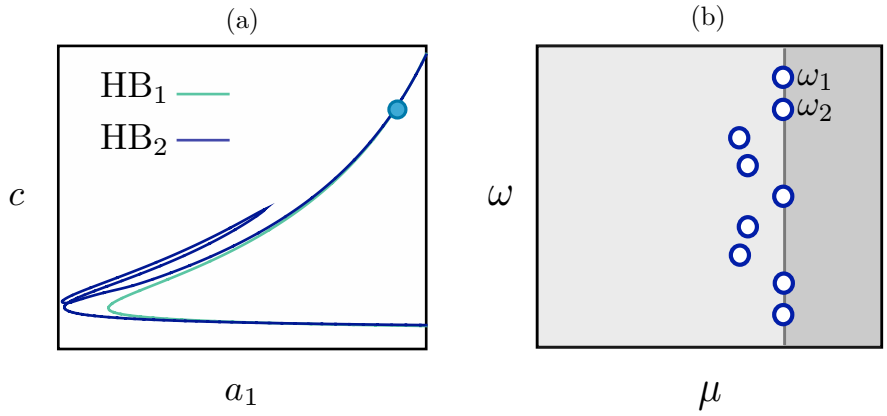


Figure 4.11 (a) Numerical continuation of first and second Hopf points in parameters a_1 and β. Here we depict the wave speed solution c on the vertical axis. At $a_1 = 11.33$ and $\beta = 30.59$ there is a Hopf-Hopf bifurcation point, all other parameters are fixed according to table 2.1. (b) Spectrum for this particular co-dimension 2, Hopf-Hopf bifurcation point, corresponding to a TW_5 solution.

4.7 Increasing the number of threshold crossings

The analysis developed in chapter 3 provides the ability to compute the bifurcation and stability properties of multiple-spike waves under a multitude of conditions. One of the benefits of this framework is its ability to efficiently compute wave solutions with an arbitrarily large number of threshold crossings. However, difficulties do emerge as spike number increases, particularly in deciphering the regions of stability in terms of the connectivity parameters a_1 and b_1. This is because the spectra become increasingly dense and complex for larger m. In the case of a TW_3 the boundary of stability was always represented by HB_1 points for all ranges of a_1 and b_1. However, for a TW_5 we find a Hopf-Hopf co-dimension 2 bifurcation at $a_1 = 11.33$, where two eigenvalue pairs cross the imaginary axis such that $\beta_{\mathrm{HB}_1} = \beta_{\mathrm{HB}_2}$, as shown in fig. 4.11. Therefore, continuing in a handful of eigenvalues close to the imaginary axis to find the boundaries of stability quickly becomes quite cumbersome and prone to error. It is better to simply compute the spectrum or run a simulation to test stability for any given solution of interest.

It is, however, possible to show from one-parameter continuations how the number of threshold crossings m effects the relation between the wave speed c and the synaptic efficacy parameter β, as well as the relative positions of graze and Hopf points. In fig. 4.12 we show all branches from from TW_1 to TW_7. As expected, we see that waves with a larger number of threshold crossings have

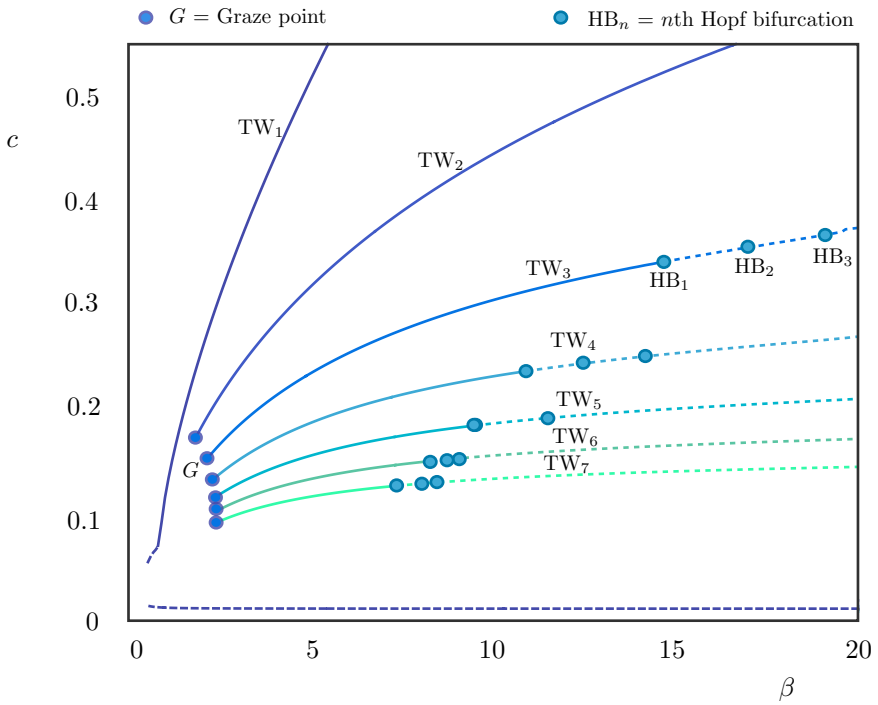


Figure 4.12 Numerical continuation of the wave speed c solution in the synaptic efficacy parameter β for TW_1 to TW_7. The markers labelled G in the region of small β depict graze points depicting a branch termination for the stable wave state, the TW_1 branch undergoes a different transition from a stable wave to an all-off state. Importantly we see that for TW_3 to TW_7 destabilise via a sequence of Hopf bifurcations. As number of threshold crossings in the wave increases the region of stability decreases.

slower speeds at any particular β. Also, it is found that their region of stability decreases as m increases, marked by the occurrence of their HB_1 at slower synaptic timescales.

In fig. 4.12 we see that the trajectory of the graze points as m increases is not entirely clear; the graze points appear to be tending towards a constant β value while the branches are getting closer and closer to one another. In order to understand the distribution of graze points for large m, we devised an algorithm that generates a suitable initial guess of a TW_{m+1} from the knowledge of the previous solution TW_m to solve the graze point Problem 4.2.1. In this study we computed graze point solutions up to $m = 150$. Convergence times is a restricting factor because it involves solving a system of $m + 1$ equations.

We show in fig. 4.13(a) a plot of the wave speed as a function of β, here we see that as m increases, the wave speed tends towards zero and the β parameter where the graze point occurs decreases. It remains to be proved analytically if $\lim_{m\to\infty} c = 0$, and if this limit is true: will its corresponding β be non-zero?

A measure of the wave width is taken to be the distance from the position of the first spike at $x = 0$ to the mth spike at $x = cT_m$. In fig. 4.13(b) we see that as m increases the wave width tends towards an asymptotic value. In addition, we find that the spike times also tend towards a fixed distribution, characterised by greater spike-time intervals at the edge of the wave and much shorter intervals at the centre.

A measure for the instantaneous firing rate of the wave can be obtained by taking the inverse of the spike-time intervals of the wave, such that

$$\eta_j = \frac{1}{T_{j+1} - T_j}, \qquad j \in \mathbb{N}_{m-1}, \tag{4.12}$$

interestingly for large m we find that the instantaneous firing rate distribution of the multiple-spike wave tends towards the firing rate profile of the stationary bump solutions found in [120]. In section 2.5 the derivation of the bump's firing rate profile was presented. Here the network was analysed in the continuum limit and a necessary assumption that neurons in the bump fired asynchronously was required. In fig. 4.13(c) we compare the firing rate profile obtained from section 2.5 and the instantaneous firing rate of a wave found in this model with $m = 150$ threshold crossings. Both profiles are in remarkably close correspondence, for $m > 150$ it is expected that they will get even closer.

This is an interesting result because it poses certain questions concerning the existence of stationary bump solutions for spiking networks in the continuum limit. It could be the case that the bumps observed in discrete network simulations are in fact just a wave solution in disguise, where the apparent asynchronicity is caused by finite-sized effects.

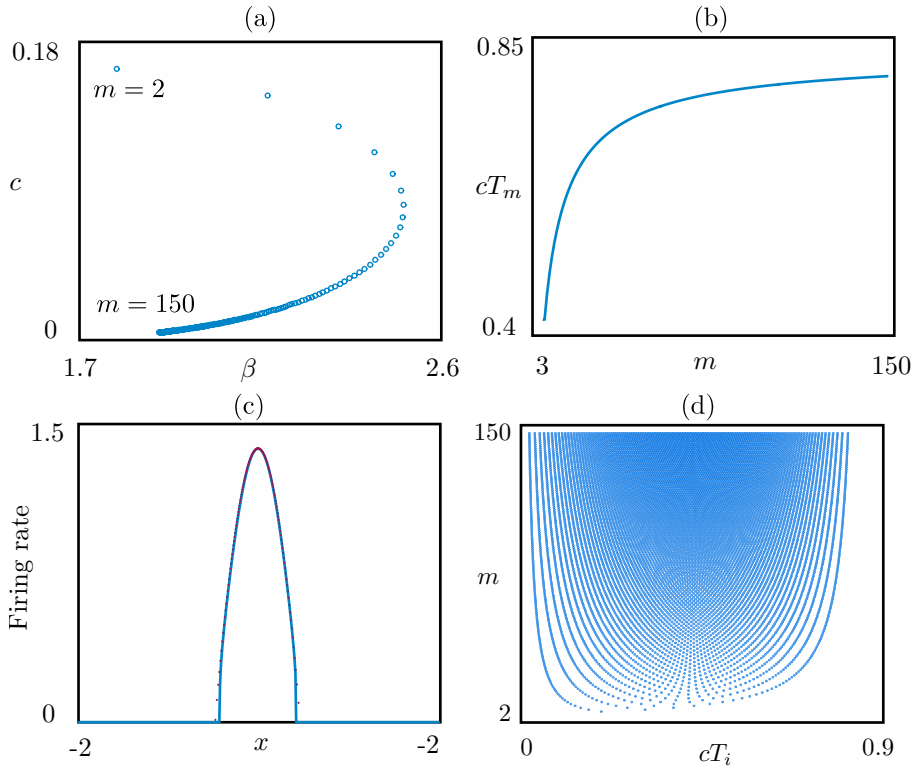


Figure 4.13 (*a*) graze points for $m \in [2, 150]$ showing the wave speed c and the synaptic efficacy β, these points represent the beginning of the TW_m branch of solutions. (*b*) wave width cT_m tending to a constant value, (*c*) the solid blue line is the gain function derived in [120] for a stationary asynchronous bump, black dots mark the measured firing rate according to eq. (4.12) at position $x = cT_i$ using the solved spike-times for a TW_{150} at its graze point (*d*) Dots represent the spike time events at $x = cT_i$ on the network for $m \in [2, 150]$.

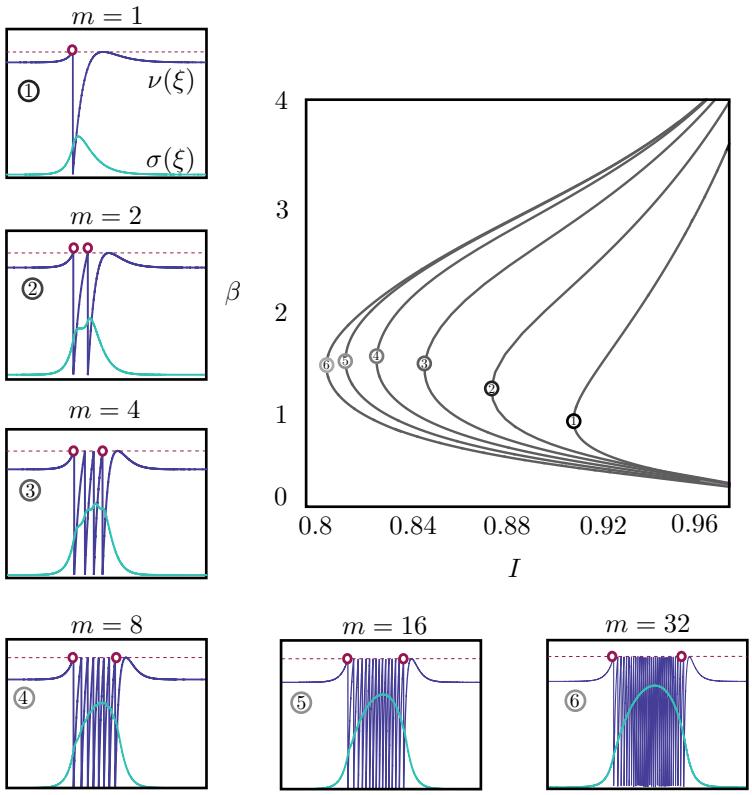


Figure 4.14 Graze point continuation in β and I marking the existence regions for six TW_m states with $m = 1, 2, 4, 8, 16, 32$. The synaptic and voltage profiles at the point where the upper and lower graze points collide are shown.

4.8 Comparison with purely excitatory network

In the case where $a_2 = 0$ the LIF network has no distal inhibition, such that the network is equivalent to the purely excitatory networks studied in the single-spike case by Bressloff and Ermentrout [13, 16, 21, 56, 143, 145]. Studying waves in the purely excitatory case allows us to understand more about how the dynamics of multiple-spike waves depend on inhibition. We are particularly interested in comparing the spike-time distributions of multiple-spike waves with and without inhibition. It is thought that the effect of lateral inhibition acts to limit the spatial width of the wave. In fig. 4.13 the multiple-spike waves tend to a constant wave width as m increases. It has also been shown that the spike time interval for TW_2 state tends to a constant as β increases.

We have demonstrated via numerical simulations in fig. 2.13 that multiple-spike wave solutions exist in the purely excitatory network. To find persistent waves, the connectivity parameters were adjusted to $a_1 = 2$ and $b_1 = 5$, noting that

$a_2 = 0$ with no inhibition kernel. It was found that upon receiving a symmetric stimulus, waves would always form in pairs and propagate in opposite directions. However, once the waves have travelled for a sufficient time, the waves can be considered localised, but with an anti-pair. This is in contrast to waves in the lateral-inhibition case whereby the network will break symmetry quickly, resulting in only one localised pulse propagating in the positive or negative direction. However, the firing times and wave speed can still be extracted and used as initial conditions to solve the wave Problem 3.5.1 in the usual manner.

In fig. 4.14 we perform a two-parameter continuation of the waves' graze points in β and I to explore the existence regions of the wave. The parameter space that the upper and lower branch encloses in the graze continuation represent non-existent solutions. In this case, the TW_1 existence region is a lot larger than the TW_{32}. The saddle-node of the graze line represents the upper and lower graze points colliding. At a specific (β^*, I^*) the wave only has one graze point. These points are annotated in fig. 4.14 with the corresponding spatial profiles. When compared to the multiple-spike waves seen in the network with lateral-inhibition there doesn't appear to be much difference in form.

In fig. 4.15 we perform one parameter continuation from each annotated solution at their special parameter pair (β^*, I^*). In this way the solution branches will only have one graze point. A plot of the wave-width cT_m is plotted as a function of β, where we see wave-width increasing with β. Solutions are taken from the wave branch corresponding to a TW_8 and used to construct synaptic profiles, which are also shown in fig. 4.15. As β increases, the modulations in synaptic input increase in amplitude and spread out. At $\beta = 5.4$ the synaptic input signal resembles an oscillatory signal with a fixed time period. This is further exemplified by the plot of the local firing rate η with cT_i obtained from the solution's spike-time distribution. Here, it is shown that at slow synaptic processing speeds the firing rate closely resembles that seen for waves in the lateral-inhibition network with large m, where there is a clear maximum in firing rate at the center of the wave. This is not the case as β is increased. Instead the firing rate tends to a constant across the entire wave structure. The waves studied in this regime are all still localised because they have finite m and the

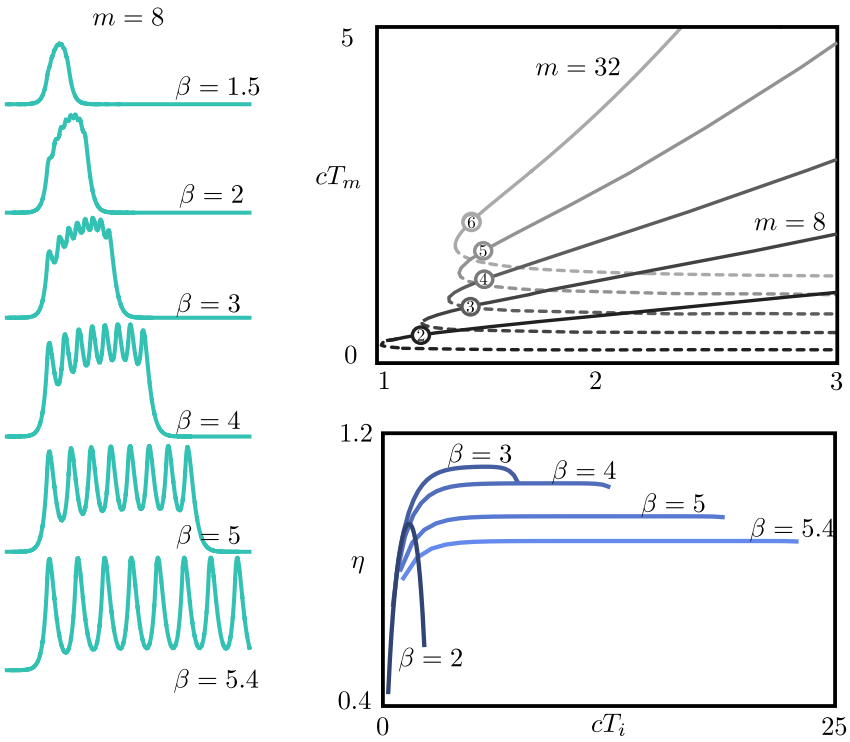


Figure 4.15 Top right: one parameter continuation for wave width cT_m in β for $m = 1, 2, 4, 8, 16, 32$, the parameter I is fixed at each waves unique I^*, so that only one graze point exists in all TW_m branches. Left: synaptic profiles for different β on TW_8 branch. Bottom right: measure of firing rate from eq. (4.12) plotted as function of cT_i for $i \in \mathbb{N}_m$.

.

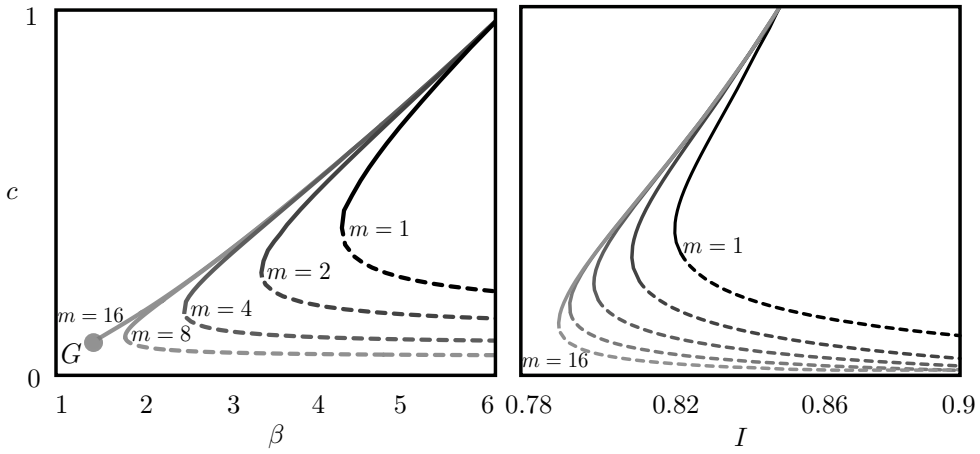


Figure 4.16 Bifurcation plots of the wave speed c for TW_m states with $m = 1, 2, 4, 8, 16$. (a) One-parameter continuations in synaptic processing rate β at fixed $I = 0.82$, there is a graze point G marking the end of the stable TW_{16} branch at $\beta = 1.44$ and $c = 0.099$, (b) similarly, continuation in external background current I fixing $\beta = 4$. Lower branches are shown to be unstable by solving Problem 3.6.4

synaptic envelope all have positive input. However, it is believed the solutions are close to a large set of periodic orbits. It is found that at a critically high β the synaptic input oscillations have grown in amplitude so that the minima equates to zero. At this point the multiple-spike state has fully dissociated and the dynamics corresponds directly to a set of non-interacting single-spike waves.

One-parameter continuations in fig. 4.16 mostly confirm the assertion claimed by [56, 143], that the wave speed for a generic multiple-spike TW_m is essentially identical to the TW_1. This is certainly the case for $\beta \gtrapprox 5.7$. However, it is found from the continuations in I and β that stable waves with larger spike numbers m exist in a larger parameter region. This can be shown by the relative positions of the TW_m's saddle-node. For example, the TW_8 in fig. 4.16(a) occurs at $\beta = 1.75$ and $c = 0.11$ while the TW_1 is at $\beta = 4.1$ and $c = 0.41$. The TW_m states wave-speed relation with β is markedly different in the purely excitatory network compared to to the lateral-inhibition case (see fig. 4.12). Notably wave speeds of multiple-spike waves in the excitatory networks are faster or equivalent to the single spike wave, whereas multiple-spike waves that exist in the lateral-inhibition network are always slower than coexistent waves with less threshold crossings m.

In addition, lateral-inhibition waves destabilise via a sequence of Hopf bifurcations as the synaptic processing speed increases, with no notable change in spike-time distribution. The inhibition constrains the waves width and maintains

a spike-time distribution where the neurons in the center of the wave fire more rapidly than edge neurons. In contrast, the spike-time intervals of waves in the excitable network tend to a constant at faster synapses (see fig. 4.15), and eventually lead to the multiple-spike waves dissociating into a set of m single-spike waves evenly distributed across the network. For this parameter regime the dissociation point for TW_m is $\beta \approx 5.8$ at $c \approx 1$.

4.9 Summary

In this chapter we have analysed the bifurcation structure of multiple-spike waves and explored the various ways a TW_m can destabilise. This has built on the work done in [13, 15, 21, 55, 56, 145] for the single-spike wave.

Some of the key findings are listed:

- Tests comparing explicitly measured wave speeds, spike-times and spatial profiles from simulation results to numerical solutions have proven to be remarkably accurate and robust.

- For critically slow synapses we find a branch-terminating non-smooth graze bifurcation, marking the end of existence of a wave state.

- In the lateral-inhibition network and for waves with $m \geq 3$, the growth of oscillations in firing times for fast synapses has led to the hypothesis that the network undergoes a Hopf instability. Our wave stability analysis has proven this to be the case by the numerical computation of the multiple-spike waves' eigenvalues, where we have seen eigenvalue pairs at critical parameter values crossing the imaginary axis.

- Waves with $m \geq 3$ destabilise via a sequence of Hopf bifurcations, but for $m = 2$ a branching point bifurcation is observed instead. It is known that the single-spike wave with large axonal delays can undergo a similar bifurcation [13]. However, in this model there is no axonal delay kernel, the instability is solely due to a multiple-spike effect.

- As seen from numerical simulations in chapter 2, the lateral-inhibition in the network allows for the formation of composite wave states. We find

that these are not an artefact of the discrete network and show the set of solution branches that exist in the case where the individual waves forming the composite states can only be a TW_1,TW_2 or TW_3. This allows us to find certain rules about the composite waves existence. In particular, the lead wave packet dictates the bifurcation properties of the composite system. The stability is also tested and is still valid.

- Within the lateral-inhibition network, our emphasis has been on fully classifying the existence and stability regions of a TW_3 state. We have presented two-parameter continuations in parameters governing the strength of excitation and inhibition in the neuron's synaptic connections. Showing the stability regions of the TW_3. We have also analysed the effects of finite-rise time in the postsynaptic potential function $\alpha(t)$ and shown that the existence region of stable waves is reduced as the rise time increases.

- As $m \to \infty$ the wave's speed tends to zero and the wave's width tends to a constant. Additionally, the firing rate profile of a wave with $m = 150$ matches up closely to the firing rate profile of stationary bump solutions found in the discrete network. This poses certain questions relating to the existence of stationary bump solutions for spiking networks in the continuum limit.

- The general features of multiple-spike waves found in a purely excitatory network correspond to the findings in the literature. We find that no Hopf bifurcations are observed for fast synaptic processing rates, instead the spike-time intervals tend to an asymptotic constant and depict periodic wave solutions at critically fast synapses.

Chapter 5

Uncertainty quantification of multiple-spike waves

5.1 Introduction

The semi-analytical results in chapter 3 analyse the influence the network's system parameters have on the existence and stability of multiple-spike waves. The wave speed and spike-time intervals are known to be useful variables in understanding the wave dynamics, which have been computed explicitly and also verified directly from numerical simulations.

So far we have studied a homogeneous network where all neurons have identical intrinsic properties and the network connectivity structure contains no spatial inhomogeneities. In reality, there is a level of uncertainty contained within the system parameters forming neuronal networks. It is of interest to test how multiple-spike waves respond to varying degrees of uncertainty in the network's system parameters.

We study two cases of uncertainty with different levels of complexity. The first involves imposing uncertainty on the homogeneous network's system parameters and then analysing how the uncertainty in the output variables propagates. An efficient method to compute the wave variable's probability distributions, expectation and variance is introduced. This approach also allows us to evaluate the voltage and synaptic input probability distributions, and how they vary with space, which has led to the observation of critical spatial regions in the voltage

and synaptic profiles that are susceptible to destabilisation, providing a useful insight into how waves in the network destabilise into other wave states.

The second study is considered more complex. It investigates a heterogeneous network, where the synaptic processing rate of each neuron in the network is different. The high-dimensionality of this type of heterogeneity does not at present allow for tractable analytical approaches, so Monte Carlo simulations are used to obtain probability distributions of the important macroscopic variables that define the multiple-spike waves in this heterogeneous network. Both studies offer interesting insights into the robustness of the multiple-spike waves and the effect uncertainty in the systems inputs have on its macroscopic variables.

Recent advances in computational power have enabled scientists to simulate complex real world phenomena using mathematical and computational models. Uncertainty Quantification (UQ) is an increasingly relevant branch of science that scrutinises the results of such experiments, in light of the knowledge that there is almost always uncertainty and error in the model's output.

One classic source of error arises from the numerical techniques used to approximate solutions of what can often be complex and non-linear equations. Another source of uncertainty stems from improper modelling assumptions. This could perhaps be when qualitative changes in the dynamics (bifurcations) of the model have not been accounted for, implying the model is not an accurate representation of the underlying dynamical process. However, the most important form of uncertainty in this study is input uncertainty. Often an input to a system is unknown, unmeasurable, or inherently random in nature. This is the type of UQ we wish to perform in this study, that is, investigating a deterministic dynamical system in the generic state variable u, taking the form

$$\frac{\mathrm{d}u}{\mathrm{d}t} = F(u, p), \qquad u(0) = u_0, \tag{5.1}$$

with parameters p and initial condition u_0. We also assume that there exists a given quantity of interest (QoI), which depends on the state variable u. We will investigate a UQ problem where we let p (and in some cases u_0) be distributed according to a known probability density function and then attempt to determine what the corresponding probability distribution of the QoI will be. This problem

is the classical forward propagation of UQ because we wish to quantify how uncertainty in one or more parameters is propagated by the deterministic model on a given QoI.

5.2 Uncertainty quantification of homogeneous network

Consider the integrate-and-fire network on the continuum as the deterministic dynamical system under investigation:

$$\begin{aligned} \partial_t v(x,t) = -v(x,t) + I + \sum_{j\in\mathbb{Z}} \int_{-\infty}^{\infty} w(x-y)\alpha\big(t-\tau_j(y)\big)\,dy \\ - \sum_{j\in\mathbb{Z}} \delta\big(t-\tau_j(x)\big), \qquad (x,t)\in\mathbb{R}\times\mathbb{R}, \\ v(x,0) = v_0(x), \end{aligned} \tag{5.2}$$

remembering that in chapters 3 and 4 multiple-spike wave solutions to this partial integro-differential system have been shown to accurately describe the measured results obtained in numerical simulations of the discrete network. Additionally, we have found that the model displays a large family of coexistent TW_m solutions, across a wide range of parameters. Throughout this thesis, we have paid close attention to the effect of changes in the synaptic timescale β on the TW_m dynamics. It therefore makes sense to study the case where β is randomly distributed, with the intention of studying how the uncertainty in this important parameter is propagated forward by the model to the QoI. In this case, the QoI of the TW_m under investigation is the wave speed c, and the corresponding voltage and synaptic spatial profiles.

The bifurcation analysis in chapter 4 has revealed that if β is randomly distributed and the initial condition $v_0(x)$ varies, we can expect a variety of coexisting travelling wave solutions with different number of spikes to be elicited. We are interested in obtaining the probability distribution of c subject to a certain TW_m being elicited by a given initial condition $v_0(x)$. Henceforth, we indicate this particular probability distribution as $P_{c|m}$.

5.2.1 Monte Carlo approach

The Monte Carlo approach is a technique that is commonly used to study how a model responds to randomly generated inputs. It involves running a large number of simulations, each with initial inputs randomly generated according to some distribution of choice. The outputs of the simulations are then aggregated and assessed. Common measures include: the mean value of an output, the probability distribution of output values, and the range of the output value [162].

In this study, where we wish to obtain $P_{c|m}$, we can devise the following Monte-Carlo routine:

1. Extract Q samples of the synaptic timescale parameter $\{\beta^q\}_{q=1}^{Q}$ from a selected random distribution P_β.

2. Time-step eq. (5.2) with initial condition $v_0(x)$ for a fixed time horizon.

3. Reject realisations that do not display a TW_m state.

4. Measure the speed c^q directly from the firing-time history of the network, given by the set $S = \{(x_i, t) : v_i(t) = 1\}$. S is formed of points that are aligned on m disjoint lines in the (x, t)-plane.

5. Compile histograms of $P_{c|m}$ and calculate the corresponding moments.

5.2.2 Law of the unconscious statistician

The Monte-Carlo approach is a powerful and reliable way of evaluating probability distributions when there is no known way of calculating them otherwise. However, these methods are reliant on a large number of realisations of the system to gain accurate results. This can often be an extremely time consuming exercise and subject to a degree of measurement error.

We note that the analysis of the continuum network model in chapter 3 devised a travelling wave problem which can be solved to compute the precise wave speed and spike time intervals of a multiple-spike wave. Moreover, in chapter 4, numerical methods have been used to continue the travelling wave solutions in a variety of

network parameters. As a result, we are able to exploit this analysis to extract distribution moments with minimal computational expense.

If we consider $\beta \sim P_\beta$, then by implication the macroscopic variables of the system are also random variables. In chapter 4 we computed the bifurcation diagrams in the solution measures $c(\beta)$, $\{T_i(\beta)\}$. This means we have a functional relationship between the network's macroscopic variables $(c, T_2, \dots, T_m)$ and the system parameters, framed in terms of deterministic functions, which we formally denote as

$$(c, T_2, \dots, T_m) = f_m(\beta), \qquad m \in \mathbb{N}, \tag{5.3}$$

where β is now taken to be a random variable extracted from a known probability distribution P_β. We note that $f_m(\beta)$ is not known in closed form, but can be directly evaluated using the known bifurcation diagrams $c(\beta)$, $\{T_i(\beta)\}$ obtained in chapter 4. Starting from this observation, we have access to $P_{c|m}$ and its moments. The distribution $P_{c|m}$ can be estimated via an empirical measure, by extracting the samples $\{\beta^q\}_q$, computing the corresponding velocities $\{c^q = f_m(\beta^q)\}_q$ and binning them to compile histograms.

If, on the other hand, because we are interested in the moments of $P_{c|m}$, we can directly apply the theorem colloquially referred to as the *law of the unconscious statistician*. So named because statisticians have often been accused of mistaking the theorem for a definition due to its apparent simplicity [163]. The theorem implies that, if β has a continuous distribution on $\Omega \subseteq \mathbb{R}$ with a probability density function P_β, and that $f : \Omega \to \mathbb{R}$ has a measurable range, then the first and second moments of $f_m(\beta)$ are

$$\mathbb{E}\big[f_m(\beta)\big] = \int_\Omega f_m(b) P_\beta(b)\, \mathrm{d}b,$$

$$\mathrm{Var}\big[f_m(\beta)\big] = \int_\Omega \big[\mathbb{E}[f_m(\beta)] - f_m(b)\big]^2 P_\beta(b)\, \mathrm{d}b.$$

In fig. 5.1 we compare the Monte-Carlo and unconscious statistician approaches to quantify uncertainty on the speed of a TW_3 when β is normally distributed

$$\beta \sim P_\beta = \mathcal{N}(\bar{\beta}, \sigma_{\mathrm{n}}^2), \tag{5.4}$$

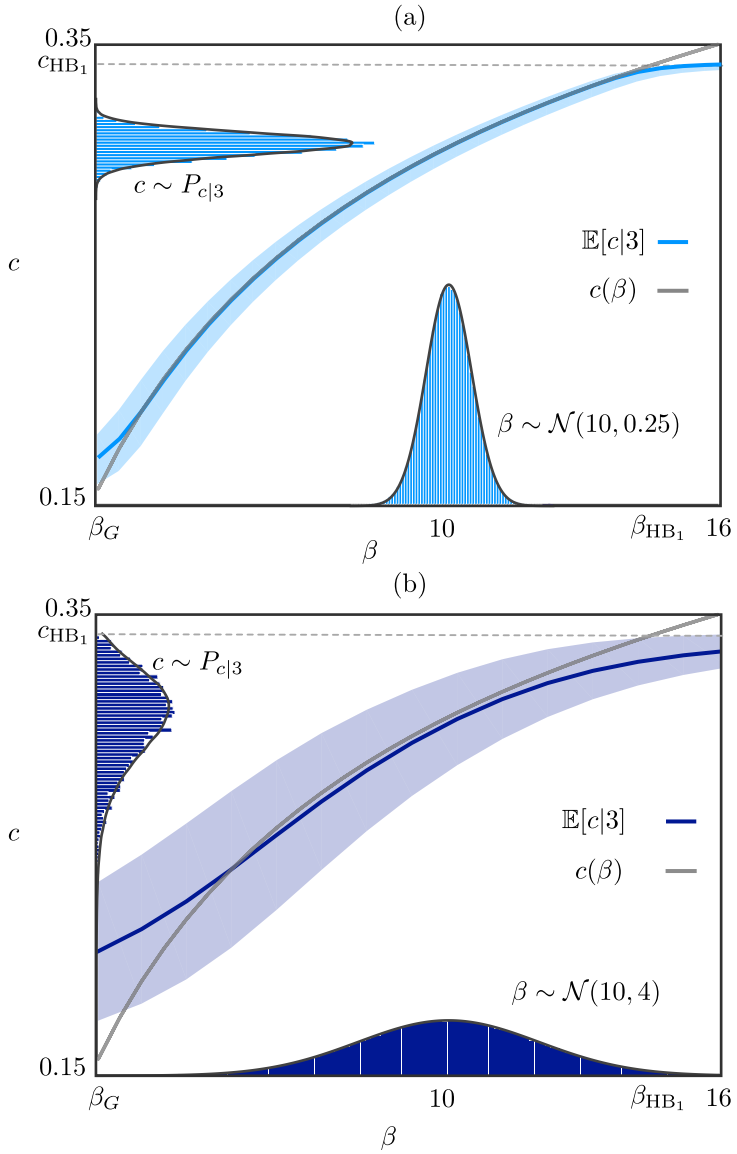


Figure 5.1 The synaptic processing rate β is assumed to be the uncertain input to the system, such that $\beta \sim \mathcal{N}(\bar{\beta}, \sigma_{\mathrm{n}}^2)$ with the mean $\bar{\beta} = 10$ and standard deviation, in (a) $\sigma_{\mathrm{n}} = 0.5$ and (b) $\sigma_{\mathrm{n}} = 2$. Histograms represent the probability density functions obtained from Monte Carlo simulations of the integrate-and-fire network eq. (2.10)–eq. (2.13) with 5×10^3 realisations. The network is initialised with synaptic and voltage spatial profiles obtained from a TW_3 solution with $\bar{\beta} = 10$. Numerical continuations of the speed performed performed in section 4.2 are used to compute the non-trivial function $f_3(\beta)$ in eq. (5.3) via interpolation, where the random variable β is sampled from its distribution 10^6 times. The resulting speed distributions are truncated at $c = c_{\mathrm{HB}_1}$ and $c = c_{\mathrm{G}}$ and fitted using kernel regression, matching up remarkably well to the Monte Carlo simulations. This technique is applied for $\beta \in [\beta_{\mathrm{G}}, 16]$, the expectation $\mathbb{E}[c|3]$ (blue lines) and standard deviation $\mathrm{std}[c|3]$ (shaded blue) is calculated from the corresponding kernel regressions for $\bar{\beta}$.

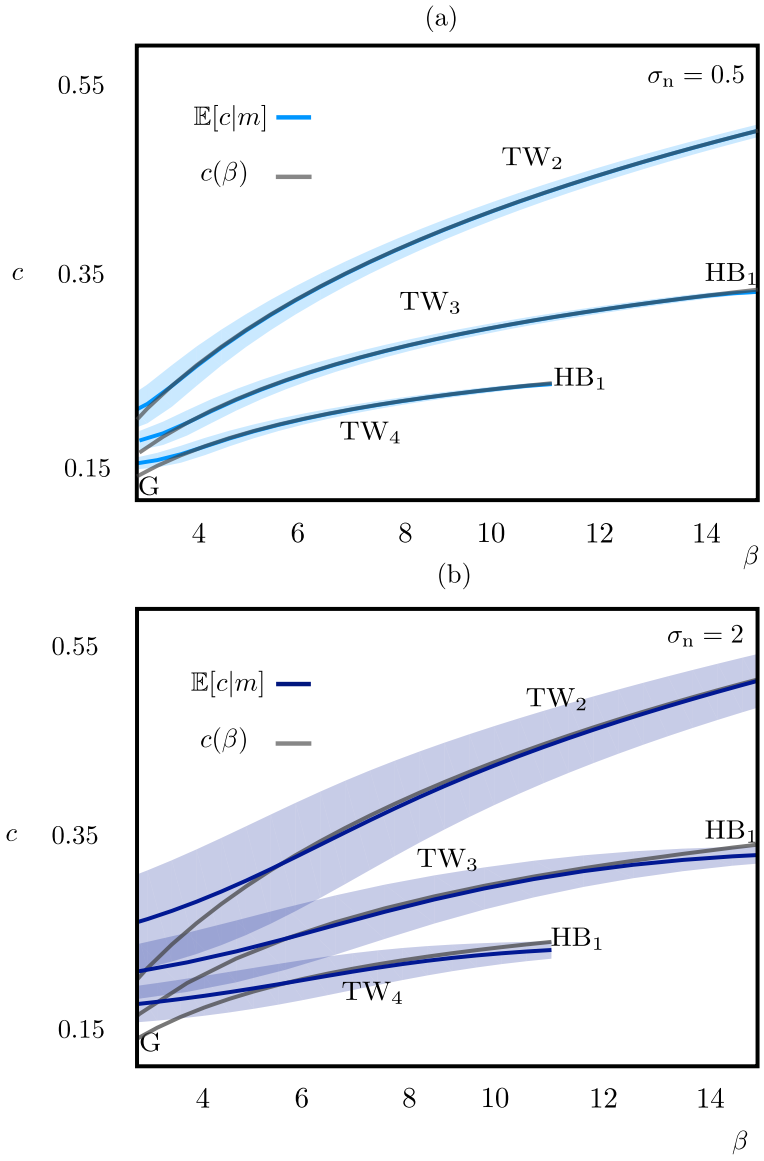


Figure 5.2 Curves of the expectation $\mathbb{E}[c|m]$ for (blue lines) and standard deviation bounds of wave speed probability density functions (shaded blue) for stable TW_2, TW_3 and TW_4 multiple-spike wave states. Uncertain input parameter $\beta \sim \mathcal{N}(\bar{\beta}_\mathrm{n}, \sigma_\mathrm{n}^2)$ for $\beta \in [2.17, 14.65]$ with standard deviation (a) $\sigma_\mathrm{n} = 0.5$ and (b) $\sigma_\mathrm{n} = 2$. The wave speed is computed via interpolation of eq. (5.3) at 10^6 samples of the random input β and the resultant probability distribution for the wave speed is truncated and fitted as in fig. 5.1.

with $\bar{\beta}$ the mean and σ_{n}^2 the variance of P_β. In this experiment, we take $v_0(x) = \nu(x, \bar{\beta})$, where ν is constructed using the analytical expression eq. (3.11) with $(c, T) = f_3(\bar{\beta})$.

We begin by performing a test at $\bar{\beta} = 10$ for two different levels of uncertainty in β. In each experiment we take 5×10^3 β samples for the Monte Carlo simulations and 10^6 samples for inputs to the semi-analytical function eq. (5.3) with $m = 3$. The empirical distributions P_β are illustrated on the horizontal axis in fig. 5.1(a-b) as bar plots and fitted using a non-parametric kernel fitting toolbox in Matlab (grey lines). Similarly, the probability distributions $P_{c|3}$ denoting the compilations of the directly measured speeds of the Monte-Carlo simulations and the outputted speeds from the 10^6 evaluations of eq. (5.3) are presented on the y-axis in fig. 5.1(a-b). Here we see that both the Monte Carlo approach and the unconscious statistician method are in excellent agreement. The difference is that the latter procedure takes a few seconds to complete 10^6 evaluations of eq. (5.3), as opposed to the 5×10^3 Monte Carlo simulations of the system, which can take many hours (dependent on n). Therefore, comparatively, the unconscious statistician procedure is a considerably more efficient method of computing $P_{c|3}$ than the Monte Carlo approach. Also accurate, because it can obtain smooth kernel regression fits from considerably more data points in realistic time frames. This can be seen by comparing the grey lined kernel fits for $P_{c|3}$ on the y-axis in fig. 5.1(a-b) to the bar plot outputs from the Monte Carlo simulations, where we see fluctuations around the kernel fits due to the smaller number of realisations used.

Taking advantage of the efficiency of the unconscious statistician procedure, we have in fig. 5.1 varied the mean $\bar{\beta}$ of P_β for $\beta \in [\beta_{\mathrm{G}}, 16]$ and plotted the mean and standard deviation intervals of each $P_{c|m}$ using eq. (5.4). The results are superimposed on the deterministic bifurcation diagram $c(\beta)$ for comparisons. It can be seen from these results that the system's graze and Hopf bifurcation points significantly influence the statistical moments. For example, when β is near the first Hopf point at $\beta_{\mathrm{HB}_1} = 14.65$, the expectation value $\mathbb{E}[c|3]$ is less than the speed obtained from $c(\beta)$. Here the speed distribution $P_{c|3}$ has a long tail, extending out to higher speeds, but stops abruptly at the speed c_{HB_1} corresponding to the first Hopf bifurcation at HB_1. If $\beta > \beta_{\mathrm{HB}_1}$ the wave is known to destabilise into a

wave state with $m < 3$. As a result, the conditional distribution $P_{c|3}$ is skewed in favour of slower speeds, leading to an expectation wave speed slower than the deterministic TW_3 solution, where there is no input uncertainty. Comparing fig. 5.1(a) and fig. 5.1(b), it can be seen that increases in the standard deviation σ_n of P_β exacerbate this response. In contrast, for $\beta < \beta_\mathrm{G}$ the TW_3 wave state does not exist because a region of the voltage profile is above the voltage threshold. In this case the wave speed distribution is skewed towards higher speeds, because only TW_3 propagate on a network with faster synaptic processing rates than β_G exist, the samples randomly selected from P_β with $\beta < \beta_\mathrm{G}$ will evolve into a bump state and are not accounted for in the conditional probability distribution. This explains why now, in the opposite sense, $\mathbb{E}[c|3] > c(\beta)$ for β near β_G.

It can be seen in fig. 5.2 that these qualitative observations in fig. 5.1 are repeated when we perform the same experiment on the TW_2 and TW_4 wave states. Additionally, we find that the standard deviation of the speed probability distribution $P_{c|m}$ decreases, as the spike number m increases.

We note that the unconscious statistician method introduced here is only capable of producing the conditional probability distributions $P_{c|m}$. However, since the initial wave state is prescribed to be the TW_m state at $\bar{\beta}$ of the distribution P_β, the interpretation of P_c which accounts for all the possible emergent coherent states: waves with $m' < m$ and bumps, is considered unimportant. This is because the P_c would be largely dependent on the choice of initial state, which is essentially arbitrary. We therefore have focused the UQ analysis on one specific TW_m state at a time.

5.2.3 Uncertainty in β and b_1

The UQ analysis is extendable to uncertainty in multiple system parameters. A motivational example is given in fig. 5.3, where the parameters β and b_1 are assumed to be uncertain. We remind the reader that b_1 is a network level parameter, which influences the balance of excitation and inhibition in the network, thus, an increase in b_1 diminishes the spatial scale of excitatory connections and increases the strength of the distal inhibitory connections. The numerical computation of

the output variables now involves evaluating the two dimensional function

$$(c, T_2, \ldots, T_m) = f_m(\beta, b_1), \tag{5.5}$$

where β and b_1 are both random variables sampled from independent probability distributions P_β and P_{b_1} respectively. In fig. 5.3(a) the surface plot of $c = f_3(\beta, b_1)$ is illustrated along with various speed contour lines. After evaluating this function, we compute probability distributions of a TW_3's wave speed c and third spike-time T_3. This is achieved by extracting from P_β and P_{b_1} 10^6 sample pairs $\{(\beta^q, b_1^q)\}_q$ and evaluating eq. (5.5) for $\{c^q, T_3^q\}_q = f_3(\beta^q, b_1^q)\}_q$, and binning to compile the probability distributions (see fig. 5.3(c)(d)). It can be seen in fig. 5.3(b) that the selected variances for the random distributions P_β and P_{b_1} are sufficiently small such that all resultant solutions are in the wave's stable parameter regime. As a result, $\mathbb{E}[c|3]$ and $\mathbb{E}[T_3|3]$ both closely match the solutions obtained from the deterministic two-parameter bifurcation diagram.

We note that the numerical computation of the output variables becomes more involved as the number of uncertain parameters increases, but in principle there is no limitation to the number of parameters considered uncertain. However, the results past two uncertain parameters are unlikely to be interpretable in any meaningful sense.

5.2.4 Uncertainty quantification of TW_3 spatial profiles

The functional relationship between a wave's macroscopic variables $(c, T_1, \ldots, T_m)$ and its system parameters can be exploited further to perform uncertainty quantification on its voltage and synaptic spatial profiles, since it has been shown in the analysis of the continuum formulation of the network that the multiple spike travelling wave profiles ν and σ are completely determined by knowledge of the vector $(c, T_1, \ldots, T_m)$. Hence, in the case where β is again taken to be uncertain, through the computation of $f_m(\beta)$, the spatial profiles of a TW_m are constructed

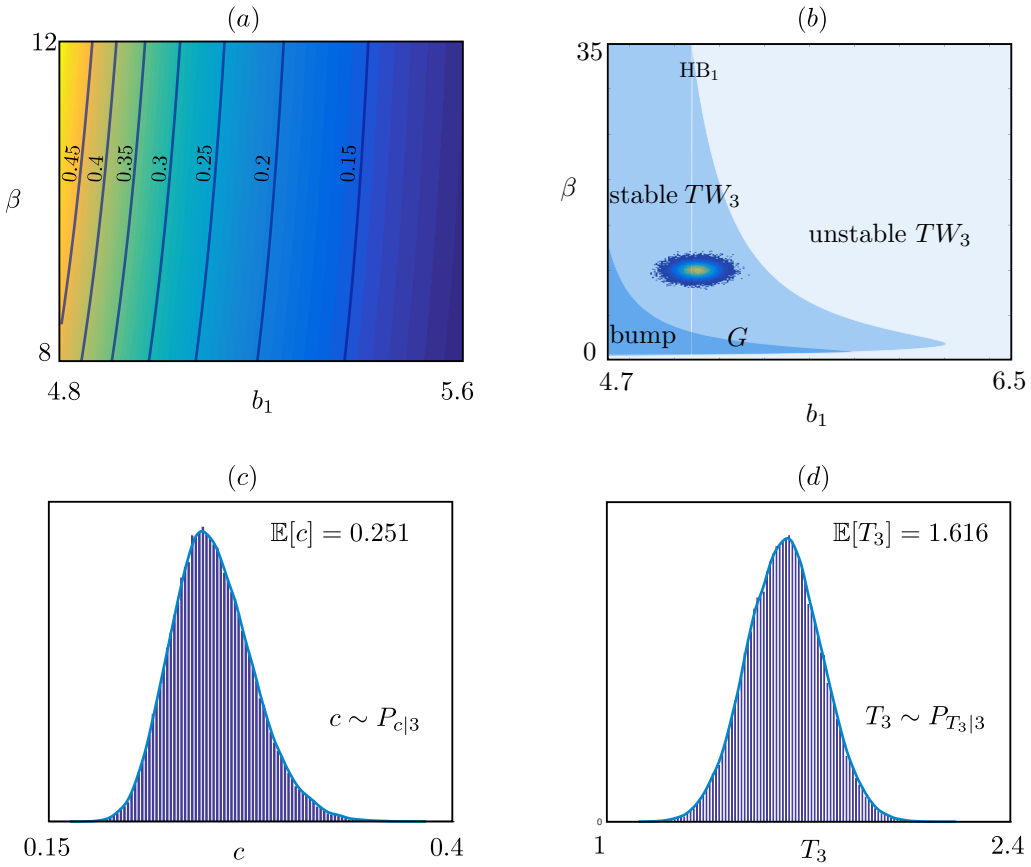


Figure 5.3 (a) Surface plot of function $c = f_3(\beta, b_1)$ for a TW_3 wave state, with the wave speed contour lines. (b) Two-parameter bifurcation diagram showing the Hopf and graze lines marking the regions of stability for the TW_3 wave state. Within the wave's stable region is depicted the chosen probability distributions of the uncertain β and b_1 parameters, normally distributed with means ($\bar{\beta} = 10, \bar{b_1} = 5.1$), and standard deviations ($\sigma_{\text{n}}^{\beta} = 0.5, \sigma_{\text{n}}^{b_1} = 0.05$). (c)(d) Fitted probability density functions for c and T_3 respectively.

in terms of its output, thus

$$\nu(\xi; f_m(\beta)) = I - \sum_{j=1}^{m} \exp\left(\frac{c(\beta)T_j(\beta) - \xi}{c(\beta)}\right) H\left(\frac{\xi - c(\beta)T_j(\beta)}{c(\beta)}\right) + \frac{1}{c(\beta)} \sum_{j=1}^{m} \int_{-\infty}^{\xi} \exp\left(\frac{s-\xi}{c(\beta)}\right) \int_0^{\infty} w(y - s + c(\beta)T_j(\beta)) p(y/c(\beta))\, dy\, ds. \tag{5.6}$$

and

$$\sigma(\xi; f_m(\beta)) = \frac{1}{c(\beta)} \sum_{j=1}^{m} \int_0^{\infty} w(y - \xi + c(\beta)T_j(\beta)) p(y/c(\beta))\, dy. \tag{5.7}$$

where $m \in \mathbb{R}$, $c \in \mathbb{R}_{\neq 0}$ and $T_1 < \cdots < T_m \in \mathbb{R}$. Therefore, the spatial profiles ν and σ are also functionally related to the system parameters, leading to the following conditional expressions for the expectation and variance at ξ for a generic TW_m wave state:

$$\mathbb{E}[\nu(\xi)] = \int_\Omega \nu(\xi; f_m(\beta)) P_\beta(b) db \tag{5.8}$$

$$\mathrm{Var}[\nu(\xi)] = \int_\Omega \left[\mathbb{E}[\nu(\xi)] - \nu(\xi; f_m(b))\right]^2 P_\beta(b) db, \tag{5.9}$$

similarly for the synaptic input σ

$$\mathbb{E}[\sigma(\xi)] = \int_\Omega \sigma(\xi; f_m(\beta)) P_\beta(b) db \tag{5.10}$$

$$\mathrm{Var}[\sigma(\xi)] = \int_\Omega \left[\mathbb{E}[\sigma(\xi)] - \sigma(\xi; f_m(b))\right]^2 P_\beta(b) db. \tag{5.11}$$

In the case where $\beta \sim P_\beta = \mathcal{N}(\bar{\beta}, \sigma_{\mathrm{n}}^2)$, results from computing the expectation and standard deviation at ξ are given in fig. 5.4. This is compared to the synaptic and voltage profile of a TW_3 with no input uncertainty in β at $\bar{\beta} = 8$, where we see a close correspondence in most of the spatial domain. However, around the spatial regions close to the second and third spiking events we see a clear discrepancy in the expectation for ν and the profile obtained for fixed $\beta = \bar{\beta}$ (see fig. 5.4(b)). Here the non-smooth, instantaneous reset condition leads to bimodal probability distributions in ν. As a result, the expectation results in this region

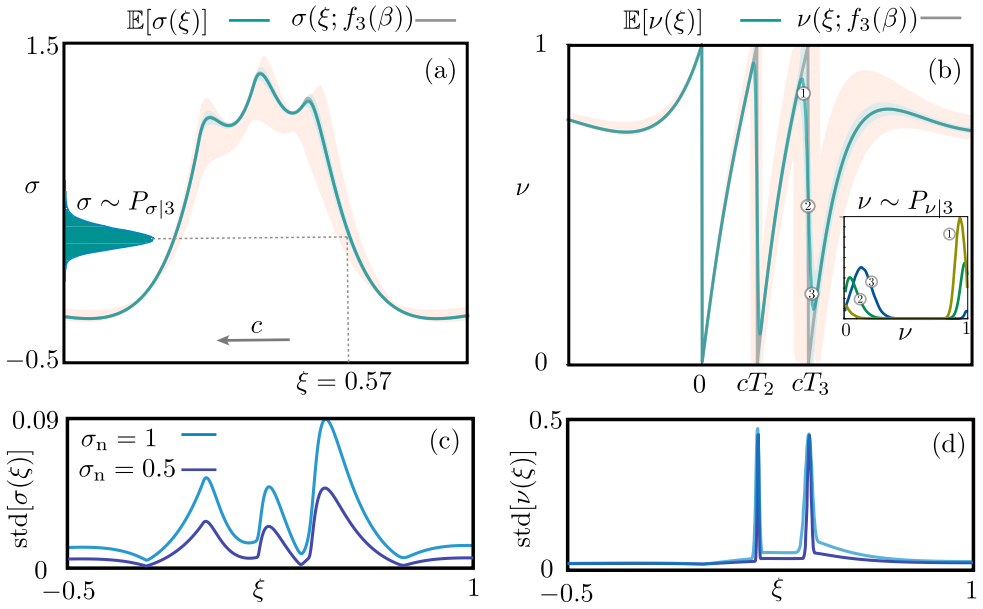


Figure 5.4 Uncertainty quantification analysis of a TW_3 assuming uncertain synaptic processing rate parameter $\beta \sim \mathcal{N}(\bar{\beta}, \sigma_n^2)$, with $\bar{\beta} = 8$ and $\sigma_n = 1$. The probability density functions for ν and σ are computed at discrete spatial positions $\xi_i = -L + 2iL/n$ with $\mathbb{N}_n = \{0, ..., n\}$, for $i \in \mathbb{N}_n$, where $n = 1024$ and $L = 1$, (a) Computed σ expectation by eq. (5.10) shown for $\xi \in [-0.5, 1]$, shaded areas represent the standard deviation (blue) and range (red) of each probability density function $\sigma \sim P_{\sigma|3}$ evaluated at ξ. Illustrated on y-axis shows $\sigma \sim P_{\sigma(0.57)|3}$. (b) Computed ν expectation by eq. (5.10) shown for $\xi \in [-0.5, 1]$, shaded areas represent the standard deviation (blue) and range (red) of each probability density function $\nu \sim \Pr(\beta)$ evaluated at ξ. Three examples of bimodal ν distributions found near $\xi = cT_3$ are given. (c)(d) Standard deviation curves std$[\sigma(\xi)]$ and std$[\nu(\xi)]$ plotted as a function of ξ by taking the square root of eq. (5.11).

are slightly deceptive. But, they do reflect the relative influence uncertainty in β has on the expected location of a spike. We see from fig. 5.4(d) two distinct peaks in the standard deviation of the ν probability distributions, centred over $\xi = cT_2$ and $\xi = cT_3$, here the width of the peaks indicate the level of variability in the spike events expected location.

Also observed in fig. 5.4 are isolated spatial regions where input uncertainty has negligible effect on the voltage or synaptic current. These are marked by near-zero standard deviations in its probability distribution, such that they resemble Dirac delta functions centred over the σ and ν values obtained with no uncertainty in β. In fig. 5.4(c-d) these special cases correspond to local minima in the standard deviation curves std$[\nu(\xi)]$ and std$[\sigma(\xi)]$.

Finally, simulations have shown that a TW_3 with too large a level of uncertainty in β will destabilise to a TW_2 or a TW_1. In such a case it is always the spikes at the tail-end of the waves profile (relative to its direction of propagation)

that decay to the quiescent state first. Interestingly, we find that the levels of variability in ν and σ vary significantly across the waves spatial profile. In particular, probability distributions of ν and σ at the tail-end of the wave indicate an increased likelihood of large deviations from the expected value. This implicitly highlights the wave profiles most vulnerable region to input uncertainty, that could lead to a destabilisation.

5.3 Heterogeneity in synaptic processing rate

In this section, we now investigate the behaviour of multiple-spike waves in a heterogeneous network, whereby the ith neuron's synaptic processing rate parameter β_i is the ith component of the vector $\beta_n \in \mathbb{R}^n$, where

$$\beta_n \overset{i.i.d.}{\sim} \mathcal{N}(\mu, \sigma_{\mathrm{n}}^2). \tag{5.12}$$

We are particularly interested in addressing the following questions:

1. How does heterogeneity affect the dynamics of the multiple-spike wave?
2. What are the probability distributions of a wave's output variables and how do they compare to the homogeneous networks?
3. How does a wave respond to increasing levels of variability in the neuron's synaptic processing rate?

5.3.1 Heterogeneous network evolution equation

The set of 2n ODEs defining the discrete integrate-and-fire network must be adapted from the description of the homogeneous network defined in section 2.3. Since the synaptic processing rate of each neuron in the network is heterogeneous, the postsynaptic response function of each neuron is now also heterogeneous, such that $\alpha_i(t) = \beta_i \exp(-\beta_i t)H(t)$. Hence, the evolution equations for the discrete

heterogeneous network is now:

$$\dot{v}_i(t) = I_i(t) - v_i(t) + s_i(t) - \sum_{j\in\mathbb{Z}_+} \delta(t - \tau_i^j), \tag{5.13}$$

$$\dot{s}_i(t) = -\beta_i s_i(t) + \frac{2L\beta_i}{n} \sum_{k\in\mathbb{N}_n} \sum_{j\in\mathbb{Z}_+} W_{ik}\delta(t - \tau_k^j), \tag{5.14}$$

remembering that the firing times can be arranged in the monotonically increasing sequence

$$0 = \tau_{i_0}^{j_0} \leq \tau_{i_1}^{j_1} \leq \ldots \leq \tau_{i_k}^{j_k} \leq, \ldots \tag{5.15}$$

with the set of $2n$ piecewise-linear evolution equations defined on the time interval $\left[\tau_{i_k}^{j_k}, \tau_{i_{k+1}}^{j_{k+1}}\right)$ given by:

$$\dot{v}_i(t) = I_i(t) - v_i(t) + s_i(t), \qquad t \in \left(\tau_{i_k}^{j_k}, \tau_{i_{k+1}}^{j_{k+1}}\right), \quad i \in \mathbb{N}_n, \tag{5.16}$$

$$\dot{s}_i(t) = -\beta_i s_i(t) \qquad t \in \left(\tau_{i_k}^{j_k}, \tau_{i_{k+1}}^{j_{k+1}}\right), \quad i \in \mathbb{N}_n, \tag{5.17}$$

with new reset conditions

$$v_{i_k}([\tau_{i_k}^{j_k}]_+) = 0, \tag{5.18}$$

$$s_l([\tau_{i_k}^{j_k}]_+) = s_l([\tau_{i_k}^{j_k}]_-) + \frac{2L\beta_{i_k}}{n} W_{li_k}, \qquad l \in \mathbb{N}_n. \tag{5.19}$$

5.3.2 Monte Carlo simulations

So far we have only performed uncertainty quantification for multiple-spike waves in a homogeneous network, when all the neuron's properties are identical. In this case the QU analysis was computed efficiently, because our work in previous chapters had developed a concrete numerical methodology to compute the wave's macroscopic variables and bifurcation properties, allowing us to avoid the use of Monte Carlo methods. However, in heterogeneous networks there is no feasible method of calculating the corresponding wave speed and spike times of multiple-spike waves explicitly, since this would involve the computation of integrals in n-dimensions [10]. The *curse of dimensionality* has limited problems of this type to $n \sim 10$. It is possible in some cases to use sparse grid quadrature techniques to solve non-local equations. But to support persistent multiple-spike wave structures

in this model, the network size must be in the hundreds at least. For this reason, we develop a Monte-Carlo algorithm which simulates the heterogeneous network and directly measures the outcomes. The methodology involves repeating the following process n_{r} times:

1. Obtain β_i for $i \in \mathbb{N}_n$ from the normal distribution defined in eq. (5.12).

2. Initialise the ith neurons by numerically solving Problem 3.5.1 for a TW_m solution at each β_i, substitute the result into eq. (3.11)–eq. (3.12) at x_i, to obtain the initial state $(v_i(0), s_i(0))$.

3. Timestep network for T time units and output the space-time firing event history $S = \{(x_i, t) : v_i(t) = 1\}$.

4. Determine whether the TW_m state has persisted for the full time horizon T, or transitioned to another wave state $\mathrm{TW}_{m'}$. If the latter, go back to 3. (initialising from the final $\mathrm{TW}_{m'}$ state).

5. Measure macroscopic variables of TW_m and document the wave state.

A TW_3 state's wave speed c is calculated by extracting the firing time functions $\tau_j(x)$ for $j = 1, 2, 3$ from the set of space-time firing events of each realisation. The gradient of τ_j for a stable wave is $1/c$, and is measured using a first-order polynomial fitting tool in Matlab. The sample mean is then taken from these measurements and used to obtain an accurate measure of the wave speed.

The average spike times and standard deviation of the spike-time intervals is calculated for each realisation by measuring at each spatial point x_i the spike-time intervals $T_j - T_{j-1}$ between the firing times T_j of the ith neuron for $j \in \mathbb{N}_m$ and taking the corresponding mean.

Probability distributions obtained from $n_{\mathrm{r}} = 10^4$ independent realisations of the heterogeneous network are given in fig. 5.5 for two different values of standard deviation in β_n: $\sigma_{\mathrm{n}} = 0.1$ and $\sigma_{\mathrm{n}} = 0.2$. In fig. 5.5(b) we observe a double peaked probability distribution for the TW_3 state's average speed. More work is needed to test the reliability of this particular result. Some preliminary tests have been done where a longer time horizon for each realisation is taken, which results in a decrease in the distance between the bimodal peaks. In addition, the number of

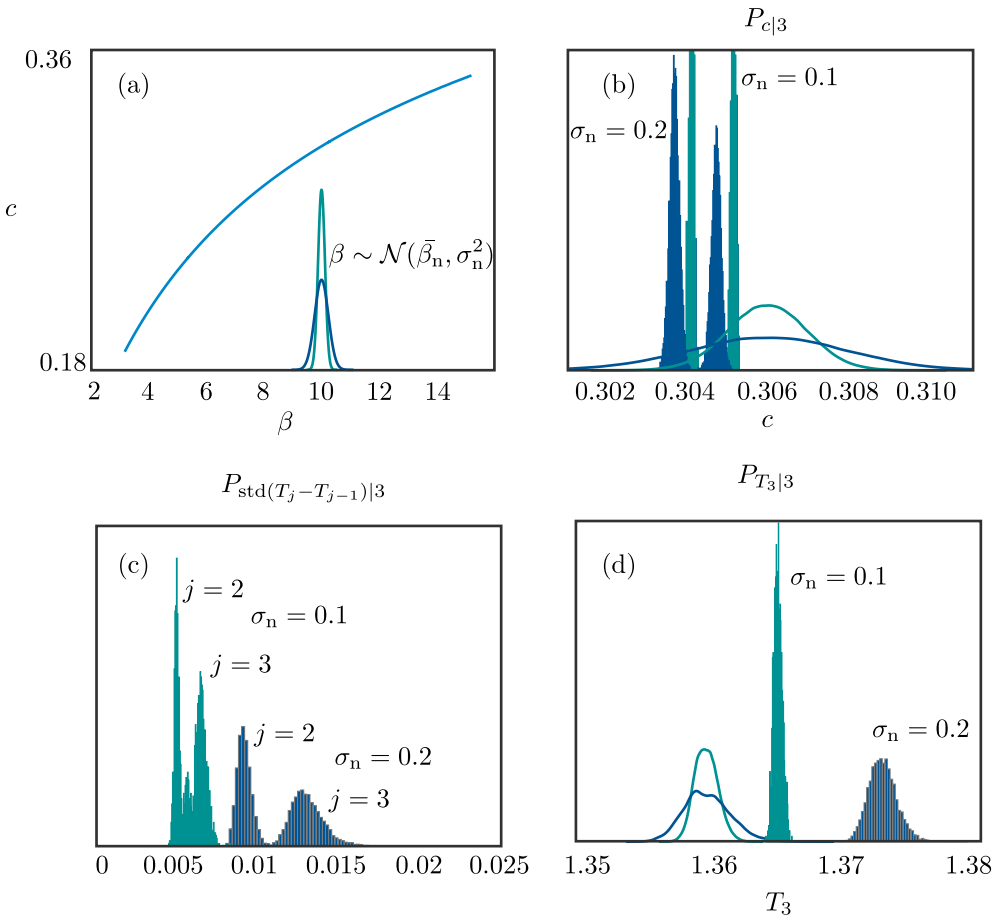


Figure 5.5 (a)The heterogeneous network assumes each neuron at x_i has an uncertain β parameter, such that $\beta_i \sim \mathcal{N}(\bar{\beta}_n, \sigma_n^2)$ for $i \in \mathbb{N}_n$ both with $\bar{\beta} = 10$ and standard deviations $\sigma_n = 0.1$ and $\sigma_n = 0.2$. (b)(c) 10^4 Monte Carlo realisations of the heterogeneous network, with $n = 1024$ neurons, are simulated for a time horizon of $T = 15$. The initial state of each realisation $(s_i(0), v_i(0))$ corresponds to the computed solution at β_i using eq. (3.11)–eq. (3.12). Probability density functions of the measured wave speed, standard deviation of spike time intervals and spike time interval T_3 respectively are shown. Plotted for reference in (b) and (d) are the probability distributions obtained from the uncertainty quantification analysis in section 5.2 for the homogeneous network, where only β at a network level is uncertain.

neurons n is known to have an effect on the position of the bimodal peaks. Slower wave speeds are found for smaller n, and the peaks have greater separation. We note however that the difference is comparable to the measurement error in c.

Another observation is that the width of the distributions in this heterogeneous network is smaller than the fitted probability distributions found from UQ analysis of the homogeneous network, which possess a much larger spread in probable wave speeds. The fitted kernel regressions of $P_{c|3}$ and $P_{T_3|3}$ for the homogeneous network are also plotted in fig. 5.5(b)(d) for comparison with this heterogeneous network.

Another significant finding from the speed distributions is the clear decrease in expected speed for waves in this heterogeneous network when compared to the expected wave speed in the homogeneous network. It can be seen in fig. 5.5(b) that increasing σ_{n} leads to the peaks of the speed distributions shifting further away from the peak of the homogeneous distributions. Similarly, the distributions for the third spike time T_3 in fig. 5.5(d) suggest heterogeneity increases the spike-times.

Additionally, we note from fig. 5.5(c) that the spike time interval between the third and second spike $T_3 - T_2$ has a greater amount of variability than the second and first spikes $T_2 - T_1$. This we find is indicative of the manner in which waves destabilise, in the sense that the tail-end of the wave's profile receives a greater level of variability than the front (see fig. 5.6(b)). We note that this result is in correspondence with the findings in the homogeneous network analysis in section 5.2.4.

The speed probability distribution P_c in fig. 5.6(a) is obtained from $n_{\mathrm{r}} = 10^4$ Monte Carlo realisations with $\sigma_{\mathrm{n}} = 0.5$. The level of variability between neuron's synaptic processing rate is now sufficiently large to cause the TW_3 to destabilise into a TW_2 in some cases. An example of such a destabilisation is illustrated in fig. 5.6(b), where we see the TW_3 state terminating at $t \approx 2.3$ and a TW_2 state then accelerating to its faster average speed. The variance in the newly formed TW_2 state's spike-time interval $T_2 - T_1$ remains constant after it has stabilised to its steady state speed. In fig. 5.6(b) the variance in $T_2 - T_1$ does not change significantly for longer simulation times, because it can be seen that the wave is now already travelling at a constant speed. We see that the heterogeneity has

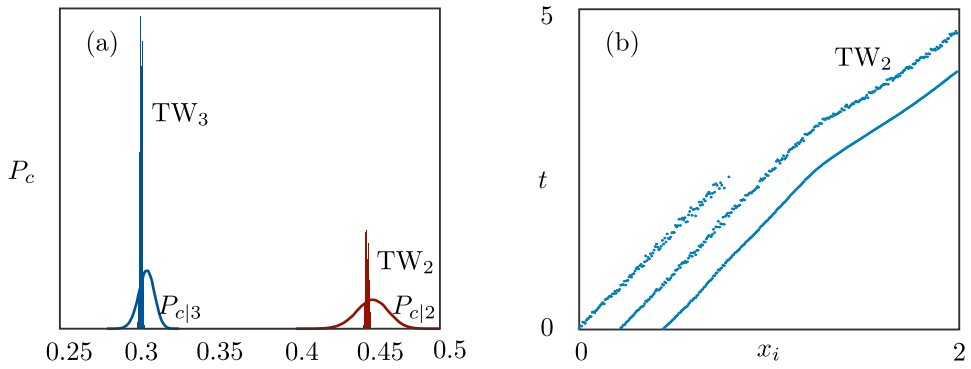


Figure 5.6 If the variance in the neuron's synaptic processing rate is sufficiently high, the initialised TW_3 on the heterogeneous network is unstable, resulting in a destabilisation to a TW_2 state (a) Histograms depicting P_c obtained from Monte Carlo simulations with $\sigma_n = 0.5$. This is compared against the conditional probability distributions $P_{c|3}$ and $P_{c|2}$ in the homogeneous network. Here it can be seen that the range of possible speeds is significantly smaller and also the expected wave speed is slower in the heterogeneous network. (b) Raster plot illustrating destabilisation of unstable TW_3 to stable TW_2. Network size is same as previous experiments with $n = 1024$ and simulation time $T = 15$.

decreased the expected wave speed for a TW_2. Although, the margin of difference between the homogeneous distributions expected speed result is less significant.

Finally, relating back to the double-peaked speed distributions $P_{c|3}$ for $\sigma_n = 0.1$ and $\sigma_n = 0.2$ in fig. 5.5(b), we find that for $\sigma_n = 0.5$, the equivalent conditional distributions for the TW_2 and TW_3 states are single-peaked. This provides some evidence to support our claim that the double-peaked distributions in fig. 5.5(b) are a transient phenomena due to the short horizon time T used.

5.4 Summary

To summarise, we have considered the case where there is a known functional relationship between the multiple-spike waves output variables and the network's system parameters. An efficient method to compute the wave variable's probability distributions, expectation and variance is introduced. These results have been tested by comparisons made to Monte Carlo simulations, where we see that they are in excellent agreement. This approach also allows us to evaluate the voltage and synaptic input probability distributions, and how they vary with space, which has led to the observation of critical spatial regions in the voltage and synaptic profiles that are susceptible to destabilisation, providing a useful insight into how waves in the network destabilise into other wave states.

The knowledge of the wave's bifurcation points has allowed for the complete evaluation of the TW_m state's expectation and standard deviations across its entire region of stability. We note that with sufficiently large levels of parameter variability, the bifurcation points have a significant impact on the expectation values, when compared to the bifurcation diagrams obtained in chapter 4 where there is no uncertainty.

When the heterogeneous network is considered, only Monte-Carlo methods can be applied. In doing so, we have found that the calculated expectation of the wave speeds are slower than the homogeneous network, with significantly lower levels of variability in the speeds probability distributions as well. However, there are similarities such as the increased variabilities at the tail-end of the waves propagation, suggesting a similar mechanism for wave destabilisation.

Chapter 6

Morris-Lecar spiking network

6.1 Introduction

In the previous chapters we have analysed the dynamics of multiple-spike waves found in synaptically coupled networks of leaky integrate-and-fire neurons. In spite of the complex dynamics emerging from the collective interactions at a network level, the LIF neuron model is considered a gross simplification of a neuron's true voltage dynamics. With this is mind, a natural extension to this work is to build networks of neurons whose state variables have a more direct and realistic biological interpretation. In doing so, such single neuron models are capable of displaying a richer level of dynamics. In particular, they can reproduce an important neuro-computational property, whereby there is a coexistence between the neuron's resting and repetitive spiking state—known as 'intrinsic bistability' [160]. Understanding how this neuronal feature affects the network level dynamics is a key component in this particular study.

We remind the reader of the general form of a neural spiking network composed of conductance-based neurons, introduced in section 1.6

$$\begin{aligned} \frac{\mathrm{d}v_i}{\mathrm{d}t} &= f(v_i, z_i) + s_i(t) \\ \frac{\mathrm{d}z_i}{\mathrm{d}t} &= g(v_i, z_i), \end{aligned} \tag{6.1}$$

for a population of neurons indexed by $i \in \mathbb{N}_N$, where $v_i \in \mathbb{R}$ is the voltage of the ith neuron, and $z_i \in \mathbb{R}^l$ are the ionic gating variables. The evolution of spiking networks is determined by the initiation and fast completion of action potentials

by individual neurons. These are referred to as spiking events and often can be characterised in terms of specific firing times, which, we note, deeply influences their mathematical treatment. This is in contrast to mean field approaches which work on a coarser spatio-temporal scale, prescribing a neural activity measure in a particular spatial region to the average behaviour of a population of neurons, thus eliminating any notion of spiking events. An important open question concerns their collective behaviour, that is, the study of the behaviour of network of neurons of type eq. (6.1), where neurons are synaptically coupled to each other with activity exchanged in response to the firing of action potentials.

In general, assembling a network of conductance-based neurons entails two main steps: (i) Modelling the generation of synaptic currents s_i; this step inevitably requires some modelling assumptions, which we will describe in detail in the following section; (ii) Choosing an appropriate conductance-based model for a single neuron; in section 6.3 we put forward our choice of model that will be used throughout this chapter.

6.2 Synaptically connected network of conductance-based neurons

A key difference between most conductance-based neuron models and the LIF neuron is how the action potential mechanism is modelled. In the LIF neuron, the action potential occurs as a non-smooth event, encoded as a precise spike time event, where in the discrete case, the jth neuron's voltage $v_j(t)$ attains a given voltage threshold v_{T} from below at time τ_j^m, for the mth time. Hardwired into the evolution equation is a resetting mechanism, which instantaneously resets $v_j(t)$ back to a voltage v_{R}. As a result, the input $\Delta_{\mathrm{LIF}}(t)$ received by neuron i from the jth neuron firing action potentials is a sequence of weighted Dirac-delta distributions, as illustrated in fig. 6.1. In contrast, more biophysically relevant conductance-based models typically have smooth and continuous voltage signatures with action potentials characterised by large excursions from the neuron's resting state on a fast timescale (see fig. 6.2(a)). Therefore, we do not have precisely determinable spike times like in the LIF case. Hence, to achieve similar results in

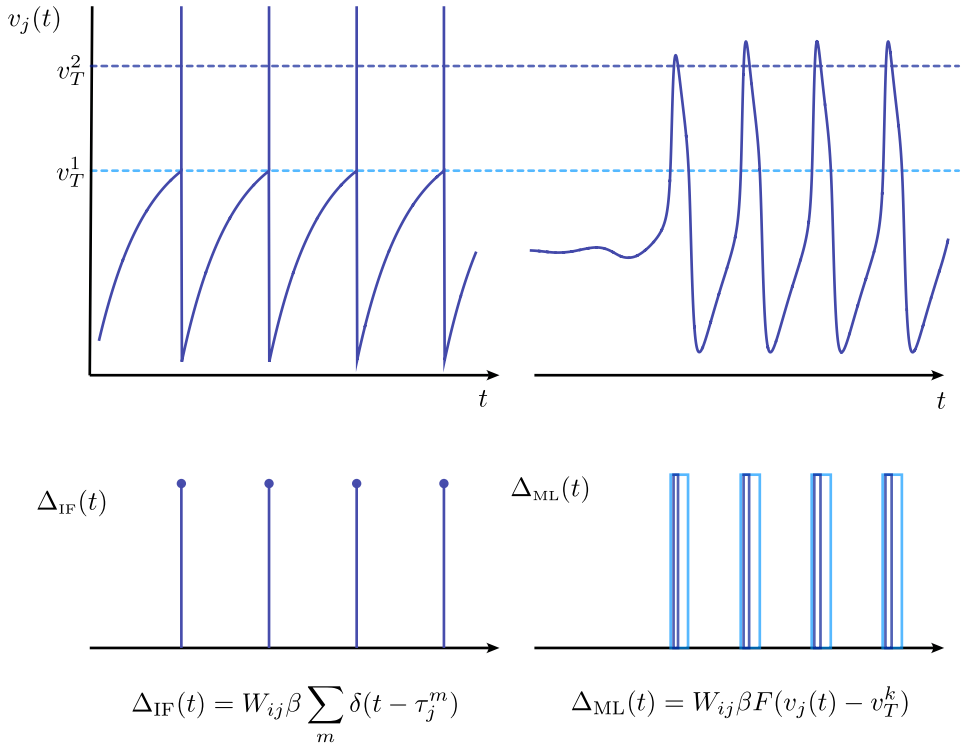


Figure 6.1 Top: voltage time signals of action potential sequences exhibited by jth neuron modelled by the non-smooth integrate-and-fire model with voltage threshold v_{T}^1, and the Morris-Lecar conductance-based model with two voltage thresholds illustrated (dashed lines). Bottom: the input received by the ith neuron in response to the jth neurons activity, light and dark blue lines in $\Delta_{\text{ML}}(t)$ correspond to the voltage threshold v_{T}^k depicted in its voltage time profile above.

modelling the input of the ith conductance-based neuron, in response to the jth neuron firing, we proceed by applying minimal changes, as follows: we prescribe an arbitrary, yet sufficiently high, voltage threshold v_{T} to guarantee we are picking up a true action potential and not sub-threshold oscillations. The voltage signal of an action potential will traverse the threshold from above and below. Instead of having a precise firing time, we have a window of time during which the jth neuron is actively transmitting input to the ith neuron. We therefore replace the sequence $W_{ij}\beta\sum_m \delta(t-\tau_j^m)$ with the continuous function $\beta W_{ij}F(v_j(t)-v_{\mathrm{T}})$, where F can be regarded as a spike-detection function, which we will take to be a steep sigmoid. We note that the faster the action potential crosses the threshold from above and below, the more $F(v_j(t)-v_{\mathrm{T}})$ resembles a Dirac-delta function. This is exemplified in fig. 6.1, where we see that voltage thresholds chosen to be closer to the peaks of the voltage signal have smaller time windows where $v_j(t) > v_{\mathrm{T}}$, and therefore have inputs tending towards the LIF neuron's sequence of Dirac-delta distributions. Hence, under this prescription, the model still captures the "firing sequence" of action potentials, even though the precise firing times are not explicitly used to prescribe the evolution equation of the network.

Taking on board these assumptions, we now construct a neuronal network of conductance-based neurons with a similar style to the LIF network studied throughout this thesis. We first consider the discrete LIF network formulation obtained in section 2.2, written as:

$$\begin{aligned}\frac{\mathrm{d}v_i}{\mathrm{d}t} &= I_i(t) - v_i(t) + s_i(t) - \sum_{m\in\mathbb{Z}_+}\delta(t-\tau_i^m),\\ \frac{\mathrm{d}s_i}{\mathrm{d}t} &= -\beta s_i(t) + \frac{2L}{N}\sum_{j\in\mathbb{N}_N}(\Delta_{\mathrm{IF}}(t))_i,\end{aligned}$$

where L is the spatial half-width, N is the network size with neurons indexed by $i\in\mathbb{N}_N$ and $(\Delta_{\mathrm{IF}}(t))_i$ is the input received by the ith neuron due to the jth neuron's activity, which is summed for all $j\in\mathbb{N}_N$.

Now, if $\Delta(t)_i = \beta W_{ij}F(v_j(t)-v_{\mathrm{T}})$ approximates a sharp Dirac-delta firing sequence similar to $(\Delta_{\mathrm{IF}}(t))_i$, and the LIF voltage dynamics is replaced by a generic conductance-based model of the form given in eq. (6.1), we arrive at a

network model for conductance-based neurons, given by

$$\begin{aligned}\frac{\mathrm{d}v_i}{\mathrm{d}t} &= f(v_i, z_i) + s_i(t)\\ \frac{\mathrm{d}z_i}{\mathrm{d}t} &= g(v_i, z_i)\\ \frac{\mathrm{d}s_i}{\mathrm{d}t} &= -\beta s_i(t) + \frac{2L\beta}{N}\sum_{j\in\mathbb{N}_N} W_{ij}F(v_j(t) - v_\mathrm{T}),\end{aligned} \tag{6.2}$$

which is inspired by the LIF network studied in this thesis. In this chapter, we analyse coherent structures found in this particular network with a Morris-Lecar neuron (described in the next section). However, we note that a lot of the mathematical analysis we develop can readily be adopted for any other conductance-based neuron model that can be expressed in the same general form as eq. (6.1).

To make analytical progress, we will consider a directly spatially-extended continuous network, such that eq. (6.2) is transformed to

$$\begin{aligned}\partial_t v(x,t) &= f(v,z) + s(x,t)\\ \partial_t z(x,t) &= g(v,z)\\ \partial_t s(x,t) &= -\beta s(x,t) + w * (F \circ v),\end{aligned} \tag{6.3}$$

where

$$w * (F \circ v) = \int_{-\infty}^{\infty} w(x-y)F(v(y,t) - v_\mathrm{T})dy, \tag{6.4}$$

denotes a spatial convolution between the spike-detection function F at position y and the synaptic connectivity footprint of the network w. We note that under this set-up eq. (6.3) is spatially homogeneous and isotropic.

6.3 Single neuron Morris-Lecar

Now that we have described our method of constructing a network of synaptically connected generic conductance-based neurons, to make progress we must also decide which single neuron model to use. Modelling voltage dynamics at a single neuron level has a long tradition, initiated by the seminal work of Hodgkin and Huxley explaining the underlying excitable processes of the neuron in terms of ion

channels. As a result, an abundance of neuron models has been developed that take advantage of the precise neuronal mechanisms governing a neuron's voltage dynamics. These have been tested extensively with experimental data, and have shown to be in remarkable agreement with experimental recordings [99, 109].

In the literature a wide variety of conductance-based models of neurons have been derived from first principles. As mentioned before Hodgkin and Huxley supplied the first precise biophysical representation of a neuron voltage dynamics [99]. The model is made up of four coupled nonlinear differential equations, which for the most part is considered a hard problem to mathematically analyse at a network level, making it difficult to gain an intuitive understanding of the network dynamics [73]. In addition, more complex conductance-based models, appending extra ionic gating variables to the Hodgkin-Huxley neuron model have been introduced since, based on more advanced experimental methods that have shown that neurons possess a larger number of voltage-dependent conductances than that modelled by Hodgkin-and-Huxley [71, 109].

However, many studies have decided to reduce the Hodgkin-Huxley formulation to more mathematically amenable and conceptually simple models, while attempting to preserve many of its important dynamical features. Prominent examples of these models are typically named after their authors, for instance: FitzHugh [64], McCulloch and Pitts [136], Abbott and Kepler [1], Hopfield [100], Morris and Lecar [139]—to mention a few. We stress that neuronal models produced by these authors are reductions of the complex Hodgkin-Huxley model, but are still capable of drawing direct relations between quantities measured experimentally and the reduced model's parameters [100, 109]. Moreover, they are still capable of displaying complex nonlinear behaviour in their own right, including: generation of multiple limit cycles, coexistence and multi-stability of orbits with complex dynamical features, and chaotic behaviour. Notably, conductance-based models often feature a separation of time scales between the voltage variable (fast) and the gating variables (slow) [46]. Typical periodic orbits of single-neuron conductance-based models display a rapid increase from a base voltage level to a maximum voltage value, followed by a fast reset. These voltage time-profiles provide a biophysically realistic model of action potentials and neuronal spiking.

These features are an emergent feature of the models, as opposed to LIF neuron models, where the reset is taken to be instantaneous and the action potential mechanism is hardwired into the evolution equations.

We now introduce the Morris-Lecar neuron model, which we will use throughout this chapter. The choice is based on striking a compromise between mathematical tractability and biological relevance. The conductance-based model introduced by Morris and Lecar [139] in 1981 possesses several important neuronal features, which we will describe in this section. We should point out that our choice of model in many senses is not restrictive to the network level analysis that follows in later sections of this chapter. There are many other neuron models available that would supply qualitatively similar results, provided they have the same functional arrangement as eq. (6.1). The FitzHugh-Nagumo neuron model is a prominent example of one of these cases [64].

The Morris-Lecar model is a two-variable system first used to describe the voltage membrane potential of a giant barnacle muscle fibre [139]. It has been shown to display many of the key properties seen from in vivo and vitro experiments monitoring neuronal activity. One vital property is the ability to produce sharp non-linear depolarisation away from a resting state if a voltage threshold is reached—a key characteristic of an action potential. Another important property exhibited by the neuron is a transition from an excitatory to oscillatory state, marked by a region of bistability. It can also exhibit two of the main classes of neuronal excitability.

The simplest form of this model has three ionic currents: the voltage-sensitive inward Ca^{2+} current with instant activation facilitating excitation, a delayed voltage-dependent K^+ conductance for recovery, and a leakage current. These ionic currents all contribute to the voltage dynamics in the following way

$$C\frac{dv}{dt} = -g_{Ca}m_\infty(v - v_{Ca}) - g_K n(v - V_K) - g_L(v - v_L) + I, \tag{6.5}$$

$$\frac{dn}{dt} = (n_\infty(v) - n)/\tau(v), \tag{6.6}$$

where v is the voltage potential of the membrane with capacitance C and n is a recovery variable. The control parameter I represents an applied stimulus

or background current I_{app} for the neuron. This parameter is important in determining the neuron's dynamical state. In the network formulation we will take $I = I_{\text{app}} + I_{\text{syn}}$ where I_{syn} is the synaptic drive current received from other neurons in the network that are active.

The parameters g_{Ca}, g_K and g_L are maximal conductances terms and v_{Ca}, v_K and v_L represent the corresponding calcium, potassium and leak current resting potentials.

The calcium and leakage currents I_{Ca} and I_L typically act by depolarising the membrane. Whereas, the potassium current I_K is dependent on the recovery variable n and is responsible for the proceeding hyperpolarisation seen in an action potential. The recovery variable is the normalised K^+ ionic conductance, interpreted as the associated probability that a K^+ ion channel is in a conducting state.

The non-linear conductance probability functions $m_\infty(v)$ and $n_\infty(v)$ originate from the assumption that conducting and non-conducting ion channels in an equilibrium state have a Boltzmann distribution. Thus, their functional form is taken to be

$$m_\infty(v) = \frac{1}{2}\big(1 + \tanh\big[\frac{v - v_1}{v_2}\big]\big), \tag{6.7}$$

$$n_\infty(v) = \frac{1}{2}\big(1 + \tanh\big[\frac{v - v_3}{v_4}\big]\big). \tag{6.8}$$

The function $\tau(v)$ in eq. (6.6) is a voltage-dependent time constant, governing the potassium channels relaxation time in response to shifts in voltage away from equilibrium. Its functional form is

$$\tau(v) = \frac{\varphi}{\cosh[\frac{v - v_3}{2v_4}]}, \tag{6.9}$$

where the parameter φ is responsible for setting the speed of the recovery process and can vary widely depending on the type of cell and the temperature of the medium.

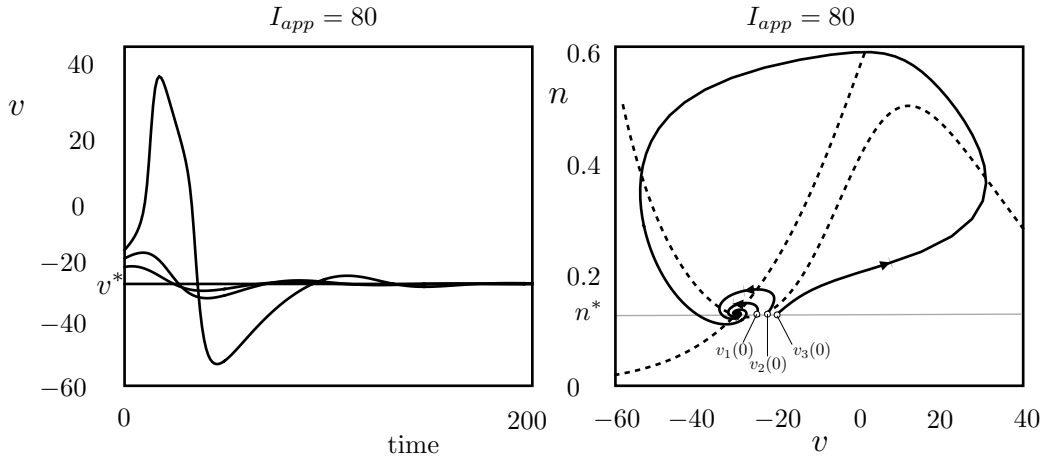


Figure 6.2 (a) Time course of a Morris-Lecar neuron's voltage $v(t)$ where it shown that a small perturbation from the resting state decays quickly back to rest, whereas a large perturbation leads to the generation of an action potential. (b) Phase plane of the voltage and recovery variable showing the trajectories during a sub-threshold and supra-threshold perturbation from the neurons steady-state.

6.3.1 Excitability

The Morris-Lecar neuron under the parameter regime listed in table 6.1 for $I_{\text{app}} < 88.35$ is in an excitable state—a key feature seen in most neurons. A neuron with a sufficiently small perturbation will simply decay back to its steady state value. However, if a perturbation is large enough and crosses a certain threshold value, the neuron will then generate an action potential. In fig. 6.2(a) we see two trajectories that are initialised suitably close to the neuron's rest state v^*, n^* and can be seen to quickly settle back to rest after some subthreshold decaying oscillations. The other trajectory depicts a much larger excursion from the rest state, whereby the initialised state is above threshold and therefore leads to the Morris-Lecar representation of an action potential.

The phase space of the two-dimensional Morris-Lecar system is the plane (v, n). Plotting the phase plane is a very useful way of understanding the nature of solutions. For clarity, we now rewrite eqs. (6.5) and (6.6) in the form used in eq. (6.1) to describe a generic conductance-based neuron model, with functions f

Parameters	φ	v_1	v_2	v_3	v_4	g_{Ca}	g_K	g_L	v_{Ca}	v_K	v_L	C
	0.04	-1.2	18	2	30	4.4	8	2	120	-84	-60	20

Table 6.1 Parameter values for the class II Morris-Lecar neuron with a subcritical Hopf bifurcation at $I_{app} = 93.8$ taken from [63].

and g, dependent on the voltage v and the recovery variable n, such that

$$\begin{aligned} \frac{dv}{dt} &= \frac{1}{C}\big[- g_{Ca} n_\infty (v - v_{Ca}) - g_K n (v - V_K) - g_L (v - v_L) + I_{\text{app}}\big] = f(v, n), \\ \frac{dn}{dt} &= (n_\infty(v) - n)/\tau(v) = g(v, n), \end{aligned} \tag{6.10}$$

noting that we have divided the voltage equation by C and made $I = I_{\text{app}}$. In fig. 6.2(b) the same three trajectories in (a) are shown on the (v, n) plane, the solution of eq. (6.10) at time t with the mth initial condition $(v_m(0), n^*)$ is the point on the plane $(v_m(t), n_m(t))$. The arrows mark how the solution changes in time.

Nullclines are a key ingredient associated with phase-plane analysis and an important tool to understand the behaviour of the solutions. They show the zero contour lines of the vector field. Hence, the v-nullcline is defined as $dv/dt = f(v, n) = 0$, illustrated by cubic shaped dashed line in fig. 6.2(b) and the n-nullcline is $dn/dt = g(v, n) = 0$ given by the monotonically increasing curve intersecting the v-nullcline at the equilibrium (v^*, n^*).

The nullclines split the phase plane into four separate regions or quadrants: $f > 0$, $g > 0$; $\quad f > 0$, $g < 0$; $\quad f < 0$, $g > 0$; $\quad f < 0$, $g < 0$. A single action potential passes through all four regions and eventually returns to the stable equilibrium point.

It is clear from fig. 6.2(b) that the voltage threshold v_T for firing a full action potential is in the interval $v_2(0) < v_T < v_3(0)$. The threshold can be ascertained by noting that if φ is small the three intersections made by the grey horizontal line through the equilibrium state, the middle and right branch of the cubic v-nullcline delineate regions where the vector field is pointing towards or away from the equilibrium point. For example, the initial point of a trajectory $(v_3(0), n_3(0))$ lies

to the right of the intersection made with the middle branch, below the v-nullcline where $dv/dt > 0$, such that the vector field points in a rightward direction and the voltage therefore increases in time, moving away from the equilibrium point and is attracted to the right branch of the v-nullcline.

The stability of the neuron model's fixed points (v^*, n^*) can be computed by calculating the Jacobian of the coupled system given by eq. (6.10), yielding the characteristic equation to solve for two eigenvalues:

$$P_{\text{ML}}(\lambda) = \begin{vmatrix} \partial_v f - \lambda & \partial_n f \\ \partial_v g & \partial_n g - \lambda \end{vmatrix} = 0. \tag{6.11}$$

If any of the corresponding eigenvalue solutions have negative real parts, the fixed point is said to be asymptotically stable. However, if there is at least one eigenvalue with positive real part—the fixed point is unstable.

6.3.2 Bistability and transition to oscillatory state

A key reason why the Morris-Lecar neuron model has been selected for this network is that it can exhibit an important neuro-computational property, whereby there is a coexistence between the neuron's resting and repetitive spiking state, known as 'intrinsic bistability'. Here a brief, appropriately timed current stimulus can switch the neuron's state from excitatory to oscillatory. The dynamical phenomenon was characterised by Rinzel in 1978 [160] who identified the bistable properties in a reduced two-variable Hodgkin-Huxley model, which explained dynamically the two stable potential states found in experimentation of the squid giant axon [176].

The parameter regime for the Morris-Lecar neuron in this study is chosen such that it includes a region of bistability similar to [160]. It is of interest to identify the influence bistability has on the dynamics of the propagating coherent structures found in a network consisting of Morris-Lecar neurons.

In the Morris-Lecar equations, the dynamical origin of the bistability is due to a sub-critical Hopf bifurcation, which gives rises to periodic orbits. In fig. 6.3, for $88.35 \leq I_{\text{app}} \leq 93.3$, the neuron is bistable because there exists both stable fixed point solutions and stable orbits. Periodic solutions or limit cycles of this form satisfy the condition $(v(t), n(t)) = (v(t+T), n(t+T))$ where T is a positive

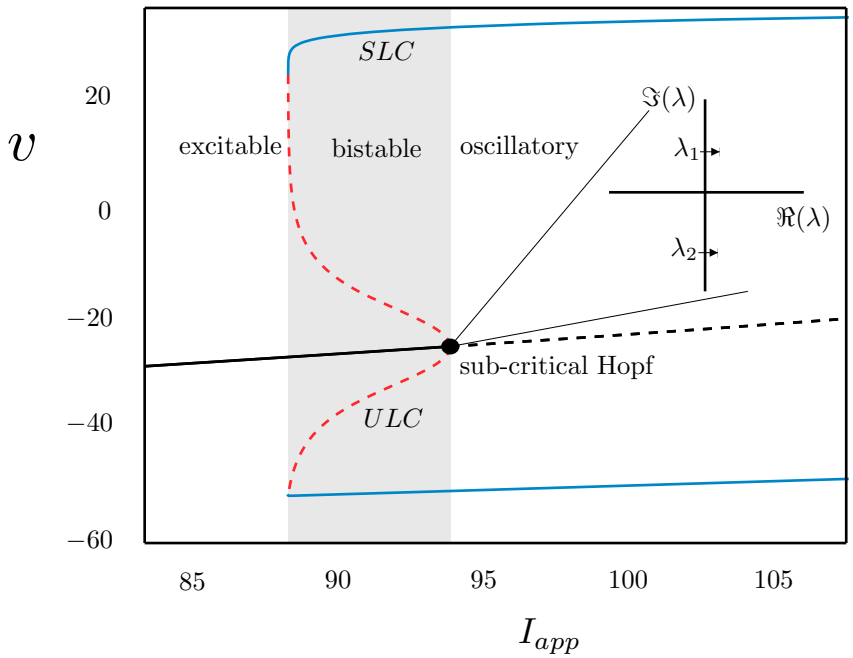


Figure 6.3 Bifurcation diagram depicting the neuron rest state as function of the stimulus current I_{app} and the stable and unstable non-zero frequency periodic orbits that emerge at $I_{\text{app}} \approx 88.35$, the subcritical Hopf bifurcation ends the bistable regime where the neuron can also be at rest. Parameters: see table 6.1

constant period. The bistable region is marked by two events: the first is at a critical $I_{\text{app}} = 88.35$, when a stable limit cycle (SLC) and the unstable limit cycle (ULC) come into existence At this point the amplitude of the SLC and ULC are the same. This marks the beginning of the bistable region. The second event is the sub-critical Hopf point at $I_{\text{app}} = 94.8$, where the ULC orbit disappears, after this the equilibrium point is unstable and the neuron is no longer bistable because the SLC is the only local attractor. This is a classic feature of a sub-critical Hopf bifurcation.

The sub-critical Hopf is characterised by eigenvalues crossing the imaginary axis from the left, taking on a positive real part. In fig. 6.3, the position of the Hopf is marked with an illustration of the eigenvalue crossing. The main part of fig. 6.3 depicts in black the fixed points for the neuron's voltage as I_{app} changes—dashed lines mean the solution is unstable. Also plotted is the maximum and minimum voltage values for the periodic solutions. As was explained previously, the bistable region is essentially defined by the existence of an unstable limit cycle solution. The phase-planes in fig. 6.4 show both the stable and unstable limit cycles at $I_{\text{app}} = 88.5$ and $I_{\text{app}} = 93$. We can see that if a neuron is initialised within the

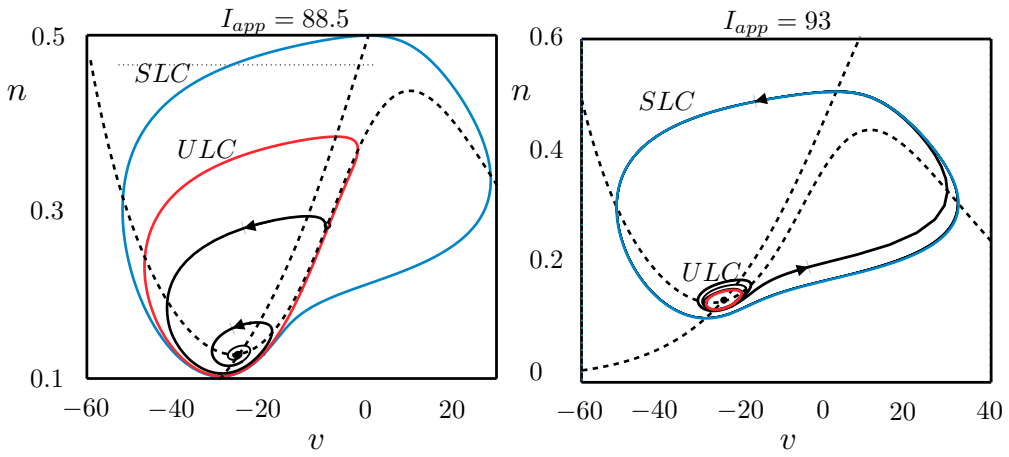


Figure 6.4 (a) Phase-planes depicting SLC and ULC orbits at $I_{\text{app}} = 88.5$ and the trajectory of a neuron initialised within the ULC domain. (b) Phase-planes depicting SLC and ULC orbits at $I_{\text{app}} = 93$ and the trajectory of a neuron initialised just outside the ULC domain.

region marked by the ULC the trajectory will be attracted to the stable fixed point and repelled by the ULC.

On the other hand, we see that for $I_{\text{app}} = 93$ the neuron is now initialised just outside the ULC orbit. In this case, the trajectory orbits around the ULC but increases in amplitude with every turn, eventually evolving to the SLC.

The sub-critical Hopf is one albeit common way a neuron can bifurcate from an excitable state to an oscillatory state. In this case there is a region of bistability marked by the sudden existence of a large amplitude periodic solution with a non-zero period. This is a typical feature displayed by class II neurons, which are usually associated to fast spiking neurons.

However, there are other ways a neuron can switch state, for instance, a saddle-node on a limit cycle (SNLC), which does not have a bistable region. Instead, limit cycles bifurcate locally to the fixed point and are stable. As a result, the neuron can have arbitrarily small frequencies, instead modelling a class I neuron.

6.4 Waves in Morris-Lecar network

We now present results obtained from direct numerical simulations of a discrete synaptically coupled network of Morris-Lecar neurons, in accordance with the system of N coupled ODEs given by eq. (6.2). The functions f and g embed the dynamics of the Morris-Lecar neuron as defined in eq. (6.10). We now write the

spatially extended continuous network as

$$\begin{aligned}\partial_t v(x,t) &= f(v,n) + s(x,t)\\ \partial_t n(x,t) &= g(v,n)\\ \partial_t s(x,t) &= -\beta s(x,t) + w * (F \circ v),\end{aligned} \tag{6.12}$$

taking a smooth sigmoidal form for the spike-detection function F, with the form

$$F(v) = \frac{1}{1+\exp(k(v-v_T))}, \tag{6.13}$$

where in the limit $k \to \infty$, F can be described as a Heaviside step function. Later we show that in this limit further analytical results can be obtained explicitly.

We note that if we choose w to be a simple exponentially decaying function $w(x) = a\exp(-b|x|)$, then both F and w have rational functions as their Fourier transforms. Hence, we can rewrite the integro-differential evolution equation for the synaptic current in eq. (6.12) as follows

$$\partial_t \hat{s}(k,t) = -\beta \hat{s}(k,t) + \hat{w}(k)\widehat{(F \circ v)}(k,t). \tag{6.14}$$

Now, with the knowledge that

$$\hat{w}(k) = \frac{2ab}{b^2+k^2}, \tag{6.15}$$

we can apply the convolution theorem and take the inverse Fourier transform to eq. (6.14) and arrive at

$$(b^2 - \partial_x^2)(\partial_t + \beta)s = 2abF(v). \tag{6.16}$$

This allows us to write eq. (6.12) as a PDE system which will be useful later

$$\begin{aligned}\partial_t v(x,t) &= f(v,n) + s(x,t)\\ \partial_t n(x,t) &= g(v,n)\\ (b^2 - \partial_x^2)(\partial_t + \beta)s &= 2abF(v).\end{aligned} \tag{6.17}$$

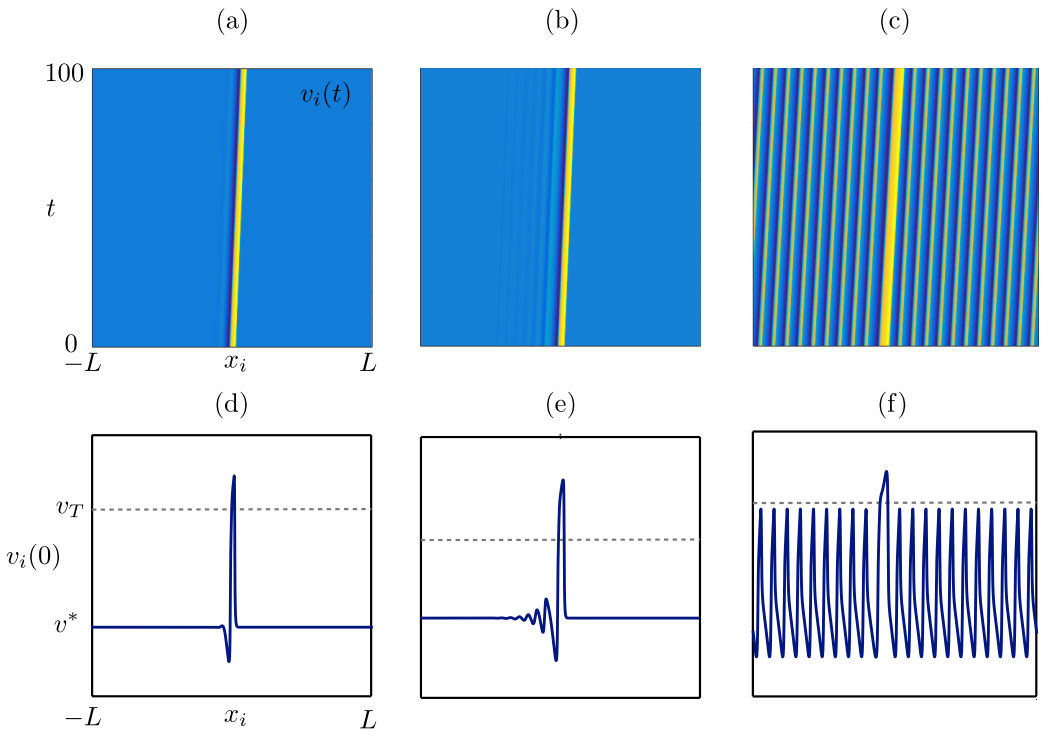


Figure 6.5 Key examples of single-spike waves found in network marking the Morris-Lecar neurons excitable, bistable and oscillatory parameter regime respectively, as illustrated in fig. 6.3. (a–c) Depict space-time voltage histories on a discrete spatial lattice with 2048 grid points and domain size $L = 250$ for (a) $I_{\text{app}} = 85$, (b) $I_{\text{app}} = 89$, (c) $I_{\text{app}} = 97$. (d–f): network waves voltage spatial profile. Neuron parameters are given in table 6.1 and network parameters: $a = 2, b = 2, k = 10, v_T = 35, \beta = 0.124$, with purely excitatory and exponentially decaying synaptic connectivity kernel $w(x) = a \exp(-b|x|)$.

The Morris-Lecar continuous network in its integro-differential form in eq. (6.12) is well approximated when the discrete network, given by eq. (6.2), is timestepped with a sufficiently large N. Similar to the LIF network, the system is posed on a ring of width $2L$, $\mathbb{S} = \mathbb{R}/2L\mathbb{Z}$ with neurons indexed using the set $\mathbb{N}_N = \{0, \ldots, N\}$ and occupying the discrete positions $x_i = -L + 2iL/N$, for $i \in \mathbb{N}_N$. The distance-dependent synaptic connectivity structure is, as before, bounded and even.

Travelling waves are obtained by initialising all neurons at their equilibrium state (v^*, n^*) and applying a brief excitatory stimulus to a localised region. The functional form of the stimulus is important in determining the number of spikes the waves elicits. We present in fig. 6.5 the three main forms of persistent single-spike waves at values of I_{app} that correspond to the Morris-Lecar neuron in its excitable, bistable and oscillatory regime (see fig. 6.3). In fig. 6.5(d) all neurons are in the excitable regime, with $I_{\text{app}} = 85$, here we see just one voltage peak in the pulses spatial profile, connecting back to the neurons equilibrium state v^*. This means that each neuron fires one action potential as the wave passes over it.

As I_{app} approaches the neuron's bistable regime, subthreshold voltage oscillations begin to develop. We see in fig. 6.5(e) the same sharp voltage peak in the wave's spatial profile, but now it is followed by a decaying oscillatory tail back to the neuron's equilibrium. We find that when $I_{\text{app}} \approx 89$ there is an abundance of travelling wave states with this same decaying tail feature, but with differing spatial decay rates, frequencies and amplitudes.

Further increasing I_{app}, moving into the neuron's oscillatory regime, we see that the suprathreshold pulse connects to a stable periodic orbit, this we believe is an artefact of posing the network on a ring, thus, may not occur on an infinite domain. Here our choice of voltage threshold v_T is greater than the maximum voltage value of the periodic orbits.No synaptic input is generated from these subthreshold voltage oscillations, because it is only the suprathreshold voltage peaks which is classed as an action potential capable of inducing synaptic input. Therefore, the wave in fig. 6.5(f) transmits a single pulse in a network of rhythmically oscillating neurons, which are phase-shifted in accordance with the pulse's wave speed.

Stellate cells in the entorhinal cortex have been shown experimentally to fire action potentials while also exhibiting subthreshold oscillations in voltage

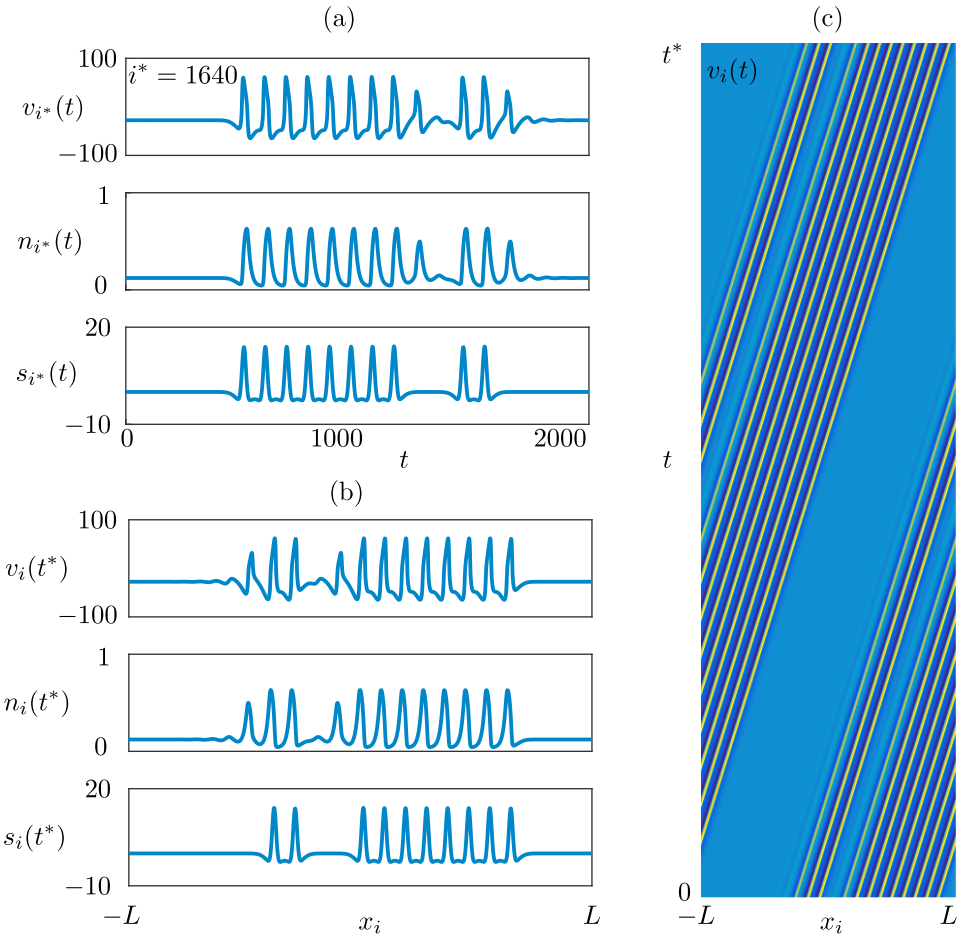


Figure 6.6 Example of multiple-spike wave in Morris-Lecar network with lateral-inhibition kernel. In this case a TW_8 has made a connection with a TW_2, forming a composite system reminiscent of that observed in the LIF network. (a) Temporal dynamics of variables (v, n, s) for neuron positioned at $x_{i^*} = -L/2$ on network as multiple-spike wave passes over. (b) Spatial profiles of (v, n, s) at time $t^* = 2000$. (c) Space-time history plot of voltage variable. Neuron's parameters are given in table 6.1, network parameters: $a_1 = 40, a_2 = 7, b_1 = 0.003, b_2 = 0.05, k = 10, v_T = 35, \beta = 0.8, N = 6560, L = 10\pi$. In this case the synaptic connectivity models lateral-inhibition, taking w to be a difference of two Gaussians, such that: $w(x) = \sum_{k=1}^{2}(-1)^{k-1} a_k \exp(-x^2/b_k)$.

potential [6]. These subthreshold oscillations at a network level have been classed as an effective mechanism for the detection and amplification of weak signals [174]. The oscillations predictably bias the open-time probability of a multitude of voltage-gated channels [127]. It is therefore seen as an energy-efficient solution for periodically elevating the voltage potential close to threshold, and thus providing discrete windows of opportunities in time for neurons to be activated with minimal input amplitude. This ensures the network is independent of incoherent background sensory signals, such that only appropriately timed input will induce a response from the network [103]. This phase biasing effect is a type of input selection mechanism, but in the case of the waves studied here, it could also be viewed as a more reliable mechanism for transmitting the suprathreshold pulse across the network, if compared to waves traversing through a network of excitable cells.

We also note from network simulations of eq. (6.12) that there is a qualitative increase in the directly measured wave speed as I_{app} increases. Interestingly, at the transition from the neurons excitable to bistable regime there is an apparent jump in the wave speed branch, this will be explored in detail later.

In fig. 6.5 we have chosen the synaptic connectivity to be purely excitatory with w modelled by a decaying exponential function. We will later perform a numerical study on the waves found with this particular connectivity structure due to its relative simplicity, allowing for more robust numerical results and concise analytical results. However, direct time simulations have confirmed that the Morris-Lecar network is able to support a large variety of persistent travelling waves under various synaptic connectivity schemes. For example, we see in fig. 6.6 a composite wave system composed of a TW_8 connected to a TW_2. In this case a Mexican hat function is used for the synaptic connectivity. Our findings have suggested that multiple-spike waves can be found in both purely excitatory and excitatory lateral-inhibitory networks. However, within the parameter set-ups we have studied, we find that connections between multiple-spike waves is more likely to form in the lateral-inhibition case.

To conclude, we have shown evidence that the Morris-Lecar network model is capable of producing localised and non-localised travelling wave structures across

a broad range of parameter values. Multiple-spike waves have been found, but, unlike the waves in the LIF network, the voltage spikes are not grouped within a single modulated synaptic envelope. Further study is needed to determine if multiple-spike waves like that seen in fig. 4.15 for the LIF network can be obtained. But, the fact that we have found persistent travelling wave structures that exhibit a broad range of dynamics gives reason to proceed in our analysis. However, we remind the reader that in this case, we do not have a precisely computable set of firing-time functions, which was the basis behind the analysis of waves in the LIF network. Hence, it is anticipated that different tools and techniques must be employed to make analytical and semi-analytical progress in analysing these particular travelling waves. As a result, we will need to adopt some aspects of standard travelling wave analysis in reaction-diffusion equations [28, 166] and neural field equations [18] to proceed. In passing, we stress that this model does indeed hold some structural similarities with neural field models. Although, it has not been derived based on population averaging theory assumptions, but rather from simple first principles, and thus keeping to similar spatio-temporal scales as the LIF network. Importantly, we find that information on the equilibria of a single Morris-Lecar neuron and its corresponding bifurcation structure heavily influences the network-level travelling waves dynamics. This is made clearer in the analysis of the travelling waves in the following sections.

6.5 Deriving a first-order system

We now seek to find travelling wave solutions to the Morris-Lecar network given by eq. (6.12). A general solution to eq. (6.12) is written as $u(x,t) = (v,n,s)(x,t)$. Solutions must travel with constant shape and velocity to be a travelling wave solution. Therefore, we rewrite eq. (6.12) in a frame of reference moving at a constant wave speed c

$$\begin{aligned} \partial_t v &= c\partial_\xi v + f(v,n) + s \\ \partial_t n &= c\partial_\xi n + g(v,n) \\ \partial_t s &= c\partial_\xi s - \beta s + w * (F \circ v), \end{aligned} \tag{6.18}$$

where a travelling wave is a stationary solution to eq. (6.18). To facilitate analysis we look for travelling wave solutions in the equivalent PDE formulation eq. (6.17) in the same co-moving reference frame, such that

$$\begin{aligned} -c\frac{\mathrm{d}v}{\mathrm{d}\xi} &= f(v,n) + s \\ -c\frac{\mathrm{d}n}{\mathrm{d}\xi} &= g(v,n) \\ (b^2 - \frac{\mathrm{d}^2}{\mathrm{d}\xi^2})(-c\frac{\mathrm{d}}{\mathrm{d}\xi} + \beta)s &= 2abF(v). \end{aligned} \tag{6.19}$$

To proceed further, we introduce new variables such that $u = (v, n, s, \frac{\mathrm{d}s}{\mathrm{d}\xi}, \frac{\mathrm{d}^2 s}{\mathrm{d}\xi^2}) = (v, n, s, q, r)$ and arrive at the equivalent first-order 5-dimensional ODE system:

$$\frac{\mathrm{d}u}{\mathrm{d}\xi} = \frac{1}{c}\begin{pmatrix} -f(v,n) - s \\ -g(v,n) \\ cq \\ cr \\ 2abF(v) - b^2\beta s + cb^2 q + \beta r \end{pmatrix} = G(u,c). \tag{6.20}$$

This formulation is useful in our analysis because the types of travelling waves we have found in section 6.4 corresponds to a variety of homoclinic connections. We want to study these connections, and can do this by studying the equilibrium of the spatial-dynamical system eq. (6.20). We also note that the first-order system can be solved numerically, which will be undertaken in section 6.7.

6.6 Necessary condition for homoclinic connections

Further progress can be made by first noticing that $u^* = (v^*, n^*, 0, 0, 0)$ is an equilibrium of eq. (6.20), where (v^*, n^*) is the Morris-Lecar neuron's resting state. Before seeking a homoclinic connection to this equilibrium, we derive a necessary condition for the existence of such a homoclinic connection to the fixed point at u^*.

We start by considering homogeneous perturbations around the time independent fixed points of the first-order system of ODEs in eq. (6.20), such that

$u(t) = u^* + \exp(\lambda t)\tilde{u}$. Evaluating the system's Jacobian matrix gives

$$\mathbf{M} = \begin{pmatrix} -\partial_v f/c & -\partial_n f/c & -1/c & 0 & 0 \\ -\partial_v g/c & -\partial_n g/c & 0 & 0 & 0 \\ 0 & 0 & 0 & 1 & 0 \\ 0 & 0 & 0 & 0 & 1 \\ 2ab\partial_v F/c & 0 & -b^2\beta/c & b^2 & \beta/c \end{pmatrix},$$

which is used to calculate the eigenvalue problem

$$\det(\mathbf{M} - \lambda\mathbf{I}) = 0. \tag{6.21}$$

In full, this is written as

$$\det(\mathbf{M} - \lambda\mathbf{I}) = \begin{vmatrix} -\partial_v f/c - \lambda & -\partial_n f/c & -1/c & 0 & 0 \\ -\partial_v g/c & -\partial_n g/c - \lambda & 0 & 0 & 0 \\ 0 & 0 & -\lambda & 1 & 0 \\ 0 & 0 & 0 & -\lambda & 1 \\ 2ab\partial_v F/c & 0 & -b^2\beta/c & b^2 & \beta/c - \lambda \end{vmatrix}$$

$$= - \begin{vmatrix} -\partial_v f/c - \lambda & -\partial_n f/c & -1/c & 0 \\ -\partial_v g/c & -\partial_n g/c - \lambda & 0 & 0 \\ 0 & 0 & -\lambda & 1 \\ 2ab\partial_v F/c & 0 & -b^2\beta/c & b^2 \end{vmatrix}$$

$$+(\beta/c - \lambda) \begin{vmatrix} -\partial_v f/c - \lambda & -\partial_n f/c & -1/c & 0 \\ -\partial_v g/c & -\partial_n g/c - \lambda & 0 & 0 \\ 0 & 0 & -\lambda & 1 \\ 0 & 0 & 0 & -\lambda \end{vmatrix},$$

and now simplifying further by calculating the 4 determinant terms above along the fourth column and last row respectively:

$$= b^2 \begin{vmatrix} -\partial_v f/c - \lambda & -\partial_n f/c & -1/c \\ -\partial_v g/c & -\partial_n g/c - \lambda & 0 \\ 0 & 0 & -\lambda \end{vmatrix} - \begin{vmatrix} -\partial_v f/c - \lambda & -\partial_n f/c & -1/c \\ -\partial_v g/c & -\partial_n g/c - \lambda & 0 \\ 2ab\partial_v F/c & 0 & -b^2\beta/c \end{vmatrix}$$

$$+\lambda(\beta/c - \lambda) \begin{vmatrix} -\partial_v f/c - \lambda & -\partial_n f/c & -1/c \\ -\partial_v g/c & -\partial_n g/c - \lambda & 0 \\ 0 & 0 & -\lambda \end{vmatrix}.$$

We now see that it is possible to factor out the characteristic polynomial of the **single Morris-Lecar neuron** scaled by the wave speed c

$$P_{\text{ML}}(\eta) = \begin{vmatrix} \partial_v f - \eta & \partial_n f \\ \partial_v g & \partial_n g - \eta \end{vmatrix},$$

hence,

$$P_{\text{network}}(\lambda) = P_{\text{ML}}(-c\lambda)\big[-b^2\lambda + \frac{b^2\beta}{c} - \lambda^2(\frac{\beta}{c} - \lambda)\big] + \frac{2ab}{c^2}\partial_v F(\partial_n g/c + \lambda). \quad (6.22)$$

We note that we are only considering voltages close to the equilibria at v^*, where by definition $v^* \ll v_T$. Therefore, if we take the limiting case, where the spike-detection function F is a Heaviside, eq. (6.22) can be simplified further, since $F = 0$ for $v \leq v_T$, such that $\partial_v F = 0$. As a result, eigenvalues associated to the steady state of eq. (6.20) satisfy the problem

$$P_{\text{network}}(\lambda) = P_{\text{ML}}(-c\lambda)(\beta/c - \lambda)(\lambda^2 - b^2) = 0. \quad (6.23)$$

Three eigenvalue solutions of eq. (6.23) can be directly inspected. We make two further observations: firstly, there is always a positive and negative eigenvalue $\pm b$ as a solution to $P_{\text{network}}(\lambda) = 0$, which suggests that a homoclinic connection to u^* can exist for all neuron parameter values, provided $b \neq 0$. Secondly, a powerful theorem in dynamical systems due to Shilnikov can now be easily applied [169]. The theorem implies that if eq. (6.20) possesses a homoclinic orbit with

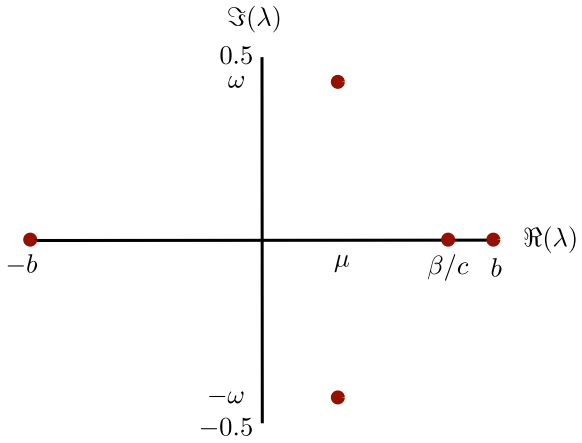


Figure 6.7 Eigenvalue solutions to the linearised system given by eq. (6.20) obtained by solving eq. (6.23) for a travelling wave solution with speed $c = 0.1542$, with network parameters: $a = 2$, $b = 1$, $k = 10$, $v_T = 35$, $\beta = 0.124$, $I_{\text{app}} = 64$. The conjugate pair of eigenvalues, $\mu \pm i\omega = 0.33 \pm 0.43i$.

speed $c = c^*$, and if the linearisation around its equilibria u^*, where a homoclinic connection is made, gives rise to a real eigenvalue γ, and a complex conjugate pair of eigenvalues, $\mu \pm i\omega$, with γ and μ having opposite signs, and also $0 < |\mu| < |\gamma|$, then there must exist an infinite number of periodic orbits for values of c near c^*. Moreover, the system is also expected to contain Smale-horseshoe dynamics [63]. If these conditions are satisfied we would therefore expect highly complex dynamical behaviour in the travelling wave solutions.

We test to see if the Shilnikov condition is met in the Morris-Lecar network by first numerically solving the first-order system eq. (6.20) to obtain the wave speed c. More details on the methodology for achieving this is given in the next section, but for now we assume it to be done and present in fig. 6.7 the eigenvalue solutions to the linearisation of eq. (6.20) satisfying $P_{\text{network}}(\lambda) = 0$. Here we see that there is indeed a complex conjugate pair with real part $\mu = 0.4$ and another real eigenvalue with opposite sign $\gamma = -1$, such that $0 < |\mu| < |\gamma|$. Hence, the Shilnikov condition is met and we should expect complex dynamical behaviour in travelling wave solutions supported within the network.

6.7 Travelling wave solutions bifurcation structure

Travelling wave solutions are numerically obtained by solving the two-point boundary value problem (BVP). In this study we use the AUTO continuation software package [50] to obtain bifurcation diagrams of the travelling wave solutions on a large but finite domain with periodic boundary conditions. This requires us to re-scale the spatial-dynamical first-order system of ODEs given by eq. (6.20), so that $\xi \in [0, 1)$ and then append a phase condition, which gives the following travelling wave problem to solve for (u, c):

$$\begin{aligned} \frac{1}{2L}\frac{\mathrm{d}u}{\mathrm{d}\xi} - G(u, c) &= 0 \\ u(0) - u(1) &= 0 \\ \Phi(u, u_{\mathrm{ref}}) &= 0 \end{aligned} \tag{6.24}$$

with the phase condition

$$\Phi(u, u_{\mathrm{ref}}) = \int_0^1 \frac{\mathrm{d}}{\mathrm{d}\xi}\left[u_{\mathrm{ref}}(\xi)(u(\xi) - u_{\mathrm{ref}}(\xi))\right] \mathrm{d}\xi, \tag{6.25}$$

minimising the L_2-distance from a reference function $u_{\mathrm{ref}}(\xi)$.

The AUTO continuation software package is well suited to numerically continue problem eq. (6.24) in the network's system parameters because of its adaptive mesh numeric capabilities and ability to pick up the waves states that are characterised by a homoclinic orbit connecting to a periodic state. We note that other continuation packages such as HomCont [29] are also capable of obtaining solutions for many of the waves found in the direct numerical simulations seen in section 6.4.

6.7.1 Wave speed dependence on I_{app}

We now present the results from the numerical continuation of the travelling wave solutions in the parameter I_{app}. In fig. 6.8 the wave speed is plotted as a function of I_{app}, where the Morris-Lecar neuron's excitable, bistable and oscillatory regions are shaded accordingly. We also depict the orbits of solution profiles $(v(\xi), n(\xi), s(\xi))$ in each of these regimes in fig. 6.8.

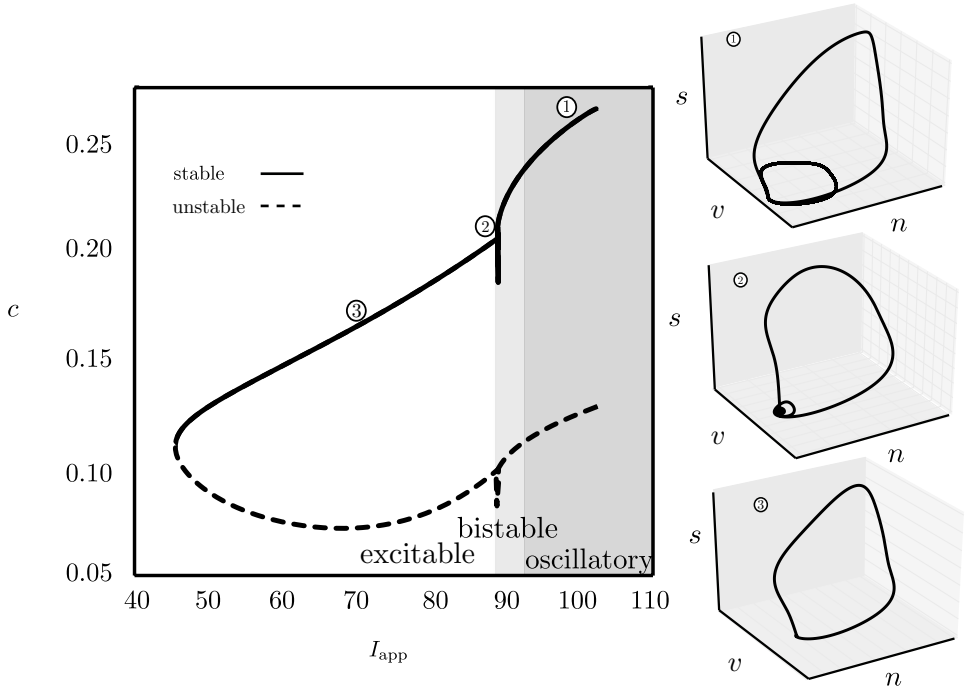


Figure 6.8 Bifurcation diagram showing how wave speed c changes with I_{app}. The solved solutions shown in fig. 6.3 are annotated accordingly on the diagram and presented as voltage profiles as a function of ξ. Network parameters: $(k, a, b, \beta) = (10, 2, 1, 1.1)$. Neuron parameters are unchanged (except I_{app}). Stability is probed by time-stepping for $T = 500$ and testing for transience.

It is known that the single neuron enters a bistable regime at $I_{\text{app}} = 88.35$. This transition from the neuron's excitable to bistable regime marks the onset of an interesting range of bifurcation structure in the travelling wave solutions, that is at the network level.

Prior to this transition we see in the excitable regime a stable fast branch of wave solutions with monotonically increasing wave speeds as I_{app} is increased. As is typical in similar network models exhibiting waves, we also find an unstable slow branch of solutions. The solid and dashed lines mark stable and unstable solutions respectively. Stability of the waves was probed by perturbing the solved solution profiles $(v(\xi), n(\xi), s(\xi))$ and performing direct numerical simulations to see if the wave persists. The solution profiles of the waves found in the excitable regime depict one single homoclinic orbit connecting to a fixed point saddle at the neuron's rest state (v^*, n^*, s^*). As mentioned before, when I_{app} approaches the neuron's bistable regime, $v(\xi)$ and $n(\xi)$ develop decaying oscillatory tails. The amplitude and number of these oscillations increase as I_{app} tends towards

the neuron's bistable region. This phenomenon is characteristic of a homoclinic connection to a saddle-focus.

We have verified that the waves exhibiting this feature are stable up until the sharp transition seen in fig. 6.8. The transition point actually takes place just within the neuron's bistable region at $I_{\text{app}} \approx 89$. Here we find a large set of unstable travelling wave solutions characterised by complex low amplitude subthreshold oscillations in $v(\xi)$ and $n(\xi)$. These complex solutions are anticipated after our analysis of the homoclinic connections in section 6.6.

We find that stable travelling waves resume shortly after the sharp transition in fig. 6.8, but now the homoclinic orbit is connected to a periodic state. These subthreshold periodic orbits seem to correspond to the periodic orbits of the Morris-Lecar neurons in both frequency and amplitude.

The L_2 norm $\|u\|$ is a solution measure which enables us to gain a better resolution of the bifurcation structure at the sharp transition. In fig. 6.9 a zoomed in perspective of the sharp transition is depicted for $\|u\|$ as a function of $I_{\text{app}} \in [89.05, 89.1]$. Here we see two slanted snaking ladders. The voltage profile at the bottom of the light blue snaking structure is a limiting case of the decaying oscillatory tail, with the tail now spanning the entire spatial domain. It depicts a homoclinic orbit connected to the neuron's unstable periodic orbit and a saddle-focus. We observe that at each turn of the snaking diagram, one of the unstable oscillations is promoted to the neuron's larger amplitude stable periodic orbit. This peak promotion process continues until all the unstable oscillations are replaced with stable oscillations (assuming L is finite), at which point the wave is stable. Hence, snaking is seen to be the mechanism by which the homoclinic to saddle-focus solutions connect to the homoclinic to (stable) periodic solutions.

Interestingly, the dark blue snaking structure in fig. 6.9 displays solutions that contain two suprathreshold pulses, whereby each neuron fires twice as the wave envelope passes over. The transition from homoclinic to periodic solutions to saddle-focus solutions (this time with two homoclinic orbits) via snaking remains the same. But, it can be inferred that beyond the sharp snaking structure at $I_{\text{app}} \approx 89$, there has been a switch to a double pulse state. The next section explores this phenomenon further.

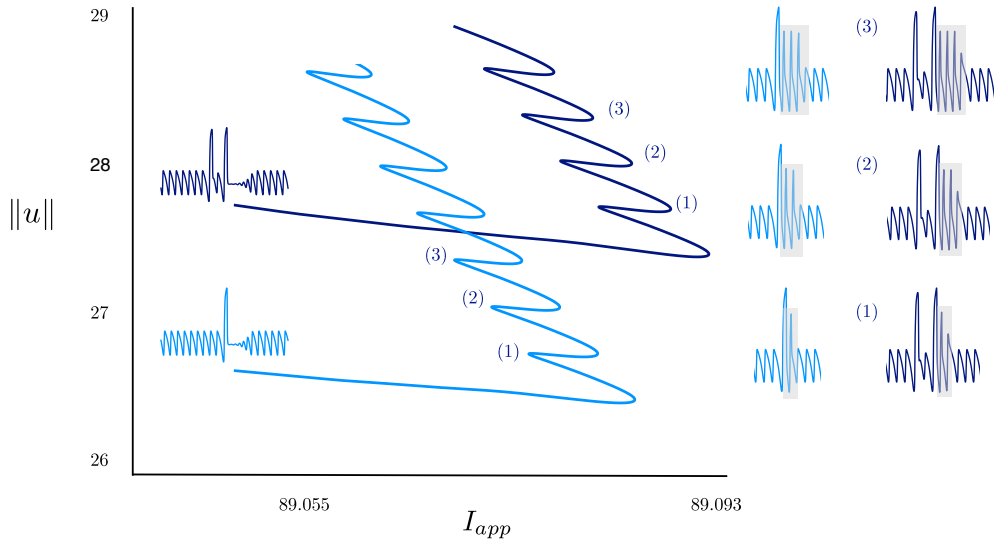


Figure 6.9 Left: Zoomed in perspective of continuation at sharp transition in fig. 6.8 using L_2 norm as the solution measure. We see that the snaking is slanted and we have found a double pulse branch as well, implying that there is a single to double pulse transition further along. Right: spatial voltage profiles showing smaller unstable periodic orbits connecting to stable periodic orbits for the single and double pulse branches. As you move up the slanted snaking ladder, at each turn, there is a bump promotion of the voltage solution from the smaller to larger periodic orbit.

6.7.2 Snaking connections to double pulse

In this section we investigate the connection the single pulse has with the double pulse. In fig. 6.10(a) we plot $\|u\|$ over a larger range of I_{app}, allowing us to visualise the entire snaking structures for the single and double pulse states. We also highlight the regions in the bifurcation diagram where a very large set of homoclinic to saddle-focus solutions are found which are reminiscent of the Shilnikov dynamics expected. All are characterised by a sudden drop in $\|u\|$, exemplified in fig. 6.10(b). The two near horizontal branches found at $33.0 \leq \|u\| \leq 33.8$ in fig. 6.10(a) contain the stable single and double pulse solutions connected to the neuron's stable periodic state. In fig. 6.10(d) we show a wider perspective of these two solution branches. On the lower branch we see single pulse to periodic solutions up until the sharp fold at $I_{\text{app}} \approx 115$. Near this sharp fold we observe the development of small oscillations in the network's synaptic activity $s(\xi)$. This is because the maximum voltage of the sub-threshold oscillations is now close enough to the voltage threshold, and thus, due to the smooth sigmoidal spike-detection function, small bumps of synaptic activity

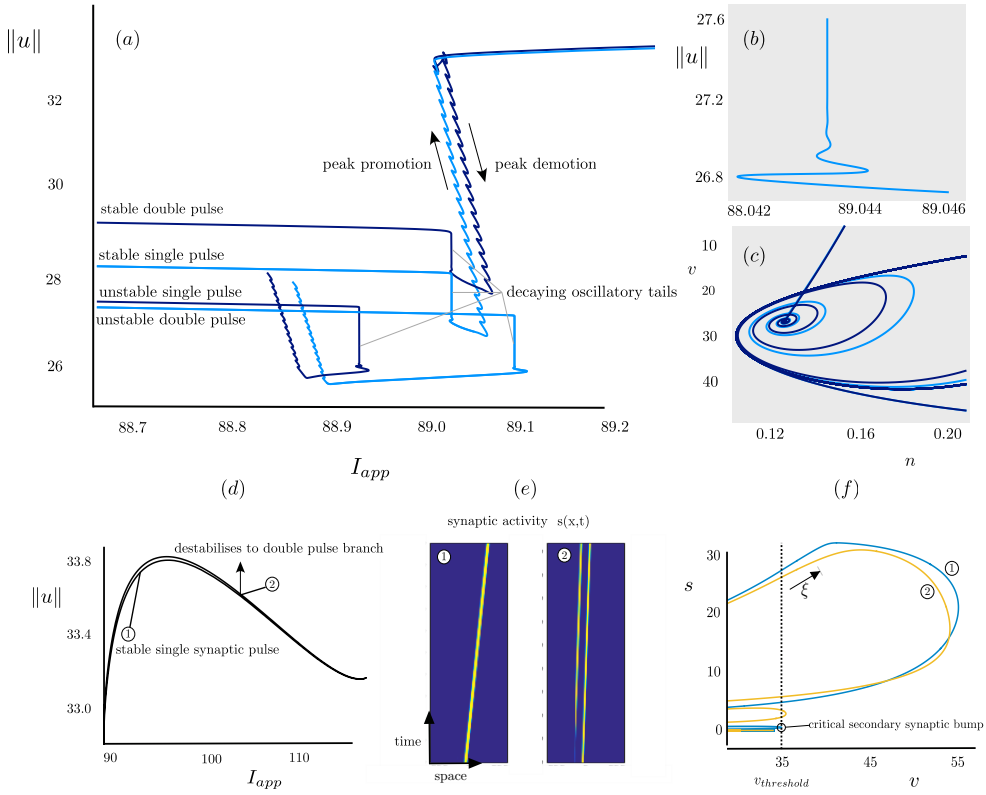


Figure 6.10 (a) bifurcation diagram containing single and double pulse branches (light and dark blue respectively), the highest branches contain a continuous transition to a double pulse solution. (b-c) example of Shilnikov dynamics showing two solution portraits around the saddle-focus point. (d) bifurcation diagram of pulse solutions in oscillatory medium with two solutions annotated to depict transition from single to double pulse. (e) time-histories of synaptic activity. (f) synaptic activity vs.voltage showing two low amplitude synaptic bumps exist, the synaptic bump in solution (2) is large enough to push the voltage activity in that spatial region above the voltage threshold v_T leading to a destabilisation to the double pulse state.

centred over the sub-threshold voltage peaks are observed. In fig. 6.10(f) we show two examples of these synaptic oscillations, corresponding to solutions annotated on fig. 6.10(d). It has been found from numerical simulation that the single pulse to periodic solutions on the lower branch in fig. 6.10(d) are stable, the amplitude of the synaptic oscillations is not sufficiently large to influence the dynamics. However, solutions on the upper branch all possess one secondary synaptic peak which causes the wave to destabilise into a double pulse solution—similar to the simulation in fig. 6.10(e). We note that the amplitude of the secondary synaptic peaks on the upper branch grow in amplitude as solutions get closer to the snaking structure at $I_{\text{app}} \approx 89$, where they eventually reach the same amplitude as the primary synaptic peak. At this point they become a stable double pulse solution connected to the neuron's stable periodic orbit. Therefore, the dark blue snaking structure connects these two different types of travelling wave solution with a double homoclinic loop.

As a final remark we point out that the periodic orbits are connected to each other on a ring, but this may not be true on an infinite domain. This will be a subject of future investigation possibly using Homcont, but for now we are satisfied with connections made between the periodic orbits of the Morris-Lecar neuron and the travelling waves in the network. It is important to emphasise the novelty of the results obtained in this section from this particular type of network construction. It has been made clear from the derivation of the necessary condition for homoclinic connections, and also the numerical analysis of bifurcation structure of the network's travelling wave solutions, that the dynamics of the individual neuron model is crucial to gaining a full understanding of the network-level dynamics.

6.8 Multi-point boundary value problem

The two-point BVP travelling wave problem presented so far is numerical, but we highlight that it is also possible to pose a multi-point BVP to construct travelling wave solutions. This treatment is interesting because it possesses certain

similarities with the spiking network model studied in the previous chapters, where we were able to form analytical solutions to the synaptic profile.

6.8.1 Construction of pulse in Heaviside limit

We now take the Heaviside limit of the Morris-Lecar network's sigmoidal spike-detection function F, such that $k \to \infty$. In this case, depending on whether the neuron's voltage is above or below threshold v_T, the neuron will fire maximally, or not at all. This simplification allows for the spatial convolution term in eq. (6.18) to be evaluated analytically. Hence, an expression for the single pulse's synaptic profile $s(\xi)$, which is dependent on the wave speed c and wave width Δ, can be obtained. We can then develop a multi-point BVP, which can be solved to construct the travelling pulse.

We start by applying the travelling wave transformation $\xi = x - ct$ to the system of partial differentials in eq. (6.18) and note that for $\xi < \xi_1$ or $\xi > \xi_2$ no neurons are firing, such that

$$-c\frac{\mathrm{d}v}{\mathrm{d}\xi} = f(v,n) + s \tag{6.26}$$

$$-c\frac{\mathrm{d}n}{\mathrm{d}\xi} = g(v,n) \tag{6.27}$$

$$-c\frac{\mathrm{d}s}{\mathrm{d}\xi} = -\beta s + \int_{\xi_1}^{\xi_2} w(\xi - y)dy, \tag{6.28}$$

where we define the wave width as $\Delta = \xi_2 - \xi_1$. Furthermore, without loss of generality we take $\xi_1 = 0$ and for readability we will define the integral above to be the function

$$\Psi(\xi, \Delta) = \int_0^{\Delta} w(\xi - y)\,\mathrm{d}y. \tag{6.29}$$

Now it is possible to solve eq. (6.28) to obtain a solution for the synaptic activity $s(\xi)$. Using integrating factors and applying the boundary conditions $\lim_{\xi\to\pm\infty} s(\xi) = 0$ gives

$$\int_{\xi}^{\infty} \frac{\mathrm{d}[s\exp(-\beta x/c)]}{\mathrm{d}x}\,\mathrm{d}x = -\frac{1}{c}\int_{\xi}^{\infty} \exp(-\beta x/c)\Psi(x,\Delta)\,\mathrm{d}x$$

$$-s(\xi)\exp(-\beta\xi/c) = -\frac{1}{c}\int_{\xi}^{\infty} \exp(-\beta x/c)\Psi(x,\Delta)\,\mathrm{d}x,$$

such that a functional expression for $s(\xi)$ which depends on the wave speed c and the wave width Δ has been obtained. For clarity, we define this function as $S(\xi, c, \Delta)$, where

$$S(\xi, c, \Delta) = \frac{\exp(\beta\xi/c)}{c} \int_{\xi}^{\infty} \exp(-\beta x/c)\Psi(x, \Delta)\, \mathrm{d}x. \tag{6.30}$$

In this case we use a more generic connectivity kernel that can also include lateral-inhibition, with the following functional form

$$w(x) = \sum_{k=1}^{2} (-1)^{k-1} a_k \exp(-b_k|x|). \tag{6.31}$$

We must split the integral appropriately ensuring $x - y > 0$ for all ξ. To achieve this the wave is split into three regions, such that:

$$S(\xi, c, \Delta) = S_{\mathrm{L}}(\xi, c, \Delta)1_{-\infty,0}(\xi) + S_{\mathrm{C}}(\xi, c, \Delta)1_{[0,\Delta)}(\xi) + S_{\mathrm{R}}(\xi, c, \Delta)1_{[\Delta,\infty)}(\xi) \tag{6.32}$$

where $1_A(\xi)$ is the indicator function for the interval A and

$$\begin{aligned} S_{\mathrm{R}}(\xi, c, \Delta) &= \frac{\exp(\beta\xi/c)}{c} \int_{\xi}^{\infty} \mathrm{d}x \exp(-\beta x/c) \int_{0}^{\Delta} \mathrm{d}y w(x - y) \\ &= \exp(\beta\xi/c) I_1(\xi), \end{aligned}$$

$$\begin{aligned} S_{\mathrm{C}}(\xi, c, \Delta) = \exp(\beta\xi/c)\big[& I_1(\Delta) + \frac{1}{c} \int_{\xi}^{\Delta} \mathrm{d}x \exp(-\beta x/c) \int_{0}^{x} \mathrm{d}y w(x - y) \\ & + \frac{1}{c} \int_{\xi}^{\Delta} \mathrm{d}x \exp(-\beta x/c) \int_{x}^{\Delta} \mathrm{d}y w(y - x)\big] \\ = \exp(\beta\xi/c)\big[& I_1(\Delta) + I_2(\xi) + I_3(\xi)\big], \end{aligned}$$

$$\begin{aligned} S_{\mathrm{L}}(\xi, c, \Delta) = \exp(\beta\xi/c)\big[& I_1(\Delta) + I_2(0) + I_3(0) \\ & + \frac{1}{c} \int_{\xi}^{0} \mathrm{d}x \exp(-\beta x/c) \int_{0}^{\Delta} \mathrm{d}y w(y - x)\big] \\ = \exp(\beta\xi/c)\big[& I_1(\Delta) + I_2(0) + I_3(0) + I_4(\xi)\big], \end{aligned}$$

with the analytical expressions for the four double integrals that construct $\sigma(\xi, c, \Delta)$ given as:

$$I_1(\xi) = \sum_{k=1}^{2}(-1)^{k-1}\frac{a_k e^{-\xi(b_k+\beta/c)}\left(e^{b_k\Delta}-1\right)}{b_k(\beta+b_k c)},$$

$$I_2(\xi) = \sum_{k=1}^{2}(-1)^{k-1}\frac{a_k}{b_k}\left(\frac{e^{-\Delta(\beta/c+b_k)}-e^{-\xi(b_k+\beta/c)}}{\beta+b_k c}+\frac{e^{-\beta\xi/c}-e^{-\beta\Delta/c}}{\beta}\right),$$

$$I_3(\xi) = -\sum_{k=1}^{2}(-1)^{k-1}\frac{a_k}{b_k}\left(\frac{-b_k c e^{-\beta\Delta/c}}{\beta(b_k c-\beta)}+\frac{e^{-b_k(\Delta-\xi)-\beta\xi/c}}{b_k c-\beta)}+\frac{e^{-\beta\xi/c}}{\beta}\right),$$

$$I_4(\xi) = -\sum_{k=1}^{2}(-1)^{k-1}\frac{a_k e^{-b_k\Delta}\left(e^{b_k\Delta}-1\right)\left(e^{(b_k-\beta/c)\xi}-1\right)}{b_k(b_k c-\beta)}.$$

In order to construct the wave we split the pulse into regions delineated by the two spatial points at $\xi = 0$ and $\xi = \Delta$, where the voltage solution is equivalent to the voltage threshold v_T. For a network with spatial domain $\xi \in [-L, L]$, the regions are taken to be

$$\xi^- \in [-L, 0), \quad \xi^0 \in [0, \Delta), \quad \xi^+ \in [\Delta, L).$$

However, it is more convenient to solve the regions in the dimensionless spatial variables x^{-1}, x^0, $x^+ \in [0, 1]$ by rescaling under the following transformations:

$$\xi^- = L(x^- - 1), \quad \xi^0 = \Delta x^0, \quad \xi^+ = (L-\Delta)x^+ + \Delta,$$

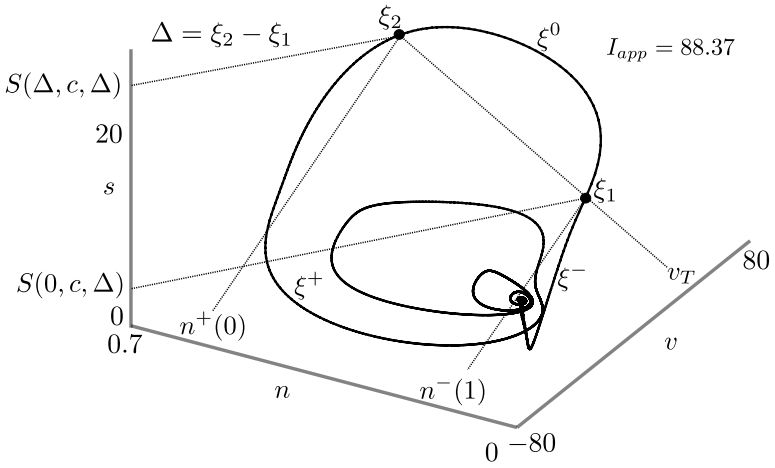


Figure 6.11 Phase plot of constructed single pulse with decaying oscillatory tail at $I_{\text{app}} = 88.37$ parametrised by: ξ^- - spanning from solution at $(v^*, n^*, 0)$ to $(v_T, n^-(1), S(0, c, \Delta))$, ξ^0 - from $(v_T, n^0(0), S(0, c, \Delta))$ to $(v_T, n^0(1), S(\Delta, c, \Delta))$ and ξ^+ - from $(v_T, n^+(0), S(\Delta, c, \Delta))$ to $(v^*, n^*, 0)$.

giving the full BVP problem to solve:

$$
\begin{aligned}
-c\,\mathrm{d}_\xi v^- &= L[f(\underline{v}^-, \underline{n}^-) + \sigma(\xi^-, c, \Delta)] \\
-c\,\mathrm{d}_\xi n^- &= Lg(\underline{v}^-, \underline{n}^-) \\
-c\,\mathrm{d}_\xi v^0 &= \Delta[f(\underline{v}^0, \underline{n}^0) + \sigma(\xi^0, c, \Delta)] \\
-c\,\mathrm{d}_\xi n^0 &= \Delta g(\underline{v}^0, \underline{n}^0) \\
-c\,\mathrm{d}_\xi v^+ &= (L - \Delta)[f(\underline{v}^+, \underline{n}^+) + \sigma(\xi^+, c, \Delta)] \\
-c\,\mathrm{d}_\xi n^+ &= (L - \Delta) g(\underline{v}^+, \underline{n}^+),
\end{aligned}
$$

with the following boundary conditions

$$
\begin{aligned}
v^-(0) - v^* &= 0 \\
n^-(0) - n^* &= 0 \\
v^0(0) - v^-(1) &= 0 \\
n^0(0) - n^-(1) &= 0 \\
v^+(0) - v^0(1) &= 0 \\
n^+(0) - n^0(1) &= 0
\end{aligned}
$$

and integral conditions:

$$c(h - v^*) + L \int_0^1 [f(v^-, n^-) + S(\xi^-, c, \Delta)\, \mathrm{d}x = 0$$
$$\int_0^1 [f(v^0, n^0) + S(\xi^0, c, \Delta)\, \mathrm{d}x = 0.$$

Finite difference methods can be used to compute this particular BVP. In fig. 6.11 we give a representation of such a solution.

6.9 Enhanced Morris-Lecar Network

To end this chapter we present preliminary data for a Morris-Lecar network model with an extra layer of complexity to the Morris-Lecar neuron model previously used in this chapter. In doing so, the neurons are capable of exhibiting a more complicated firing pattern than a single action potential response or periodic repetitive firing. This particular mode of firing is commonly referred to as 'bursting', and is characterised by a silent phase of near equilibrium resting dynamics followed by an active phase of multiple, rapid, spikelike oscillations. Bursting has been observed in numerous neuronal structures in the brain, for instance, the generation of respiratory rhythms within the pre-Botzinger complex and in certain thalamic cells involved in the generation of spindle waves observed during sleep.

This is because each spike corresponds to a loop in phase space and trajectories cannot cross each other in a two-dimensional phase plane. Hence, a minimal model for bursting must include at least three dependent variables.

Models for bursting usually involve multiple timescales with fast variables governing spike generation and slow variables controlling the slow modulation of a silent phase. Mathematical classifications of the numerous mechanisms behind bursting are usually framed in terms of geometric properties of the phase-space dynamics. Summarising these is beyond the scope of this thesis. Formal classification of bursting mechanisms have been given by Rinzel [161]. Instead, the central aim of this chapter is to ascertain whether coherent travelling wave structures can be supported in this particular spiking network construction, when

a neuron model capable of bursting is adopted. We note that Ermentrout states that a two-variable neuron model is not capable of supporting bursting [63]. He attributes this to the fact that one spike corresponds to a loop in phase-space, and in a two-dimensional phase plane the trajectories will not cross. Thus, the minimum number of dependent variables needed for bursting is three.

We therefore choose a three-variable Morris-Lecar neuron model in [63], which is capable of modelling three different types of bursting: square-wave, elliptic and parabolic, and incorporate this particular neuron model into our network framework to give:

$$\begin{aligned}
\partial_t v &= f(v,n) + s - \frac{g_{KCa}}{C}\frac{r}{r+\kappa}(v - v_K) \\
\partial_t n &= g(v,n) \\
\partial_t r &= \varepsilon h(v,r) \\
\partial_t s &= -\beta s + w * (F \circ v).
\end{aligned} \tag{6.33}$$

Here, a slow calcium concentration variable r is appended to the original two-variable Morris-Lecar neuron. No change has been made to the construction of the spiking network in terms of its synaptic dynamics—only the intrinsic neuron dynamics has been altered. This affects the voltage equation, which now includes a potassium-dependent calcium current formed by: a gating variable, modelled by a simplified Hill function in terms of the calcium concentration r; the voltage difference $(v - v_K)$; and g_{KCa}, denoting the currents maximal conductance. The slow-dynamics of the calcium concentration variable r is prescribed by the function h, with the form

$$h(v,r) = -\frac{1}{C}\Big[\mu g_{Ca} m_\infty(v)(v - v_{\mathrm{Ca}}) + k_{\mathrm{Ca}} r\Big], \tag{6.34}$$

noting that ε ensures the dynamics is slow for $\varepsilon \ll 1$. The parameter μ is simply used to convert current into a concentration flux term and k_{Ca} represents a calcium removal rate.

Parameters	v_T	β	κ	g_{KCa}	μ	g_{Ca}	C	ε	k_{Ca}
	15	0.5	10	0.25	0.2	4	20	0.003	1

Table 6.2 Parameter regime exhibiting persistent travelling wave states in spiking network of three-variable Morris-Lecar neurons eq. (6.33)

The network eq. (6.33) can easily be re-expressed as a system of 6 first-order equations and solved numerically in the same way as that seen in section 6.5. But first, wave solutions must be found from numerical simulations of eq. (6.33).

After exhaustive numerical simulation of the enhanced ML network in known parameter regimes obtained from [63] that are able to produce square-wave or elliptic bursters in the neuron dynamics, we have not managed to find any stable localised, or non-localised, travelling wave structures composed of neurons bursting that persist. We suspect from this investigation that stable localised waves with this type of neuron bursting is not observable in simulation, because the bursting in neurons is intrinsic and no changes in the level of synaptic activity can switch this process on or off. Instead it would require variations in the parameters of the neuron model itself to achieve this. As a result, we focus on a tailored parameter regime that we have found by trial and error to exhibit a rich repertoire of persistent coherent structures. Here the functions f and g in eq. (6.33) are identical in form with the two-variable ML neuron, with the same parameters values as in table 2.1 except for those listed in table 6.2. Some examples of travelling wave solutions in an excitable network regime are shown in fig. 6.13.

AUTO continuations of travelling waves with respect to I_{app} (fig. 6.12) have confirmed that the network still supports homoclinic to saddle travelling wave solutions similar to the ones observed in the network of two-variable Morris-Lecar neurons, see fig. 6.13(d). This is primarily because for $I_{\text{app}} < 89$ the neurons are in an excitatory state. Moreover, close to the Hopf at $I_{\text{app}} \approx 89$ the presence of the stable periodic orbits lead to a homoclinic to saddle-focus connection, see fig. 6.13(c). The stability is again probed by numerical simulation, with results suggesting the fast speed branch of solutions in fig. 6.12 for $I_{\text{app}} < 89$ is stable.

The bifurcation diagram in fig. 6.12 also depicts a series of unstable snaking branches emanating from the slow unstable branch. We observe from the spatial profiles of the corresponding wave solutions on these branches that each turn on

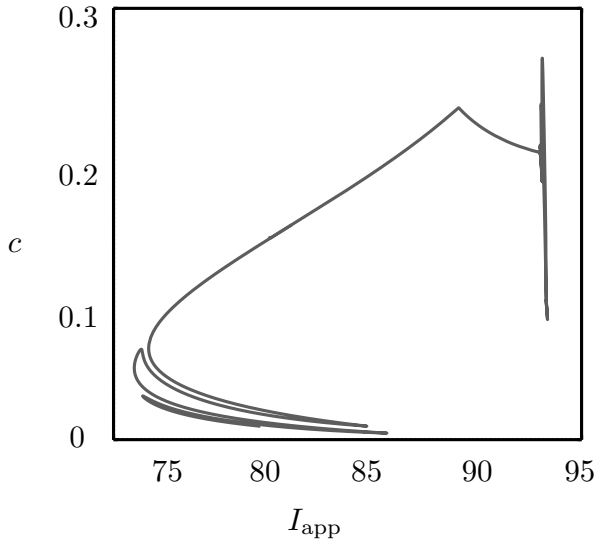


Figure 6.12 AUTO continuation of wave speed as a function of I_{app} for travelling wave solutions to eq. (6.33). Additional parameters are given in table 6.2, all other parameters are the same as in table 2.1. In this case, the stability properties of the solutions are not annotated.

this snaking structure yields an additional voltage spike. A key distinction between the double pulse waves found in the previous two-variable neuron model is that all the voltage spikes are attained within one modulated synaptic envelope—similar to the multiple-spike waves found in the LIF network. An example showing the spatial profiles of a three-spike wave solution found on one of the unstable snaking branches in fig. 6.12 is depicted in fig. 6.13(f). We also show its corresponding phase diagram in fig. 6.13(e) depicting the orbital trajectory of the fast variables, (v, n, s), parametrised by ξ. Here we see the homoclinic orbit departing the network's equilibrium and making three loops with $s > 0$, the system is clearly attracted to a periodic orbit, but we see that after each loop (or spike) the calcium concentration drops closer to its equilibrium state, where eventually the level of calcium cannot support spiking and the homoclinic orbit returns to the resting equilibrium state again.

Future work is needed to ascertain whether stable versions of this multiple-spike wave can be found. It is likely that varying the relative timescale between the fast and slow subsystem, or possibly modifying other network parameters such as the voltage threshold or the strengths of synaptic connectivity could lead to finding these stable waves. But in any case it is encouraging to find multiple-spike

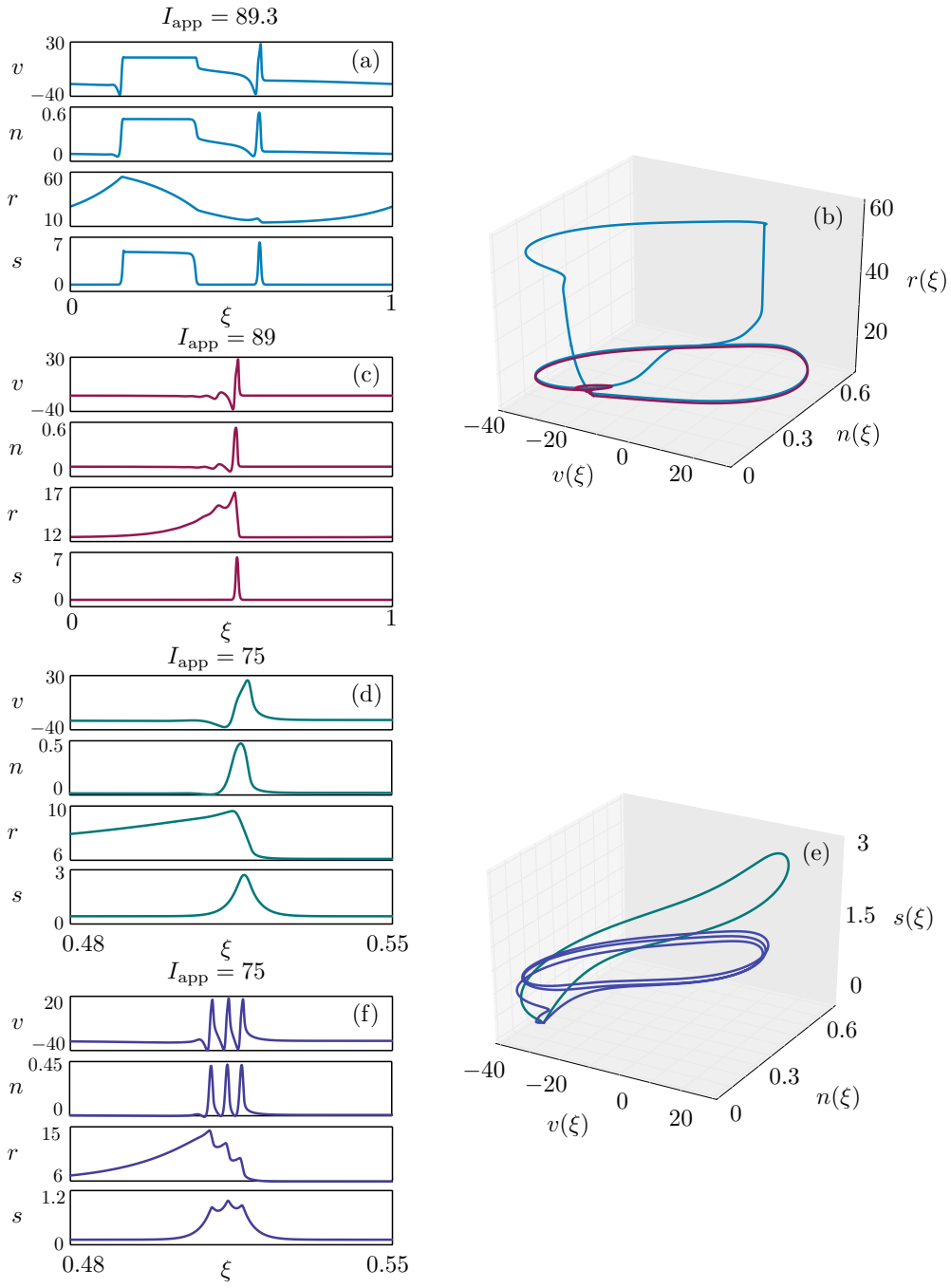


Figure 6.13 Spatial profiles and phase plots of travelling wave solutions to eq. (6.33). Additional parameters are given in table 6.2, all other parameters are the same as in table 2.1.

waves states in this network of biophysically realistic neurons with such close correspondence to the waves in the LIF network.

For $I_{\text{app}} > 89$ the network's equilibrium state becomes unstable and the homoclinic orbit makes connections to various unstable periodic orbits. We note that many of these states are an artefact of constructing the network on a finite domain with periodic boundary conditions. We therefore present only one example at $I_{\text{app}} = 89.3$ to highlight the type of connections that can be made to yield wave solutions. Thus, the spatial profiles given in fig. 6.13(a) show that the slow calcium concentration r variable has formed a non-localised periodic orbit across the entire spatial domain composed of one large amplitude peak, extending across the majority of the domain, and a small amplitude peak which appears as a spatial modulation in the overall r spatial profile.

In the phase orbits of (v, n, r) in fig. 6.13(b), the blue lines rising vertically out of the (v, n) plane mark the spatial region of the network where there is a shallow, positive gradient in the r profile—up until its maximum at $r \approx 57$. In this spatial region the fast variables are all close to their equilibrium states. However, once the maxima of the large peak in r is reached, there is a connection made to a hyperpolarised state in v, n and s. The system appears to have two steady states, with the connection between them happening over a narrow spatial region, which means the dynamics is fast. Now in the spatial regions where r slowly decreases from its maximum, the fast variables remain at this fixed hyperpolarised state. We note that in isolation the large peak in the r profile would represent a wave front solution, or heteroclinic orbit. However, in this case there is the connection made to a small amplitude peak in r, which leads to the onset of a typical single pulse state. It has been observed from simulations that the connection between the pulse and wave front is not stable, because the two structures appear to propagate at different speeds. Interestingly, the fact that this enhanced network can support structures with differing propagation speeds leads to some exotic coherent structures. For instance, in fig. 6.14 at $I_{\text{app}} = 150$ we have found spatially localised chevron shaped structures that oscillate in time—we refer to these as 'oscillons'. These structures are formed by the synchronous birth of travelling pulses at the chevron edges that propagate inwards towards

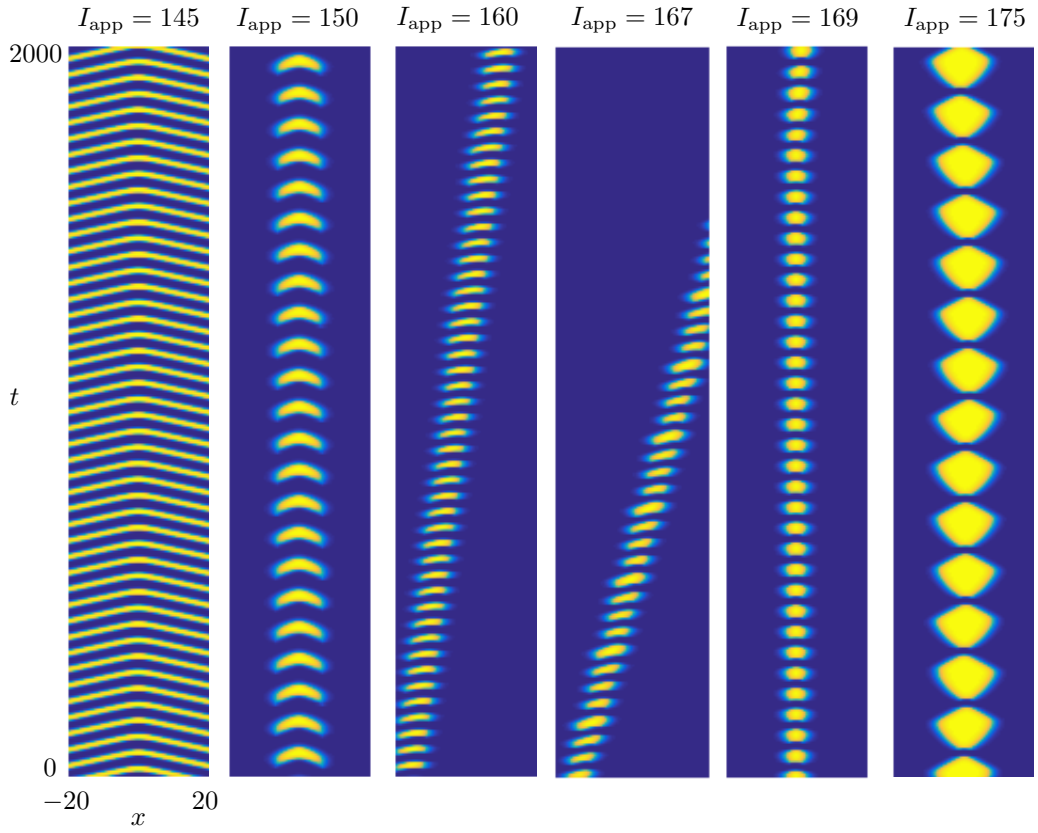


Figure 6.14 Space-time synaptic histories of stationary and propagating oscillon structures obtained from numerical simulations of eq. (6.33).

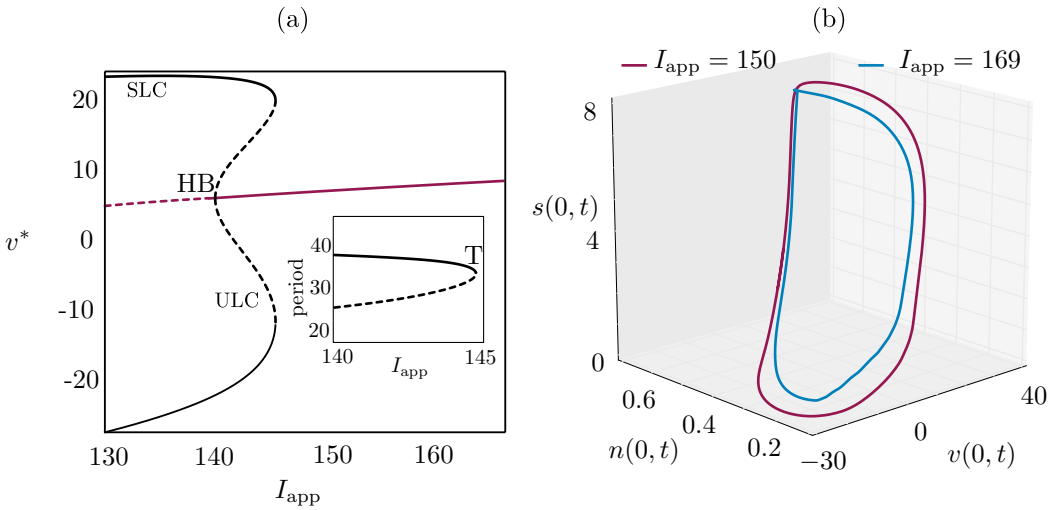


Figure 6.15 (a) Voltage steady states with max/min values of periodic orbits as a function of the applied current parameter I_{app}. The fixed points change stability at the Hopf point HB and a Takens-Boktanov point T marks the transition from unstable to stable periodic solutions. (b) One periodic orbit in (v, n, s) of neuron at $x = 0$ for the two oscillons illustrated in fig. 6.14 at I_{app} annotated. The time period of each orbit is approximately 36 time units with neglible variability as I_{app} changes.

the center and annihilate each other repeatedly. The frequency of the oscillon is related to the period of the neuron's stable limit cycle, which we can see from fig. 6.15(a) is nearby in parameter space.

Furthermore, the edges of the oscillons represent the same heteroclinic connection from the low to high states seen in fig. 6.13(b). These edges delineate a spatially localised region of low calcium concentration where the fast variables are in an active regime. Whereas, outside this localised structure the calcium concentration is high and the neurons are at an equilibrium. We find that decreasing I_{app} leads to the widening of the spatially localised region, eventually the entire network is formed of oscillating neurons. This is expected when considering the region of bistability in the neurons bifurcation diagram in fig. 6.15(a).

An unexplained phenomenon, which warrants further study, is the breaking of symmetry of the oscillon structure at $I_{\text{app}} \approx 160$ leading to the oscillon propagating left or right. Simulations of the synaptic history in $160 \leq I_{\text{app}} \leq 167$ suggest there is a relationship between I_{app} and the propagation speed of the new structure. Moreover, we see that increasing I_{app} also leads to an increasingly complex sequence of oscillations contained within one period of the oscillon. Curiously, for $I_{\text{app}} > 169$ the oscillons display a wide variety of internal dynamics but do not propagate and remain spatially-localised. More advanced techniques are required in order to properly analyse the dynamics of the oscillon structures beyond numerical simulations. It is likely that fast-slow analysis could be of benefit, also, capturing the dynamics of the heteroclinic wave front solutions may be useful in further understanding these structures.

6.10 Summary

To summarise, we have constructed a synaptically coupled neural network composed of a biophysically relevant Morris-Lecar neurons in a fast spiking parameter regime. The formulation of this network was based upon the structural properties within the leaky integrate-and-fire network studied in the previous chapters, and as a result, is on a similar spatio-temporal scale.

A necessary condition for the existence of the various homoclinic connections observed in these travelling wave solutions has been derived, where the characteristic polynomial for the Morris-Lecar single neuron, scaled by the wave speed c, is found to be a factor.

Travelling wave solutions have been solved numerically and continued in parameter space. In doing so, we have analysed how transitioning from the neuron's excitable, bistable and oscillatory dynamical regimes affects the bifurcation structure of the travelling waves. In addition, we have found that homoclinic to saddle and saddle-focus solutions, observed in the neuron's excitable regime, make a sharp transition via a snaking structure, to a homoclinic orbit connected to subthreshold periodic orbits, which correspond to the Morris-Lecar neuron's stable periodic orbits. We have also found a continuous connection to a double pulse state.

Also, in the Heaviside limit we have outlined a multi-point boundary value problem that can be solved to construct the travelling pulses explicitly and ascertain the waves speed and width.

Finally, a brief study of a network of an enhanced three-variable Morris-Lecar neurons have found multiple-spike wave solutions with similar properties to the TW_m states in the integrate-and-fire network. In addition, the network is seen to exhibit a variety of interesting mechanism, such as spatially localised patches of oscillatory activity surrounded by resting neurons known as oscillons. These have been shown to break symmetry and propagate.

Chapter 7

Conclusions and Future Directions

7.1 Conclusions

In this thesis we have developed a method to analyse multiple-spike wave solutions found in a spatially-extended network of synaptically-connected, excitatory leaky integrate-and-fire neurons. Direct numerical simulations have shown that the network supports a rich repertoire of localised coherent structures, including: stationary bumps, wandering bumps, drifting bumps, multiple bumps and the large family of coexistent multiple-spike waves and composite wave states we have been primarily interested in.

We have developed a method of analysing the bifurcation structure and stability of these multiple-spike wave structures, which has not been achieved to date. Most of the analysis to date focussed on the dynamics of the single-spike case.

This mathematical framework developed has enabled a concise and efficient method of constructing waves with a finite number of spikes m, where a set of firing-time functions has been linked directly to the wave solutions in the continuum model. These are easily obtained by solving numerically for the wave speed and spike-time intervals, with results from simulations providing an initial guess to the travelling wave problem. The exact voltage and spatial profiles can also be constructed from these numerically solved macroscopic variables. Furthermore, the existence and stability can be framed in terms of these firing-time functions, leading to an eigenvalue problem which can be numerically solved.

Our novel stability approach has allowed us to show that multiple-spike waves destabilise via a sequence of Hopf bifurcations when the synaptic efficacy parameter

is sufficiently fast. This is not observed in the single-spike wave stability dynamics, unless large axonal delays are included. The corresponding delayed non-smooth ODEs have, however, a very different mathematical structure with respect to the ones analysed in our network. We have also found non-smooth grazing bifurcations that provide a condition for onset of these wave states.

The analysis is suitably general to allow for the various modifications to the network to be made. We have performed a numerical bifurcation study to elucidate how changes in the synaptic connectivity structure, from lateral-inhibition to purely excitatory, affects the dynamics of the waves. We have also shown that more biophysically relevant postsynaptic responses yielded similar qualitative results, provided the rise-time is sufficiently fast. We have conducted an exhaustive parameter space study and found that the mechanisms outlined above are generic in this model.

An important finding has suggested that as the number of threshold crossings $m \to \infty$, the wave's speed tends to zero and the wave's width tends to a constant value. Additionally, by solving for a wave with $m = 150$ threshold crossings, we have shown that the firing rate profile matches up closely to the firing rate profile of statistically stationary bump solutions found in the discrete network. This poses certain questions relating to the existence of stationary bump solutions for spiking networks in the continuum limit.

We have also taken advantage of the now known functional relationship between the multiple-spike wave's output variables and the network's system parameters. This has enabled us to assess how the statistical properties of the wave speed and spike-times is affected by uncertainty for a number of the network's system parameters. These results were been verified with Monte-Carlo simulations. The knowledge of the wave's bifurcation points has allowed for the complete evaluation of the TW_m state's expectation and standard deviation across its entire region of stability. We have noted that with sufficiently large levels of parameter variability, the bifurcation points have a significant impact on the expectation values, when compared to the bifurcation diagrams where there is no input uncertainty.

The final part of this thesis, we constructed a network with similar structural properties to the LIF network, designed to still take into account the individual

neuron's spiking dynamics. This network is designed for conductance-based neurons with more biophysically realistic interpretations than the LIF network. The Morris-Lecar neuron was used as a test bed for this type of network, where we were able to find a variety of travelling wave solutions. A necessary condition for the existence of homoclinic connections for travelling wave solutions has been derived, where the characteristic polynomial for the Morris-Lecar single neuron, scaled by the wave speed c can be factored out. It was found that the dynamics of the travelling wave state was highly dependent on the individual neuron dynamics. In particular, we found that homoclinic to saddle and saddle-focus solutions observed in the neuron's excitable regime, make a sharp transition via a snaking structure, to a homoclinic orbit connected to sub-threshold periodic orbits, which correspond to the Morris-Lecar neuron's stable periodic orbits.

7.2 Future directions

In the preliminary study of the Morris-Lecar network, we analysed the spectrum of the steady states in homoclinic connections of waves and we numerically solved a two-point boundary value problem to find a variety of travelling wave solutions. This did allow us to give a good understanding of the important relationship the individual neuron dynamics had on the bifurcation structure of the waves. But the stability of these waves was not formally proved. Instead, we relied on probing stability via numerical simulation. Some preliminary work has been developed where we have constructed an Evans function to study temporal stability of the travelling waves. A numerically stable technique of computing the Evans function, giving meaningful interpretations of the resulting eigenspectra will be the subject of future work.

Our study of the enhanced Morris-Lecar network (with three-variable Morris-Lecar neurons) has also led to some interesting possibilities for future investigations. One possible direction could be to continue trying to find persistent waves in this spiking network which are composed of neurons undergoing bursting activity, or alternatively, adapting the network framework in some way to capture these states. Another, possibility could be to find stable versions of the multiple-spike

wave solutions and compare the dynamics with the analogous waves in the LIF network.

Regarding the oscillon structures, a numerical problem to solve for stationary oscillon solutions was devised, which in principle would have allowed for the continuation of the oscillons in parameter space. In the future, we should improve the convergence properties of this complex numerical scheme. One approch could be to use tools from bifurcation analysis for timesteppers, where it has been shown that the implicit linear step from a timestepping code can be used as an effective preconditioner for solving complex linear systems involving the full Jacobian conjugate gradient iteration [184]. The completion of this work could possibly elucidate much more about the oscillon's dynamics more accurately than numerical simulation. In addition, we envisage that another approach will be needed to study the propagation of the oscillons. Fast-slow analysis could provide some headway into understanding the mechanism for propagation, as well as studying the bifurcation structure of the wave front solutions which define the boundaries of the oscillon structure.

Moving back to the LIF network, we note that, in principle, the analysis of the multiple-spike waves on the one-dimensional continuum can be extended to the two-dimensional plane. Kistler *et al* have analysed plane waves and solitary waves in a two-dimensional system of LIF neurons by adopting a so-called spike response model [112]. However, their stability analysis only considered perturbations to the local field potentials, which is said to be not sufficient to guarantee asymptotic stability with respect to more generalised perturbations in the wave's firing times [19].

It would be of interest in future studies to develop an efficient method of simulating the two-dimensional integrate-and-fire network and find the equivalent two-dimensional coherent structures corresponding to multiple-spike waves in one dimension. Then it would be interesting to verify that the stability analysis developed in chapter 3 can be adapted to analyse the bifurcation properties of these two-dimensional structures, where, unlike Kistler [112], we will be using general perturbations in the firing times to obtain the full spectrum of the linearised firing

time map. This has been shown to be crucial in establishing the occurrence of Hopf bifurcations [19].

It has been observed that bumps in two-dimensions can destabilise in response to angular perturbation terms [78, 148]. It should be noted that radially-symmetric waves can already be studied with the framework we propose, without modifications. The stability of these solutions with respect to azimuthal perturbations is also possible with minor amendments of our method.

There are a few problems that are needed to be resolved in order to successfully make a conversion of 1D LIF network analysis to 2D. One would be finding an appropriate functional form for the set of firing-time functions that must describe the entire space-time firing history of a persistent 2D coherent structure found via numerical simulation. This should ideally be extendable to a large family of coexistent states (if it exists). Another factor, which is related to the choice of the firing time functions, is identifying the macroscopic variables that need to be solved to fully define the wave solution, and then also how these can be solved. It is likely that finding analytical expressions for the voltage and synaptic profiles, in the same way as that done in this study for the 1D network, will be hugely beneficial. Otherwise, numerical techniques will need to be used to evaluate a series of non-linear integrals, which will have repercussions on the efficiency of the construction of the wave's profiles, which is a significant challenge in itself, because it involves finding the appropriate domains of integration in 2D, which may not be as intuitive as the one-dimensional case.

If a routine that solves the macroscopic variables that fully characterise the coherent structure is found, the next step in testing the stability analysis for two-dimensional waves is finding an appropriate type of perturbation. Therefore, the stability analysis must also be capable of capturing a generic 2D perturbation. Determining which perturbations are most relevant to the destabilisation and making simplifying assumptions may be needed. Overall, extending our multiple-spike wave analysis to similar wave structures on the plane is, we believe, possible in principle, but it could face a variety practical issues in implementation.

A slightly less challenging adaptation to the multiple-spike wave analysis could be extending it to the two-layered one-dimensional network, consisting of a

population of excitatory and inhibitory neurons [83]. Again, only the analysis of single-spike waves has been achieved to date, which proceeds upon very similar lines to the standard one-layer model [13]. Therefore, it is expected that the analysis developed in this thesis to multiple-spike waves can be easily ported. It is likely that this two-layered model will yield more complicated wave structures, with a large family of spike-time interval distributions. However, our study of composite wave systems has demonstrated that our framework is robust to these type of structures.

A major result in this thesis has been uncovering that stationary bump solutions on the continuum appear to actually be multiple-spike waves with a large number of threshold crossing events m, propagating at near zero wave speeds. It would be of interest to prove this is true by investigating the wave solutions in the limit $m \to \infty$. This is not a trivial problem and likely needs different mathematical approaches to those used in this thesis.

Some other directions could involve finding the same multiple-spike waves in a one dimensional network of quadratic integrate-and-fire neurons. This model still involves just one voltage equation, but the dynamics of the neuron is non-linear. Therefore, it is difficult to generate analytical results. However, recent work using the Ott and Antonsen ansatz [146, 147] has been applied to continuum-limit networks of QIF neurons [118, 119, 129]. It would be interesting to find a way to mathematically analyse multiple-spike waves in QIF networks to the same level of detail as the LIF network studied here. In such a way, a comparison between the two models can be performed which can provide a more qualified interpretation of multiple-spike wave dynamics.

Bibliography

[1] Abbott, L. and Kepler, T. B. (1990). Model neurons: from hodgkin-huxley to hopfield. In *Statistical mechanics of neural networks*, pages 5–18. Springer.

[2] Abeles, M., Bergman, H., Margalit, E., and Vaadia, E. (1993). Spatiotemporal firing patterns in the frontal cortex of behaving monkeys. *Journal of neurophysiology*, 70(4):1629–1638.

[3] Aertsen, A., Gerstein, G., Habib, M., and Palm, G. (1989). Dynamics of neuronal firing correlation: modulation of "effective connectivity". *Journal of neurophysiology*, 61(5):900–917.

[4] Alexander, D. M., Jurica, P., Trengove, C., Nikolaev, A. R., Gepshtein, S., Zvyagintsev, M., Mathiak, K., Schulze-Bonhage, A., Ruescher, J., Ball, T., et al. (2013). Traveling waves and trial averaging: the nature of single-trial and averaged brain responses in large-scale cortical signals. *Neuroimage*, 73:95–112.

[5] Alexander, D. M., Trengove, C., and van Leeuwen, C. (2015). Donders is dead: cortical traveling waves and the limits of mental chronometry in cognitive neuroscience. *Cognitive processing*, 16(4):365–375.

[6] Alonso, A. and Llinás, R. R. (1989). Subthreshold na+-dependent theta-like rhythmicity in stellate cells of entorhinal cortex layer ii. *Nature*, 342(6246):175–177.

[7] Amari, S.-i. (1977). Dynamics of pattern formation in lateral-inhibition type neural fields. *Biological cybernetics*, 27(2):77–87.

[8] Aronson, D. G., Ermentrout, G. B., and Kopell, N. (1990). Amplitude response of coupled oscillators. *Physica D: Nonlinear Phenomena*, 41(3):403–449.

[9] Avitabile, D. and Schmidt, H. (2015). Snakes and ladders in an inhomogeneous neural field model. *Physica D: Nonlinear Phenomena*, 294:24–36.

[10] Bellman, R. (2003). *Dynamic Programming*. Dover Books on Computer Science Series. Dover Publications.

[11] Benucci, A., Frazor, R. A., and Carandini, M. (2007). Standing waves and traveling waves distinguish two circuits in visual cortex. *Neuron*, 55(1):103–117.

[12] Boonstra, T. W., Daffertshofer, A., Breakspear, M., and Beek, P. J. (2007). Multivariate time–frequency analysis of electromagnetic brain activity during bimanual motor learning. *Neuroimage*, 36(2):370–377.

[13] Bressloff, P. (1999). Synaptically Generated Wave Propagation in Excitable Neural Media. *Physical Review Letters*, 82(14):2979–2982.

[14] Bressloff, P. and Coombes, S. (1999a). Symmetry and phase-locking in a ring of pulse-coupled oscillators with distributed delays. *Physica D: Nonlinear Phenomena*, 126(1):99–122.

[15] Bressloff, P. and Coombes, S. (1999b). Travelling waves in chains of pulse-coupled integrate-and-fire oscillators with distributed delays. *Physica D: Nonlinear Phenomena*, 130(3-4):232–254.

[16] Bressloff, P. C. (2000). Traveling waves and pulses in a one-dimensional network of excitable integrate-and-fire neurons. *J. Math. Biol.*, 40(2):169–98.

[17] Bressloff, P. C. (2001). Traveling fronts and wave propagation failure in an inhomogeneous neural network. *Physica D: Nonlinear Phenomena*, 155(1):83–100.

[18] Bressloff, P. C. (2011). Spatiotemporal dynamics of continuum neural fields. *Journal of Physics A: Mathematical and Theoretical*, 45(3):033001.

[19] Bressloff, P. C. (2014a). Waves in neural media. *Lecture Notes on Mathematical Modelling in the Life Sciences*.

[20] Bressloff, P. C. (2014b). *Waves in Neural Media*. Lecture Notes on Mathematical Modelling in the Life Sciences. Springer New York, New York, NY.

[21] Bressloff, P. C. and Coombes, S. (2000). Dynamics of strongly-coupled spiking neurons. *Neural computation*, 12(1):91–129.

[22] Bressloff, P. C., Cowan, J. D., Golubitsky, M., Thomas, P. J., and Wiener, M. C. (2001). Geometric visual hallucinations, euclidean symmetry and the functional architecture of striate cortex. *Philosophical Transactions of the Royal Society of London B: Biological Sciences*, 356(1407):299–330.

[23] Brown, E., Moehlis, J., and Holmes, P. (2004). On the phase reduction and response dynamics of neural oscillator populations. *Neural computation*, 16(4):673–715.

[24] Brunel, N. and Van Rossum, M. C. (2007). Lapicque's 1907 paper: from frogs to integrate-and-fire. *Biological cybernetics*, 97(5-6):337–339.

[25] Bullmore, E. and Sporns, O. (2012). The economy of brain network organization. *Nature reviews. Neuroscience*, 13(5):336.

[26] Buzsaki, G. (2006). *Rhythms of the Brain*. Oxford University Press.

[27] Camperi, M. and Wang, X. J. (1998). A model of visuospatial working memory in prefrontal cortex: recurrent network and cellular bistability. *Journal of computational neuroscience*, 5(4):383–405.

[28] Champneys, A., Harris, S., Toland, J., Warren, J., and Williams, D. (1995). Algebra, analysis and probability for a coupled system of reaction-diffusion equations. *Philosophical Transactions of the Royal Society of London A: Mathematical, Physical and Engineering Sciences*, 350(1692):69–112.

[29] Champneys, A. R., Kuznetsov, Y. A., and Sandstede, B. (1996). A numerical toolbox for homoclinic bifurcation analysis. *International Journal of Bifurcation and Chaos*, 6:867–888.

[30] Chervin, R., Pierce, P., and Connors, B. (1988). Periodicity and directionality in the propagation of epileptiform discharges across neocortex. *Journal of Neurophysiology*, 60(5):1695–1713.

[31] Chklovskii, D. B. (2004). Exact solution for the optimal neuronal layout problem. *Neural computation*, 16(10):2067–2078.

[32] Chow, C. C. (1998). Phase-locking in weakly heterogeneous neuronal networks. *Physica D: Nonlinear Phenomena*, 118(3):343–370.

[33] Chow, C. C. and Coombes, S. (2006). Existence and wandering of bumps in a spiking neural network model. *SIAM Journal on Applied Dynamical Systems*, 5(4):552–574.

[34] Citri, A. and Malenka, R. C. (2008). Synaptic plasticity: multiple forms, functions, and mechanisms. *Neuropsychopharmacology : official publication of the American College of Neuropsychopharmacology*, 33(1):18–41.

[35] Cohen, A. H., Ermentrout, G. B., Kiemel, T., Kopell, N., Sigvardt, K. A., and Williams, T. L. (1992). Modelling of intersegmental coordination in the lamprey central pattern generator for locomotion. *Trends in neurosciences*, 15(11):434–438.

[36] Cohen, L., Keynes, R., and Hille, B. (1968). Light scattering and birefringence changes during nerve activity. *Nature*, 218(5140):438–441.

[37] Compte, A., Brunel, N., Goldman-rakic, P. S., and Wang, X.-j. (2000). Synaptic Mechanisms and Network Dynamics Underlying Spatial Working Memory in a Cortical Network Model. *Cereb. Cortex*, 10(9):910–923.

[38] Compte, A., Reig, R., Descalzo, V. F., Harvey, M. A., Puccini, G. D., and Sanchez-Vives, M. V. (2008). Spontaneous high-frequency (10–80 hz) oscillations during up states in the cerebral cortex in vitro. *Journal of Neuroscience*, 28(51):13828–13844.

[39] Compte, A., Sanchez-Vives, M. V., McCormick, D. A., and Wang, X.-J. (2003). Cellular and network mechanisms of slow oscillatory activity ($<$ 1 hz) and wave propagations in a cortical network model. *Journal of neurophysiology*, 89(5):2707–2725.

[40] Coombes, S. (2005). Waves, bumps, and patterns in neural field theories. *Biological cybernetics*, 93(2):91–108.

[41] Coombes, S. and Byrne, Á. (2016). Next generation neural mass models. *arXiv preprint arXiv:1607.06251*.

[42] Coombes, S., Lord, G., and Owen, M. (2003). Waves and bumps in neuronal networks with axo-dendritic synaptic interactions. *Physica D: Nonlinear Phenomena*, 178(3-4):219–241.

[43] Coombes, S., Schmidt, H., and Bojak, I. (2012). Interface dynamics in planar neural field models. *The Journal of Mathematical Neuroscience*, 2(1):9.

[44] Cremers, D. and Herz, A. V. M. (2002). Traveling waves of excitation in neural field models: equivalence of rate descriptions and integrate-and-fire dynamics. *Neural computation*, 14(7):1651–1667.

[45] Delaney, K., Gelperin, A., Fee, M., Flores, J., Gervais, R., Tank, D., and Kleinfeld, D. (1994). Waves and stimulus-modulated dynamics in an oscillating olfactory network. *Proceedings of the National Academy of Sciences*, 91(2):669–673.

[46] Desroches, M., Guckenheimer, J., Krauskopf, B., Kuehn, C., Osinga, H. M., and Wechselberger, M. (2012). Mixed-mode oscillations with multiple time scales. *Siam Review*, 54(2):211–288.

[47] Destexhe, A., Bal, T., McCormick, D. A., and Sejnowski, T. J. (1996). Ionic mechanisms underlying synchronized oscillations and propagating waves in a model of ferret thalamic slices. *Journal of neurophysiology*, 76(3):2049–2070.

[48] Diekman, C. O. and Golubitsky, M. (2014). Network symmetry and binocular rivalry experiments. *Journal of mathematical neuroscience*, 4:12.

[49] Diesmann, M., Gewaltig, M.-O., and Aertsen, A. (1999). Stable propagation of synchronous spiking in cortical neural networks. *Nature*, 402(6761):529–533.

[50] Doedel, E. J., Champneys, A. R., Fairgrieve, T. F., Kuznetsov, Y. A., Sandstede, B., Wang, X., et al. (1997). Continuation and bifurcation software for ordinary differential equations (with homcont). *AUTO97, Concordia University, Canada*.

[51] Einstein, A. (1956). *Investigations on the Theory of the Brownian Movement*. Courier Corporation.

[52] Elga, A., Touretzky, D., and Redish, a. (1996). A coupled attractor model of the rodent head direction system. *Network: Computation in Neural Systems*, 7(4):671–685.

[53] Ermentrout, B. (1994). Reduction of conductance-based models with slow synapses to neural nets. *Neural Computation*, 6(4):679–695.

[54] Ermentrout, B. (1996). Type i membranes, phase resetting curves, and synchrony. *Neural computation*, 8(5):979–1001.

[55] Ermentrout, B. (1998a). Neural networks as spatio-temporal pattern-forming systems. *Reports on Progress in Physics*, 61(4):353–430.

[56] Ermentrout, B. (1998b). The analysis of synaptically generated traveling waves. *Journal of computational neuroscience*, 5(2):191–208.

[57] Ermentrout, G. and Kopell, N. (1990). Oscillator death in systems of coupled neural oscillators. *SIAM Journal on Applied Mathematics*, 50(1):125–146.

[58] Ermentrout, G. B. (1981). n: m phase-locking of weakly coupled oscillators. *Journal of Mathematical Biology*, 12(3):327–342.

[59] Ermentrout, G. B. and Cowan, J. D. (1979). A mathematical theory of visual hallucination patterns. *Biological cybernetics*, 34(3):137–150.

[60] Ermentrout, G. B. and Kleinfeld, D. (2001). Traveling electrical waves in cortex: insights from phase dynamics and speculation on a computational role. *Neuron*, 29(1):33–44.

[61] Ermentrout, G. B. and Kopell, N. (1984). Frequency plateaus in a chain of weakly coupled oscillators, i. *SIAM journal on Mathematical Analysis*, 15(2):215–237.

[62] Ermentrout, G. B. and McLeod, J. B. (1993). Existence and uniqueness of travelling waves for a neural network. *Proceedings of the Royal Society of Edinburgh: Section A Mathematics*, 123:461–478.

[63] Ermentrout, G. B. and Terman, D. H. (2010). *Mathematical foundations of neuroscience*, volume 35. Springer Science & Business Media.

[64] FitzHugh, R. (1961). Impulses and physiological states in theoretical models of nerve membrane. *Biophysical journal*, 1(6):445–466.

[65] Frackowiak, R., Markram, H., and Markram, H. (2015). The future of human cerebral cartography : a novel approach. *Phil. Trans. R. Soc. B*, B 370: 201.

[66] Freeman, W. J. and Barrie, J. M. (2000). Analysis of spatial patterns of phase in neocortical gamma eegs in rabbit. *Journal of neurophysiology*, 84(3):1266–1278.

[67] Funahashi, S., Chafee, M. V., and Goldman-Rakic, P. S. (1993). Prefrontal neuronal activity in rhesus monkeys performing a delayed anti-saccade task. *Nature*, 365(6448):753–756.

[68] Fuster, J. M. and Alexander, G. E. (1971). Neuron Activity Related to Short-Term Memory.

[69] Gabriel, A. and Eckhorn, R. (2003). A multi-channel correlation method detects traveling γ-waves in monkey visual cortex. *Journal of neuroscience methods*, 131(1):171–184.

[70] Garcia-Lopez, P., Garcia-Marin, V., and Freire, M. (2010). The histological slides and drawings of cajal. *Frontiers in neuroanatomy*, 4.

[71] Gerstner, W. (1995). Time structure of the activity in neural network models. *Physical review E*, 51(1):738.

[72] Gerstner, W. and Kistler, W. (2002). *Spiking Neuron Models Cambridge University Press*. Cambridge.

[73] Gerstner, W., Sprekeler, H., and Deco, G. (2012). Theory and simulation in neuroscience. *Science (New York, N.Y.)*, 338(6103):60–5.

[74] Gerstner, W., Van Hemmen, J. L., and Cowan, J. D. (1996). What matters in neuronal locking? *Neural computation*, 8(8):1653–1676.

[75] Giese, M. A. (2012). *Dynamic neural field theory for motion perception*, volume 469. Springer Science & Business Media.

[76] Glass, L. and Mackey, M. C. (1988). *From clocks to chaos: the rhythms of life*. Princeton University Press.

[77] Goldman-Rakic, P. (1995). Cellular basis of working memory. *Neuron*, 14:477–485.

[78] Goldstein, R. E., Muraki, D. J., and Petrich, D. M. (1996). Interface proliferation and the growth of labyrinths in a reaction-diffusion system. *Physical Review E*, 53(4):3933.

[79] Golomb, D. (1998). Models of neuronal transient synchrony during propagation of activity through neocortical circuitry. *Journal of neurophysiology*, 79(1):1–12.

[80] Golomb, D. and Amitai, Y. (1997). Propagating neuronal discharges in neocortical slices: computational and experimental study. *Journal of neurophysiology*, 78(3):1199–1211.

[81] Golomb, D. and Ermentrout, G. B. (1999). Continuous and lurching traveling pulses in neuronal networks with delay and spatially decaying connectivity. *Proceedings of the National Academy of Sciences*, 96(23):13480–13485.

[82] Golomb, D. and Ermentrout, G. B. (2000). Effects of delay on the type and velocity of travelling pulses in neuronal networks with spatially decaying connectivity. *Network: Computation in Neural Systems*, 11(3):221–246.

[83] Golomb, D. and Ermentrout, G. B. (2001). Bistability in pulse propagation in networks of excitatory and inhibitory populations. *Physical Review Letters*, 86(18):4179.

[84] Gong, P. and Van Leeuwen, C. (2009). Distributed dynamical computation in neural circuits with propagating coherent activity patterns. *PLoS Computational Biology*, 5(12).

[85] González-Ramírez, L. R., Ahmed, O. J., Cash, S. S., Wayne, C. E., and Kramer, M. a. (2015). A Biologically Constrained, Mathematical Model of Cortical Wave Propagation Preceding Seizure Termination. *PLOS Computational Biology*, 11(2):e1004065.

[86] Grinvald, A., Lieke, E. E., Frostig, R. D., and Hildesheim, R. (1994). Cortical point-spread function and long-range lateral interactions revealed by real-time optical imaging of macaque monkey primary visual cortex. *Journal of Neuroscience*, 14(5):2545–2568.

[87] Gross, G. W., Rhoades, B. K., Azzazy, H. M., and Wu, M.-C. (1995). The use of neuronal networks on multielectrode arrays as biosensors. *Biosensors and Bioelectronics*, 10(6-7):553–567.

[88] Gutkin, B. S., Bard Ermentrout, G., and O'Sullivan, J. (2000). Layer 3 patchy recurrent excitatory connections may determine the spatial organization of sustained activity in the primate prefrontal cortex. *Neurocomputing*, 32-33:391–400.

[89] Haken, H. (2007). *Brain dynamics: an introduction to models and simulations*. Springer Science & Business Media.

[90] Han, F., Caporale, N., and Dan, Y. (2008). Reverberation of recent visual experience in spontaneous cortical waves. *Neuron*, 60(2):321–327.

[91] Hansel, D., Mato, G., and Meunier, C. (1993). Phase dynamics for weakly coupled hodgkin-huxley neurons. *EPL (Europhysics Letters)*, 23(5):367.

[92] Hansel, D., Mato, G., and Meunier, C. (1995). Synchrony in excitatory neural networks. *Neural computation*, 7(2):307–37.

[93] Hartline, H. K. and Ratliff, F. (1972). Inhibitory interaction in the retina of limulus. *Physiology of Photoreceptor Organs*, pages 381–447.

[94] Häusser, M. (2000). The hodgkin-huxley theory of the action potential. *Nature neuroscience*, 3:1165–1165.

[95] Heitmann, S., Gong, P., and Breakspear, M. (2012). A computational role for bistability and traveling waves in motor cortex. *Frontiers in Computational Neuroscience*, 6(September):1–15.

[96] Hellwig, B. (2000). A quantitative analysis of the local connectivity between pyramidal neurons in layers 2/3 of the rat visual cortex. *Biological cybernetics*, 82(2):111–121.

[97] Hirsch, J. A. (2003). Synaptic physiology and receptive field structure in the early visual pathway of the cat. *Cerebral cortex (New York, N.Y. : 1991)*, 13(1):63–69.

[98] Hodgkin, A. L. and Huxley, A. F. (1939). Action potentials recorded from inside a nerve fibre. *Nature*, 144(3651):710–711.

[99] Hodgkin, A. L. and Huxley, A. F. (1952). A quantitative description of membrane current and its application to conduction and excitation in nerve. *The Journal of physiology*, 117(4):500.

[100] Hopfield, J. J. (1984). Neurons with graded response have collective computational properties like those of two-state neurons. *Proceedings of the national academy of sciences*, 81(10):3088–3092.

[101] Hoppensteadt, F. C. and Izhikevich, E. M. (2012). *Weakly connected neural networks*, volume 126. Springer Science & Business Media.

[102] Huang, X., Troy, W. C., Yang, Q., Ma, H., Laing, C. R., Schiff, S. J., and Wu, J.-Y. (2004). Spiral waves in disinhibited mammalian neocortex. *Journal of Neuroscience*, 24(44):9897–9902.

[103] Hutcheon, B. and Yarom, Y. (2000). Resonance, oscillation and the intrinsic frequency preferences of neurons. *Trends in neurosciences*, 23(5):216–222.

[104] Isaac, R. C. . J. T. R. (2010). Emergence of cortical inhibition by coordinated sensory-driven plasticity at distinct synaptic loci. *Nature Neuroscience*, Vol. 82 no. 3(13):1240–1248.

[105] Ito, J., Nikolaev, A. R., and Van Leeuwen, C. (2005). Spatial and temporal structure of phase synchronization of spontaneous alpha eeg activity. *Biological cybernetics*, 92(1):54–60.

[106] Izhikevich, E. M. (2003). Simple model of spiking neurons. *IEEE Transactions on neural networks*, 14(6):1569–1572.

[107] Keener, J. and Sneyd, J. (2010). *Mathematical physiology: I: cellular physiology*. Springer Science & Business Media.

[108] Keller, H. B. (1977). Numerical solution of bifurcation and nonlinear eigenvalue ploblems. *Applications of bifurcation theory*, pages 359–384.

[109] Kepler, T. B., Abbott, L., and Marder, E. (1992). Reduction of conductance-based neuron models. *Biological Cybernetics*, 66(5):381–387.

[110] Kilpatrick, Z. P. and Ermentrout, B. (2013). Wandering bumps in stochastic neural fields. *SIAM Journal on Applied Dynamical Systems*, 12(1):61–94.

[111] Kim, U., Bal, T., and McCormick, D. a. (1995). Spindle waves are propagating synchronized oscillations in the ferret LGNd in vitro. *Journal of neurophysiology*, 74(3):1301–1323.

[112] Kistler, W. M., Seitz, R., and Van Hemmen, J. L. (1998). Modeling collective excitations in cortical tissue. *Physica D: Nonlinear Phenomena*, 114(3-4):273–295.

[113] Klassen, J., Pinkwater, D., and Huff, S. (2011). *I want my hat back*. Candlewick Press.

[114] Kleinfeld, D., Delaney, K., Fee, M., Flores, J., Tank, D., and Gelperin, A. (1994). Dynamics of propagating waves in the olfactory network of a terrestrial mollusk: an electrical and optical study. *Journal of Neurophysiology*, 72(3):1402–1419.

[115] Koch, C. and Segev, I. (1998). *Methods in neuronal modeling: from ions to networks*. MIT press.

[116] Kuramoto, Y. (2012). *Chemical oscillations, waves, and turbulence*, volume 19. Springer Science & Business Media.

[117] Laing, C. R. (2005). Spiral waves in nonlocal equations. *SIAM Journal on Applied Dynamical Systems*, 4(3):588–606.

[118] Laing, C. R. (2014). Derivation of a neural field model from a network of theta neurons. *Physical Review E*, 90(1):010901.

[119] Laing, C. R. (2016). Phase oscillator network models of brain dynamics. *Computational Models of Brain and Behavior*.

[120] Laing, C. R. and Chow, C. C. (2001). Stationary bumps in networks of spiking neurons. *Neural computation*, 13(7):1473–94.

[121] Laing, C. R. and Longtin, A. (2001). Noise-induced stabilization of bumps in systems with long-range spatial coupling. *Physica D: Nonlinear Phenomena*, 160(3-4):149–172.

[122] Laing, C. R. and Troy, W. C. (2003). PDE methods for nonlocal models. *SIAM Journal on Applied Dynamical Systems*, 2(3):487–516.

[123] Laing, C. R., Troy, W. C., Gutkin, B., and Ermentrout, G. B. (2002). Multiple Bumps in a Neuronal Model of Working Memory. *SIAM Journal on Applied Mathematics*, 63(1):62–97.

[124] Lam, Y.-W., Cohen, L. B., Wachowiak, M., and Zochowski, M. R. (2000). Odors elicit three different oscillations in the turtle olfactory bulb. *Journal of Neuroscience*, 20(2):749–762.

[125] Liley, D. T., Cadusch, P. J., and Dafilis, M. P. (2002). A spatially continuous mean field theory of electrocortical activity. *Network: Computation in Neural Systems*, 13(1):67–113.

[126] Livingstone, M. S. (1996). Oscillatory firing and interneuronal correlations in squirrel monkey striate cortex. *Journal of neurophysiology*, 75(6):2467–2485.

[127] Llinás, R. R. (1988). The intrinsic electrophysiological properties of mammalian neurons: insights into central nervous system function. *Science*, 242(4886):1654–1664.

[128] Lord, G. and Thümmler, V. (2012). Computing Stochastic Travelling Waves. *SIAM Journal on Scientific Computing*, 34(1):24–43.

[129] Luke, T. B., Barreto, E., and So, P. (2013). Complete classification of the macroscopic behavior of a heterogeneous network of theta neurons. *Neural computation*, 25(12):3207–3234.

[130] MacKay, D. M. and McCulloch, W. S. (1952). The limiting information capacity of a neuronal link. *Bulletin of Mathematical Biology*, 14(2):127–135.

[131] Macknik, S. L. and Martinez-Conde, S. (2004). The spatial and temporal effects of lateral inhibitory networks and their relevance to the visibility of spatiotemporal edges. *Neurocomputing*, 58-60:775–782.

[132] Marder, E. and Calabrese, R. L. (1996). Principles of rhythmic motor pattern generation. *Physiological reviews*, 76(3):687–717.

[133] Maria Cecilia Angulo, Jean Rossier, E. A. (1999). Postsynaptic Glutamate Receptors and Integrative Properties of Fast-Spiking Interneurons in the Rat Neocortex. *American Physiological Society*, Vol. 82 no. 3(20):1295–1302.

[134] Massimini, M., Huber, R., Ferrarelli, F., Hill, S., and Tononi, G. (2004). The sleep slow oscillation as a traveling wave. *Journal of Neuroscience*, 24(31):6862–6870.

[135] McCormick, D. A. and Contreras, D. (2001). On the cellular and network bases of epileptic seizures. *Annual review of physiology*, 63(1):815–846.

[136] McCulloch, W. S. and Pitts, W. (1943). A logical calculus of the ideas immanent in nervous activity. *The bulletin of mathematical biophysics*, 5(4):115–133.

[137] Miller, E. K., Erickson, C. A., and Desimone, R. (1996). Neural mechanisms of visual working memory in prefrontal cortex of the macaque. *Journal of neuroscience*, 16(16):5154–5167.

[138] Miller, P. (2013). Stabilization of Memory States by Stochastic Facilitating Synapses. *The Journal of Mathematical Neuroscience*, 3(1):19.

[139] Morris, C. and Lecar, H. (1981). Voltage oscillations in the barnacle giant muscle fiber. *Biophysical journal*, 35(1):193–213.

[140] Nádasdy, Z., Hirase, H., Czurkó, A., Csicsvari, J., and Buzsáki, G. (1999). Replay and time compression of recurring spike sequences in the hippocampus. *Journal of Neuroscience*, 19(21):9497–9507.

[141] Nauhaus, I., Busse, L., Carandini, M., and Ringach, D. L. (2009). Stimulus contrast modulates functional connectivity in visual cortex. *Nature neuroscience*, 12(1):70–76.

[142] Nolte, G., Ziehe, A., Nikulin, V. V., Schlögl, A., Krämer, N., Brismar, T., and Müller, K.-R. (2008). Robustly estimating the flow direction of information in complex physical systems. *Physical review letters*, 100(23):234101.

[143] Osan, R., Curtu, R., Rubin, J., and Ermentrout, B. (2004). Multiple-spike waves in a one-dimensional integrate-and-fire neural network. *Journal of Mathematical Biology*, 48(3):243–274.

[144] Osan, R. and Ermentrout, B. (2001). Two dimensional synaptically generated traveling waves in a theta-neuron neural network. *Neurocomputing*, 38-40:789–795.

[145] Osan, R. and Ermentrout, B. (2002). The evolution of synaptically generated waves in one-and two-dimensional domains. *Physica D: Nonlinear Phenomena*, 163(3):217–235.

[146] Ott, E. and Antonsen, T. M. (2008). Low dimensional behavior of large systems of globally coupled oscillators. *Chaos: An Interdisciplinary Journal of Nonlinear Science*, 18(3):037113.

[147] Ott, E. and Antonsen, T. M. (2009). Long time evolution of phase oscillator systems. *Chaos: An interdisciplinary journal of nonlinear science*, 19(2):023117.

[148] Owen, M. R., Laing, C. R., and Coombes, S. (2007). Bumps and rings in a two-dimensional neural field: splitting and rotational instabilities. *New Journal of Physics*, 9(10):378.

[149] Oşan, R., Chen, G., Feng, R., and Tsien, J. Z. (2011). Differential consolidation and pattern reverberations within episodic cell assemblies in the mouse hippocampus. *PloS one*, 6(2):e16507.

[150] Perin, R., Berger, T. K., and Markram, H. (2011). A synaptic organizing principle for cortical neuronal groups. *Proceedings of the National Academy of Sciences*, 108(13):5419–5424.

[151] Petersen, C. C., Grinvald, A., and Sakmann, B. (2003). Spatiotemporal dynamics of sensory responses in layer 2/3 of rat barrel cortex measured in vivo by voltage-sensitive dye imaging combined with whole-cell voltage recordings and neuron reconstructions. *Journal of neuroscience*, 23(4):1298–1309.

[152] Pinto, D. J. and Ermentrout, G. B. (2001). Spatially structured activity in synaptically coupled neuronal networks: I. traveling fronts and pulses. *SIAM journal on Applied Mathematics*, 62(1):206–225.

[153] Pinto, D. J., Patrick, S. L., Huang, W. C., and Connors, B. W. (2005). Initiation, propagation, and termination of epileptiform activity in rodent neocortex in vitro involve distinct mechanisms. *Journal of Neuroscience*, 25(36):8131–8140.

[154] Ploner, C. J., Gaymard, B., Rivaud, S., Agid, Y., and Pierrot-Deseilligny, C. (1998). Temporal limits of spatial working memory in humans. *European Journal of Neuroscience*, 10(2):794–797.

[155] Prechtl, J. C., Cohen, L. B., Pesaran, B., Mitra, P. P., and Kleinfeld, D. (1997). Visual stimuli induce waves of electrical activity in turtle cortex. *Proceedings of the National Academy of Sciences of the United States of America*, 94(14):7621–7626.

[156] Prut, Y., Vaadia, E., Bergman, H., Haalman, I., Slovin, H., and Abeles, M. (1998). Spatiotemporal structure of cortical activity: properties and behavioral relevance. *Journal of neurophysiology*, 79(6):2857–2874.

[157] Rankin, J., Avitabile, D., Baladron, J., Faye, G., and Lloyd, D. J. (2014). Continuation of localized coherent structures in nonlocal neural field equations. *SIAM Journal on Scientific Computing*, 36(1):B70–B93.

[158] Ribary, U., Ioannides, A., Singh, K. D., Hasson, R., Bolton, J., Lado, F., Mogilner, A., and Llinas, R. (1991). Magnetic field tomography of coherent thalamocortical 40-hz oscillations in humans. *Proceedings of the National Academy of Sciences*, 88(24):11037–11041.

[159] Richardson, K. A., Schiff, S. J., and Gluckman, B. J. (2005). Control of traveling waves in the mammalian cortex. *Physical review letters*, 94(2):028103.

[160] Rinzel, J. (1985). Excitation dynamics: insights from simplified membrane models. In *Fed. Proc*, volume 44, pages 2944–2946.

[161] Rinzel, J. (1987). *A formal classification of bursting mechanisms in excitable systems*. Springer.

[162] Robert, C. P. (2004). *Monte carlo methods*. Wiley Online Library.

[163] Ross, S. M. (2013). *Applied probability models with optimization applications*. Courier Corporation.

[164] Rubino, D., Robbins, K. A., and Hatsopoulos, N. G. (2006). Propagating waves mediate information transfer in the motor cortex. *Nature neuroscience*, 9(12):1549.

[165] Salvador, R., Suckling, J., Coleman, M. R., Pickard, J. D., Menon, D., and Bullmore, E. (2005). Neurophysiological architecture of functional magnetic resonance images of human brain. *Cerebral cortex*, 15(9):1332–1342.

[166] Sandstede, B. (2002). Stability of travelling waves. *Handbook of dynamical systems*, 2:983–1055.

[167] Sauseng, P., Klimesch, W., Gruber, W., Doppelmayr, M., Stadler, W., and Schabus, M. (2002). The interplay between theta and alpha oscillations in the human electroencephalogram reflects the transfer of information between memory systems. *Neuroscience letters*, 324(2):121–124.

[168] Sherrington, C. (1910). *The integrative action of the nervous system*. CUP Archive.

[169] Shil'nikov, L. P. (2001). *Methods of qualitative theory in nonlinear dynamics*, volume 5. World Scientific.

[170] Skaggs, W. E., Knierim, J. J., Kudrimoti, H. S., and McNaughton, B. L. (1995). A model of the neural basis of the rat's sense of direction. *Advances in neural information processing systems*, 7(1984):173–180.

[171] Somers, D. C., Nelson, S. B., and Sur, M. (1995). An emergent model of orientation selectivity in cat visual cortical simple cells. *Journal of Neuroscience*, 15(8):5448–5465.

[172] Sporns, O. (2010). *Networks of the Brain*. MIT press.

[173] Stepanyants, A., Hirsch, J. A., Martinez, L. M., Kisvárday, Z. F., Ferecskó, A. S., and Chklovskii, D. B. (2007). Local potential connectivity in cat primary visual cortex. *Cerebral Cortex*, 18(1):13–28.

[174] Steriade, M. and Timofeev, I. (2003). Neuronal plasticity in thalamocortical networks during sleep and waking oscillations. *Neuron*, 37(4):563–576.

[175] Strong, S. P., Koberle, R., van Steveninck, R. R. d. R., and Bialek, W. (1998). Entropy and information in neural spike trains. *Physical review letters*, 80(1):197.

[176] Tasaki, I. and Hagiwara, S. (1957). Demonstration of two stable potential states in the squid giant axon under tetraethylammonium chloride. *The Journal of general physiology*, 40(6):859–885.

[177] Terman, D., Rubin, J. E., Yew, a. C., and Wilson, C. J. (2002). Activity patterns in a model for the subthalamopallidal network of the basal ganglia. *The Journal of neuroscience : the official journal of the Society for Neuroscience*, 22(7):2963–76.

[178] Thomson, A. M. (2000). Molecular frequency filters at central synapses. *Progress in neurobiology*, 62(2):159–196.

[179] Thomson, A. M. and Morris, O. T. (2002). Selectivity in the inter-laminar connections made by neocortical neurones. *Journal of neurocytology*, 31(3-5):239–246.

[180] Thomson, A. M., West, D. C., Wang, Y., and Bannister, A. P. (2002). Synaptic connections and small circuits involving excitatory and inhibitory neurons in layers 2–5 of adult rat and cat neocortex: triple intracellular recordings and biocytin labelling in vitro. *Cerebral cortex*, 12(9):936–953.

[181] Thul, R., Smith, G. D., and Coombes, S. (2008). A bidomain threshold model of propagating calcium waves. *Journal of mathematical biology*, 56(4):435–63.

[182] Traub, R. D., Contreras, D., Cunningham, M. O., Murray, H., LeBeau, F. E., Roopun, A., Bibbig, A., Wilent, W. B., Higley, M. J., and Whittington, M. A. (2005). Single-column thalamocortical network model exhibiting gamma oscillations, sleep spindles, and epileptogenic bursts. *Journal of neurophysiology*, 93(4):2194–2232.

[183] Traub, R. D., Miles, R., and Jefferys, J. (1993). Synaptic and intrinsic conductances shape picrotoxin-induced synchronized after-discharges in the guinea-pig hippocampal slice. *The Journal of Physiology*, 461(1):525–547.

[184] Tuckerman, L. S. and Barkley, D. (2000). Bifurcation analysis for timesteppers. *Numerical methods for bifurcation problems and large-scale dynamical systems*, 119(543-466).

[185] van Vreeswijk, C. (1996). Partial synchronization in populations of pulse-coupled oscillators. *Physical Review E*, 54(5):5522.

[186] Wang, X. J. (1999). Synaptic basis of cortical persistent activity: the importance of NMDA receptors to working memory. *The Journal of neuroscience : the official journal of the Society for Neuroscience*, 19(21):9587–603.

[187] Wasylenko, T. M., Cisternas, J. E., Laing, C. R., and Kevrekidis, I. G. (2010). Bifurcations of lurching waves in a thalamic neuronal network. *Biological Cybernetics*, 103(6):447–462.

[188] Whitteridge, D. (1958). The physiology of nerve cells. by jc eccles. baltimore: The johns hopkins press. 1957. pp. ix+ 270. 30s. *Experimental Physiology*, 43(1):133–134.

[189] Wilson, H. R., Blake, R., and Lee, S. H. (2001). Dynamics of travelling waves in visual perception. *Nature*, 412(6850):907–10.

[190] Wilson, H. R. and Cowan, J. D. (1972). Excitatory and inhibitory interactions in localized populations of model neurons. *Biophysical journal*, 12(1):1–24.

[191] Wimmer, K., Nykamp, D. Q., Constantinidis, C., and Compte, A. (2014). Bump attractor dynamics in prefrontal cortex explains behavioral precision in spatial working memory. *Nature neuroscience*, 17(3):431–9.

[192] Winfree, A. T. (2001). *The geometry of biological time*, volume 12. Springer Science & Business Media.

[193] Wu, J.-Y., Guan, L., Bai, L., and Yang, Q. (2001). Spatiotemporal properties of an evoked population activity in rat sensory cortical slices. *Journal of neurophysiology*, 86(5):2461–2474.

[194] Wu, J.-y., Guan, L., and Tsau, Y. (1999). Propagating activation during oscillations and evoked responses in neocortical slices. *Journal of Neuroscience*, 19(12):5005–5015.

[195] Wu, J.-Y., Xiaoying Huang, and Chuan Zhang (2008). Propagating waves of activity in the neocortex: what they are, what they do. *The Neuroscientist : a review journal bringing neurobiology, neurology and psychiatry*, 14(5):487–502.

[196] Xu, W., Huang, X., Takagaki, K., and Wu, J.-y. (2007). Compression and reflection of visually evoked cortical waves. *Neuron*, 55:119–129.

[197] y Cajal, S. R. (1995). *Histology of the nervous system of man and vertebrates*, volume 1. Oxford University Press, USA.

[198] Yoshimura, Y., Dantzker, J. L., and Callaway, E. M. (2005). Excitatory cortical neurons form fine-scale functional networks. *Nature*, 433(7028):868–873.

[199] Zhang, K. (1996). Representation of spatial orientation by the intrinsic dynamics of the head-direction cell ensemble: a theory. *Journal of Neuroscience*, 16(6):2112–2126.